New Algorithms for Enhancing Ultrasonic NDE of Difficult Materials

Rui Gongzhang

Department of Electronic and Electrical Engineering

University of Strathclyde

A thesis submitted for the degree of

Doctor of Philosophy

February 2017

This thesis is the result of the author's original research. It has been composed by the author and has not been previously submitted for examination which has led to the award of a degree.

The copyright of this thesis belongs to the author under the terms of the United Kingdom Copyright Acts as qualified by University of Strathclyde Regulation 3.50. Due acknowledgement must always be made of the use of any material contained in, or derived from, this thesis.

Signed:

Date:

Abstract

In Non-Destructive Evaluation (NDE) inspection, a range of materials exist that exhibit a heterogeneous or acoustically scattering microstructure, for example austenitic steels and Inconel alloys, and are used extensively across many industrial sectors. When inspected using conventional ultrasound techniques, defect signals are significantly corrupted by noise from randomly distributed scatterer associated with the material microstructure. In some cases, even defects that are much larger than the grain size distribution in the microstructure can be difficult to detect. This Thesis presents an investigation into the development of new algorithms to suppress backscattering noise in the received ultrasonic echoes associated with both individual transducers and phased arrays.

Using the fact that structural noise in these difficult materials is frequency coherent, frequency diversity based techniques like the well-known Split Spectrum Processing have been developed. However, conventional algorithms are either ineffective or sensitive to the variations of material characteristics, especially when the signal to noise ratio (SNR) is low.

A frequency diversity based technique, Moving Bandwidth Split Spectrum Processing (MB-SSP), has been developed, which is less influenced by material characteristics. MB-SSP first selects an ascending series of frequency bands and a trace is reconstructed for each selected band in which a defect is present: this occurs when all frequency components are in uniform sign. Combining all reconstructed signals through averaging gives a probability profile of potential defect positions.

A range of supervised machine learning techniques has also been employed to further improve detect capability, if the pre-acquired training data is available. Instead of investigating the structure and pattern of the spectrum of an individual echo, the proposed method focuses on the distinction between the ensembles of

defect signals and clutter noise. A training process is used to establish the statistical analysis, based on which a hypothesis test is then applied to the received echoes to indicate defects. The approach is designed to be adaptive to the material microstructure and characteristics due to the statistical training aspect of the technique.

The concept of applying clustering algorithms to further reduce the influence of artefact noise remaining in A-scan data after processing by MB-SSP or a conventional defect detection algorithm is also discussed. The segmental signals that potentially contain defects in the processed A-scans are clustered into groups. The distinction and similarity between each group and the ensemble of randomly selected noise segments can be observed by applying a classification algorithm. Each class will then be labelled as either a 'legitimate reflector' or 'artefact' based on this observation and the expected probability of detection (PoD) and the probability of false alarm (PFA) determined.

Finally, the developed A-scan based noise reduction algorithms have been extended into phased array imaging. Here the techniques are applied to the raw Full Matrix Capture (FMC) datasets prior to processing by an appropriate imaging algorithm. Total Focusing Method (TFM) and the focused B-scan imaging is applied to both standard and pre-processed FMC datasets on both simulated data and experimental data from coarse-grained materials. Importantly, the background noise is significantly suppressed in every case using the pre-processed FMC data.

Acknowledgements

First of all, I would like to offer my sincere gratitude to my Supervisor Prof. Anthony Gachagan, who has provide the invaluable academic guidance and support throughout the past few years, especially for the grammatical and technical advice during my Thesis writing. This thesis would not have been possible without his support.

I would also like to extend my thanks to Dr. Jinchang Ren and Dr. Minghui Li, for the inspiration they have provided in my research.

I would like to thank all members in CUE, for their valuable and kindly assistance. Thanks to Dr. Bo Xiao and Dr. Timothy Lardner for their friendship and many helpful suggestions. Thanks to Dr. Jerzy Dziewiewiez and Walter Galbraith for their support in my experiments. Thanks to Lynn Morrison and Rhona Nicholson for their help throughout my time in CUE. In addition, many thanks to Huan Zhao, Haoyu Fang and Jie Gao for their support during my most difficult time.

I would also like to thank E.oN, especially Dr. Colin Brett, for the financial support and providing test samples.

My gratitude extends to all my friends. Thanks to Rong Fu for her countless encouragement and moral support throughout my entire study. Thanks to Dr. Ding Wang for his friendship and support. Thanks to Dr. Yi Jing, Dr. Sirui Li, Dr. Yiming Gao and Xiaoke Su and all my other classmates who have also completed their PhD in Strathclyde, and best wishes to them all. Thanks also to my friend Nataliya Gorban for her moral support during the critical period of my PhD.

Special thanks to my parents, Min Gongzhang and Lihua Han, for their endless love in my life.

Finally, and most importantly, I am eternally grateful to my girlfriend Zhiqing Fu, for her unwavering support, patience, unconditional love and all the sacrifice she made during the past eight years. She is always there encouraging me when I feel anxious in the study. Without her, the completion of my PhD would not be possible.

List of Acronyms

AHDM	*Array High Dispersion Model*
ANN	*Artificial Neural Networks*
ANFIS	*Adaptive-network-based Fuzzy Inference System*
API	*Array Performance Indicator*
ASCII	*American Standard Code for Information Interchange*
CAFI	*Correlation for Adaptively Focused Imaging*
CDF	*Cumulative Distribution Function*
CPU	*Central Processing Unit*
CUDA	*Compute Unified Device Architecture*
CWT	*Continuous Wavelet Transform*
DAX	*Dual Apodization with Cross-correlation*
DFT	*Discrete Fourier Transform*
DORT	*Decomposition of the Time Reversal Operator (abbreviated from French words)*
DWT	*Discrete Wavelet Transform*
ECDF	*Empirical Cumulative Distribution Function*
FFT	*Fast Fourier Transform*
FMC	*Full Matrix Capture*
FSPC	*Frequency Spatial Polarity Coherence*
FT	*Fourier Transform*

GA	*Genetic Algorithm*
GP-GPU	*General Purpose Graphical Processing Unit*
GPU	*Graphical Processing Unit*
HDM	*High Dispersion Model*
HMC	*Half Matrix Capture*
IFT	*Inverse Fourier transform*
ISODATA	*Iterative Self-Organizing Data Analysis Technique*
kNN	*k-Nearest Neighbors*
LDM	*Low Dispersion Model*
MB-SSP	*Moving Bandwidth Split Spectrum Processing*
MIN	*Minimization*
MLP	*Multilayer Perceptron*
NB	*Naïve Bayes*
NDE	*Non-Destructive Evaluation*
NMIN	*Normalised Minimization*
NNCC	*Nearest Neighbour Cross-Correlation*
OD	*Optimal Detection*
PAC	*Phased Array Controller*
PD	*Probability of Detection*
PCA	*Principal Component Analysis*
PCI	*Phase Coherence Imaging*
PFA	*Probability of False Alarm*
PRDM	*Potential Real Defect Miner*
PSF	*Point Spread Function*

PT	*Polarity Thresholding*
PTS	*Polarity Thresholding with Scaling*
RF	*Radio Frequency*
ROC	*Receiver Operating Characteristic*
SAE	*Stacked Autoencoders*
SAFT	*Synthetic Aperture Focusing Technique*
SASACI	*Sub-Aperture Spatially Averaged Correlation Imaging*
SDH	*Side Drilled Hole*
SDSA	*Spectral Distribution Similarity Analysis*
SNR	*Signal to Noise Ratio*
SRC	*Segment Recognition Classifier*
SSP	*Split Spectrum Processing*
STFT	*Short-Time Fourier Transform*
SVM	*Support Vector Machine*
TFM	*Total Focusing Method*
TNR	*True Negative Rate*
TPR	*True Positive Rate*
TR-MUSIC	*Time Reversal with Multiple Signal Classification*
TRM	*Time Reversal Mirror*
UT	*Ultrasonic Testing*
VTFM	*Vector Total Focusing Method*
WCSS	*Within-Cluster Sum of Squares*
WT	*Wavelet Transform*

Table of Contents

Chapter 1

Introduction

This Chapter states the motivation for the work, contribution to knowledge, list of publications, and finally, provides a synopsis of each Chapter in the Thesis.

1.1 Motivation for the work

Non-Destructive Evaluation (NDE) plays an essential role in modern engineering. Contemporary NDE techniques are widely used in a range of fields, such as civil engineering, aerospace, manufacturing and power generation [1]. It is important for industry to maintain structural integrity of safety critical components like turbine blade, aircraft wings, and high-pressure pipes [2]. One of the major techniques used in NDE is Ultrasonic Testing (UT), which uses high frequency sound waves to conduct inspections and make measurements. These include flaw detection/evaluation, dimensional measurement and material characterization [3].

However, many materials used in industry exhibit heterogeneous or acoustically scattering properties which inhibit conventional ultrasonic inspection techniques. For example, new 'superalloys' that have been developed to operate in environments of extreme high pressure and heat [4], and the alloys used in aircraft engine turbines to resist a large amount of stress. These materials are critical to safety and must be test regularly [5]. However, the grain size in these materials are usually comparable in scale to the propagating ultrasonic wavelength, which results in interaction between the ultrasonic waves and the granular microstructure [6]. Figure 1.1 illustrates the microstructure distribution for an Inconel 617 sample [7]. Figure 1.1(a) shows the highly polished surface required for analysis using Spatially Resolved Acoustic

Spectroscopy (SRAS) [8] and Figure 1.1(b) presents the measured spatial distribution of the grains within the material microstructure. Interestingly, this sample is representative of an equiaxed-grain material exhibiting macroscopically isotropy but microscopically randomly oriented grains. This material belongs to a class of materials often referred to as 'difficult materials' in ultrasound NDE.
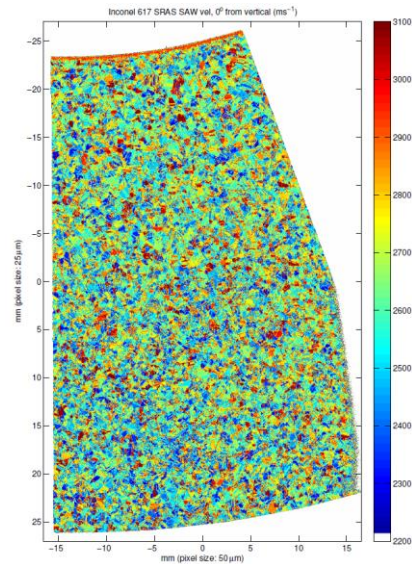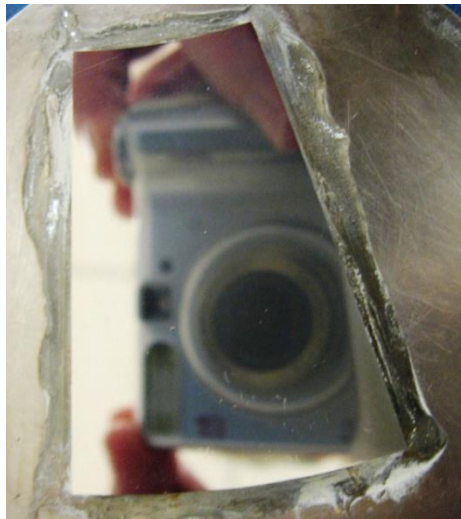
(a) Cut and polished section of sample   *(b) SRAS surface acoustic wave map*

Figure 1.1. SRAS image of the Inconel 617 sample illustrating the distribution of the material microstructure [6].

The granular microstructures of materials are formed in metalworking processes such as casting and welding. During the solidification process, atoms of the molten metal start to bond together at random nucleation sites and begin to form crystals. As the solidification continues, the crystals grow separately in size until adjacent crystals come into contact with each other. Due to the randomness of the locations of the nucleation sites and the growth direction of the crystals, the crystals are formed with various geometries and orientations [9]. These crystals are usually referred to as grains in engineering materials and the interface between adjacent grains is named a grain boundary. When inspecting with ultrasound, these grain structures can cause wave scattering and hence, they have also been referred as scatters. Importantly, for Ultrasonic NDE, the grain structure of the materials can generate strong coherent noise, which can significantly distort or mask the echoes of interest. Unlike

electronic noise which is usually caused by thermal effects on electronic circuits of ultrasonic devices, grain noise is time invariant and cannot be simply removed by applying time domain averaging. One way to reduce the effect of scattering is to lower the frequency of the inspection ultrasound wave and hence, increase the acoustic wavelength of the propagating ultrasonic energy. However, the resolution of received signals will be reduced and inhibit the inspection of small targets. To detect and size these small targets, a sufficiently high frequency must be selected. Moreover, since the flaw echoes and grain noise occupy similar portions of the frequency band of the transduction system, conventional bandpass filtering techniques also fail to suppress grain noise without affecting the information comprising the flaw echoes [10].

With the presence of strong grain noise, the detection capability of target echoes can be significantly decreased. In this Thesis, a number of advanced signal-processing-based techniques are proposed to overcome the challenges associated with inspection using conventional ultrasonic methods. Note that the targets of interest within a component (for example flaws, side-drilled holes, and component back wall) will be referred as a 'legitimate reflector' throughout this Thesis.

1.2 Contributions to knowledge

- A new frequency diversity based signal processing algorithm named Moving Bandwidth Split Spectrum Processing (MB-SSP) was developed to overcome the well-known parameter sensitive issue of Split-Spectrum Processing (SSP). This algorithm was inspired by medical imaging literature where target information with different spectrum characteristics is extracted in a 'local' frequency range. MB-SSP maintains a comparable signal-to-noise ratio (SNR) level compared with SSP, but it is less sensitive to material properties.

- Most of the previous research focused on pattern recognition and/or machine learning techniques have been rarely explored in the field of grain noise reduction in ultrasonic NDE. The implementation and analysis of a number of supervised classification algorithms (Naïve Bayes (NB), k-Nearest Neighbors

(kNN), Support Vector Machine (SVM), and Multilayer Perceptron (MLP)) with different feature extraction approaches has been evaluated. With a training process using pre-acquired data, classification algorithms can distinguish legitimate reflectors from noise and hence, improve defect detection ability.

- In recent years, Deep Learning has become more popular in a variety of applications. In this Thesis, combining Deep Learning with ultrasound signal processing has resulted in the feature within the ultrasound signals being automatically extracted. This leads to a better defect detection capability and enhanced SNR in the generated results.

- Another contribution of this research is to investigate how artificial neural networks can be used to prune the wavelet coefficients, in an attempt to increase detection capability. Importantly, this approach is computationally efficiency compared with techniques that using neural networks as a classifier.

- Development of a new algorithm based on unsupervised clustering, Potential Real Defect Miner (PDRM), to improve ultrasound signal/image clarity for inspection of difficult materials. With the help of a clustering algorithm (*k-means*), the false alarm echoes (artefect echoes) which remain in the results processed by other algorithms can be further eliminated.

- A new imaging algorithm, Frequency Spatial Polarity Coherence (FSPC) was developed to produce images with reduced grain noise compared with conventional imaging algorithms, like focused B-scan and TFM. This algorithm is an extension of MB-SSP and both frequency diversity and spatial diversity information from the raw dataset have been combined to improve image SNR.

1.3 List of publications

1. R. Gongzhang, M. Li, T. Lardner and A. Gachagan, "Robust defect detection in ultrasonic non-destructive evaluation (NDE) of difficult materials,"

Ultrasonics Symposium-2012., IEEE International, Dresden, 2012, pp. 467-470.

2. R. Gongzhang, M. Li, B. Xiao, T. Lardner and A. Gachagan, "Robust frequency diversity based algorithm for clutter noise reduction of ultrasonic signals using multiple sub-spectrum phase coherence," *Review of Progress in Quantitative Nondestructive Evaluation-2013*, AIP Conference Proceedings 1581, American Institute of Physics, Baltimore, MA, 2013, pp. 1948-1955.

3. R. Gongzhang, A. Gachagan, B. Xiao, "Clutter noise reduction for phased array imaging using frequency-spatial polarity coherence," *Review of Progress in Quantitative Nondestructive Evaluation-2014*, AIP Conference Proceedings 1650, American Institute of Physics, Boise, ID, 2014, pp. 1648-1656.

4. R. Gongzhang, A. Gachagan, "Advanced defect detection algorithm using clustering in ultrasonic NDE," *Review of Progress in Quantitative Nondestructive Evaluation-2015*, AIP Conference Proceedings 1706, American Institute of Physics, Minneapolis, Minnesota, 2015, pp. 180009-1-9.

5. B. Xiao, M. Li, R. Gongzhang, R. O'Leary, and A. Gachagan, "Image denoising via spectral distribution similarity analysis for ultrasonic non-destructive evaluation," *Review of Progress in Quantitative Nondestructive Evaluation-2013*, AIP Conference Proceedings 1581, American Institute of Physics, Baltimore, MA, 2013, pp. 1941-1947.

6. T. Lardner, M. Li, R. Gongzhang, and A. Gachagan, "A New Speckle Noise Suppression Technique Using Cross-correlation of Array Sub-apertures in Ultrasonic NDE of Coarse Grain Materials," *Review of Progress in Quantitative Nondestructive Evaluation-2013*, AIP Conference Proceedings 1511, American Institute of Physics, Denver, CO, 2013, pp. 865-871.

7. B. Xiao, R. Gongzhang, T. Lardner, R. L. O'Leary and A. Gachagan, "Ultrasonic imaging of coarse-grained materials using adaptive frequency compounding," *IEEE Transactions on Ultrasonics, Ferroelectrics and Frequency Control*, 2017. (Submitted)

1.4 Structure of Thesis

The body of research work is presented over eight Chapters.

Chapter 2 introduces background knowledge related to the research topics associated with the Thesis. The general concept of ultrasound inspection including ultrasonic devices and data presentation are explained. Signal processing tools like Fourier Transform (FT) and Wavelet Transform (WT) are also introduced. Existing grain noise reduction algorithm approaches are also reviewed. Finally, experimental arrangements and the specifications of a number of material samples to be used for experimental validation later in the Thesis are also described.

Chapter 3 introduces a novel and reliable A-scan based signal processing technique that can be used to reduce grain noise. An analytic model is presented to analyse the algorithm and generate simulation data. Signal to Noise ratio (SNR), Probability of Detection (PoD), and Probability of False Alarm (PFA) are also defined to quantify the performance of the proposed algorithm.

Chapter 4 introduces the basic concept of combining ultrasound noise reduction and pattern recognition / machine learning techniques. Three different supervised classification techniques are applied, with two different feature extraction methods. Scenarios with different training condition are analysed and discussed.

Chapter 5 further explores the application of supervised classification. Artificial Neural Networks (ANN) is introduced to improve the defect detection capability and grain noise reduction in ultrasound inspection of difficult materials. Multilayer Perceptron (MLP) is initially used to demonstrate the concept. Deep Learning network is also investigated later in this Chapter. In addition, an advanced wavelet filtering technique combine with MLP is presented.

Chapter 6 presents another new algorithm development that can further reduce artefact noise in the results which were generated by other algorithms. It employs the concept of unsupervised clustering and can also be used to identify the best region to select training data for other classification algorithms.

Chapter 7 shows the extension of A-scan based algorithms that are covered in Chapters 3 – 6 into advanced phased array imaging. This results in a new algorithm designed for phased array imaging being presented. The new algorithm investigates the polarity coincidence for both different frequency components and signals received by different array elements to eliminate the grain noise in array images.

Chapter 8 concludes the Thesis and provides suggestions for future work towards the goal of enhanced UT inspection of difficult materials.

In ultrasonic NDE, signal and imaging processing can be used in many different applications, such as defect characterisation, defect classification, super-resolution imaging, and phase aberration correction. It should be noted that the work presented in the Thesis is focussed on improving defect detection only and is not concerned with conventional array signal and image processing techniques. However, it can be considered as complementary since the higher sensitivity and SNR exhibited through the application of improved defect detection can undoubtedly facilitate the cross-fertilization into other areas.

Chapter 2

Background review

This Chapter reviews the background knowledge related to the research undertaken in the Thesis. The concept of ultrasonic devices is first introduced, along with the basic knowledge of different NDE scans and imaging algorithms. Basic signal processing tools and some advanced grain noise reduction algorithms are then introduced. Finally, the experimental configuration, modelling and processing platforms used in the Thesis are described.

2.1 Ultrasonic devices

In NDE, a typical ultrasonic inspection system contains three functional units: transducer; electronic instrumentation; and display. A concept diagram is shown in Figure 2.1.
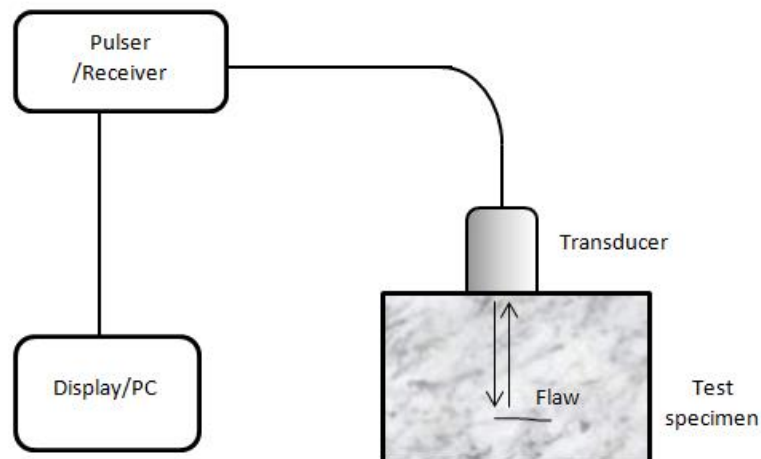
Figure 2.1. Schematic diagram of a typical ultrasonic inspection system.

A transducer is a device that converts one physical quantity into another [11]. An ultrasonic transducer is an electromechanical device that converts an electrical voltage into a mechanical pressure wave or vice versa. An ultrasonic probe can either contain one single transducer or a group of transducers which is known as an array probe [12]. An individual transducer in the array is usually referred as an element.

A pulser/receiver is an electronic device that can produce high voltage electrical pulse excitation, such as a signal generator when using a single element transducer, or a phased array controller (PAC) for an array probe. A PAC contains multiple channels which can be actively controlled, simultaneously. The received signals usually require a computer with an appropriate installed (manufacturer's) software to display the received echoes.

For a typical system operation, the transducer is driven by the pulser and transmits a high-frequency ultrasonic wave packet/burst into the specimen. If a reflector (for example, a flaw) is present within the propagation path of the wave in the specimen, a proportion of the sound energy will be reflected and/or diffracted by the flaw and then captured by the receiver. In many cases, coupling media including gels, various oils and water may be applied between the transducer and specimen surface to enhance the ultrasound energy transfer efficiency.

The reflected wave is received by the system and is then displayed on an appropriate device, such as an oscilloscope or a monitor of a computer. Relevant information such as location or size of the reflector can then be determined.

2.1.1 Concept of an ultrasonic transducer

The core of an ultrasonic transducer is its active component that converts energy between electrical and mechanical domains. The most common material chosen for this active part is a piezoelectric material.

A schematic diagram of the piezoelectric transducer is shown in Figure 2.2.
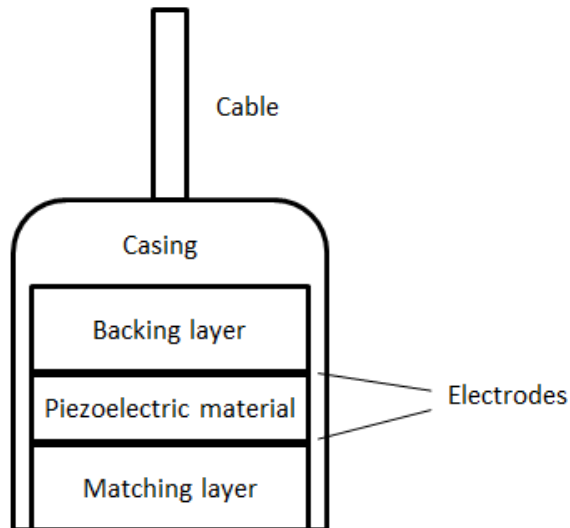
Figure 2.2. Schematic diagram of an ultrasonic transducer

A piezoelectric ultrasound transducer contains several layers, along with a case to provide electrical shielding and a cable to provide connection to appropriate electronic hardware. The piezoelectric material deforms when a voltage is applied across its electrodes, known as the inverse piezoelectric effect, and will generate a voltage when subjected to an external pressure stimulus through the direct piezoelectric effect [13-15]. The backing layer is used for absorbing energy emanating from the rear face of the piezoelectric layer, to minimise reverberation within the transducer. In addition, one or more matching layers are attached at the front of the transducer to ensure a better acoustic impedance match between the piezoelectric layer and the inspection material [16-18]. For many applications a single quarter wavelength matching layer solution is used, where the material (Z_2) is effectively the geometric mean between the active layer acoustic impedance (Z_1) and the load impedance (Z_3), as shown in Eq. (2.1),

$$Z_2 = \sqrt{Z_1 \times Z_3}$$
(2.1)

where $Z = \rho v$, ρ is the density of the material and v is the sound velocity.

2.1.2 Transducer parameters selection

The parameters of the transducer should be properly chosen to match the inspection scenario. Usually, the most important parameters are the centre frequency of the transducer and the operational bandwidth.

The centre frequency of the transducer is a critical parameter as it influences the spatial resolution of the received signals. High-frequency waves have a smaller wavelength and can interact with smaller particles/features which will benefit the inspection of small defects. Generally, particles with a size greater than half of the wavelength will interact with the incident waves. However, higher frequency waves are usually more attenuated compared with lower frequency waves, especially for coarse-grain materials where the grain size is comparable or larger than the ultrasonic wavelength. On the contrary, lower frequency waves are less attenuated but result in a lower spatial resolution and small features will not be resolved [19]. Transducers with a lower centre frequency typically also have a longer ring-down time [20], which is the time that the transducer reaches equilibrium after excitation. During the ring-down time, any signals received by the transducer will be masked by this ring-down 'signal', as the excitation signal has much higher energy compared with the received echoes.

The bandwidth of a transducer reflects the effective operating range of the transducer frequency response. The bandwidth is measured at a certain drop-off point from the maximum amplitude of the frequency response spectrum, typically at 50% drop-off point, or -6dB. The bandwidth can be expressed using either Hertz or as a fraction of the centre frequency. Commercial transducers usually have a fractional bandwidth between 30% to >100% [21]. Transducers with a wider bandwidth can significantly benefit the grain noise reduction techniques, as the grain noise is more sensitive to different frequencies while any features in the sample will be coherent across the operating frequency range. Details will be discussed further in Section 2.5.2.

2.1.3   Single transducer probe and phased array probe

Conventional ultrasonic probes are generally monolithic and contain only one transducer, or active element. The detection using single transducer probe is relatively simple and easy to be applied, as it only requires a pulser-receiver instrument and an oscilloscope.

However, due to the dispersion of the wave, reflectors that are not directly under the probe may also be detected [9]. This increases the difficulty of inspection due to the effect of the off-axis reflectors [22]. One way to reduce this effect is by adding a physical focusing to the probe by curving its surface [12]. The direction of the reflector is more certain in this case as the energy leaking to off-axis reflectors has been reduced [23].

Another way to focus the ultrasonic beam is by introducing a phased array probe. Phased array probe is constructed by grouping a number of transducers into a single transducer housing. Typically, a phased array probe can contain between 16 to 256 transducers, with each individual transducer called an element of the array. When connected to a phased array controller, the elements in the array can be activated in a desired order, to manipulate the mechanical wavefront propagating from the front face of the device to produce electronic beam steering. Different configurations of array elements are implemented; it can be arranged in either 1-D, 2-D or annularly [24], where Figures 2.3-2.5 show the schematic diagram of each configuration, respectively.
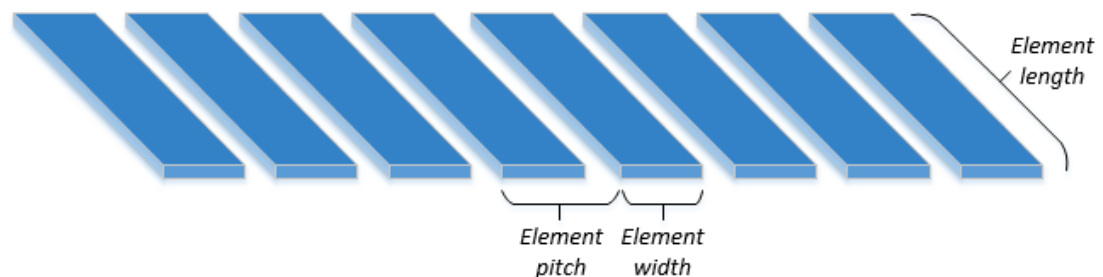
Figure 2.3. Schematic diagram of 1-D array layout, where blue indicates an active array element.
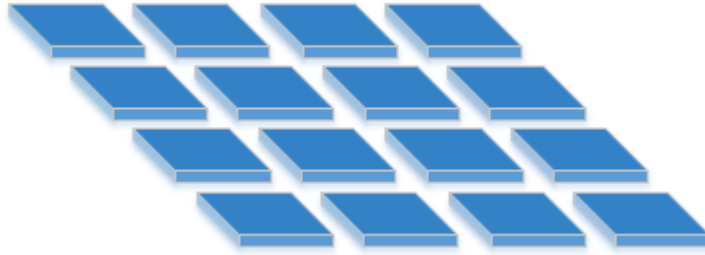
Figure 2.4. Schematic diagram of 2-D array layout, where blue indicates an active array element.

Figure 2.5. Schematic diagram of annular array layout, where blue indicates an active array element.

The most commonly used commercial array configuration is the 1-D array, which has linearly distributed elements, as shown in Figure 2.3. Generally, the length of an element in a 1-D linear array is much larger than the width of the element. This means the element in a 1-D array is usually larger than those in a 2-D array configuration, hence 1-D elements can generate higher energy into the inspection median and can result in a higher sensitivity. Additionally, the long rectangular shape of the array element makes the ultrasound beam more directional, which avoids the off-axis echoes from reflectors that lie outside the inspection plane.

Compared with a 1-D array, a 2-D array, as illustrated in Figure 2.4, can generate 3-D volumetric images and provide more explicit defect information. A 2-D array

configuration can have a more complicated element arrangement to adapt to different situations, for example a sparse array element layout.

An annular array, as illustrated in Figure 2.5, can be used to provide a range of on-axis focal depths, which in effect is simulating the performance of different single element devices [24].

The design of the phased array should avoid producing grating lobes [25]. Grating lobes are the unwanted energy emitted from the array off-axis which may occur when the pitch size between elements in an array is greater than half a wavelength [26]. As grating lobes are beam patterns formed at an angle to the (on-axis) mainlobe, the angular positions of the grating lobe can be calculated as:

$$\beta_{grating} = \sin^{-1}\frac{m\lambda}{p}, m = \pm1, \pm2, \cdots \qquad (2.2)$$

where λ is the ultrasound wavelength of the array centre frequency, p is the array element pitch size. To avoid the generation of grating lobes, the element pitch must be smaller than half a wavelength of the array centre frequency.

Compared with conventional signal element probes, the phased array is more convenient and flexible at inspections, as it can easily focus the ultrasound beam at different points by simply changing the delay law. Phased array can quickly inspect a larger area by steering the beam without physically moving the probe. Additionally, with the help of Full Matrix Capture (FMC) [27], many advanced imaging algorithms can be applied to post-processing of the dataset and improving the quality of the images. More details about array imaging algorithms will be discussed in Section 2.3.

However, the phased array is more complicated to design and manufacture compared with conventional single element transducer designs, and hence the cost of the phased array is more expensive. In addition, the inspection using a phased array requires the help of a phased array controller (PAC) to coordinate the transmitting/receiving of each element. Most PACs are bundled with the manufacturer's software which is used to drive the array. Raw data is often difficult to be export from the software into a file that can be used by other programs. Another

drawback of phased array probe is that the element size is limited to avoid issues like grating lobes generation. Also, for the ease of inspection, the overall size of the probe cannot be too large which also limit the size, and number of the elements. Compared with a single transducer probe configuration, the small element size reduces the energy transmitted into the sample and the corresponding receive sensitivity.

2.2 Data presentation

Ultrasonic data can be collected and displayed in a number of different formats in NDE. This Section will briefly introduce the commonly used formats like A-scan, B-scan, and C-scan [28], along with a new data acquisition technique named Full Matrix Capture (FMC) [27].

2.2.1 A-scan Representation

Amplitude scan (A-scan) is the most straightforward method to express the information received by the transducer. It is the basic way to store the received raw signal. An A-scan is the amplitude distribution of echo signals along the depth of test specimen when the transducer remains at a static point on the surface of the specimen. A typical A-scan is shown in Figure 2.6 as an example.

The depth of a reflector in the specimen can be calculated from its echo in the A-scan, based on the wave propagation time and the sound velocity in the material. The location of the reflector can be estimated based on the direction that the transducer is facing, especially if the ultrasonic beam is well focused. However, off-axis reflectors often contribute to the response due to the beam spread, hence it makes the absolute positioning of a reflector difficult for a single A-scan. Additionally, these off-axis scatterers can easily mask the echo of the reflector if the material contains large grains.
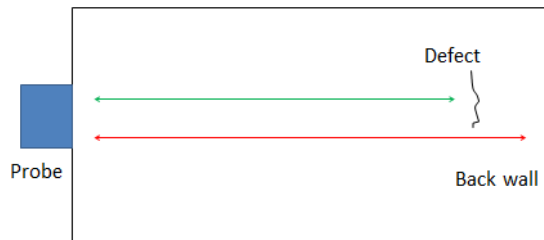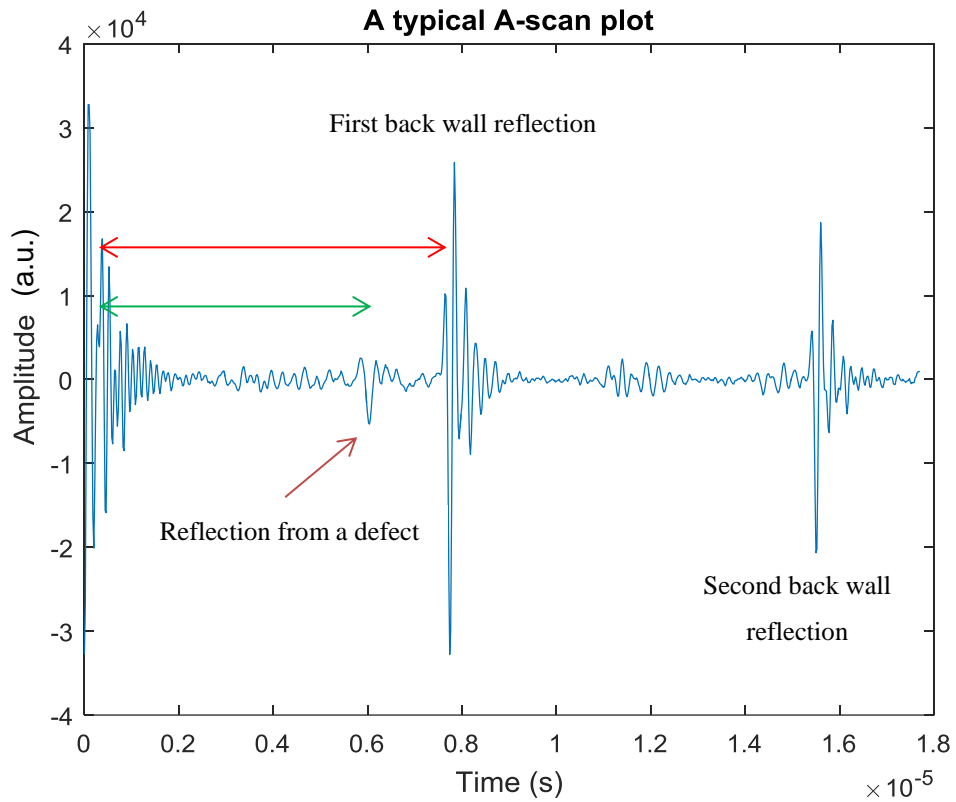
Figure 2.6. An example of A-scan plot, where the red line indicates the backwall reflection and the green line illustrates the reflection from the defect.

2.2.2 B-scan Image

The B-scan is a 2-D profile image; it presents the cross-sectional view of the test specimen, as illustrated in Figure 2.7. The B-scan image can be seen as a group of parallel aligned A-scans, which can either be displayed as a waterfall plot or by plotting the signals in each A-Scan which exceed a set threshold value. In a B-scan image, the two axes are the time-of-flight of the ultrasonic wave and the position of the transducer. The example illustrated in Figure 2.8 effectively presents an A-scan

(x-dimension) for every spatial position of the transducer (y-dimension). Compared with the simple A-scan representation, the B-scan image is more visual and can be used to locate and size a reflector.

An example B-scan is also given in Figure 2.8, where each line/row is effectively a single A-scan at certain location relative to the sample. Compared with the simple A-scan representation, the B-scan image is more visual and can be used to locate and size a reflector.
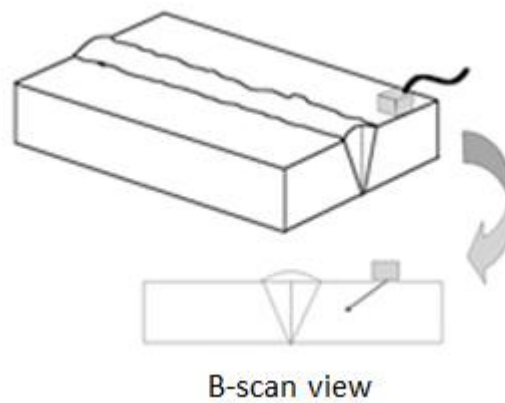
Figure 2.7. Concept diagram of B-scan [29].
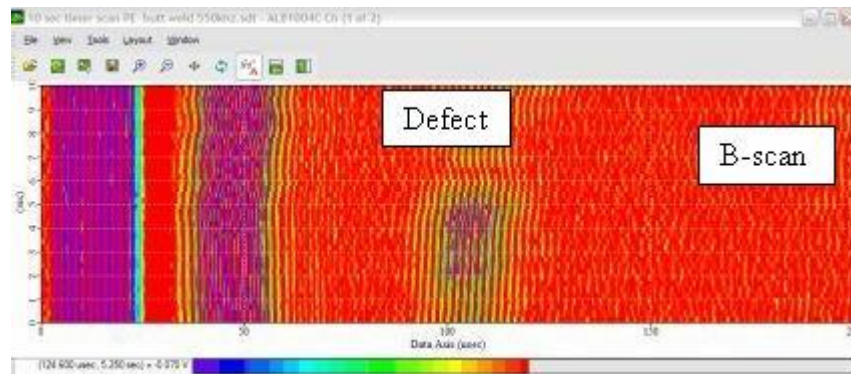
Figure 2.8. An example image of B-scan [30].

2.2.3   C-scan Imaging

The C-scan is also a 2-D image that provides a profile view of a slice of the test specimen. The section plane is parallel to the probe surface and is orthogonal to the

ultrasonic beam, as shown in Figure 2.9. C-scan images are usually produced with an automated data acquisition system, like a computer-controlled immersion scanning system. The intensity of the received signal is expressed through a brightness map and it is usually gated, with the example shown Figure 2.10 presenting the amplitude variation from an air-coupled inspection of a carbon-fibre sample. The colour map of a C-scan image can also represent the received time-of-flight information [28].
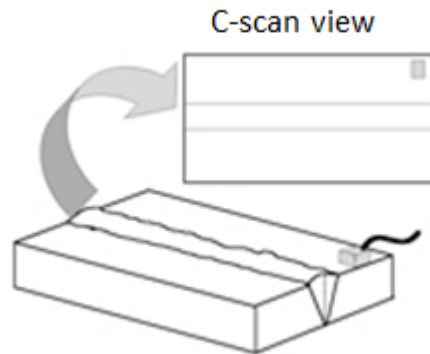
Figure 2.9. Concept diagram of C-scan [29].
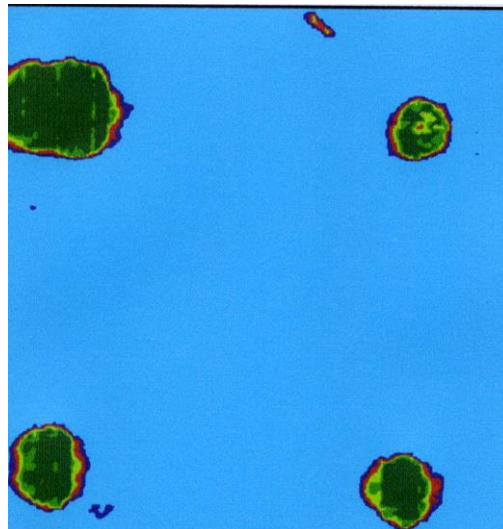
Figure 2.10. An example image of C-scan [31]. This image is purely for illustrate purpose: defect are indicated by green colourscale and blue represent background.

2.2.4 Full Matrix Capture (FMC)

The conventional use of the phased array probe is to emulate and improve the performance of a single element probe. To achieve this, the array elements are excited follow a series of pre-defined time delays (or focal laws) to physically form a focused beam, or steered the beam angle during the inspection. The received signals are summed and can be seen as one single A-scan similar to a conventional single element probe. The benefit of the phased array is that it is more flexible than the conventional monolithic probe which has a fixed focusing point and a non-adjustable beam angle.

The Full Matrix Capture (FMC) approach [27] is an alternate way to achieve data acquisition and stores the received signals in a special format which can be used for post processing. It stores the A-scan of every combination of transmit-receive elements of the entire array elements in a matrix.

Figure 2.11 shows the mechanism of the FMC approach. Only one element of the array is excited, while all elements including the excited one are used to receive the returning echoes from the propagating wave in the sample. This procedure is repeated for every element of the array until all A-scans for every possible combination of transmitter-receiver pairs have been recorded.
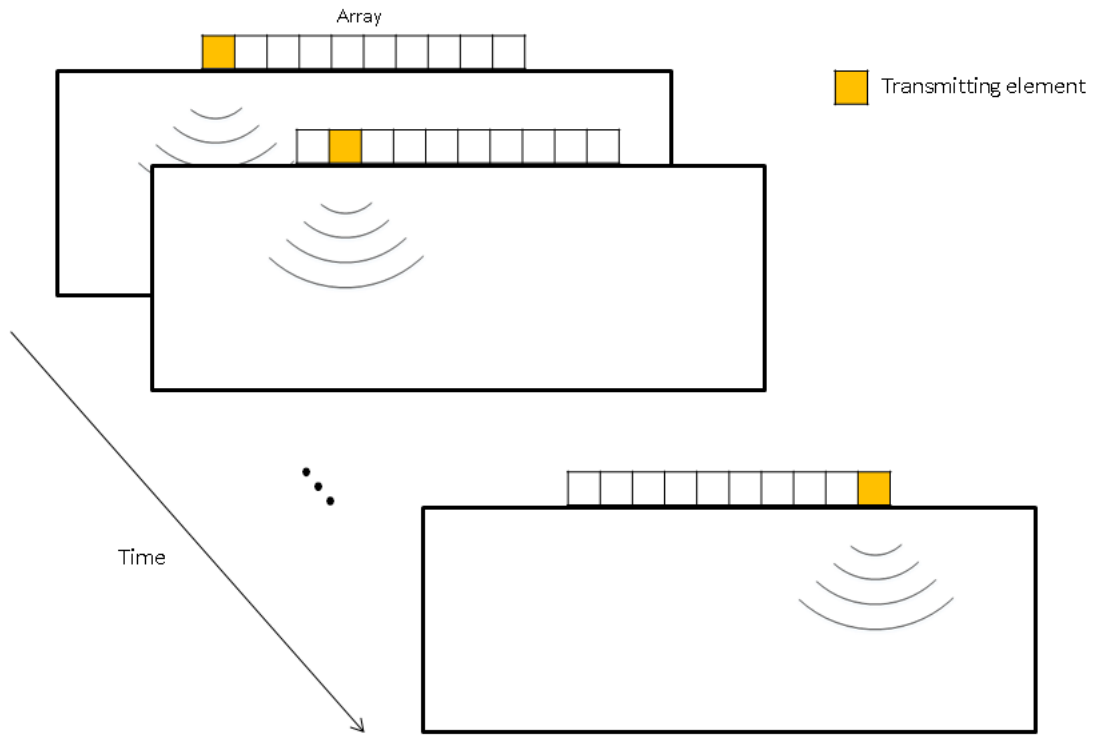
Figure 2.11. Schematic diagram of FMC.

The data is saved in a matrix of A-scans as shown in Figure 2.12, in a specific order that is based on the index of the transmitting-receiving combinations. $h_{tx,rx}$ is the received A-scan signal of a transmitting-receiving elements pair, tx is the index of transmitting element, rx is the index of receiving element.

$$
\begin{array}{|c|c|c|c|}
\hline
h_{1,1} & h_{1,2} & \cdots & h_{1,rx} \\
\hline
h_{2,1} & h_{2,2} & \cdots & h_{2,rx} \\
\hline
\vdots & \vdots & \ddots & \vdots \\
\hline
h_{tx,1} & h_{tx,2} & \cdots & h_{tx,rx} \\
\hline
\end{array}
$$

Figure 2.12. An illustration of an FMC dataset. $h_{tx,rx}$ is the A-scan trace of a transmitting-reiceiving elements pair, tx is the index of transmitting element, rx is the index of receiving element.

20

Theoretically, any beamforming that is based on the superposition of signals from combinations of element channels can be transferred to post-processing via the FMC dataset. Also, with the use of FMC, imaging algorithms that can generate higher quality images but are difficult to be applied on-line using the conventional methods/hardware, can now be easily applied off-line.

Compared with the conventional on-line inspection, the FMC does not require a pre-calculated delay law to achieve focusing in the transmitting or receiving, which makes the inspection arrangement easier and can potentially produce a larger inspection range.

Another advantage of using the FMC is that it can generate images with a much higher resolution. Although, this was, until recently, at the expense of time to conduct the NDE data collection due to low data transfer efficiency between the instrumentation and the host PC. Now, the introduction of fast optical communication links (Ultrasound FlexRIO modules, Diagnostic Imaging Ltd; www.diagnosticsonar.com) and increased computational power through GP-GPU hardware [32], it is possible to collect FMC and process into a high-resolution image in real-time. [33, 34]

Additionally, if every element of an array has the same performance, the A-scan of a transmitter-receiver pair should be identical to the A-scan of the same element pairing but with a swapped transmitter-receiver order. When under this assumption, the FMC could be reduced into a half matrix captured (HMC) by effectively removing (approximately) one half (symmetric section) of the matrix. [33, 34]

2.3   Array imaging

Many array imaging algorithms have been developed and are widely used in industry, such as the plane B-scan, focused B-scan, sectorial B-scan, and the total focusing method (TFM) [27]. The first three algorithms can be considered as standard

inspection techniques in conventional phased array systems, but can also be implemented by post-processing FMC data. TFM constructs images from FMC data so that it can only be applied in post-processing. This Section will briefly introduce these algorithms, along with other advanced array imaging algorithms.

2.3.1 Plane B-scan Imaging

Plane B-scan is the simplest processing method among all these five methods. The approach is to scan the ultrasonic beam in a similar way to one transducer probe physically moving in one direction across the sample. Since the beam spread is significant if only one element is fired each time, several adjacent elements will be fired simultaneously as an effective transmitting aperture to enhance the energy of ultrasonic beam and reduce the beam divergence. The firing sequence for each array element in the aperture is called a focal law and the concept of the plane B-scan, which is the simplest focal law, is shown in Figure 2.13. The word 'plane' in its name means the wavefront of the beam is a plane wave, and the wavefront is parallel to the array surface since all elements in the aperture are fired at the same time. The aperture is moving from one side of the array to the other side, to scan the entire imaging area of the test specimen, under the array transducer. The scanning resolution of the plane B-scan is equal to the element pitch size. As all elements in the aperture are excited simultaneously, the beam has no focusing which results in a poor resolution when compared to other imaging algorithms.

If producing a plane B-Scan image through post-processing, the image intensity at a certain point (x, z) is calculated as:

$$I(x,z) = \left| \sum_{tx=M_1}^{M_2} \sum_{rx=M_1}^{M_2} h_{tx,rx}(\frac{2z}{v}) \right| \tag{2.3}$$

where $h_{tx,rx}$ is the A-scan of a transmitter-receiver pair in the FMC dataset, tx and rx denote the indices of the selected array element respectively, M_1 and M_2 are the indices of the starting and ending element of an aperture, z is the axial distance into the sample from the array position, and v is the sound velocity in the load material.
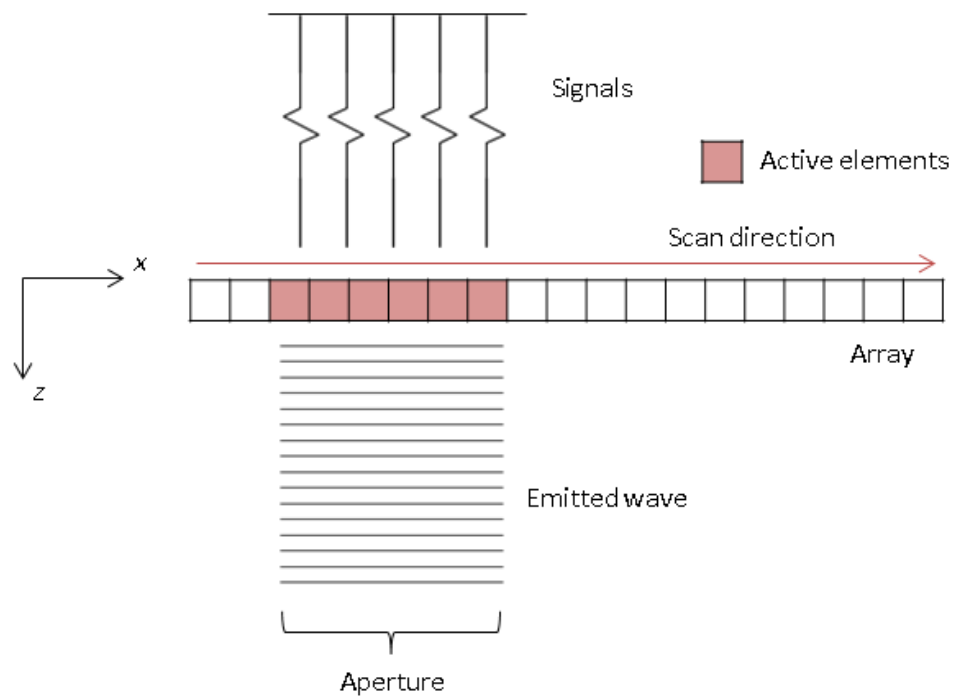
Figure 2.13. Schematic diagram of plane B-scan inspection.

2.3.2 Focused B-scan Imaging

The scan mechanism of the focused B-scan is similar to the plane B-scan, with the aperture moving from one side of the array to the other side, and the intensity of a point in the image is determined by the received signal of the elements inside the aperture. The improvement of the focused B-scan compared with the plane B-scan is to apply beam focusing inside the aperture.

In conventional phased array systems, the elements within an aperture are applied with a symmetric focal law in transmission to focus the beam at a particular depth. The received signals are delayed with the same focal law as used in transmission. All received signals in the aperture will then be combined to form a single A-scan line of the B-scan image. The focusing depth is usually chosen at a particular depth of interest. The principle of the focused B-scan is similar to synthetic aperture focusing technique (SAFT) [35-38] and the concept of the focused B-scan is shown in Figure

2.14. Here, the wave front of this type of scan method has a spherical wavefront directly below the aperture, and the centre of the sphere is the focusing point. Importantly, the resolution of the focused B-scan should be better than the plane B-scan at the focused depth.
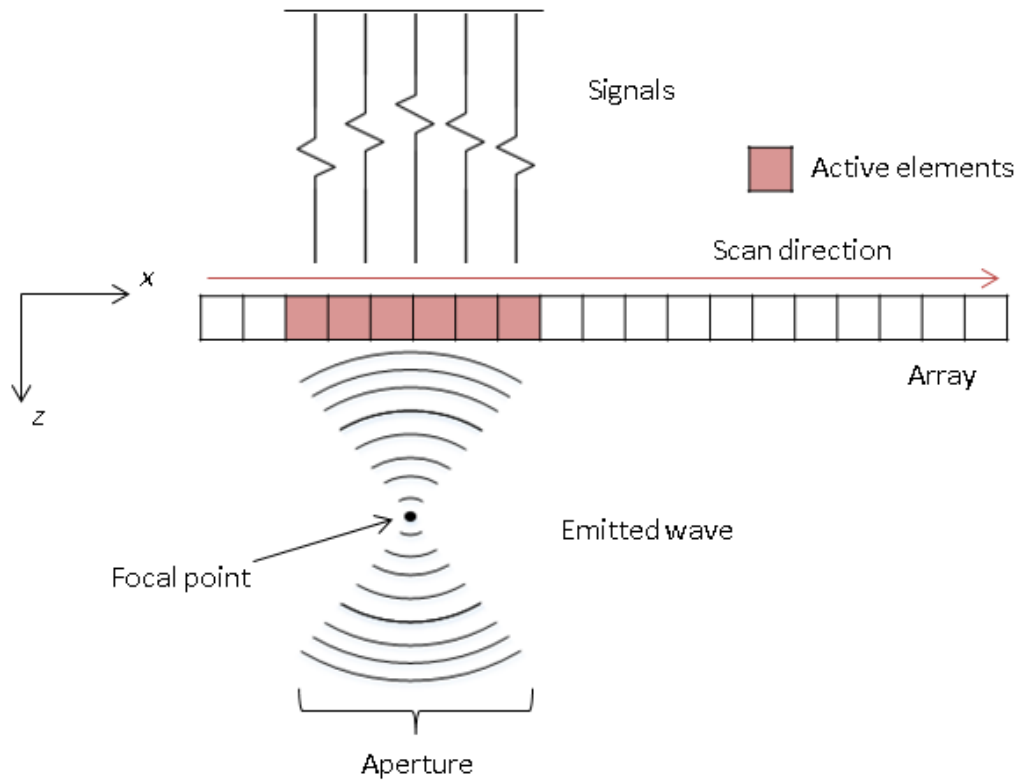
Figure 2.14. Schematic diagram of focused B-scan inspection.

In conventional phased array systems, the transmission can focus on several different depths before moving to next aperture to improve the resolution over a larger area. This is usually referred as the Dynamic Depth Focusing [39]. Applying a set of different focal depths requires multiple excitations of the transmission aperture, which will reduce the scan speed and hence, the number of focal depths implemented is usually constrained. Interestingly, the reception focusing is achieved electronically and will not affect the frame rate significantly; therefore the focusing on the reception can be much finer [40].

As both the transmission focusing and reception focusing can be simulated in post-processing when using FMC data, the focal depths of both procedures can potentially

be unlimited. Therefore, the intensity of a point in the focused B-scan image can be calculated as:

$$I(x,z) = \left| \sum_{tx=M_1}^{M_2} \sum_{rx=M_1}^{M_2} h_{tx,rx}(\frac{\sqrt{(x_{tx}-x)^2+z^2}+\sqrt{(x_{rx}-x)^2+z^2}}{v}) \right| \qquad (2.4)$$

where x_{tx} and x_{rx} is the coordinate of the transmitting element and the receiving element, respectively and x represents the lateral distance from the point relative to the centre of the array.

2.3.3 Sector B-scan Imaging

The sector B-scan usually employs all array elements to steer the ultrasound beam for the purpose of inspecting areas that are not directly beneath the array. The array elements are excited following a sequence of time delays to adjust the angle of the wavefront in a conventional phased array system. Unlike the plane B-scan and the focused B-scan, a polar coordination system (r, θ) based on the depth and the beam angle is commonly employed to record the images. If the sequence of time delays applied to the array elements is linear, the steered wave front will be retained as plane since no focusing is involved. The received signals of all elements will then be summed up to generate one synthetic A-scan as an individual scan-line. Figure 2.15 shows the concept diagram of the sector B-scan.

In post-processing using the FMC data, the intensity of a point in a sector B-scan image can be expressed as:

$$I(r,\theta) = \left| \sum_{tx=1}^{N} \sum_{rx=1}^{N} h_{tx,rx}(\frac{2r + x_{tx}\sin\theta + x_{rx}\sin\theta}{v}) \right| \qquad (2.5)$$

where N is the total number of array elements.

Like Dynamic Depth Focusing, the sector B-scan can also have a set of focused depths if multiple transmissions with different focal laws are applied. With the beam steered and focused, both the image resolution and the inspection range can be improved.
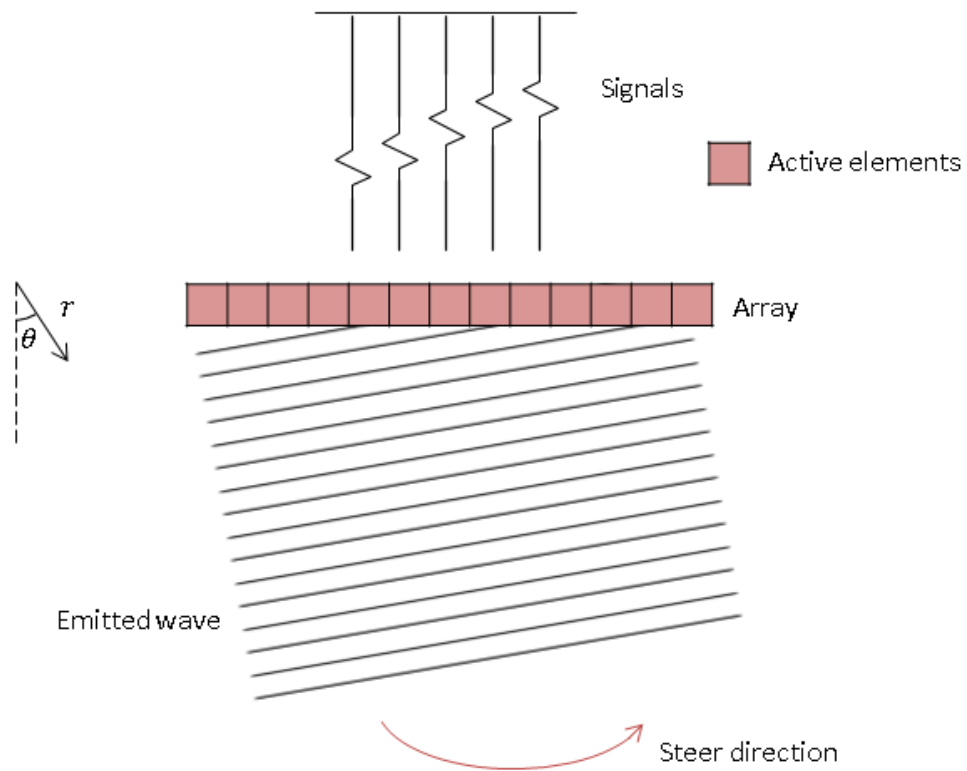
Figure 2.15. Schematic diagram of sector B-scan inspection.

2.3.4 Total focusing method

The TFM is an advanced imaging algorithm that can generate higher resolution images compared to all of the above conventional imaging algorithms. In a TFM image, every pixel is a focused point. This is a good example of using the benefits of FMC and post-processing, because a high density of focused points is unrealistic for online inspection that uses multiple transmissions and focal laws.

The post-processing of TFM is similar to the focused B-scan, except all array elements are involved now for calculating the intensity of a single pixel. Figure 2.16 shows the concept of the TFM algorithm.
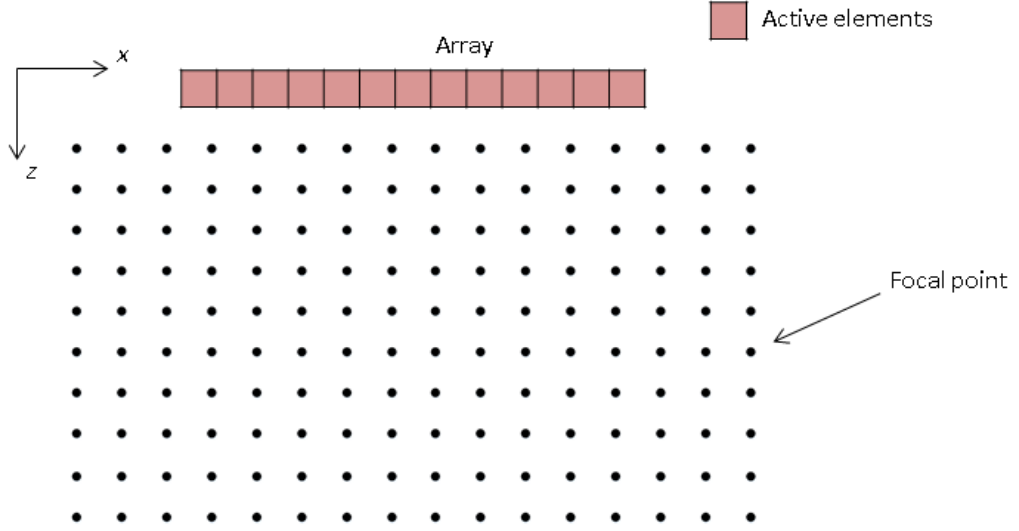
Figure 2.16. Schematic diagram of TFM imaging algorithm.

The equation for computing a TFM image is,

$$I(x,z) = \left| \sum_{tx=1}^{N} \sum_{rx=1}^{N} h_{tx,rx} \left(\frac{\sqrt{(x_{tx} - x)^2 + z^2} + \sqrt{(x_{rx} - x)^2 + z^2}}{v} \right) \right| \qquad (2.6)$$

Literature has stated that the TFM image commonly has a better SNR compared with the three conventional imaging algorithms introduced in Sections 2.3.1-2.3.3, since the TFM has involved the maximum amount of information from all transmitter-receiver pairs of the array for every imaging pixel [27, 41]. As grain noise is more spatially coherent than a legitimate reflector, involving a larger number of array elements means increasing the spatial diversity for the inspection and hence, the potential to suppress the grain noise.

The higher spatial resolution of the TFM images compared with the conventional algorithms is also stated in the literature by Holmes et al. [27]. An array performance indicator (API) was defined based on the point spread function (PSF) to measure the imaging quality of a point-like reflector. It has been shown that the TFM image has an 80% reduction in API compared with the plane B-scan, indicating a better representation of the reflector in the TFM image.

2.3.5   Advanced imaging algorithms

In addition to the discussed four imaging algorithms, many advanced techniques have been developed in recent years for ultrasonic phased array inspection, to adapt for various practical scenarios.

The Vector Total Focusing Method (VTFM) is an extension from TFM and designed to detect the orientation of the reflector, as in practice the legitimate reflector is not always point-like. The process is similar to TFM, but sub-array imaging is used to detect the direction of energy contribution for each image pixel [42]. For the reflectors that are not directly covered by the array, Multi-mode TFM is developed that uses specific reflections and mode conversions to enhance the detectability of such reflectors [43]. Since the surface of a test specimen can sometimes be arbitrary which inhibit the normal application of the focal law, an autofocusing algorithm has also been developed [44].

Fan et al [45] pointed out that the spatial resolution of TFM images is diffraction limited, known as Rayleigh limit. This is improved by the super-resolution techniques such as the Time reversal with multiple signal classification (TR-MUSIC) [46, 47]. It has been proved that TR-MUSIC algorithm has a significantly lower API compared with the standard TFM approach [45].

Phase aberration correction methods have also been exploited to improve focusing in the inspection of coarse-grained materials, as such materials are inhomogeneous and the wave speed varies at different locations in the sample. The Nearest Neighbour Cross-Correlation (NNCC) algorithm can adjust the phase difference by measuring the similarity between the signals of adjacent elements [48-50]. Time reversal mirror (TRM) algorithm corrects the phase aberration by re-transmitting the time-reversed reflection signal that was previously received [51, 52]. However, for highly scattered materials an iterative inspection approach is usually needed [53]. The decomposition of the time reversal operator (DORT, abbreviated from French words) is extended from the TRM methodology and can avoid the iterative process of the TRM by eliminating the grain noise interference [53].

Sparse signal representation (SSR) algorithms have also been widely used in ultrasonic NDE for many applications, such as increasing image resolution and improving defect characterisation, as reviewed by Zhang et al [54].

Defect characterisation is also an important area in ultrasonic NDE. Tant et al [55] have proposed an analytical approach to objectively size cracks using ultrasonic phased array data. Zhang et al [56] has also done research defect characterisation using scattering matrices.

Defect classification is another important and challenging issue in ultrasonic NDE. Different defects exist in industrial materials, such as crack, stomata, incomplete penetration and slag inclusion. Many signal processing methods have been proposed to achieve automated classification for these defects. Haykin [57] has proposed a method to use Multilayer Perceptron (MLP) and Wavelet Transform (WV) to classify defects in welding. Chen et al [58] have provided an alternative way to achieve this by applying Layered Multiple Support Vector Machine (LMSVM) and Wavelet Packet.

In addition, Pamel et al [59] has proposed a method to evaluate the defect detection performance in ultrasonic phased array imaging, based on the statistical tools including Probability of Detection (PoD), Probability of False Alarm (PFA) and the related Receiver Operating Characteristic (ROC) curve.

A good review paper for ultrasound signal processing for NDE can be found in [60], which presents recent developments and describes many typical ultrasound signal processing techniques.

Importantly, many algorithms have been developed for array imaging to reduce the effect of grain noise in the inspection of coarse-grained materials. Details will be further discussed in Section 2.5.

2.4 Signal processing tools

Before discussing grain noise reduction algorithms for ultrasonic inspection of difficult materials in Section 2.5, several basic signal processing tools are introduced in this Section which will support the ongoing algorithm developments described later in the Thesis.

2.4.1 Fourier transform

The Fourier transform (FT) is named after the French mathematician, Fourier [61] and is a mathematical tool that decomposes a waveform (a function or a signal) into an alternate representation in the frequency domain, characterized by sinusoidal functions. It is similar to the way of expressing music using notes. The FT is not limited to time based signals, but in many cases, the raw signal is commonly referred to as the time domain signal. Detail techniques can be found in many text books, such as [62].

Short-time Fourier transform (STFT) is a modified version of FT which is usually used to analyse the localised segmental signal since the FT spectrum is an overall analysis of the entire signal. STFT reflects the local sectioning of a signal that changes over time into the frequency domain, by dividing the entire signal into short segments then transforming each segment into a spectrum. The STFT spectrum can be seen as a 2-D time-frequency representation of the original time domain signal.

To divide the longer signal into shorter segments, STFT uses a fixed length function which usually referred as a window. STFT can be mathematically expressed as:

$$F_{stft}(\tau, \omega) = \int_{-\infty}^{\infty} f(t)w(t - \tau)e^{-i\omega t}dt \tag{2.14}$$

where $w(t)$ is the window function and τ is the time index of the STFT spectrum. Generally, a window function is a non-negative, smooth, "bell-shaped" curve [63].

An example STFT of a quadratic chirp that starts at 100 Hz and crosses 200 Hz at $t = 1$ s are shown in Figure 2.17. Red colour in the image represent higher energy. Since

the example chirp signal has an raising frequency, the highest energy at different time instants that shows in the STFT plot is moving from 100MHz at $t = 0s$ to 500 at $t = 2s$.
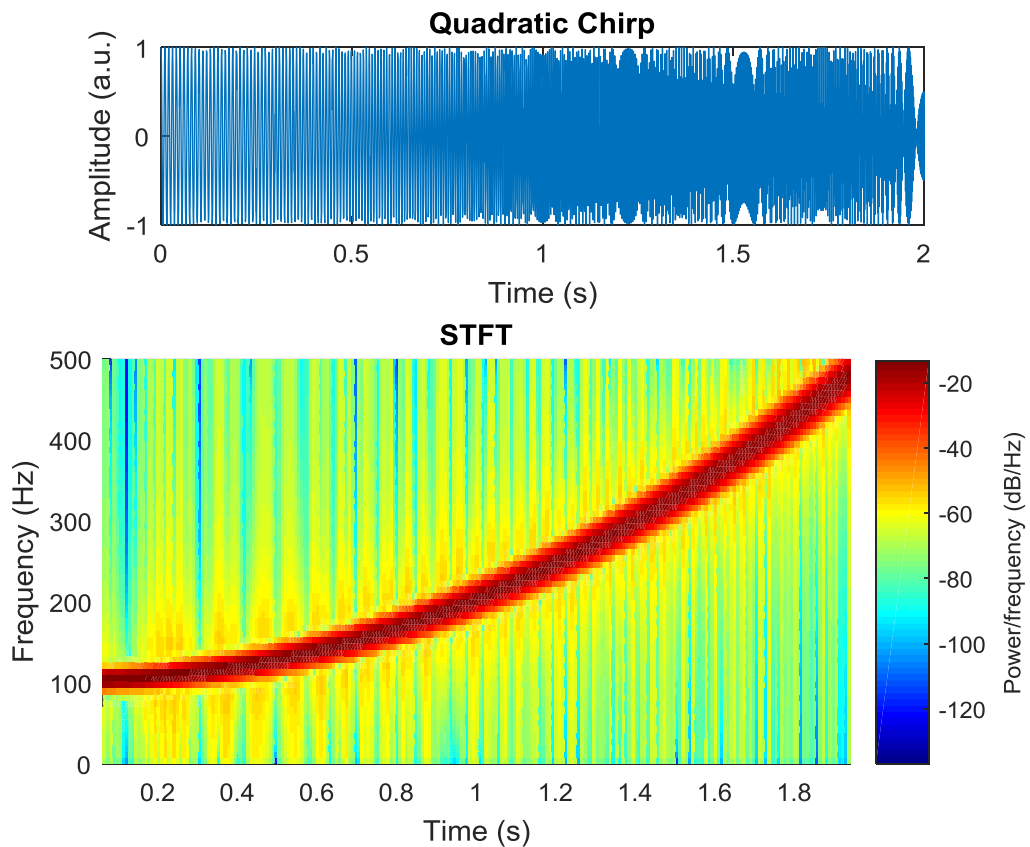
Figure 2.17. An example STFT of a quadratic chirp signal.

2.4.2 Wavelet transform

The Fourier transform is good for analysing smooth signals but has less optimal performance on fast changing signals and the analysis of localised signals, as it needs as infinite sinusoidal basis to construct the sharp changes. Although STFT has improved the capability of analysing localised signals, the analysis lacks flexibility since the spectrum resolution of the time axis is dependent on the window function, which is fixed during the configuration phase. The Wavelet transform (WT) has a better solution to these issues. The current WT theory was first proposed by Morlet in 1974 [64, 65]. Compared with FT, WT focuses more on the localised transform

between the time domain and frequency domain. WT is similar to STFT but has a more flexible resolution in both time and frequency domain.

The wavelet spectrum is usually expressed as a 2-D spectrum like the STFT. The time axis is consistent with the original signal and the frequency axis is replaced by a similar factor depending on the type of the wavelet transform.

To transfer the time domain signal into a frequency domain representation, the WT extracts details and information using a pre-set function by scaling [66]. This function is commonly referred as the mother wavelet.

The mother wavelet can be any function $h(t)$ which satisfies the admissibility condition [67]:

$$\int_0^\infty \frac{|H(\omega)|^2}{\omega} d\omega = C < +\infty \tag{2.15}$$

where $H(\omega)$ is the spectrum of $h(t)$, C is a constant. Any continuous function which is band limited and has a zero D.C. value can thus be used as a mother wavelet [66].

Figure 2.18 gives some examples of the mother wavelets.

The selection of a mother wavelet is typically based on the feature of the signal of interest. For example, a Haar(db1) wavelet [68] could be chosen for signals with sharp features and a higher order Daubechies [69] wavelet may have better performance for a smoother signal.

The size of the window in the time domain when extracting the information in the wavelet transform is no longer constant as it is a function of scaling. This results in a more natural description of the signal. Weiss [70] proposes that the WT is the correlation between the input signal and a set of basic wavelets, which is usually referred as daughter wavelets. The daughter wavelets are the scaled and shifted version of the mother wavelets.
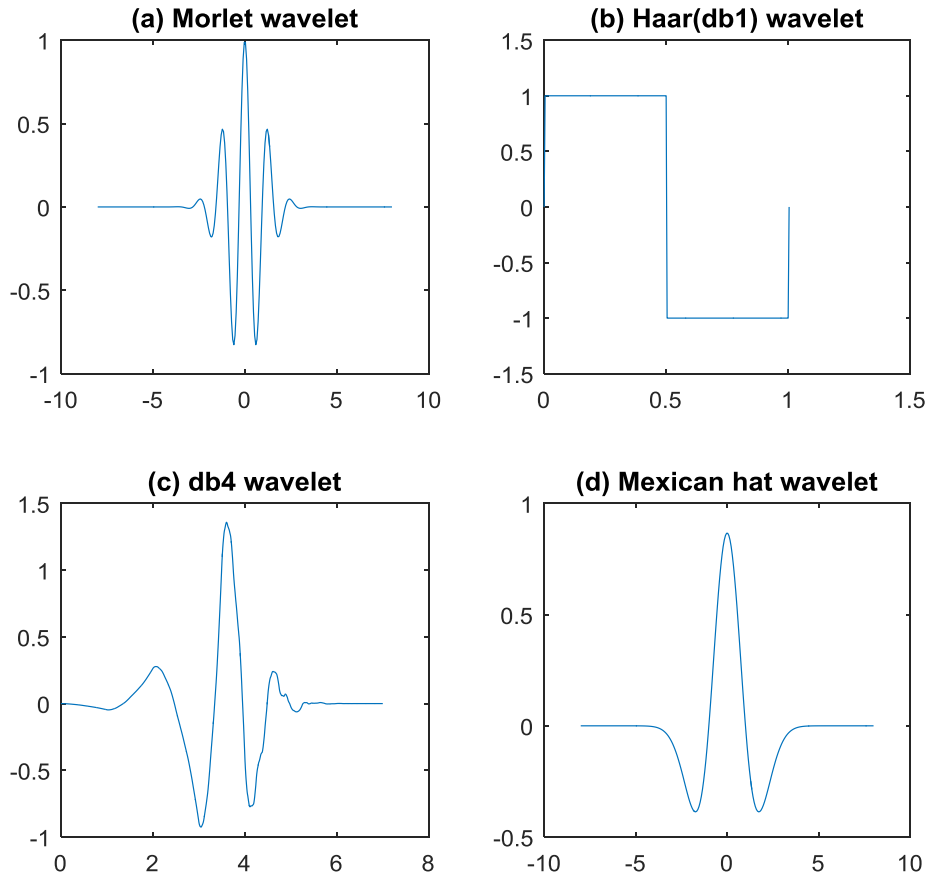
Figure 2.18. Examples of mother wavelet. (a) Morlet wavelet, (b) Haar (Daubechies 1) wavelet, (c) Daubechies 4 wavelet, (d) Mexican hat wavelet.

Like the Fourier transform which is defined as the sum over all time of the product of the original signal $f(t)$ and a complex exponential, the continuous wavelet transform (CWT) is defined as the sum over all time of the product of $f(t)$ and the daughter wavelets [66]:

$$W_S(a, b) = \int_{-\infty}^{\infty} f(t) h_{a,b}^*(t) dt \tag{2.16}$$

where $h_{a,b}(t)$ is the daughter wavelet, a is the dilation factor (scaling) and b is the shift (position). Note that $*$ denotes a complex conjugate operation. The output of the CWT $W_S(a, b)$ is called the wavelet coefficients, which is a function of both the

33

scaling and the shifting. The Shifts correlate with the time delays of the original signal, while the Scales function like the frequencies in the Fourier transform. Higher scales correspond to lower frequencies and vice versa. A pseudo-frequency which is deduced from the scale is sometimes used in the spectrum plot to improve understanding and comparison.

The scale of the CWT can be chosen at any value hence has been named 'continuous.' An inverse transform function of the CWT can be defined as [66]:

$$f(t) = \int\limits_{-\infty}^{\infty} \int\limits_{-\infty}^{\infty} W_s(a,b) h_{a,b}(t) \frac{da}{a^2} db \qquad (2.17)$$

Note that since the CWT is a redundant transform and there is not a unique way to define its inverse transformation [71].

An example time-frequency 2-D CWT plot of the chirp signal in Figure 2.17 is given in Figure 2.19. The time axis is same with the raw signal and the scales axis represent the spectrum energy distribution at different time instant. Higher intensity in the figure represent higher energy.
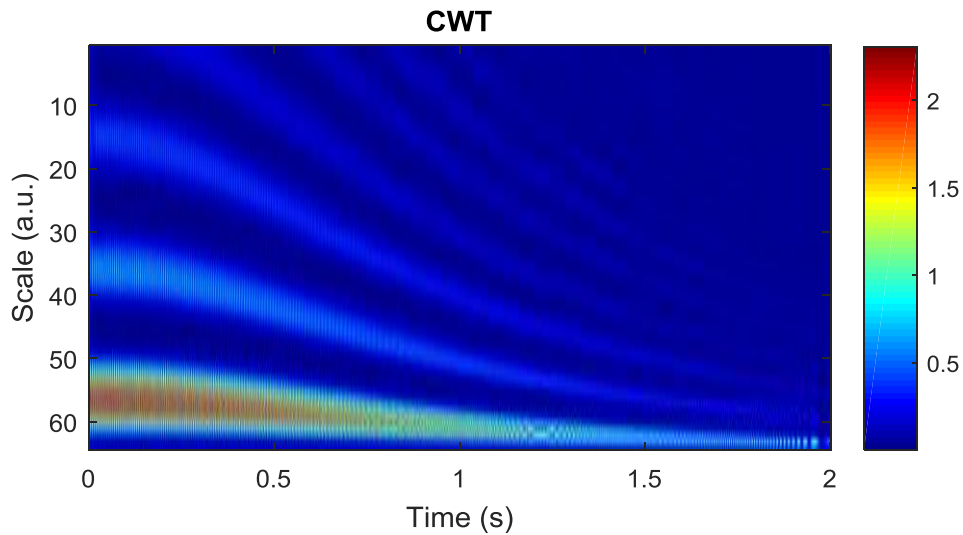
Figure 2.19. An eample CWT of the chirp signal in Figure 2.17.

As the number of scales in the CWT is large, since it can choose any possible value, the computation power required is correspondingly relatively large and it may also

generate redundant data. A discrete wavelet transform (DWT) [69] can be used to mitigate the above issues by only calculating certain scales and shifts based on the power of two. Mallat [72] has developed an efficient way to calculate the DWT by filtering and significantly increased the computational speed.

Basically, in DWT a signal is filtered by a high pass filter and a low pass filter to generate two decomposed signals which are commonly referred as approximations and details. As for many signals, important information is usually in the lower frequency part; therefore the decomposed approximation signal can be further filtered into a second level approximation and detail. This process can be iterated, as shown in Figure 2.20.

To avoid generating redundant data, for each level of decomposition, the signal is downsampled to half of its original length. The 2-D spectrum of the DWT is usually illustrated by times and levels.

For those interested in analysing the higher frequency components of the signal, a wavelet packet [73] can be applied. The wavelet packet is similar to the DWT, but instead of discarding the detail signals, the wavelet packet also decomposes the detail into a new pair of approximation and detail at each level. Compared with the DWT, the wavelet packet is more generalised and can offer a richer possibility for signal analysis.
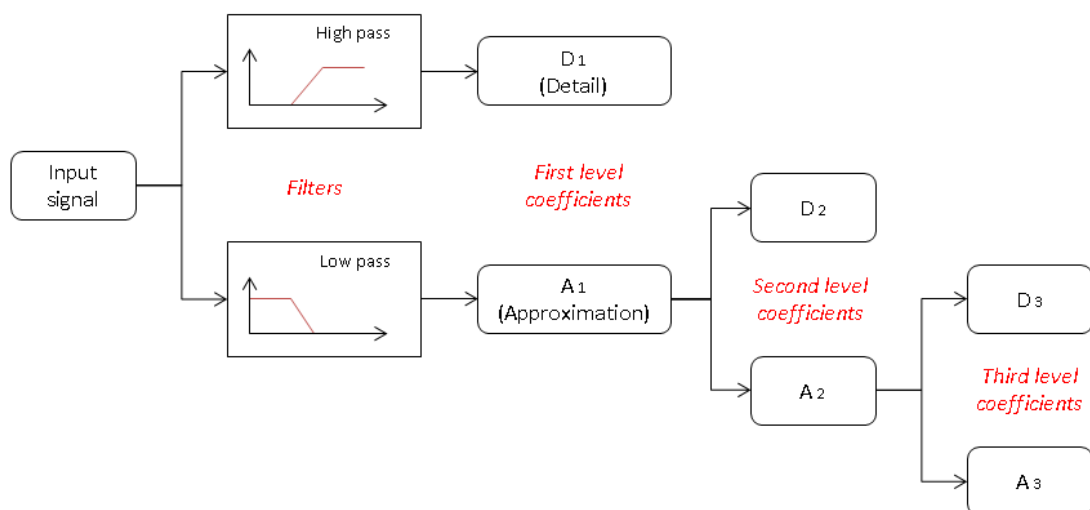
Figure 2.20. Discrete wavelet transformation decomposition tree.

2.4.3 Other signal processing tools

The Hilbert transform is often applied in practice when imaging [74]. It extends a real signal into the complex plane to derive its analytic representation. In ultrasonic signal processing and imaging, the Hilbert transform is usually used to calculate the envelope of a signal to smooth it and to neutralise the effect of wave fluctuations [75].

Filtering is also important in ultrasonic inspection as the raw signal often contains a D.C. component and high-frequency electronic noise. A bandpass filter can be applied to the raw signal before continuing with any further processing to remove these unwanted components.

Additionally, logarithmic algebra is often used to express the final images to reduce the dynamic range of image intensity. Generally, this is achieved by:

$$I_{log} = 20log_{10}(I_m)$$

(2.18)

where I_{log} is the logarithmically compressed image, I_m is the modulus of the input image, which is usually normalised to its maximum value before the calculation.

2.5 Noise reduction algorithms

As discussed in Chapter 1, many materials used in industry often exhibit heterogeneous or acoustically scattering properties, which constrain ultrasonic NDE techniques. Target echo pulses can be embedded in a strong grain noise background, even if the defect is much larger in size than the grain boundaries surrounding it.

A range of techniques have been developed to achieve noise reduction in ultrasound inspection applications along with other similar areas such as radar [76, 77], sonar [78], and communications [79-81]. Most of the existing methods are spatial diversity based or frequency diversity based. This Section will review some of these methods.

2.5.1 Spatial diversity based techniques

Spatial diversity based techniques require multiple A-scan traces that were emitted from different locations and orientations. Typically, the echoes of a legitimate reflector are more consistent when received at different locations/orientations compared with the echoes associated with the grain noise. A simple example of using spatial diversity to achieve noise reduction is to average several A-scans that were acquired in close proximity but from slightly different source locations [82, 83]. Basically, beamforming techniques that using delay and sum [84] such as conventional SAFT and the advanced array imaging algorithm TFM intrinsically operate with spatial diversity. However, the SNR improvement by this averaging process is limited if the grain noise is spatially correlated [85]. Wilhjelm et al. has proposed other combination operators in addition to averaging, including median and geometric mean. [86].

The dual apodization with cross-correlation (DAX) [87] has shown promise in reducing speckle noise in biomedical ultrasound. DAX uses two apodization functions that can be seen as spatial filters alongside basic delay and sum beamforming to create opposing signals with out-of-phase grating lobes, which are then cross-correlated. A high correlation coefficient at a certain point means that both of the signals are similar and that the signal at the point is likely to be from a reflector. Conversely, a low correlation coefficient will mean that the signals are unrelated and are likely to be either contribution from the sidelobe or speckle noise. The DAX can also be further combined with the nearest neighbour cross-correlation to improve robustness [88]. Lardner et al. have exploited the Sub-Aperture Spatially Averaged Correlation Imaging (SASACI) [89] algorithm and the Correlation for Adaptively Focused Imaging (CAFI) [90] algorithm which were inspired by the DAX approach, for grain noise reduction in the field of NDE. Li et al. have also proposed an adaptive beamformer that applies a lateral spatial filter to the delayed array data based on the statistical analysis to achieve noise suppression [91].

Phase coherence imaging (PCI) also originated from biomedical ultrasound [92] and had been extended to NDE [10]. Instead of using the summation of the signal amplitude, like conventional delay and sum techniques, the PCI calculate special

factors which are based on the statistical property (e.g. standard deviation) of the phase. Theoretically, a legitimate reflector has a more consistent phase distribution across A-scans from different elements compared with the grain noise, if the beam is well focused. A plane-wave phase-coherence imaging has also been developed by Cruza et al [93], to achieve ultrafast imaging and to improve dynamic range compared with TFM.

2.5.2   Frequency diversity based techniques

As discussed in Section 2.5.1, spatial diversity based techniques require multiple acquisitions from different transducer positions. This can be straight-forward to achieve by employing phased array techniques. However, phased array is not always available, e.g. in the case of low-frequency applications.

Grain noise in the coarse-grain material is not only coherent to different inspection orientations and locations, but also coherent to the inspection wave frequency [94].This phenomenon was originally used in radar system to achieve noise suppression and latterly has been introduced into ultrasound [95].

Techniques using this phenomenon are frequency diversity based, which distinguish legitimate reflectors from grain noise by analysis of the differences between their spectral characteristics. The grain noise is more sensitive to frequency than a legitimate reflector, as the echo from grain boundaries is a collective interference result of a group of spatially unresolvable grain scatterers. As the echo of each scatterer has its own amplitude and phase, the interference echo may have constructive or destructive amplitude at certain frequencies. This will result in the echo associated with grain noise commonly containing fewer frequency components than a legitimate reflector. In addition, as the frequency diversity based techniques require analysis of spectrum characteristics, a wider frequency band transducer is usually required.

One of the well-known frequency diversity based techniques is the split spectrum processing (SSP) technique, which was first published in 1979 [96, 97]. The process of SSP includes four steps and is described by the flowchart in Figure 2.21:

- Transform the original broadband signal into frequency domain;
- Decompose the frequency domain signal by multiplies of a set of pass-band filters;
- Apply the Inverse Fourier Transform to each filtered spectrum;
- Recombine these time domain signals using appropriate algorithms.

The decomposing of the raw A-scan trace can be achieved by conventional filtering techniques but it is commonly done by multiplies of a set of windows in the frequency domain.

Five filter (or window) specifications that may affect the results of SSP are listed below:

- The number of band-pass filters
- Total filter bandwidth
- Filter type
- The bandwidth of each filter
- Overlap of filter pass-bands
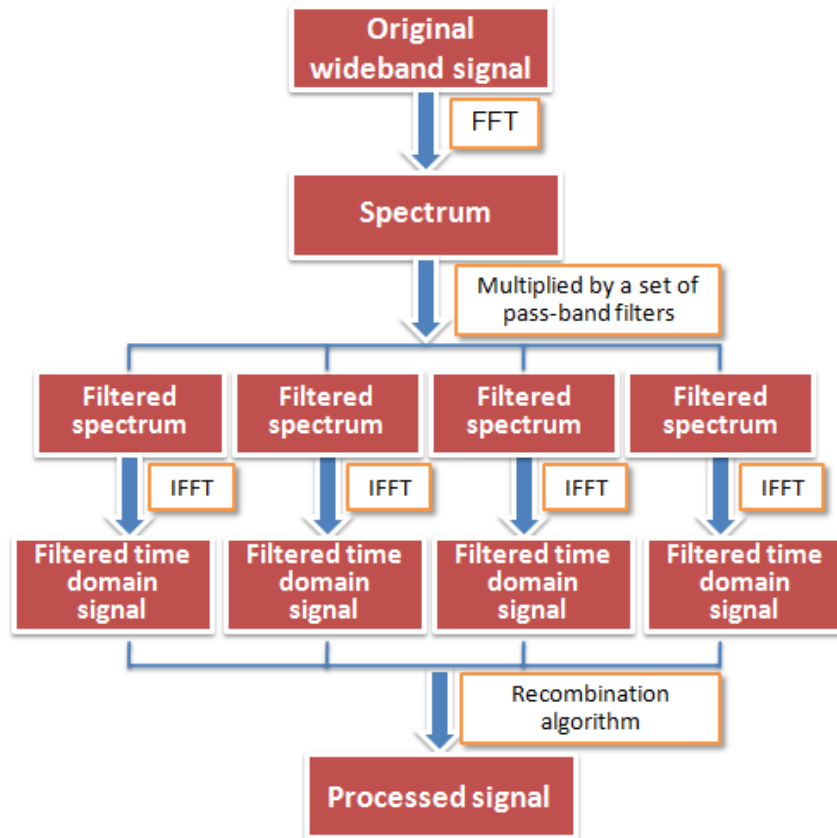
Figure 2.21. Flowchart of Split Spectrum Processing methodolgy.

Literature has shown that the number of filters can be varied in a large range, from three [98] to two hundred [99, 100]. Technically, increasing the number of filters will result in an increase in SNR. However, the computational complexity is also increased with each additional filter, while the relative SNR improvement decreases rapidly if the filter number is greater than 10 [98]. In addition, the improvement in SNR using extra filters is also limited by the frequency resolution of the spectrum. The total bandwidth of all filters is commonly chosen to be the same with the bandwidth of the transducer at its –6dB drop-off point. For materials with strong grain noise, the upper frequency band can be selected lower than that of the transducer since higher frequencies are usually more attenuated [100], see Section 3.1.3 and Figure 3.6. Gaussian filters are commonly used in most of the literature [97-99, 101, 102]. Conventionally the bandwidth of each filter is chosen to be equally sized, and all filters are uniformly distributed across the entire processing

frequency range [97, 98, 103]. Rodriguez et al. have recently proposed a new method that assigns the bandwidth of each filter to be proportional to its centre frequency [104]. Importantly, the overlap between filter bands should not be too large, or the effect of SSP may be reduced, while no overlap will result in missing information in certain frequencies. Commonly, the overlap is chosen between 0% and 25% in most of the literature [98, 100, 105], calculated at the 50% drop-off point.

After the filtered sub-spectrum has been transferred back to time domain sub-signals, the recombination algorithms will be applied to generate the result. There are mainly two types of recombination: based on order statistic or phase observation [106].

Order statistic based recombination algorithms using the inequivalent statistical information of the filtered channels to separate the legitimate reflector from grain noise, based on a particular rank (e.g. minimum, median, maximum) [103]. These algorithms are based on the coherence of the amplitude of the filtered channels, such as the Minimization (MIN) [105] algorithm and the Normalised Minimization (NMIN) [107] algorithm, as given in Eq. (2.19) and Eq. (2.20).

- *Minimisation:*

$$R(n) = \min(|Z_1(n)|, |Z_2(n)|, \cdots, |Z_j(n)|) \tag{2.19}$$

- *Normalised minimization:*

$$R(n) = \frac{\min(|Z_1(n)|, |Z_2(n)|, \cdots, |Z_j(n)|)}{\max(|Z_1(n)|, |Z_2(n)|, \cdots, |Z_j(n)|)} \tag{2.20}$$

where $R(n)$ is the reconstructed signal, $Z_j(n)$ is the split time domain sub-signal, and j is the index of the sub-signal.

Phase observation based recombination algorithms like the polarity thresholding (PT) [101] algorithm and the polarity thresholding with scaling (PTS) [108] algorithm detect the echoes of legitimate reflectors based on the phase coincidence of the filtered channels.

- *Polarity Thresholding:*

$$R(n) = \min\big(|Z_1(n)|, |Z_2(n)|, \cdots, |Z_j(n)|\big),$$

$$\text{if all } Z_j(n) > 0 \text{ or if all } Z_j(n) < 0 \tag{2.21}$$

- *Polarity Thresholding with Scaling:*

$$R(n) = \frac{J_P - J_N}{J} \cdot \min\big(|Z_1(n)|, |Z_2(n)|, \cdots, |Z_j(n)|\big), \tag{2.22}$$

where J is the total number of the sub-signals, J_P is the number of sub-signals that have positive amplitude at n, and J_N is the number of sub-signals that have negative amplitude at n.

The SSP was initially applied to single A-scans application, but later been extended to improve SAFT images by applying the SSP to each image column [109]. Dantas et al. has also extended the SSP in 2-D image processing in the medical field by applying Gabor filters [110].

One drawback of the SSP is that the output signal of the conventional SSP algorithm may suffer a decreased axial resolution due to the use of narrow bandpass filters [95]. Interestingly, a coded excitation technique has been combined with SSP to enhance the axial resolution [111].

Another commonly known drawback of the SSP is its sensitivity to parameter tuning [112], such as the range of the total bandwidth, filter number etc. This parameter setting is usually tuned through a trial-and-error process, and it is varied for different materials in practice, even for the same material with a different propagation distance. The output of SSP can be easily ruined by an inappropriate parameter setting, especially when the SNR of the received signal is low.

Many efforts have been made to address this drawback. Karpur et al. has suggested the optimal number of filters for MIN algorithm implementation [100]. Li et al. proposed a method to determine the optimal total processing bandwidth by analysing the spectral histogram of the signal [113]. Tian et al. also suggest a method to locate

the optimal processing bandwidth by using group delay moving entropy with target spectral characteristics known a priori [114].

Advanced SSP has also been exploited to reduce the parameter sensitivity problem. Erisson et al. developed a new method using a band stop filter to extract sub-signals instead of bandpass filtering [115]. Yuan et al. suggest a phase observation based method by counting the consecutive coincidence polarity at a certain time delay of the signal [116]. However, both algorithms still require a carefully selected threshold.

Another frequency diversity based algorithm has also been developed to enhance the detection capability and reliability. Gustafsson proposed a model based algorithm that defines optimal filter bands according to the statistical property of the simulated signal and noise [112]. The result is promising as the optimal filter band is adapted to the test signal, but the algorithm is strongly related to the signal and noise model which is difficult to achieve in practice. Izquierdo et al. exploited an advanced filtering technique that filters the signal with a changing bandwidth which is estimated by autoregressive techniques. The algorithm can address the frequency dependent attenuation issue which is caused by the scattering property of materials. However, it may not be suitable for highly scattering materials, which have a more complicated spectral characteristic [117]. Zhang et al [118] have also used Sparse Signal Representations algorithms to achieve grain noise reduction and ultrasonic flaw detection.

Many techniques have employed the wavelet transform as it is a more natural way to represent the signal since the selection of the mother wavelet is flexible. Abbate et al. developed an algorithm to eliminate grain noise by pruning and thresholding certain CWT coefficients [66]. Song et al. uses the wavelet transform as filters, but the results were only based on white noise simulation and high SNR experimental data [119]. Pardo et al. discussed the use of two undecimated DWT for ultrasonic NDT noise reduction [120]. Matz et al. also show a similar technique but using the wavelet packet [121].

Other techniques have also been developed that use pre-existing knowledge of the materials and signals. These techniques can adjust themselves to adapt the data by a training process. The training process allows the algorithm to capture essential characteristics of the legitimate reflector and grain noise echoes. Sun et al. proposed advanced algorithms that combine the SSP with the artificial neural network (ANN) [122] and adaptive-network-based fuzzy inference system (ANFIS) [123, 124]. Liu et al. also developed a similar technique using ANN [125].

In addition, frequency diversity based techniques can also be combined with spatial diversity based techniques [126]. As frequency diversity based techniques require information from different frequencies, a wider band transducer is more desirable. Mulholland et al. attempted to increase the transducer bandwidth by attaching multiple matching layers in the front face of a transducer [17].

2.6 Data acquisition, modelling, and processing

This Section introduces the experimental configuration, material specimens, modelling, and processing platform that is used throughout the Thesis.

2.6.1 Data acquisition

Figure 2.22 shows the commercial single element probe and the phased array probe used in the Thesis, along with their respective details in Table 2.1 and 2.2.

Two PACs were employed during this PhD research work, the DYNARAY-256/256PR (Zetec, Snoqualmie, USA, S/N: DYN-0052) and the FlawInspecta FIToolbox (Diagnostic Sonar Ltd., Livingston, UK, S/N: 150020). The DYNARAY contains 256 channels which can be active simultaneously and is shown in Figure 2.23. The sampling frequency can be selected at 25MHz, 50MHz, or 100MHz. The DYNARAY is driven by a Matlab (The MathWorks Inc., Natick, USA) script to acquire FMC datasets. This script was developed in the Centre for Ultrasonic Engineering (CUE) and uses the Dynaray open source feature. The FlawInspecta, shown in Figure 2.24, is configured with 64 simultaneously active channels and so a

multiplexing system is present to enable the 128-element phased array to be controlled. The sampling frequency of the FlawInspecta is fixed at 40MHz. The FlawInspecta is driven by a Labview (National Instruments Corporation, Austin, USA) program, again bespoke software was developed within CUE for FMC data capture. In this work, a -40V negative square pulse with a pulse length of 100ns was used to excite the array elements for both PACs.

Three different material samples are used in the Thesis, as listed and illustrated in Table 2.3. The materials presented have been measured at University of Strathclyde as the full material properties were not available from E.oN and Siemens.

Figure 2.22. The commercial single element probe (top) and the phased array probe (bottom) used in the Thesis.

Table 2.1. Specifications of the single element probe.

Manufacture	OLYMPUS
Part No.	A320S
Serial No.	718359
Element size	0.75 Inch (Diameter)
Centre frequency	5 MHz
Fractional bandwidth	49.61%

Table 2.2. Specifications of the phased array.

Array type	1-D Linear array (Vermon)
Array size	128 elements
Element pitch	0.7 mm
Centre frequency	5 MHz
Fractional bandwidth	63%
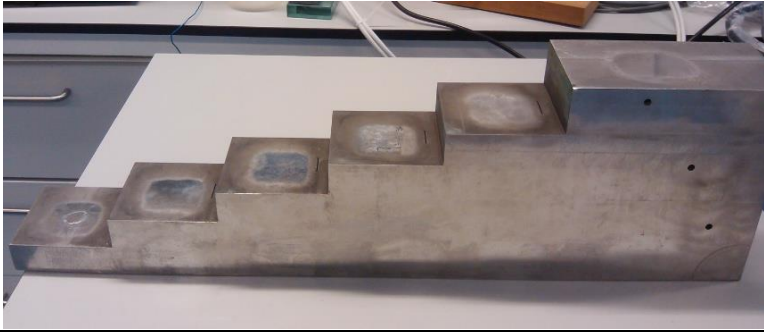
Figure 2.23. Phased array controller: DYNARAY.

Figure 2.24. Phased array controller: FlawInspecta.

Table 2.3. Specification of the experimental samples.

	Austenitic steel sample	
1		Composition: ~8% Mn, ~4% Cr
	This sample was provided by E.ON Technologies and contains no flaw. The height of the sample varies (nominally around 50mm) and the width is 79mm. The longitude wave propagation speed in this material is ~5262m/s. Austenitic stainless steels are favoured for the use as the primary coolant piping of pressurised water reactors in nuclear power plants and pipe work, plus pressure vessels in the petrochemical industry due to their outstanding resistance to corrosion and oxidation as well as better plasticity and higher strength versus typical carbon steels [127].	
	Inconel 617 sample	
2		Composition: ~60% Ni, ~20% Cr, ~10% Co
	This sample is also provided by E.ON Technologies and contains no flaw. The sample is keystone-shaped which has a height around 40mm, and a width linearly varies between 20mm and 40mm. The longitude wave propagation speed in this material is ~5679m/s. Inconel alloys are attractive construction material components in industries such as aerospace and power plants due to an exceptional combination of oxidation resistance and high-temperature modulus [128]. Material Specifications of Inconel 617 can be found at [129].	

	Inconel 625 sample	
3		Composition: ~60% Ni, ~20% Cr, ~10% Mo
	This step wedge sample is provided by Siemens AG (Berlin, Germany) and contains three side-drilled holes (SDHs). The chemical compositions of this sample are slightly different from the Inconel 617 sample. This is a large sample where the top height is 160mm. The three SDHs are at 10mm, 60mm and 105mm depth from the top surface, respectively. The longitude wave propagation speed in this sample varies across a large range, from 5200m/s to 5900m/s. Material Specifications of Inconel 625 can be found at [130].	

2.6.2 Modelling

Modelling is an important tool to simulate different scenarios conveniently. It can be used to validate and analyse algorithms with multiple configurations which may not be available experimentally due to the manufacturing time and costs. In this work, an analytic model is used to simulate signals received from difficult materials. Details of the model will be further discussed in Chapter 3 and Chapter 7.

2.6.3 Processing platform

The algorithms proposed in this work are developed using Matlab (The MathWorks Inc., Natick, USA, Version 8.6.0.267246) script. As the processing of data can take a significant amount of time, Compute Unified Device Architecture (CUDA) [131] is employed to accelerate the computational efficiency, where appropriate. The CUDA Toolkit version used in this work is v6.5. CUDA is a parallel computing program that can run multiple treads simultaneously on a General Purpose Graphical

Processing Unit (GP-GPU). A modern NVidia graphics cards contain GPUs with 2880 cores, which is significantly more when compared to modern CPU configurations. As a trade-off, the cores in GPU are much simpler than those in a CPU. Parallel computing using GPU is suitable for simple iterative tasks that can be calculated separately without affecting the final result; thus, it is an efficient tool for ultrasound imaging algorithms [132].

Chapter 3

Moving Bandwidth Split Spectrum Processing

As introduced in Chapter 2, many techniques have been developed to achieve noise reduction. Phased array imaging techniques such as the widely used Focused B-scan [27], and Total Focusing Method (TFM) [27] have already achieved great success. However, phased array techniques are not always available, e.g. in the case of low frequency inspection.

Based on the fact that structural noise in difficult materials is frequency coherent, frequency diversity based techniques like the well-known Split Spectrum Processing (SSP) have been developed [108]. However, as discussed in Chapter 2, the sensitivity of the parameter selection for SSP is well known in literature, especially when the SNR is low [112].

Other frequency diversity based algorithms such as the Wavelet Transform (WT), are also based on the spectrum differences between the grain noise and target echoes. However, the characteristic of the spectrum varies for different materials and hence, limits the versatility of these methods.

To adapt to the properties of different materials, model based frequency diversity techniques have been developed, such as Optimal Detection (OD) [112]. These techniques can adjust themselves by learning the pre-knowledge of materials. However, the learning requires a high fidelity dataset, otherwise their performance will deteriorate.

Therefore, the motivation of this Chapter is straightforward: to develop a robust frequency diversity based technique which is less affected by material properties, without the necessity of a training process. Although grain noise is generally more sensitive to frequency compared with echoes from a defect, different load materials

may have different absorbing and attenuation properties, which causes the energy spectrum of the defect signal to be distributed differently depending on the material under inspection. Moreover, even for the same material, the grain size may be vary across different regions. In addition, the propagation distance can also affect the characteristic of the received spectrum. Hence, to achieve the stated requirements, this algorithm must consider all the possibilities of energy distribution on the spectrum and extract the target echo correctly. This is difficult to achieve without knowing the spectrum characteristics in the first place.

A spectrum based technique in the field of medical imaging [133] introduced the concept of 'moving bandwidth' which can capture the target echoes with different spectrum characteristics and reduces the grain noise in 'localised frequencies'. This concept should also be suitable for NDE, and the 'moving bandwidth' can be used to achieve the proposed objective.

In this Chapter, a new frequency diversity based algorithm named Moving Bandwidth Split Spectrum Processing (MB-SSP) for structural noise reduction is presented. The algorithm is inspired by the concept of 'moving bandwidth', but focused on the reduction of the effect of phase dispersion. It uses the phase coherence to eliminate the grain noise for different frequencies and reconstruct the signal to extract useful information.

3.1 Principle and methodology of Moving Bandwidth Split Spectrum Processing

3.1.1 Summary of methodology

The procedure of the proposed MB-SSP algorithm can be summarized in four steps. A flow chart and a concept diagram are given in Figure 3.1 and Figure 3.2 to show the relationship between each step.
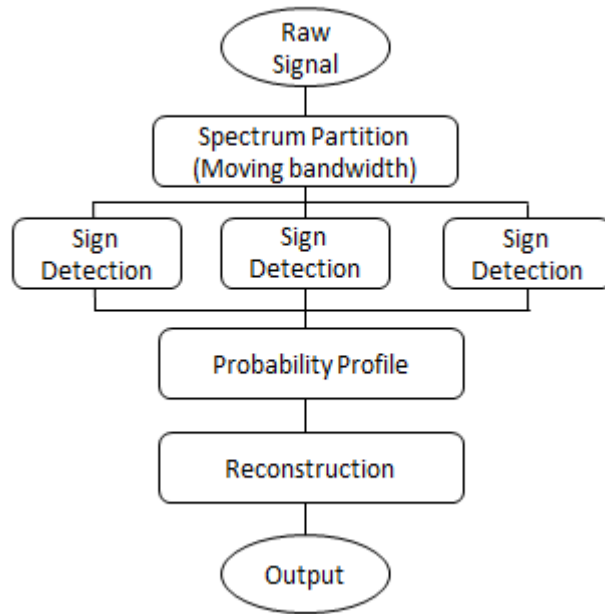
Figure 3.1. Flowchart of MB-SSP.
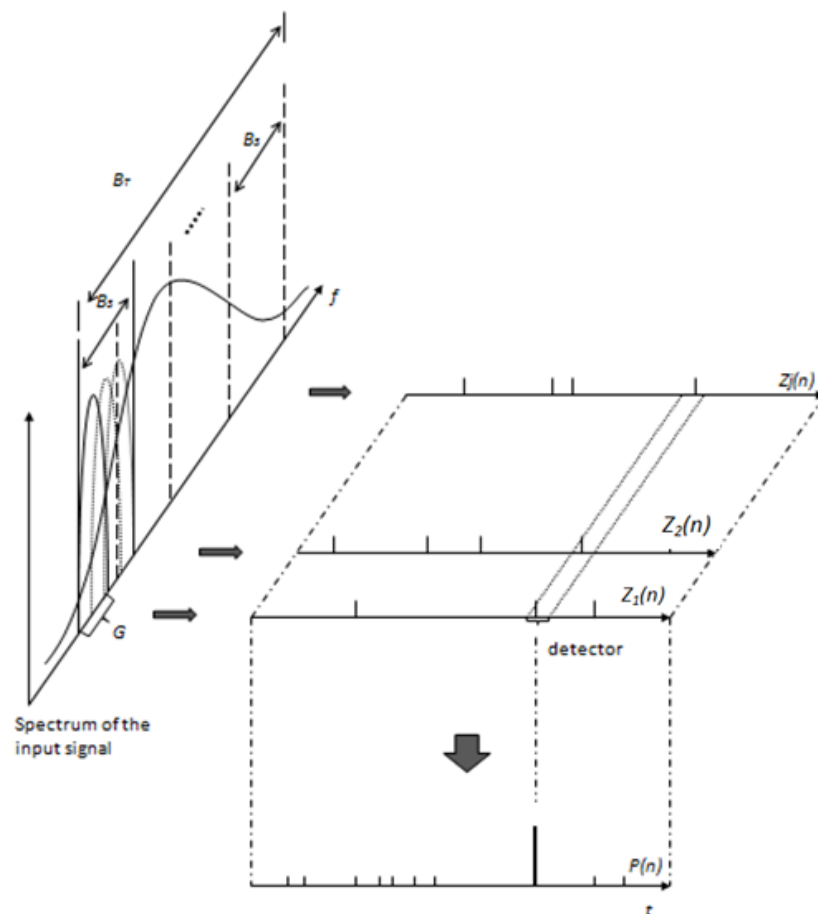
Figure 3.2. Concept figure for MB-SSP

i.   Spectrum partition by a moving bandwidth

To extract the 'localised information', the proposed algorithm firstly filters the acquired A-scan data into a set of sub-signals which contain different frequency components. A sub-signal is a time domain signal filtered from the raw A-scan signal. This is achieved by transforming the acquired RF signal into the frequency domain, using the Fourier Transform, and then applying moving window functions with bandwidth B_S to partition the spectrum, before finally applying the Inverse Fourier Transform. This procedure describes the concept of 'moving bandwidth', i.e. a set of overlapped bandpass filters. To include more information from the raw signals, the range of total processed bandwidth B_T, i.e. the span of the moving bandwidth B_S, should be chosen to be as wide as possible: typically approximately equal to 200% fractional -6dB bandwidth of the transducer centre frequency. Meanwhile, the bandwidth B_S of each filter or window cannot be too narrow, or too wide, generally selected around 80% of the fractional bandwidth of the transducer centre frequency. B_S should be moved at even intervals inside the total processed bandwidth B_T, and should overlap with ~50% of its previous location. The sub-signals extracted from each B_S will be denoted as $Y_j(n)$, n is the sampled time delay, j is the index of the sub-signals, with maximum value of J.

ii.   Sign Detection in Localisation Spectrum

For each sub-signal $Y_j(n)$ obtained from the previous step, each potential legitimate reflector location is detected as the 'localised' information of a related frequency band $B_{S,m}$, by further filtering the signal into narrow band frequency channels $r_m(n)$, and using Eq. (3.1).

$$Z(t) = \begin{cases} 1, & if\ all\ r_m(t) > 0\ or\ r_m(t) < 0 \\ 0, & otherwise \end{cases} \qquad (3.1)$$

This is similar to Polarity Thresholding (PT), but the bandwidth of each frequency channel is narrower and no amplitude information is included. Since the spectrum characteristic of a signal varies when acquired from different locations, depth and materials, for example, the number of the frequency channels may affect the correctness of the 'localised' defect extraction. Hence, different numbers of channels

are generated to make sure all useful information is included. This can be done by repeating the above process with a different number of filters.

iii.   Probability Profile Generation

After all sub-signals have been processed, a probability profile $P(n)$ will be generated to show how likely a point in the raw signal is to be a legitimate reflector echo. The 'detector' is a small window which travels along the time domain signals. The peaks contained in the window for all $Z_j(n)$ at the same time delay decides the value in $P(n)$, as shown in Eq. (3.2). Assume J sub-signals have been processed, for a certain time delay n; L_w is the length of a segmental signal containing point n.

$$P(n) = \sum_{j=1}^{J} S_j(n), \ \ j = 1,2 \cdots J$$
$$where \ S_j(n) = \begin{cases} 0, \ if \ all \ Z_j(n + l - L_w/2) = 0, \ \ l = 1,2 \cdots L_w \\ 1, \ otherwise \end{cases} \quad (3.2)$$

The length of the detecting window L_w generally should equal to $2L$, i.e. $2 * 2v/fc$, L is the range cell, which will be discussed in Section 3.1.2.

iv.   Reconstruction

The probability profile implies the position of a defect but is not intuitive for inspection. Further processing is required to extract useful information. This can be achieved by weighting the raw signal using the probability profile with a threshold Th. The threshold Th should be set between 0 and 1. Generally Th should be around 0.5 to balance the Probability of Detection (PoD) and Probability of False Alarm (PFA).

If the attenuating property of the test material is known *a priori*, then a scaling function $Ad_j(n)$ should be applied on each $S_j(n)$ to reduce the influence of grain noise at high frequencies due to long path lengths. The scaled $S_j(n)$, $Sc_j(n)$ is given by,

$$Sc_j(n) = Ad_j(n) \cdot S_j(n) \quad (3.3)$$

and the threshold Th is adjusted accordingly,

$$Th(n) = \frac{1}{2J} \cdot \sum_{j=1}^{J} Sc_j(n) \tag{3.4}$$

In this case the threshold $Th(n)$ will be frequency dependent.

3.1.2 General model analysis

In this Section and Section 3.1.3, the proposed MB-SSP algorithm will be explained mathematically.

The proposed algorithm aims to reduce grain noise and detect the presence of legitimate reflector echoes. Typically, an ultrasonic radio frequency A-scan signal received by a transducer may be expressed as,

$$r(t) = r_{Sig}(t) + r_{Noi}(t) \tag{3.5}$$

where t is time, $r(t)$ is the received signal, $r_{Sig}(t)$ contains legitimate reflector echoes and $r_{Noi}(t)$ is the additive grain noise. System electronic noise is not considered in this model.

Importantly, for a given time instant, a legitimate reflector echo may or may not be present. Therefore two possible hypotheses are assumed,

$$\begin{cases} r(t) = r_{Sig}(t) + r_{Noi}(t), & H1 \\ r(t) = r_{Noi}(t), & H0 \end{cases} \tag{3.6}$$

The noise signal $r_{Noi}(t)$ in Eq.(3.1) and Eq.(3.2) can be modelled as the superposition of echo signals reflected back from random distributed scatters. Considering the ultrasonic pulse $h(t)$ emitted from the transduce has it Fourier transform $H(\omega)$, where ω is angular frequency. Then the spectrum of an echo $R(\omega)$ from a distant reflector can be expressed as,

$$R(\omega) = \sigma H_{tran}(\omega) H_{refl}(\omega) e^{-i\omega\tau} \tag{3.7}$$

where $H_{tran}(\omega)$ is the frequency response of transducer, $H_{refl}(\omega)$ refers to the frequency response of the material, σ is the reflection coefficient, $\tau = (2x/v)$ is the propagation time where x is the transmitting distance and v is the sound velocity.

Since grain noise can be seen as the superposition of backscattered echoes from different scatterers, the received noise signal can be written as:

$$R_{Noi}(\omega) = \sum_{k=1}^{K} \sigma_k H_{tran}(\omega) H_{refl}(\omega) e^{-i\omega\tau_k} \tag{3.8}$$

K is the total number of the scatterers.

Based on the assumption in frequency diversity techniques that grain noise components are uncorrelated in different frequency channels [101], if we filtering the received signal by a set of narrow bandpass filters $H_{fil}(\omega - \omega_m)$, then the spectra of each filtered frequency channels can be represented as:

$$R_{Noi,m}(\omega) = \sum_{k=1}^{K} \sigma_k H_{tran}(\omega) H_{refl}(\omega) H_{fil}(\omega - \omega_m) e^{-i\omega\tau_k} \tag{3.9}$$

where m is the index of the filter and ω_m is its centre frequency. Let

$$G_m(\omega - \omega_m) = H_{tran}(\omega) H_{refl}(\omega) H_{fil}(\omega - \omega_m) \tag{3.10}$$

then

$$R_{Noi,m}(\omega) = \sum_{k=1}^{K} \sigma_k G_m(\omega - \omega_m) e^{-i\omega\tau_k} \tag{3.11}$$

Applying inverse Fourier transform,

$$r_{Noi,m}(t) = \sum_{k=1}^{K} \sigma_k g_m(t - \tau_k) e^{-i\omega_m(t-\tau_k)} \tag{3.12}$$

where $g_m(t)$ is the inverse Fourier transform of $G_m(\omega)$.

Similarly, an echo from a legitimate reflector can be expressed as

$$r_{Sig,m}(t) = g_m(t - \tau) e^{-i\omega_m(t-\tau)} \tag{3.13}$$

For a given time instant τ, the value of the received echo signal can be seen as the phasor sum of scatterers distributed in its range cell. A range cell is a time domain window that contains all the echoes of scatterers which can affect the amplitude and

phase of the centre time instant of the window. The length of the range cell is approximately equal to

$$L = \frac{2v}{f_c}$$

(3.14)

where f_c is the centre frequency of the transducer. Let

$$a_m(t-\tau)e^{i\theta_{m,\tau}} = \sum_{k=1}^{K} \sigma_k g_m(t-\tau_k)e^{-i\omega_m(\tau-\tau_k)}$$

(3.15)

$\theta_{m,\tau}$ is the equivalent phase angle at τ for frequency channel m,

(3.16)

$$\theta_{m,\tau} = atan2 \left\{ \sum_{k=1}^{K} A_{k,m} sin[\omega_m(\tau-\tau_k)], \sum_{k=1}^{K} A_{k,m} cos[\omega_m(\tau-\tau_k)] \right\}$$

where $A_{k,m} = \sigma_k g_m(t-\tau_k)$. All scatterers k are inside the range cell. Therefore, for the given time instant τ, substitute Eq. (3.12), (3.13) and (3.15) back into Eq. (3.6), the hypotheses *H1, H0* become,

$$\begin{cases} r_m(t) = g_m(t-\tau)e^{i\omega_m(t-\tau)} + a_m(t-\tau)e^{i[\omega_n(t-\tau)+\theta_{m,\tau}]}, & H1 \\ r_m(t) = a_m(t-\tau)e^{i[\omega_n(t-\tau)+\theta_{m,\tau}]}, & H0 \end{cases}$$

(3.17)

When $t = \tau$, $g_m(t)$ reaches its maximum value and $e^{i\omega_m(t-\tau)} = 1$; this corresponds to where the peak of the legitimate reflector echo occurs. For noise signals, since $\theta_{m,\tau}$ is related to the centre frequency and amplitude of each frequency channel, and the distances between the given point and the scatterers, it can be treated as a random distribution across $0\sim2\pi$, for different frequency channels at the same time delay.

Let $H_{refl}(\omega) = 1$, i.e. no frequency dependent attenuation is considered. Figure 3.3 shows a concept diagram of $r_m(t)$ for four different frequencies (simply identified using the *m* index) at a given time instant τ, under the condition of *H0*.

The diagram used in Figure 3.3 is a representation of Euler's formula in the complex plane. Euler's formula can be expressed as $e^{i\theta} = \cos\theta + i\sin\theta$, as shown in Figure 3.4. In the case of this Section, the complex plane of Euler's formula is used to describe the phased angle of a signal at a certain time instant. For example, when

$\theta = 90°$, $e^{i\theta} = 1$, the signal has reaches its positive peak value at the given time instant.
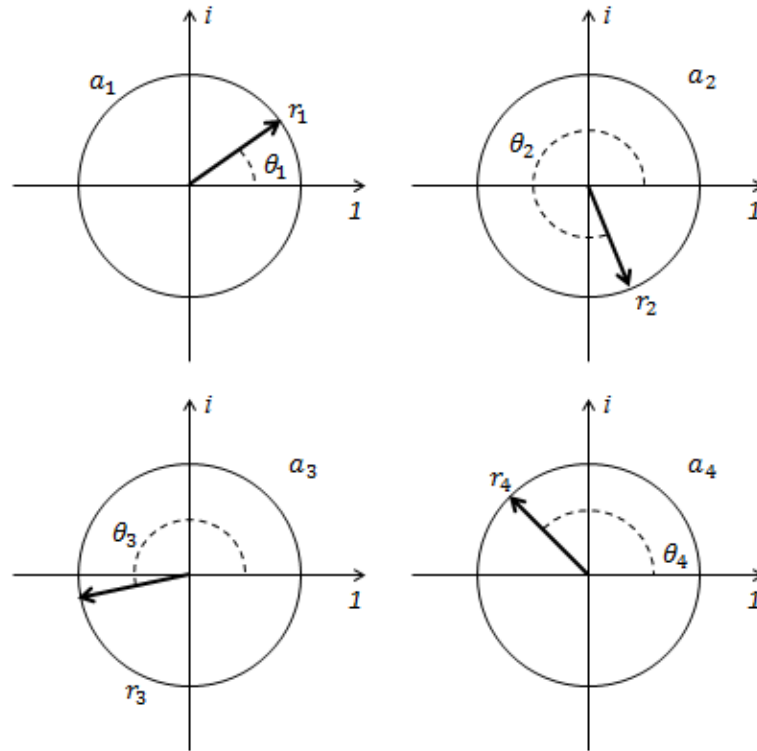

Figure 3.3. Diagram of $r_m(t)$ for four different frequencies channel (m=1, 2, 3, 4) at τ, under the condition of *H0*. Only grain noise is present in this case. The phase in different frequency channel at time instant τ is randomly distributed.

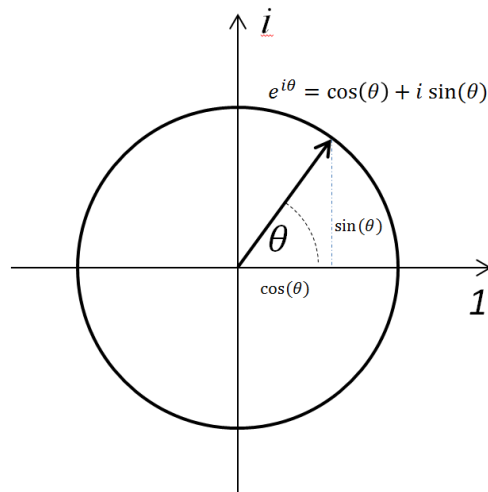$$e^{i\theta} = \cos(\theta) + i\sin(\theta)$$

Figure 3.4. Euler's formula presents in the complex plane

When under the condition of *H1*, since the peak of a legitimate reflector echo is present at τ, the amplitude and angle of $r_m(t)$ at τ will mainly be depended on the presented echo peak, especially for the situation when the echo signal from the legitimate reflector is much stronger than the noise component (SNR >>1), as can be seen in Figure 3.5.

As shown in Figure 3.5, it can be easily found that with the presence of the legitimate reflector echo, all frequency channels have same sign (in this representative case all of them are positive). Hence, we can detect all present legitimate reflector echoes in the signal by finding the time instance that all frequency channels are positive or negative, and subsequently remove the noise, as shown in Eq. (3.1).

The phase of each frequency channel is also a factor that can be used, since their distribution range is narrowed down when a legitimate reflector echo is present, as shown in Figure 3.5. However only sign information will be considered in this algorithm and the reason behind this will be explained in the next Section.

3.1.3 Frequency dependent attenuation and phase dispersion

The assumption that was made in Figure 3.3 and 3.3 assumed there is no frequency dependent attenuation. Unfortunately, an important fact is that the reflection and the propagation of ultrasonic wave in materials are both frequency dependent. For difficult materials, echoes reflected back from a distant legitimate reflector are typically significantly distorted. Importantly, parts of its frequency components are highly attenuated, and the legitimate reflector spectrum can no longer 'predominate' the entire bandwidth of the transducer. Generally, higher frequency components of an echo spectrum are more attenuated.

In addition, the spectrum energy of an echo signal reflected back from a grain is more focused on the higher frequencies. According to [134], in the Rayleigh region the amplitude frequency response is approximately in proportion to the square of frequency. An illustrative example of legitimate reflector and grain noise spectra are shown in Figure 3.6.
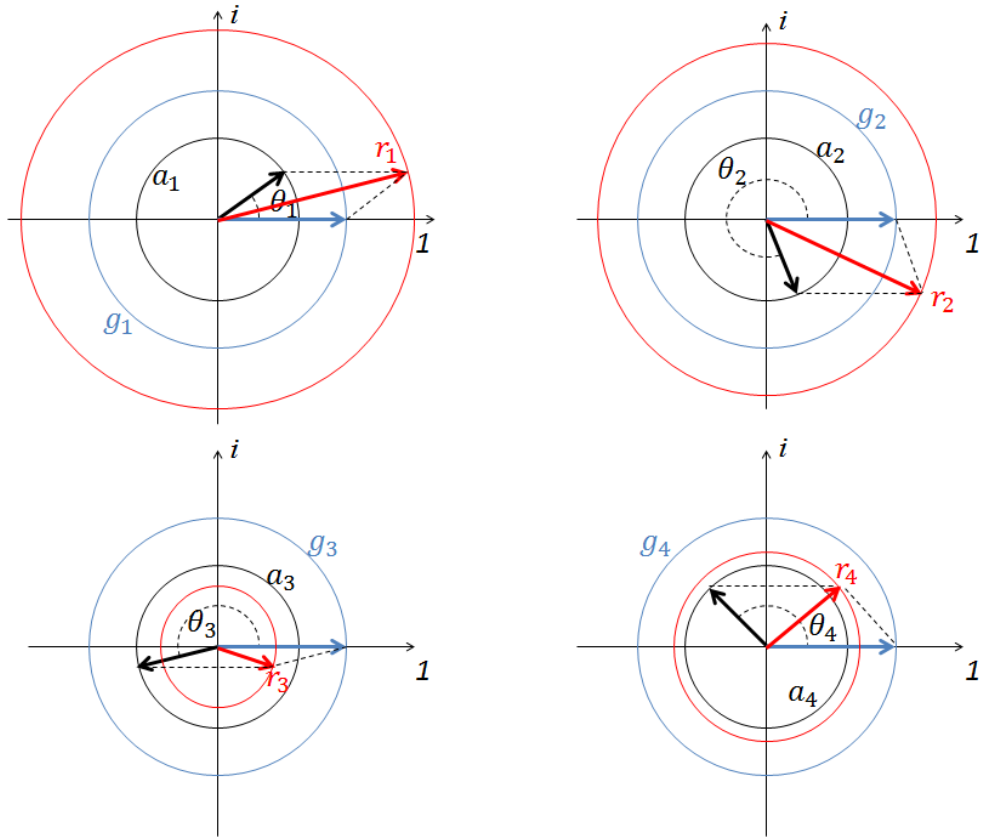
Figure 3.5. Diagram of $r_m(t)$ for four different frequency channels (m=1, 2, 3, 4) at τ, under the condition of *H1*. Both grain noise and legitimate reflector signal are presented at τ. The blue arrows represent the legitimate reflector signal, which ideally would have same energy level and same phase. Black arrows represent grain noise, and the red arrows represent $r_m(t)$ which is obtained by adding the legitimate reflector signal and grain noise at different frequencies. The polarity of $r_m(t)$ at different frequencies is agreed with legitimate reflector signal since it is larger than grain noise.

As can be seen in Figure 3.6, the spectra of legitimate reflector echoes can be significantly distorted, sometime its centre frequency may even go beyond the -6dB bandwidth of the transducer. Importantly, the noise from a difficult material can be at the same level as the legitimate reflector signal (SNR = 1), that means the legitimate reflector echo in some frequency channels may be easily buried by a strong noise component. As can be seen in Eq. (3.1), even only one channel containing no target echo is sufficient to violate the algorithm operation. Based on the analysis above, this issue is especially serious for the higher frequency channels, as can be seen in the concept diagrams shown in Figure 3.7.

To maintain the performance of the algorithm, one can apply a large set of narrow filter bands within a wider processing bandwidth to cover all the frequency range that may contain legitimate reflector echoes, and determine the time instances with the majority demonstrating coincident sign. Such similar concepts have been applied on algorithms like Scaled Polarity Thresholding and Consecutive Polarity Coincidence [108]. However, two problems arise. Firstly, with the increasing number of filter bands of the reconstructed signal will suffer a significant loss in detail, since only limited points of the signal can pass such a harsh requirement of sign coincidence for a large number of frequency channels. Secondly, an important fact has not been considering so far is that the phase velocity of each frequency channel is slightly different which will cause phase dispersion [135], as illustrated in Figure 3.8. Phase dispersion is a phenomenon that the phase velocity of a wave depends on its frequency. This will result in echo peaks from the same reflector appearing at different time instants for different frequency channels, as shown in Figure 3.9. With a wider processing bandwidth, this effect is no longer negligible.
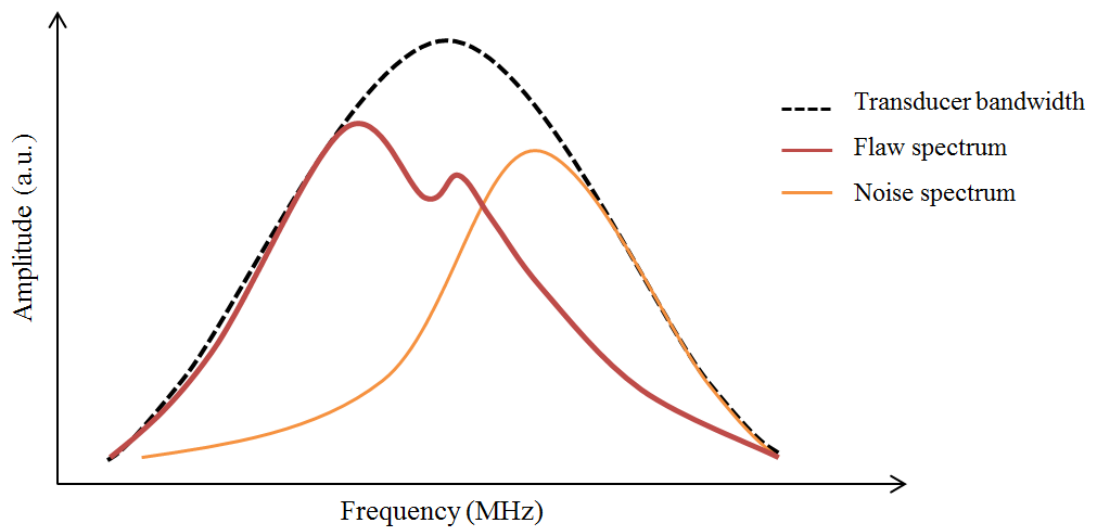
Figure 3.6. Spectrum example of legitimate reflector and grain noise.
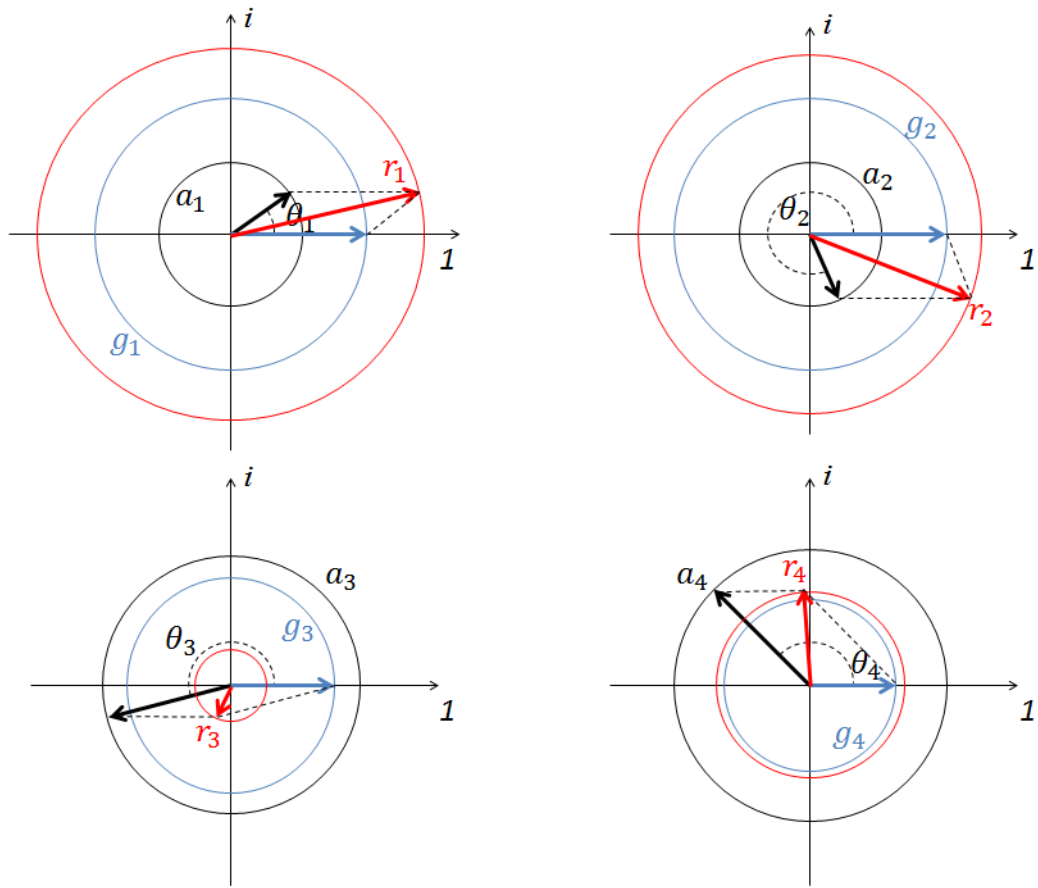
Figure 3.7. Diagram of $r_m(t)$ for four different frequencies (m=1, 2, 3, 4) at τ, under the condition of *H1,* for frequency dependent materials. Both grain noise and legitimate reflector signal are presented at τ. The blue arrows represent the legitimate reflector signal, black arrows represent grain noise, and the red arrows represent $r_m(t)$ which is obtained by adding the legitimate reflector signal and grain noise at different frequencies. The polarity of $r_m(t)$ at different frequencies is no longer agreed with legitimate reflector signal since it sometimes has smaller magnitude than noise due to the frequency dependent attenuation.
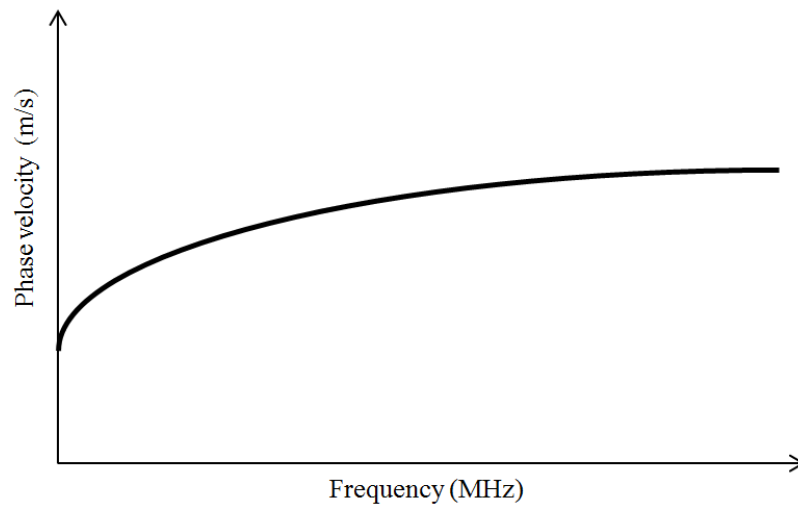
Figure 3.8. Phase velocity as a function of frequency.

63
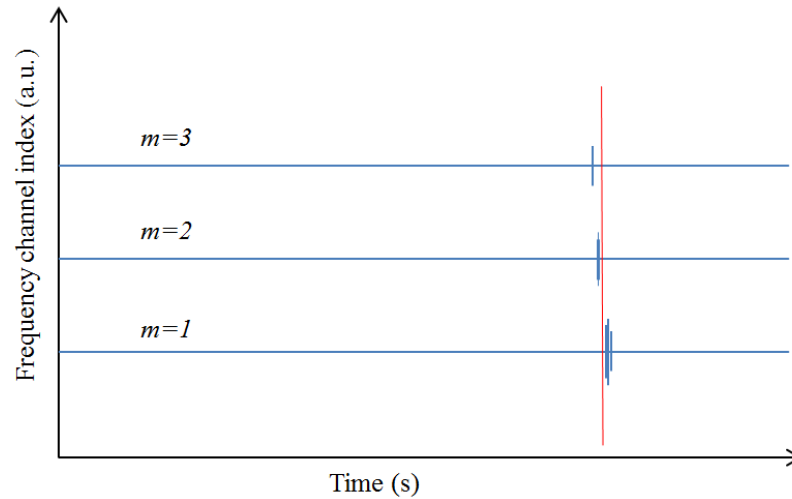
Figure 3.9. Echo peaks from the same reflector appeared at different time instant for different frequency channels. Frequency channel with higher index has a higher frequency hence a higher phase velocity.

Another way to consider this is to adjust the centre and the width of the total processing bandwidth of Eq. (3.1), in order to fit the characteristic of the legitimate reflector spectrum and let it 'predominate' the entire processing bandwidth. In this case since the processing bandwidth is reduced, the influence of phase dispersion is diminished. Also, there will only be a reduced number of filter bands inside the processing bandwidth, hence avoiding loss in detail. A knowledge of the exact frequency response of the legitimate reflector echo and the noise spectrum distribution, enables proper adjustment of this processing bandwidth of the algorithm to promote a good result. Unfortunately, the frequency response of the legitimate reflector echo and the noise cannot be explicitly known. In fact processing signals with no pre-knowledge of the legitimate reflector echo is one of the motivations of the algorithm. Hence, to avoid missing information from the raw signal and promote detection of all potential legitimate reflectors, Eq. (3.1) should be applied repeatedly across a wide frequency range with a reduced processing bandwidth and varied centre frequency to extract 'localised information' from different frequency bands of the spectrum. This procedure acts like a 'moving bandwidth'. Again, each time the processing bandwidth is moved, it must has an overlap with its previous location, to ensure no information is missing. This is also the reason why Eq. (3.1) only includes

sign information, as sign is more tolerant than phase for legitimate reflector echo detection.

However, the reduced bandwidth for each individual process leads to another problem. Based on Eq. (3.16), $\theta_{m,\tau}$ in different frequency channels are more coherent to each other since the reduced bandwidth minimises the difference of $A_{k,m}$ and ω_n in different channels. This lowers the noise reduction capability of Eq. (3.1). As discussed previously, a wider processing bandwidth will include more noise since the legitimate reflector spectrum cannot dominate the entire processing bandwidth. Thus, a compromise must be made that the processing bandwidth of Eq. (3.1) cannot be too wide or too narrow.

The moving bandwidth processing using Eq. (3.1) yields a set of processed sub-signals, containing echo peaks that potentially could be a legitimate reflector echo and artefact peaks caused by the remaining noise. Hence, further processing is required to extract the legitimate reflector echo and minimise the remaining noise components.

A simple and direct way to reconstruct a signal that indicates the location of the legitimate reflector echo is to combine all the sub-signals generated by the moving bandwidth via averaging. However with the above analysis, it can be shown that echo peaks from the same reflector are not present at the same time instance for different frequency channels. Thus, a time domain detection window is introduced to solve this. The detection window will move along the time axis, every peak covered by it will be counted. The more peaks identified, the higher value will be attributed to the reconstructed signal, hence the higher likelihood to be the location of a legitimate reflector echo.

Introducing the detection window instead of directly averaging all points at the same time instance means there is a risk to include extra noise when counting the legitimate reflector echoes, if the noise peaks are too close to the legitimate reflector. Hence the detection window length is critical to the algorithm success: too short and legitimate reflector echoes may not be counted; and must be long enough to maintain

the signal resolution. For these reasons, the length of the detection window is chosen as double length of the range cell L, in Eq. (3.14).

The reconstructed signal generated by the detection window is like a probability profile of the raw signal, and indicates the locations that are more likely to be a legitimate reflector. However this probability profile still has a lot of noise and it does not contain the detailed characteristic of the legitimate reflector signal. To solve this, the probability profile is truncated by a threshold to remove the noise, and then multiplied with the raw signal to produce the final result.

Since the attenuation is frequency dependent, if we know the attenuation property of the material, then each higher frequency channel is reduced accordingly. The new threshold level is based on the attenuation knowledge of each frequency channel.

3.2 Analysis of simulation approach

3.2.1 Simulation models

To generalize the study of the algorithm, simulated signals have been generated using analytical models.

According to Eq. (3.8), grain noise can be seen as the superposition of the echoes from different scatterers in the materials. It has been stated in literature [43] that the density of scatterers in the materials has to be greater than 5 scatterers/wavelength^2 in order to simulate Rayleigh distributed grain noise.

The energy distribution of an echo from a scatterer is determined by it reflection coefficient σ and the material frequency response $H_{refl}(\omega)$. $H_{refl}(\omega)$ is mainly dependent on the attenuation during propagation for different frequencies. Assuming a material has a constant attenuation coefficient α [134],

$$H_{refl}(\omega) = e^{-\alpha\omega^4 x} \tag{3.18}$$

where x is the propagation distance.

In the Rayleigh region, the frequency response of an echo reflected back from a distant scatterer can be expressed as [134]

$$\sigma(\omega) = \gamma \frac{V\omega^2}{xv^2} \tag{3.19}$$

where γ is a constant coefficient and V is the volume of the scatterer.

The phase shifting factor τ in $e^{-i\omega\tau}$ in Eq.(3.3) which models the delay caused by the propagation is usually assumed to be linear with no frequency dependency. However, for highly attenuated material with large α, the phase dispersion is not negligible, and hence the phase velocity v in $\tau = (2x/v)$ should also be a function of ω, noted as $v(\omega)$. Here a model, Nearly Local model, that calculates the dispersion based on the local attenuation is applied [136],

$$\frac{1}{v(\omega)} = \frac{1}{v(\omega_0)} - \frac{2\alpha \cdot (\omega^3 - \omega_0{}^3)}{3\pi} \tag{3.20}$$

where ω_0 is a reference angular frequency, $v(\omega)$ is the calculated phase velocity at an arbitrary frequency ω.

Let $\beta = \gamma V/v^2$, then Eq. (3.8) can be rewritten as,

$$R_{Noi}(\omega) = H_{tran}(\omega) \sum_{k=1}^{K} \beta \frac{\omega^2}{x_k} e^{-\alpha\omega^4 x_k} e^{-2i\omega x_k [\frac{1}{v(\omega_0)} - \frac{2\alpha \cdot (\omega^3 - \omega_0{}^3)}{3\pi}]} \tag{3.21}$$

Under general conditions, β is assumed to follow a normal distribution when there is large amounts of scatterers [134]. Similarly, the spectrum of the echo from a legitimate reflector is,

$$R_{Sig}(\omega) = s \cdot H_{tran}(\omega) e^{-\alpha\omega^4 x} e^{-2i\omega x [\frac{1}{v(\omega_0)} - \frac{2\alpha \cdot (\omega^3 - \omega_0{}^3)}{3\pi}]} \tag{3.22}$$

where s is the defect amplitude factor which indicates the ratio between the legitimate reflector echo amplitude and the noise level. The reflection coefficient σ in Eq. (3.7) is removed, since it is a constant number for a legitimate reflector signal.

Since this model assumes that scattering and attenuation are frequency dependent, hence the transmitted signal suffers a significant distortion after it propagates for a distance. Accordingly, this non-linear model is referred to as a high dispersion model (HDM) in this Thesis.

As a comparison, a low dispersion model (LDM) is also used, which assumed that the ultrasonic pulse remains essentially the same after propagates an equivalent distance,

$$r_{Noi}(t) = \sum_{k=1}^{K} \rho \cdot \delta(t - \tau_k) \qquad (3.23)$$

$$r_{Sig}(t) = s \cdot \delta(t - \tau) \qquad (3.24)$$

where ρ is the reflection coefficient of LDM.

3.2.2 Definition of Signal to Noise Ratio, Probability of Detection and Probability of False Alarm

Signal to Noise Ratio (SNR), Probability of Detection (PoD) and Probability of False Alarm (PFA) is used for quantifying analysis of the performance of the algorithm.

SNR is one of the most general methods used to quantify the quality of signals and images. Since the signal and noise are measured across the same impedance (they are acquired by the same device from the same material), amplitude is used in this work rather than power. Maximum amplitude of the signal is used in this work and many previous works [101, 108] to analyse grain noise reduction techniques since these techniques are usually processed non-linearly and they represent indicators of the defect locations, rather than defect characterisation.

In this work, the signal to noise ratio is defined as,

$$SNR = \frac{peak\ of\ the\ signal}{average\ of\ the\ noise} \qquad (3.25)$$

All SNR in this work will be shown in decibel units computed by $20log_{10}(SNR)$.

PoD and PFA, along with receiver operating characteristic (ROC) curve, are successfully been used for statistic reliability measurement in a variety of areas related to detection problems.

PoD calculates the probability of when a target is detected at the location where it should present. It indicates the ability that an algorithm can successfully find the desired targets. The higher the PoD value, the greater chance that the desired targets can be detected.

False alarm rate is also an important indicator since it shows the accuracy of an algorithm when detecting targets. PFA is the probability of when a target is detected at the location where no target should present. Higher PFA means more noise signals have been misclassified as legitimate reflector signals. Generally, output signals with higher PoD and lower PFA indicates a more appropriate parameters setting.

PoD and PFA can also be plotted against each other as a ROC curve that illustrates the performance of an algorithm at various settings of a certain parameter. ROC is a useful tool to optimize the setting of a parameter by finding the compromise point, if the parameter causes trade-off between PoD and PFA.

3.2.3   Simulated results

This Section shows the simulated MB-SSP results of modelled signals, as well as some SSP results for the purpose of comparison and analysis. Note that only PT has been applied to generate SSP results, since MB-SSP also uses polarity information to process data.

i.   *Influence of frequency dependent attenuation*

Figure 3.10 and Figure 3.12 present the modelled signals using LDM and HDM respectively, along with their SSP results in Figure 3.11 and Figure 3.13. Four example signals are given in each case. Both models use simulated signals with 5MHz centre frequency, 50% transducer bandwidth at -6dB and 100MHz sampling frequency. The attenuation factor α for the HDM is 10^{-31}, based on empirical findings from [134]. Generally, for typical alloys used in NDE, the attenuation factor

should be in the range from 10^{-31} to 10^{-28}. The legitimate reflector was placed at 45 mm, with detection amplitude factor $s = 1.5$. For the purpose of comparison, the SNR of the two models has been set at same level, though in practice the SNR level of high dispersive materials is usually much lower than low dispersive materials. The parameters of SSP in both cases are exactly same, with a processing bandwidth equal to 50% of the transducer bandwidth at -6dB and a filter number of 9. As can be seen in Figure 3.11 and Figure 3.13, where legitimate reflector echoes are successfully been detected in both cases and grain noise has been significantly been reduced, illustrating that SSP works well in both cases.

Note that the peaks appeared at locations other than 45mm in the SSP processed A-scans shown in Figure 3.11 is the noise signals that fail to be eliminated. This is referred to as artefact noise signal in this Thesis. Same issues also appeared in other processed A-scan signals which shown are Figure 3.13 and Figure 3.23.

However, for materials that have higher attenuation factor, SSP results become unstable. Figure 3.14 shows the HDM results with same parameters as Figure 3.12, except for attenuation factor α which is increased to $5 * 10^{-29}$. As can be seen in Figure 3.15, all four peaks of legitimate reflectors in the SSP results are missing, while the parameters setting of SSP is exactly the same as Figure 3.13. This is caused by the significant frequency dependent attenuation which distorted the spectrum of the legitimate reflector and hence, the legitimate reflector spectrum can no longer dominate the entire processing bandwidth. However, if the processing bandwidth of SSP is slightly adjusted, e.g. move the centre frequency of processing bandwidth from 5MHz to 4MHz in this case to ensure the predomination of legitimate reflector spectrum, then all the missing legitimate reflector echoes will be detected, as shown in Figure 3.16.
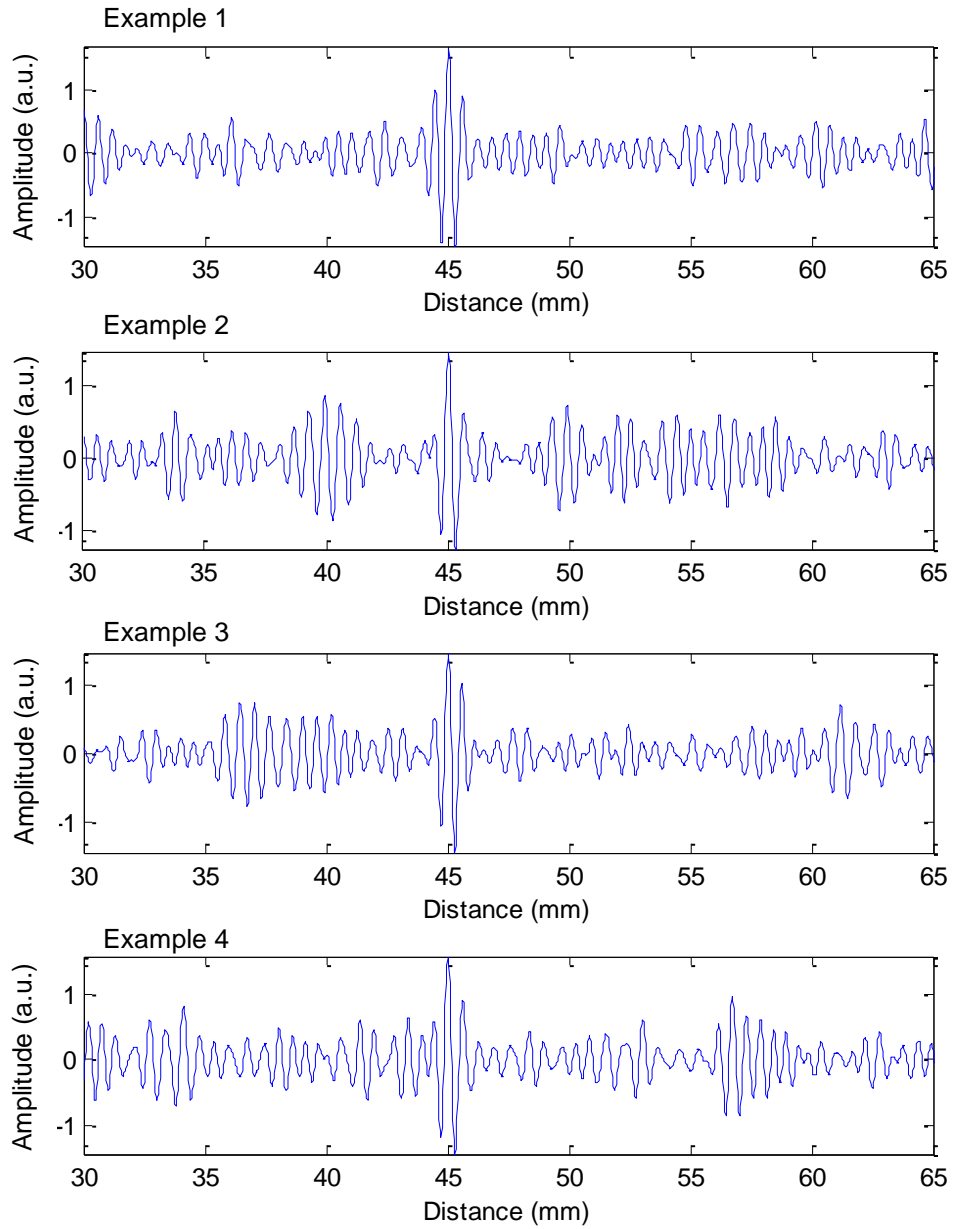
Figure 3.10. Four A-scan examples which simulated by LDM, with detection amplitude factor $s = 1.5$. The legitimate reflector echo in each A-scan is set at 45mm.
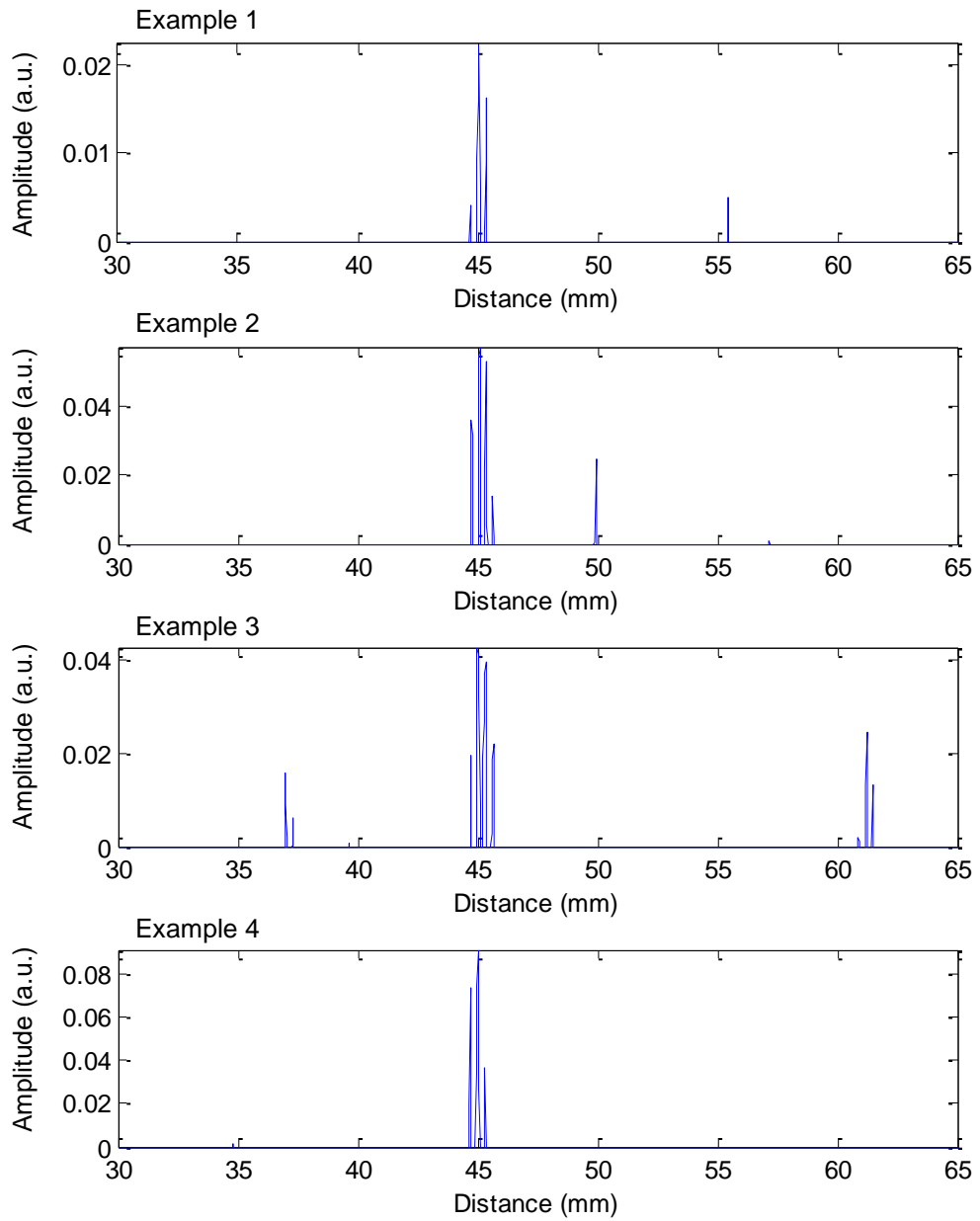
Figure 3.11. SSP results of the four A-scan signals which shown in Figure 3.10.

Figure 3.12. Four A-scan examples which simulated by HDM, with $s = 1.5, a = 10^{-31}$. The legitimate reflector echo in each A-scan is set at 45mm.
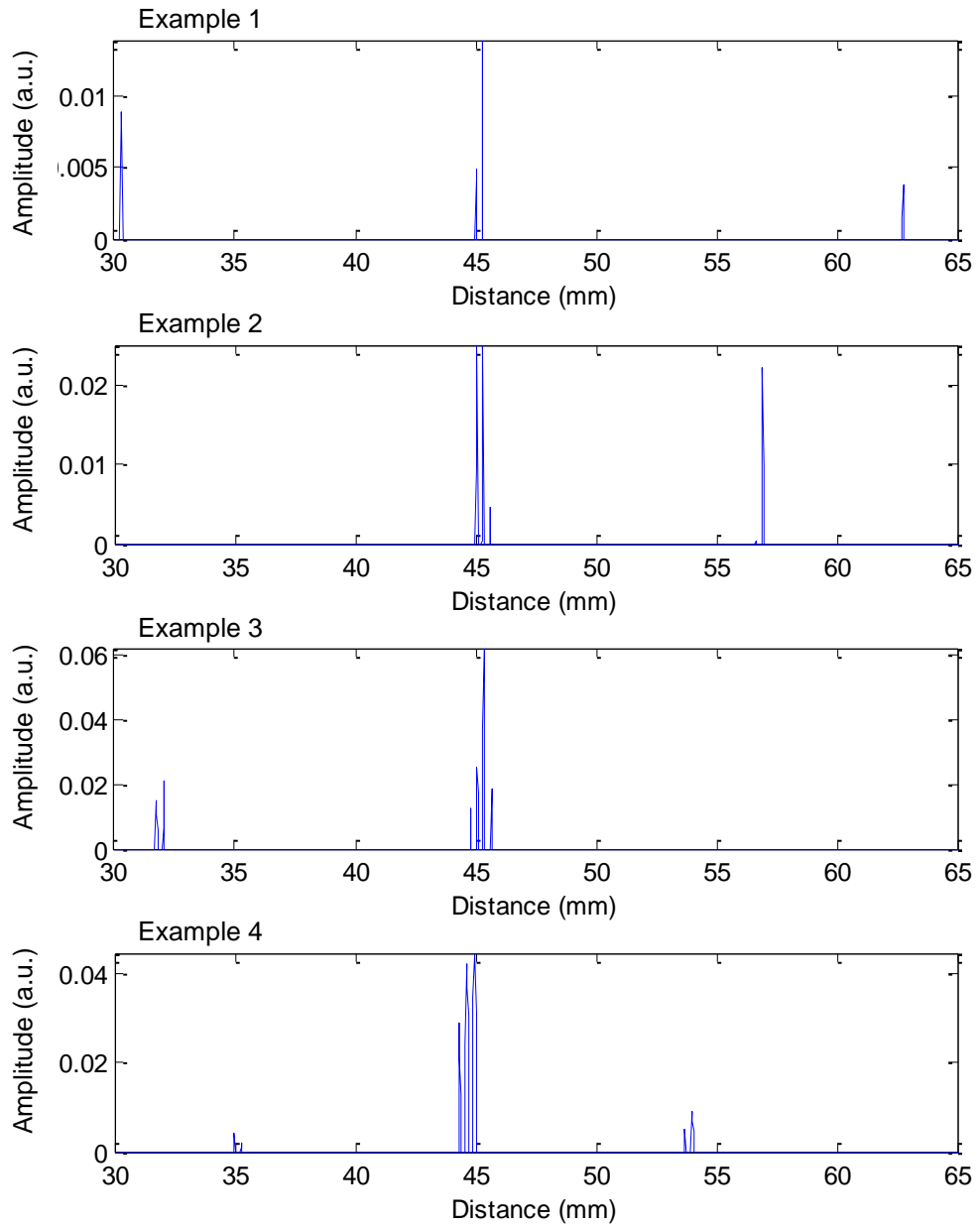
Figure 3.13. SSP results of the four A-scan signals which shown in Figure 1.10
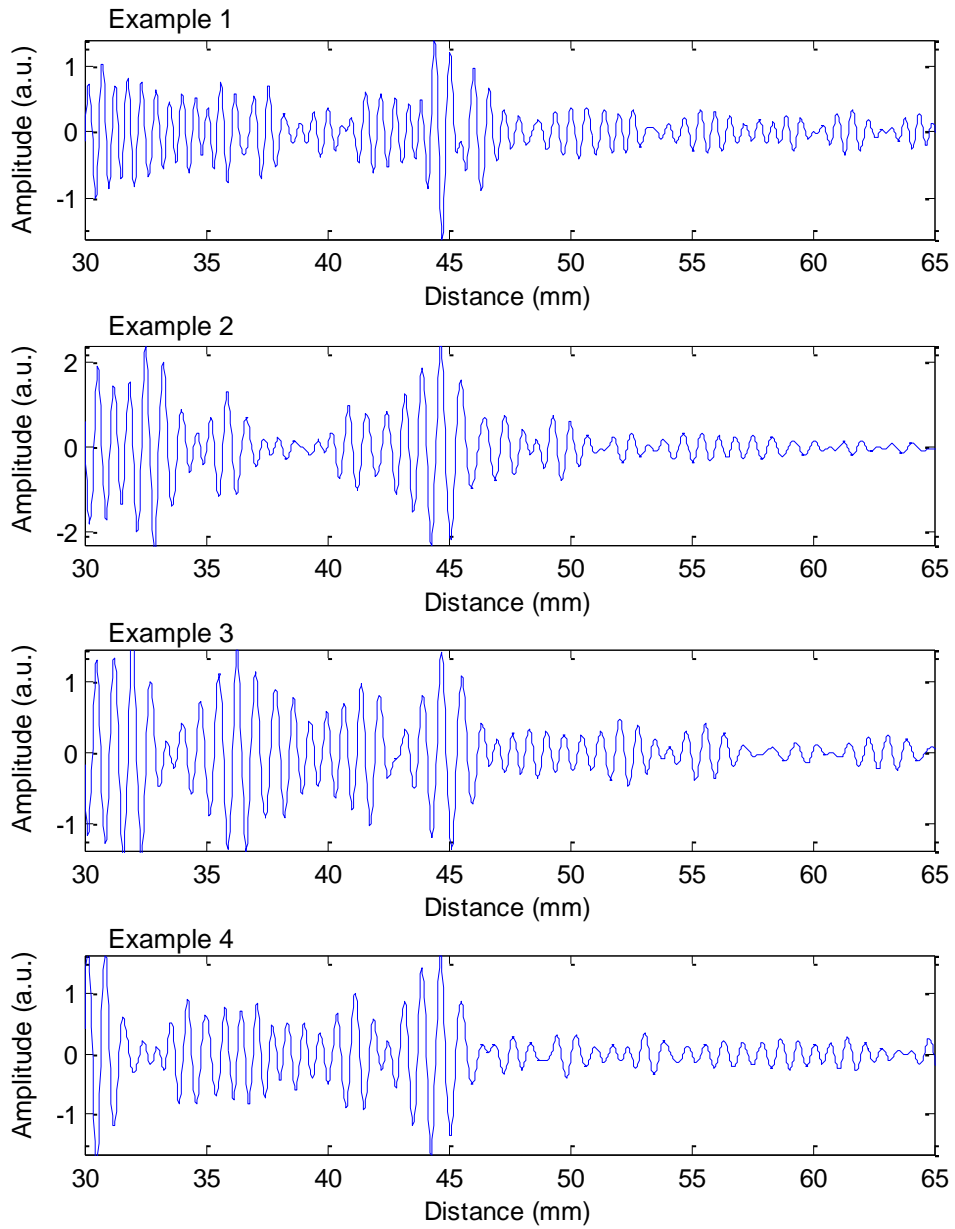
Figure 3.14. Four A-scan examples which simulated by HDM, with $s = 1.5, a = 5 * 10^{-29}$. The legitimate reflector echo in each A-scan is set at 45mm.
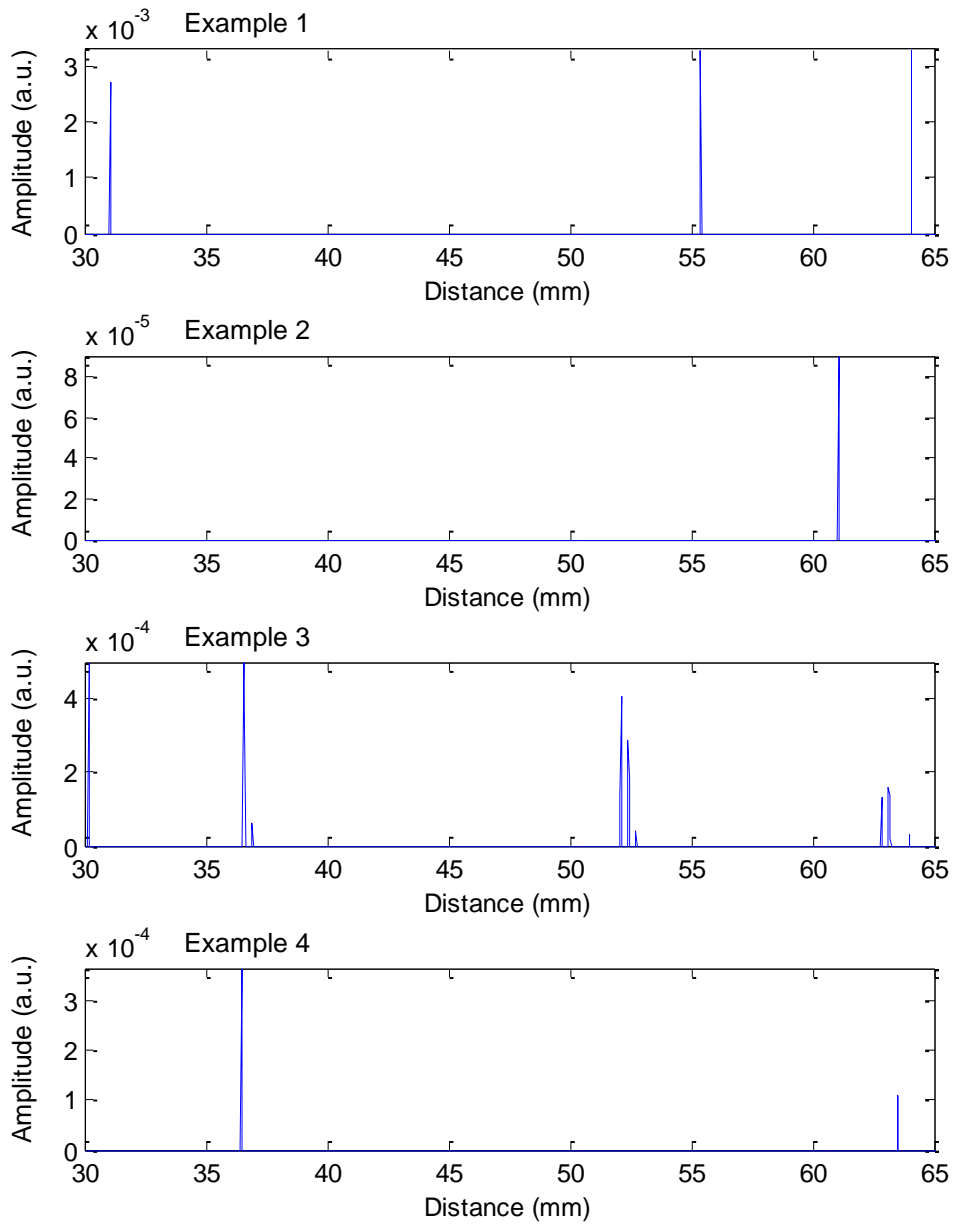
Figure 3.15. SSP results of the four A-scan signals which shown in Figure 3.14.
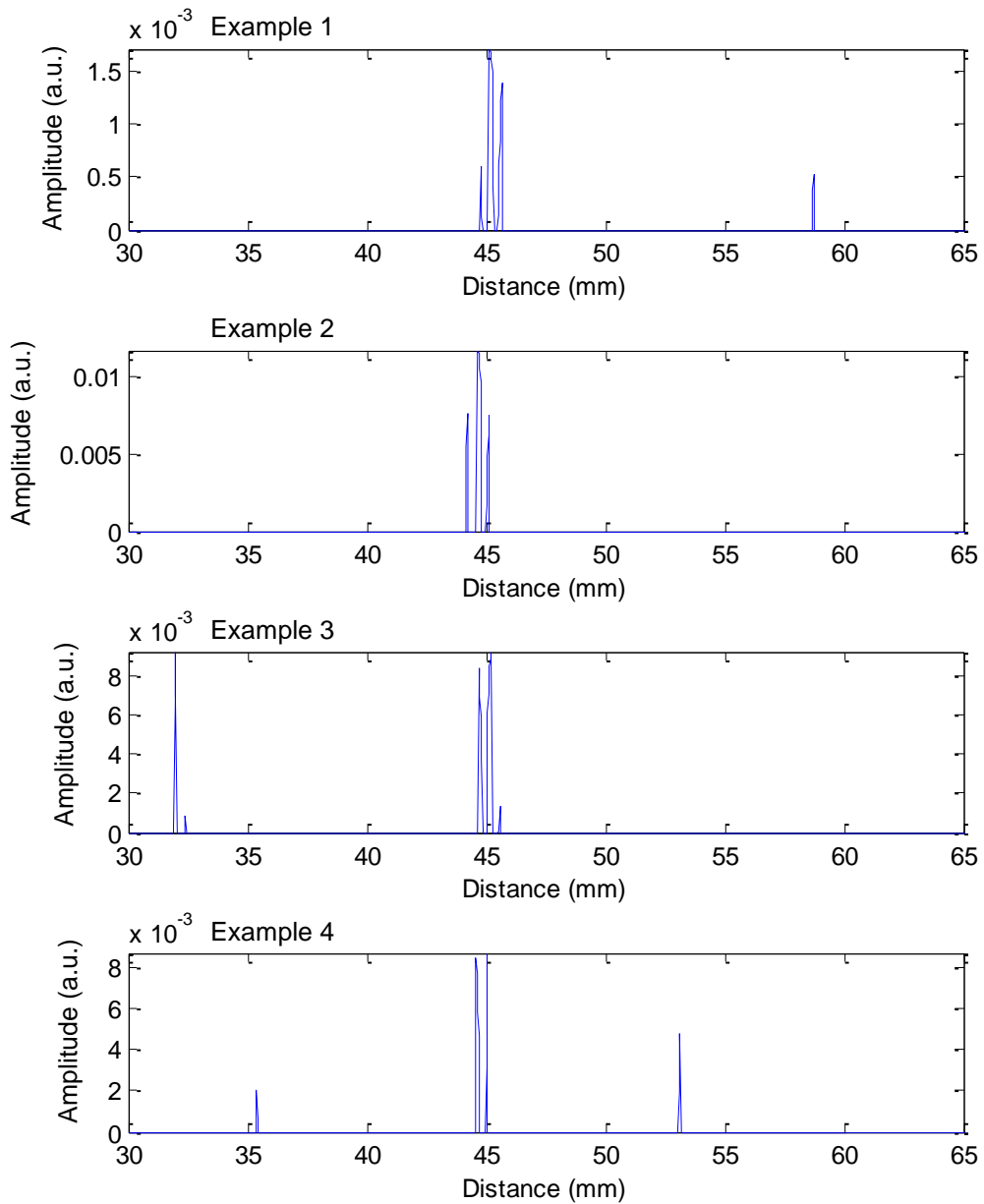
Figure 3.16. Alternative SSP results of Figure 3.14, in which a lower processing bandwidth was selected.

Figure 3.17 and Figure 3.18 are the HDM simulated results and its SSP results with $\alpha = 10^{-31}$ and $s = 1$, which shows that the strong noise can also limit the detectability of traditional SSP, since the energy of the noise may be stronger than

the legitimate reflector for some frequency channels. As can be seen in Figure 3.18, only two signals show the correct legitimate reflector location (45mm). The parameters setting of SSP is consistent with those used in Figure 3.13.
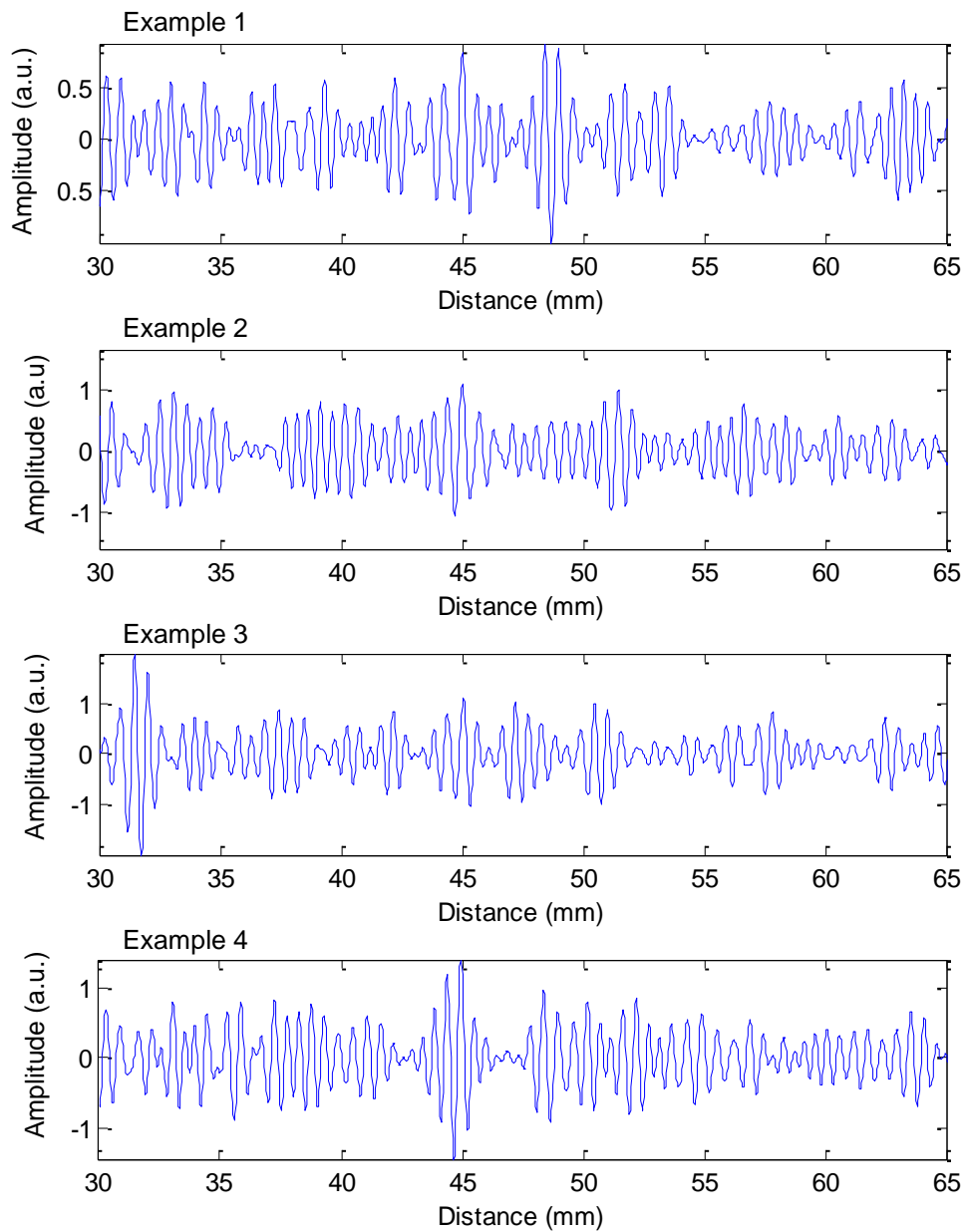
Figure 3.17. Four A-scan examples which simulated by HDM, with $s = 1, a = 10^{-31}$. The legitimate reflector echo in each A-scan is set at 45mm.

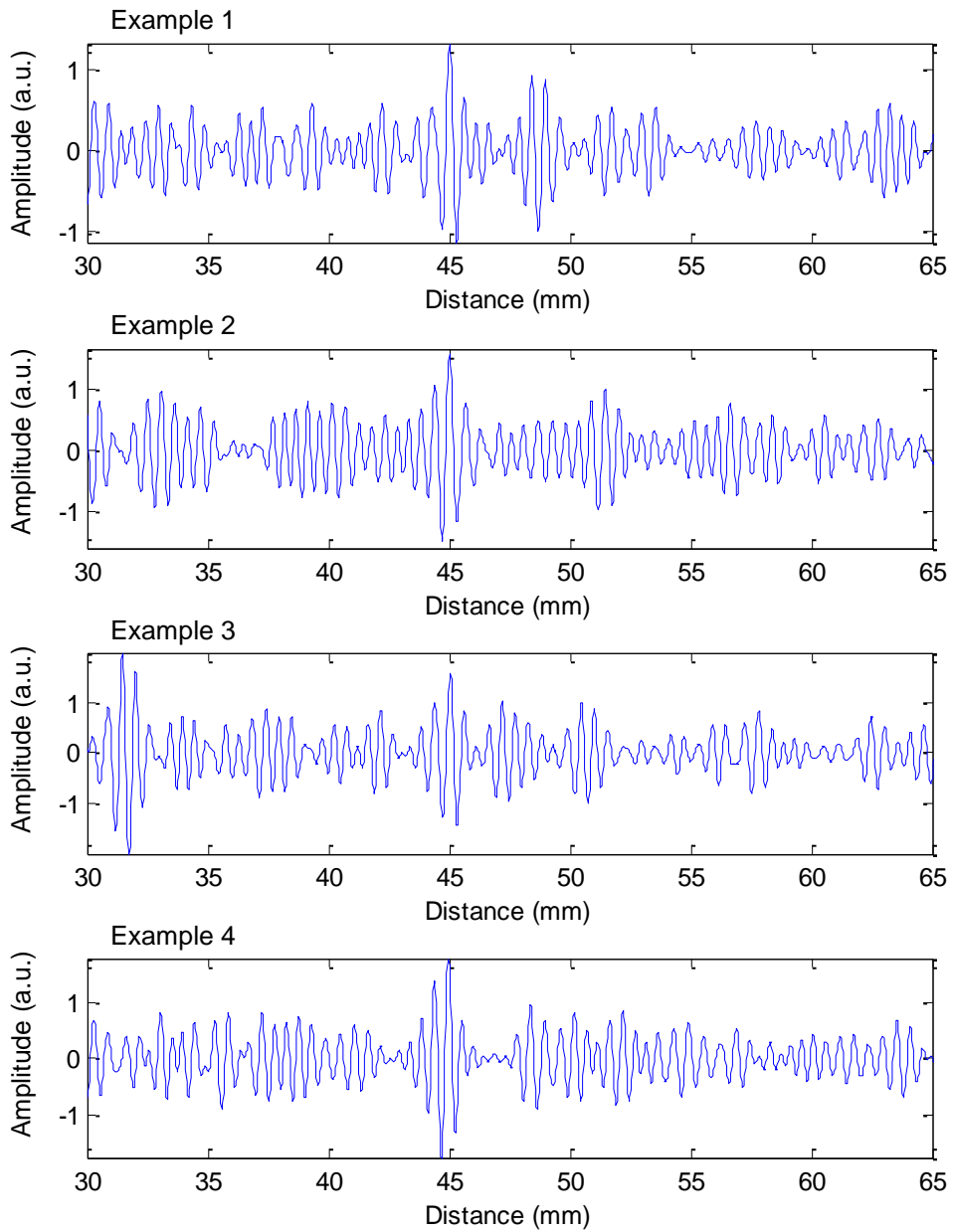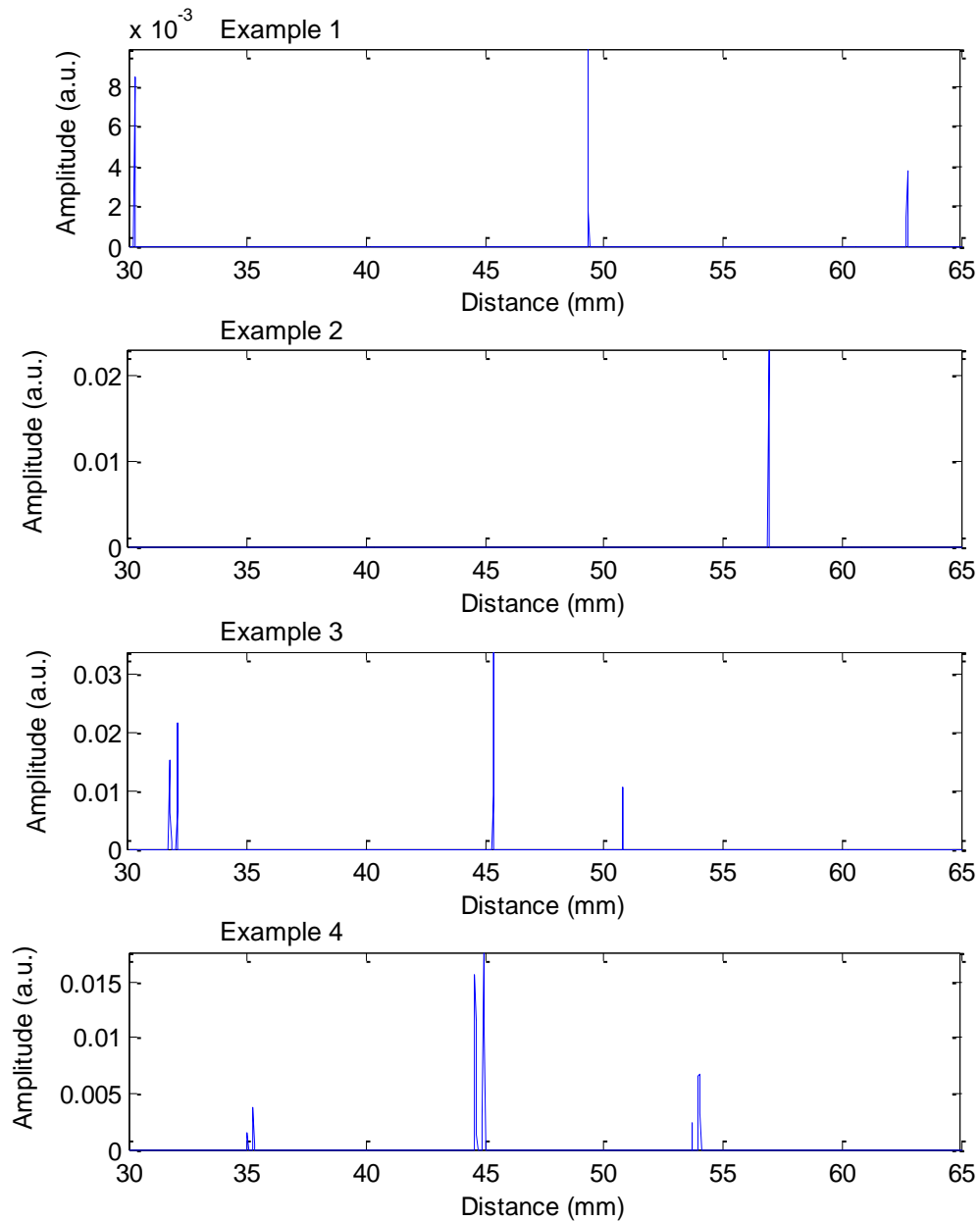Figure 3.18. SSP results of the four A-scan signals which shown in Figure 3.17.

ii. *Influence of phase dispersion*

Figure 3.19 presents the SSP results which show the influence of phase dispersion as discussed in Section 3.1.3. As can be seen in the Figure, if one tries to increase the detectability of SSP results compared with Figure 3.14, by extending the width of processing bandwidth while maintaining the bandwidth of each filter (hence

increasing the number of filters), basically nothing will be detected since the phase is slightly shifted in different frequency channels, plus the increasing number of filters make the polarity coincidence less possible. However, the results are also not acceptable if the number of the filters are maintained the same and have a wider bandwidth for each filter, as shown in Figure 3.20. Although three of the legitimate reflector has been barely detected (the narrow, pulse-like legitimate reflector echo also indicates that the phases of each frequency channel are not identical), the noise reduction ability of the algorithm is significantly reduced. As can be seen in Figure 3.20, many artefact echo peaks have been introduced.
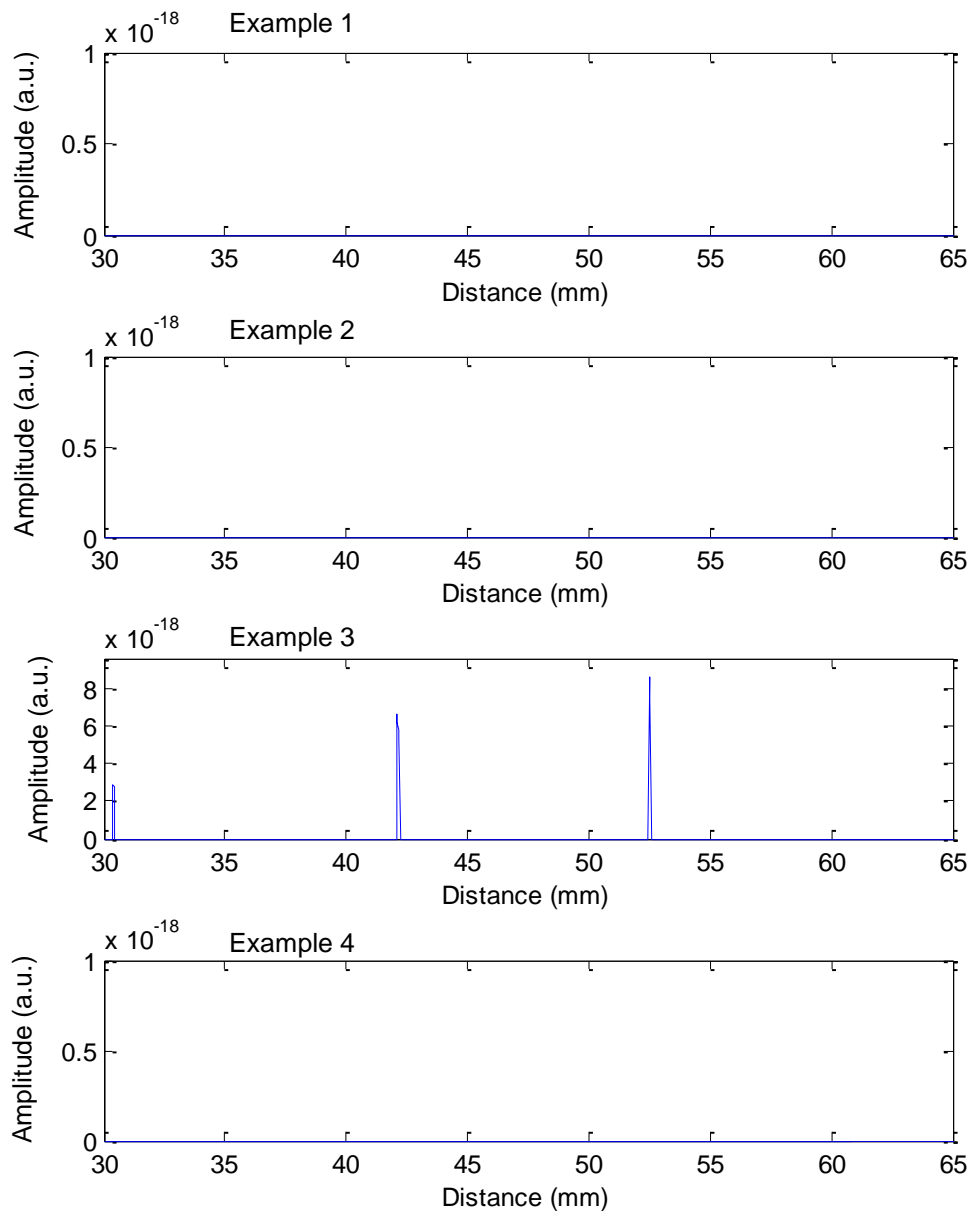
Figure 3.19. Alternative SSP results of Figure 3.14: with wider bandwidth & increased filter number.
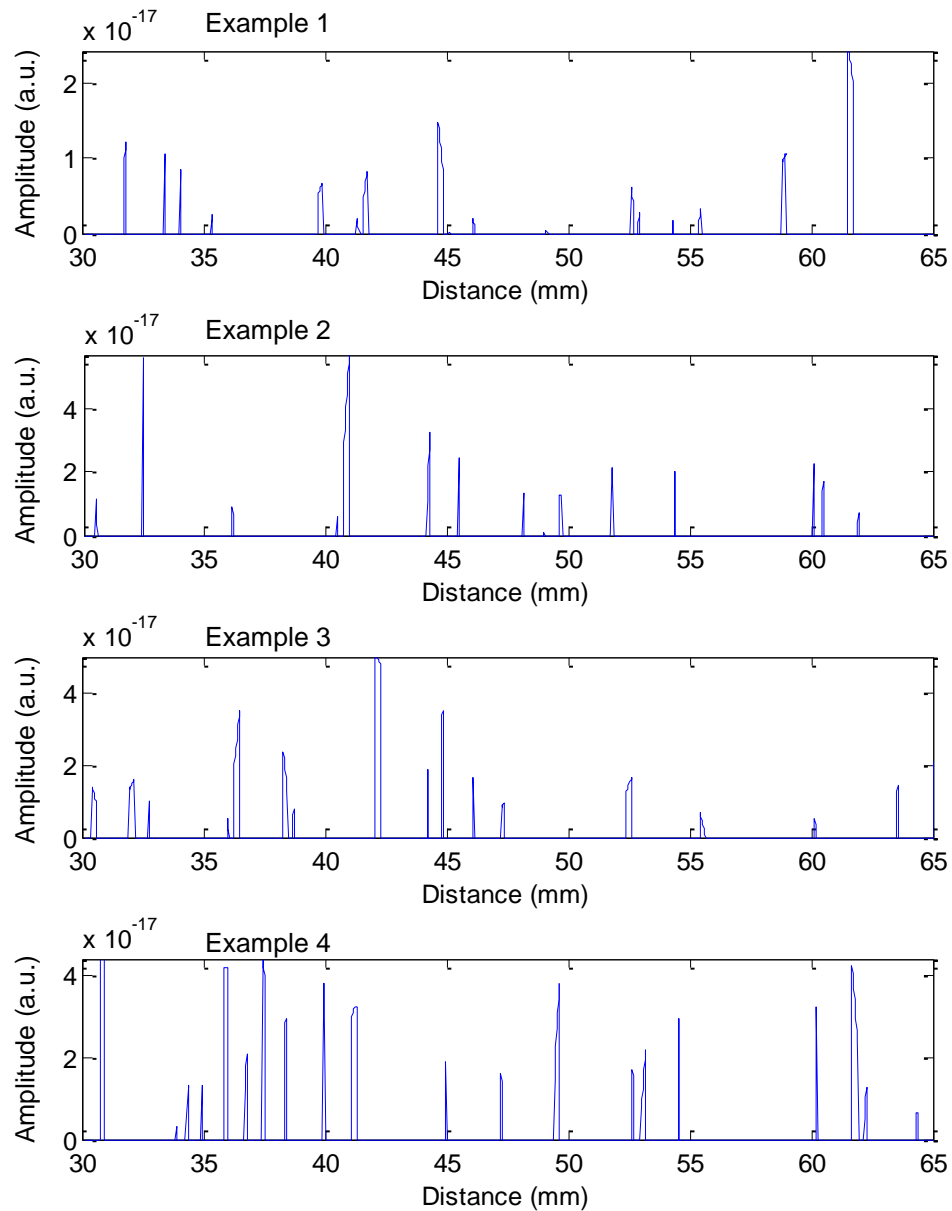
Figure 3.20. Alternated SSP results of Figure 3.14, with a wider bandwidth and wider filters.

iii.   A-scan results using MB-SSP

Figure 3.21, Figure 3.22 and Figure 3.23 are the MB-SSP results corresponding to the SSP results presented in Figure 3.12, Figure 3.14 and Figure 3.17, respectively. It can be easily observed that MB-SSP has successfully detected all legitimate

reflectors in each case while significantly reducing noise. Compared with SSP results, MB-SSP demonstrates a more stable detect capability.
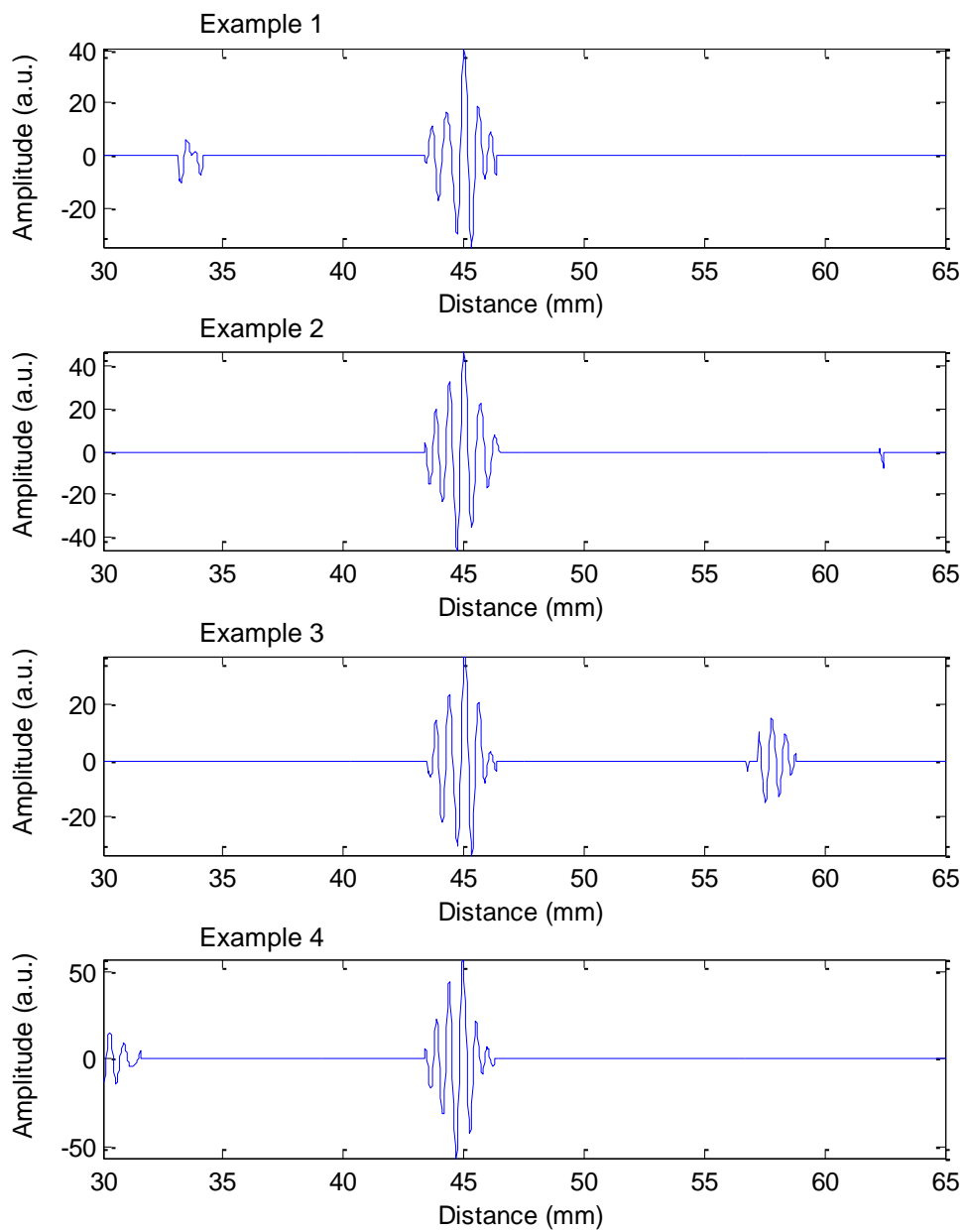
Figure 3.21. MB-SSP results of the four A-scan signals which shown in Figure 3.12.
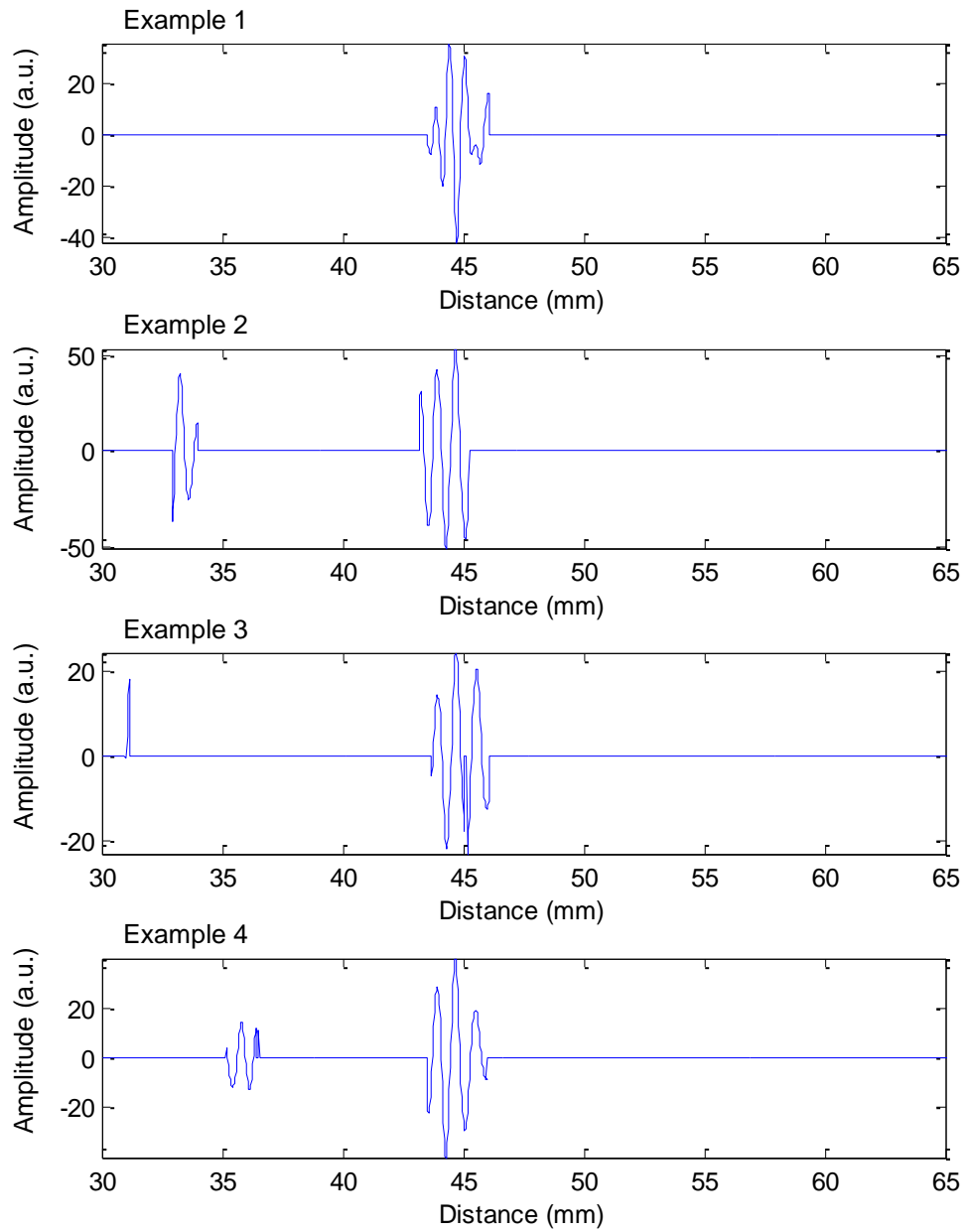
Figure 3.22. MB-SSP results of the four A-scan signals which shown in Figure 3.14.
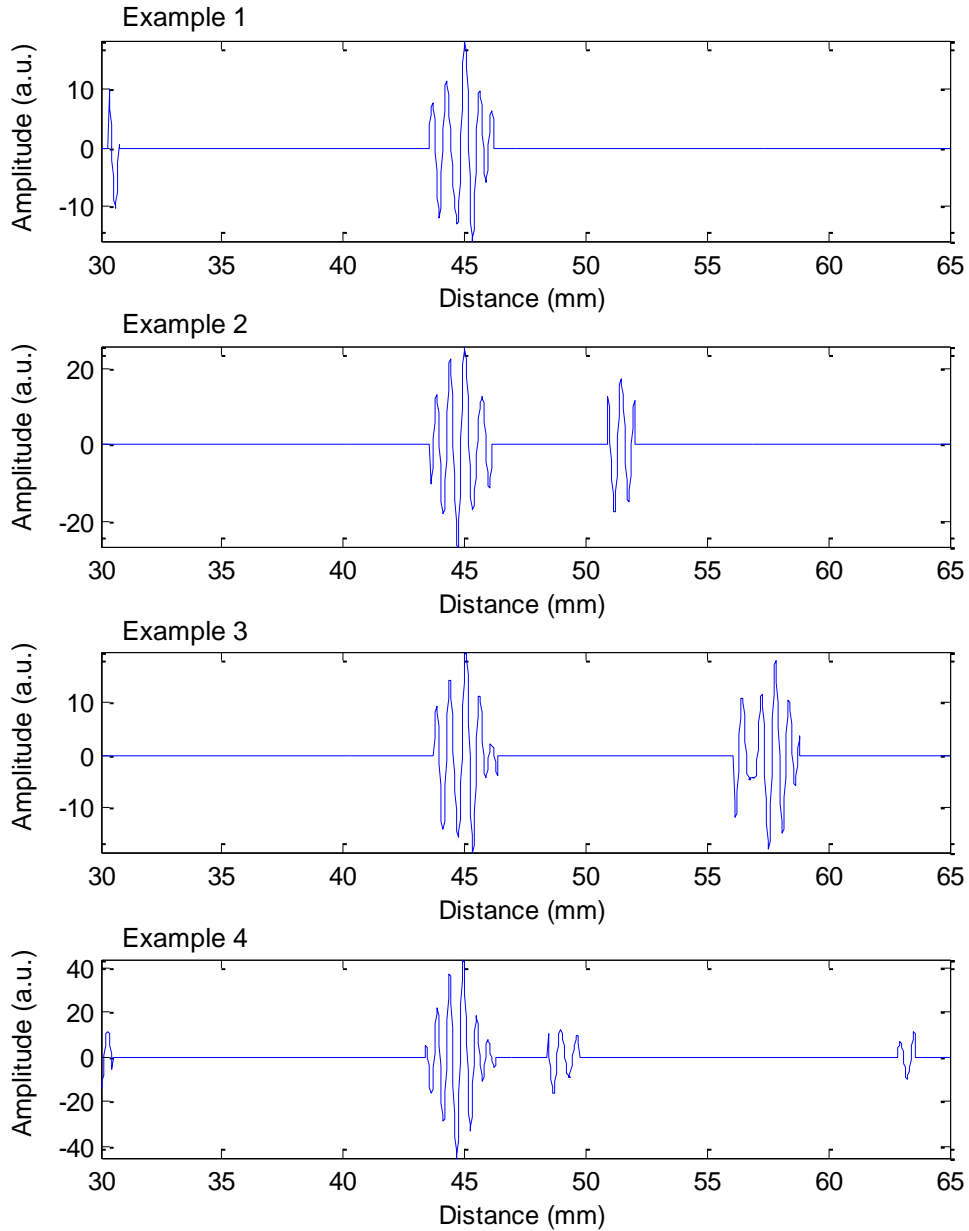
Figure 3.23. MB-SSP results of the four A-scan signals which shown in Figure 3.17.

3.2.4 Parameter analysis of MB-SSP

In this Section the PoD and PFA will be used to make the comparison and analysis of different selected parameter settings. Two groups of modelled signals are simulated using HDM for this parameters analysis, with $\alpha = 10^{-29}$ and $\alpha = 10^{-28}$

respectively. s in each group was chosen at 1, 1.5 and 2 to simulate different noise levels. For each α and s combination 1000 signals were simulated to calculate PoD and PFA. Each A-scan contains a legitimate reflector echo at ~45mm. The bandwidth at -6dB, the centre frequency and the sampling frequency of both groups are 50%, 5MHz and 100MHz, respectively.

If not specified, the parameters of MB-SSP are chosen as: 80% of the transducer's bandwidth at -6dB for B_S, up to 10 filters inside each B_S, 75% overlap between adjacent B_S, 80 sample points length for detecting window, and 0.5 for threshold Th.

The following parameters of MB-SSP will be compared and analysed:

- Overlap
- Number of filters
- Bandwidth of B_S
- Length of detecting window
- Threshold level

i. Overlap

Figure 3.24 and Figure 3.25 show the PoD and the PFA for different percentage overlap of Bs. Both figures indicate that PoD has a higher value at higher overlap, while PFA remain the same. PoD reaches a relatively stable and acceptable value at around 30% for Figure 3.24 and 50% for Figure 3.25. However, a larger overlap means more Bs partitions required, hence it will need more computation power. For this reason, the overlap should be generally chosen between 50% to 75%.
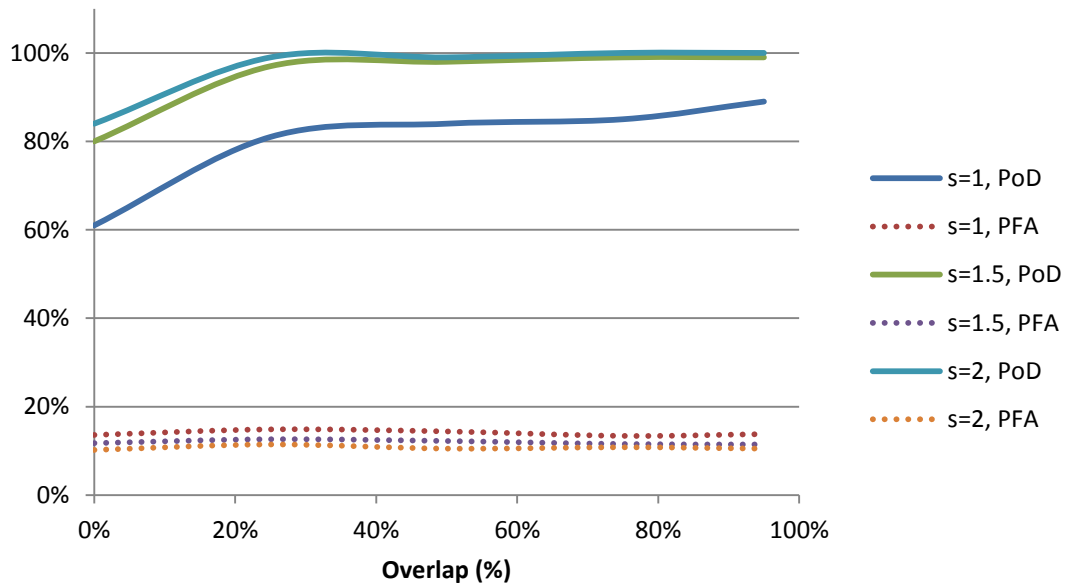
Figure 3.24. PoD and PFA for different percentage overlap of *Bs*, $\alpha=10^{-29}$.
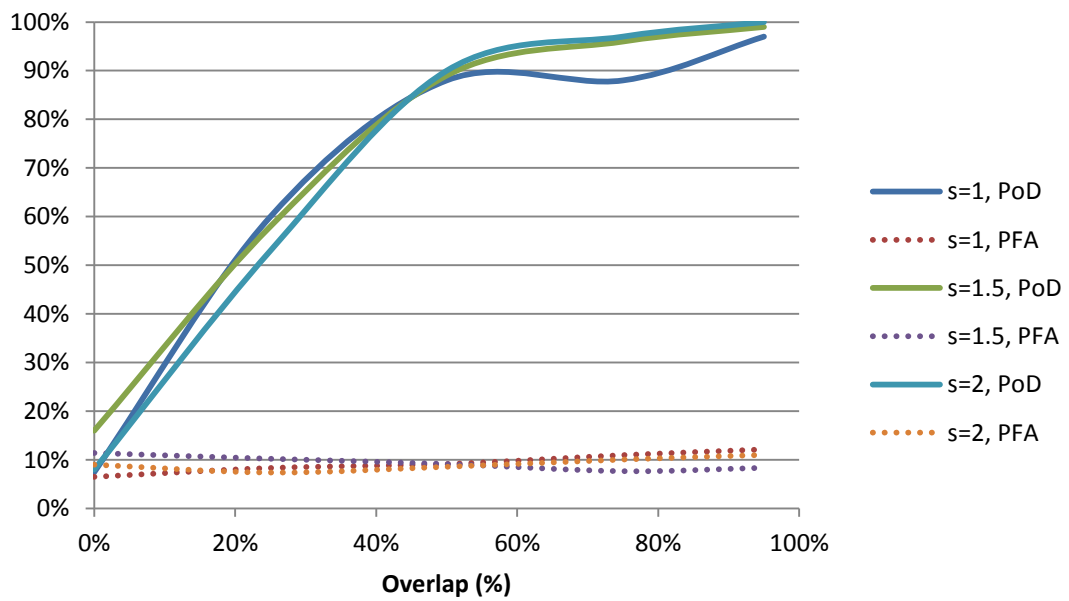
Figure 3.25. PoD and PFA for different percentage overlap of *Bs*, $\alpha=10^{-28}$.

ii. *Number of filters*

As can be seen in Figure 3.26 and Figure 3.27, the PFA has a high value when the maximum filter number inside each B_S is low, since the polarity is easier to be coincident when using small number of frequency channels. The PFA is decreasing

86

as the maximum filter number is increasing, but an increased filter number will lead to a lower PoD, especially when the noise level is high. This is because although the increased number of frequency channels enhances the noise removal capability, it is also lower than the detection capability. As a compromise, the maximum filter number inside a B_S should be chosen at a balance point around 10.
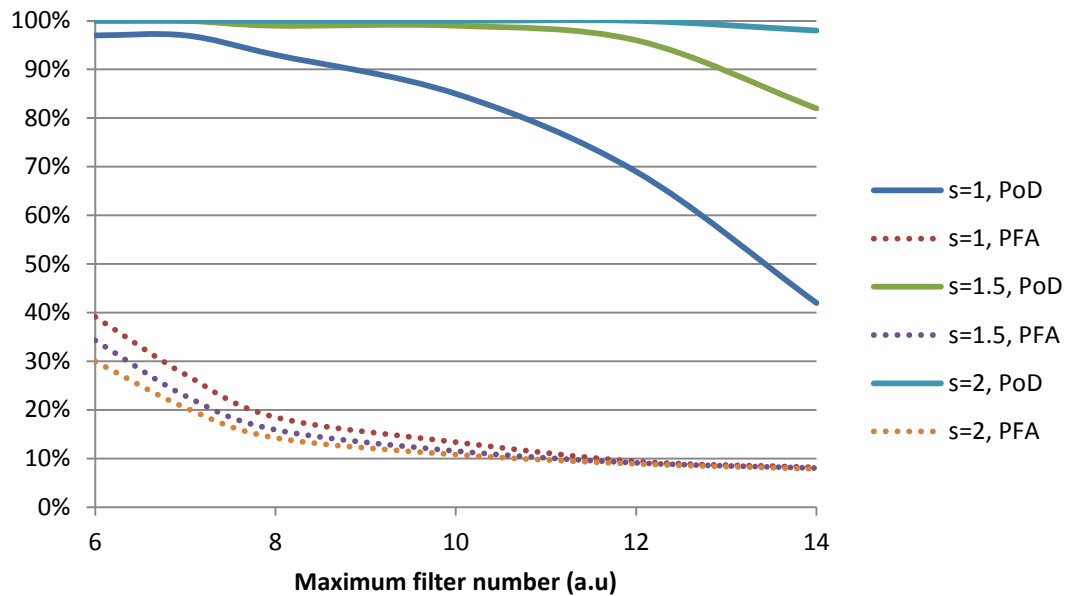
Figure 3.26. PoD and PFA for different number of filters used, $\alpha=10^{-29}$.
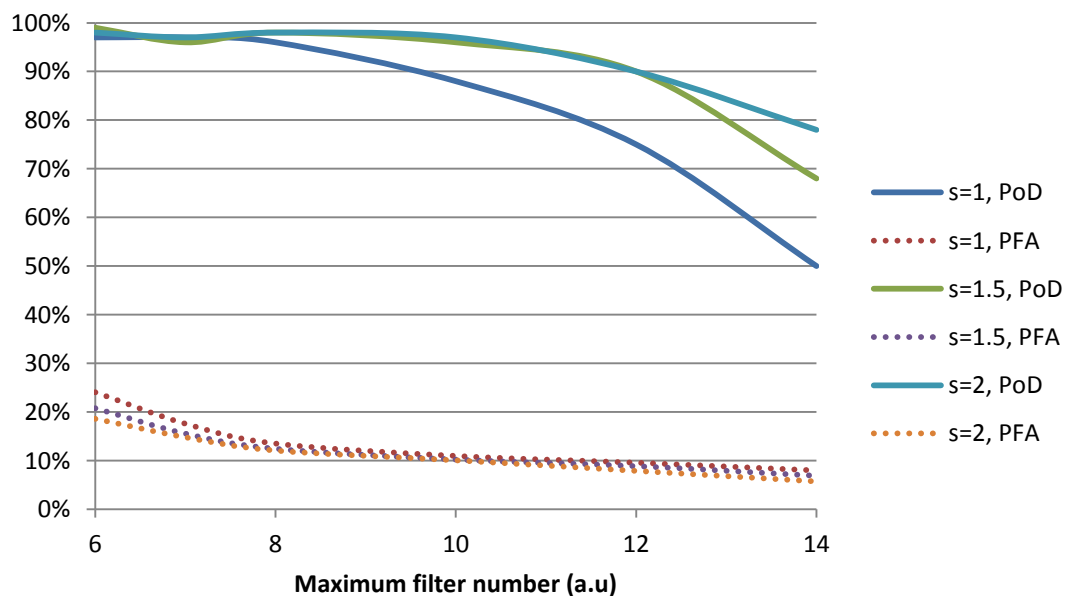
Figure 3.27. PoD and PFA for different number of filters used, $\alpha=10^{-28}$.

iii.   Bandwidth of Bs

As discussed in Section 3.1.1, the bandwidth of B_S should be chosen at around 80% of the -6dB bandwidth of transducer. This is clearly reflected from the PoD and the PFA results shown in Figure 3.28 and Figure 3.29. All PoD curve reach their peak at around 80%, with low PFA values. The performance of the algorithm is poor when the bandwidth of B_S is narrow, since the benefit of frequency diversity is not included. While it is also not acceptable if the bandwidth is too wide, since the influence of phase dispersion is increased, especially for a higher attenuation factor α.
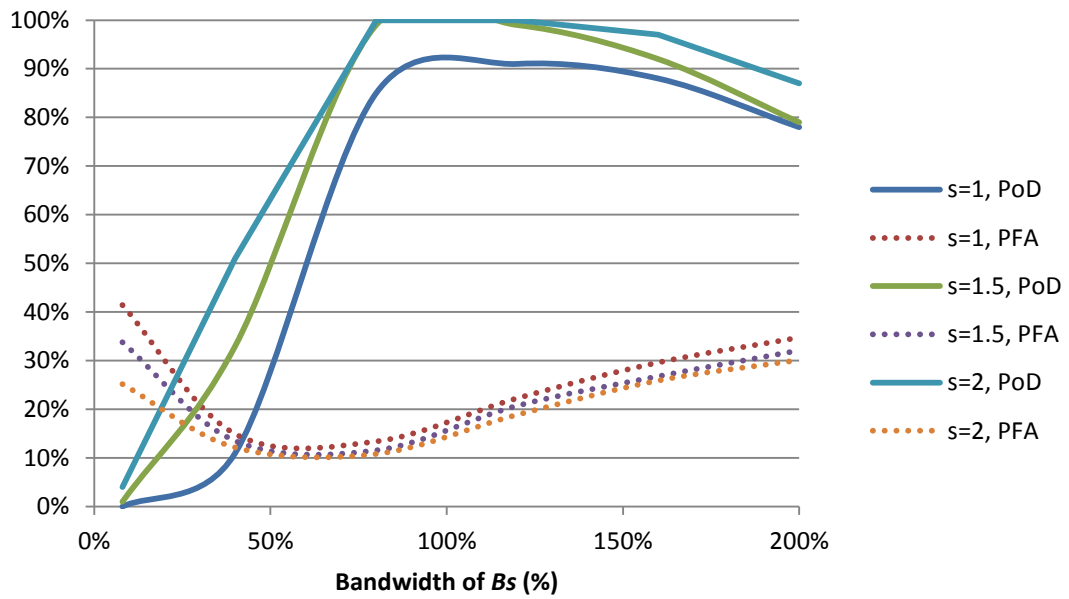
Figure 3.28. PoD and PFA for different *Bandwidth of Bs*, $\boldsymbol{\alpha}=10^{-29}$.
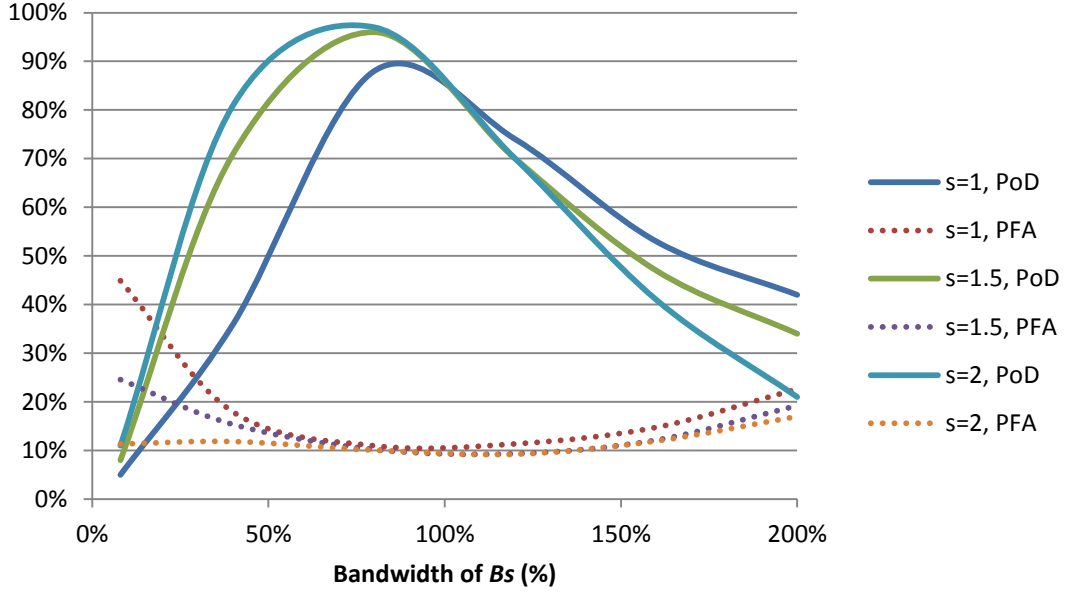
Figure 3.29. PoD and PFA for different *Bandwidth of Bs*, $\alpha=10^{-28}$.

iv.   *Length of detection window*

In this Section, the effect of the detection window length will be discussed. The detection window is a time domain window that travels along the time axis to generate the probability profile, as described in Eq. (3.2).

Figure 3.30 and Figure 3.31 show the ROC of different detecting window lengths for different α and s. It can be seen in the two figures that the optimum operating points between PoD and PFA corresponds to when window length equals to $2L$. This is coincident with the theoretical suggestion that the window length should be twice of the range cell.

Since the attenuation property of the modelled signals was known *a priori*, we can also compare the benefit of using a frequency dependent threshold. Let

$$Ad_j(n) = e^{\alpha \frac{(\omega_1{}^4 - \omega_j{}^4) \cdot v(\omega_c) \cdot n}{f_s}} \tag{3.26}$$

where f_s is the sampling frequency, ω_c is the centre angular frequency of the transducer, ω_1 and ω_j are the centre angular frequency of $Y_1(n)$ and $Y_j(n)$.
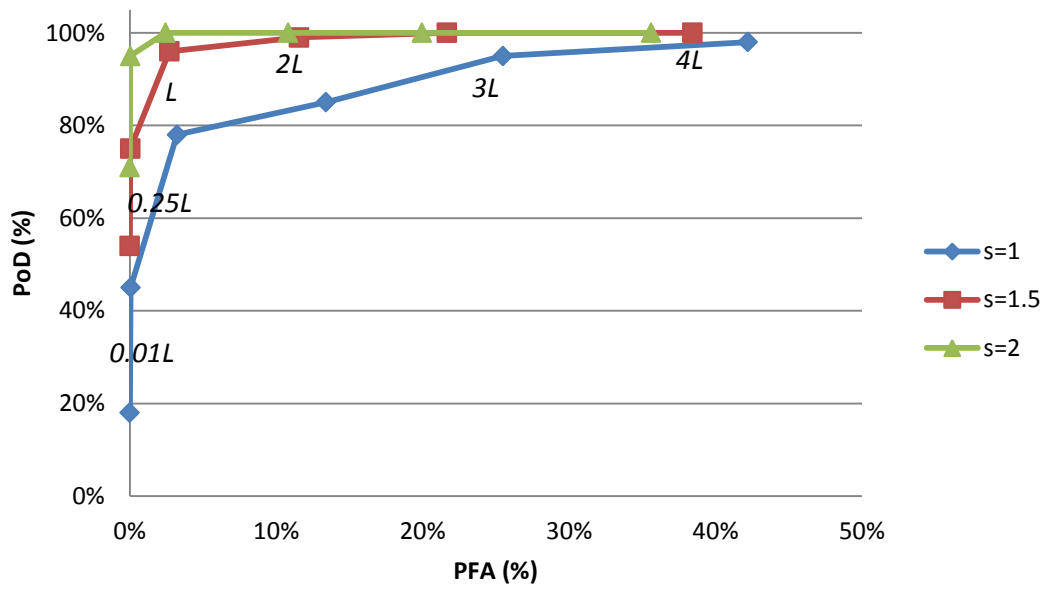
Figure 3.30. ROC for different lengths of detecting window, $\alpha=10^{-29}$.
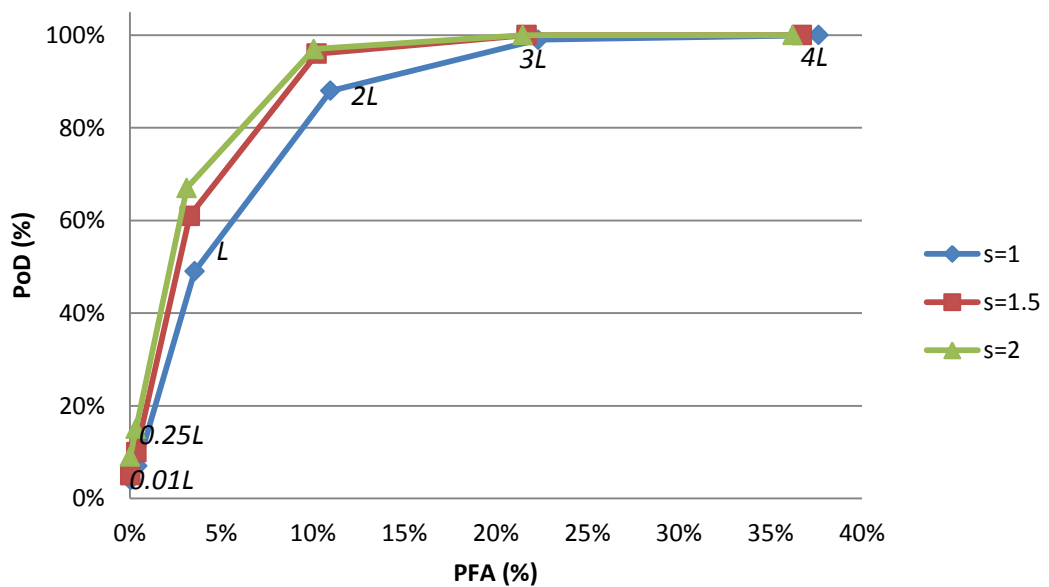
Figure 3.31. ROC for different lengths of detecting window, $\alpha=10^{-28}$.

v. Threshold level

As can be easily seen from the ROC in Figure 3.32 and Figure 3.33, PoD and PFA reach the compromise point when the threshold level *Th* is ~0.5. In both Figures, the PoD at $Th = 0.5$ is near 100% and PFA is less than 10%.
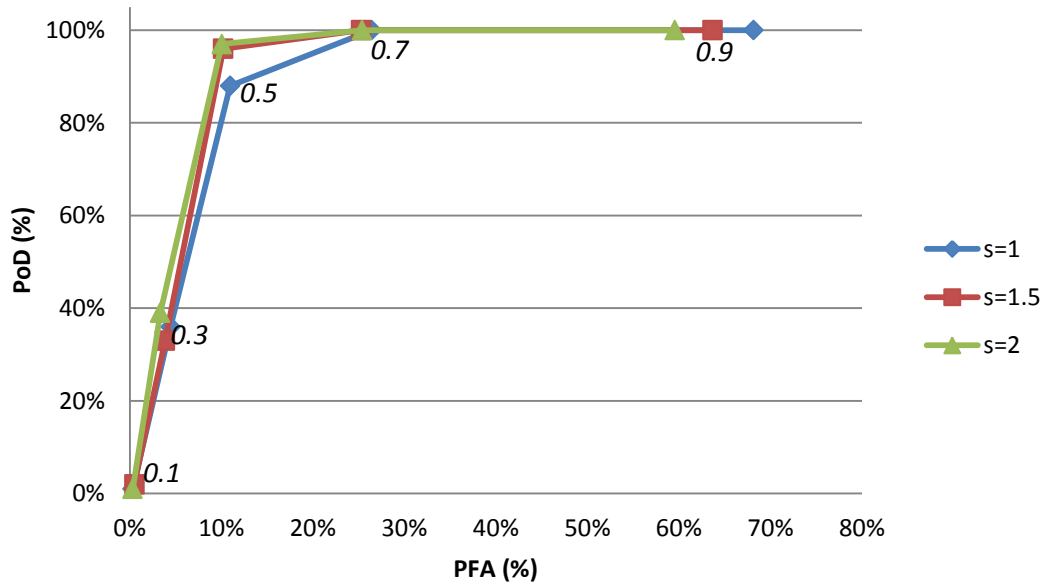
Figure 3.32. ROC for different threshold level, $\alpha=10^{-29}$.
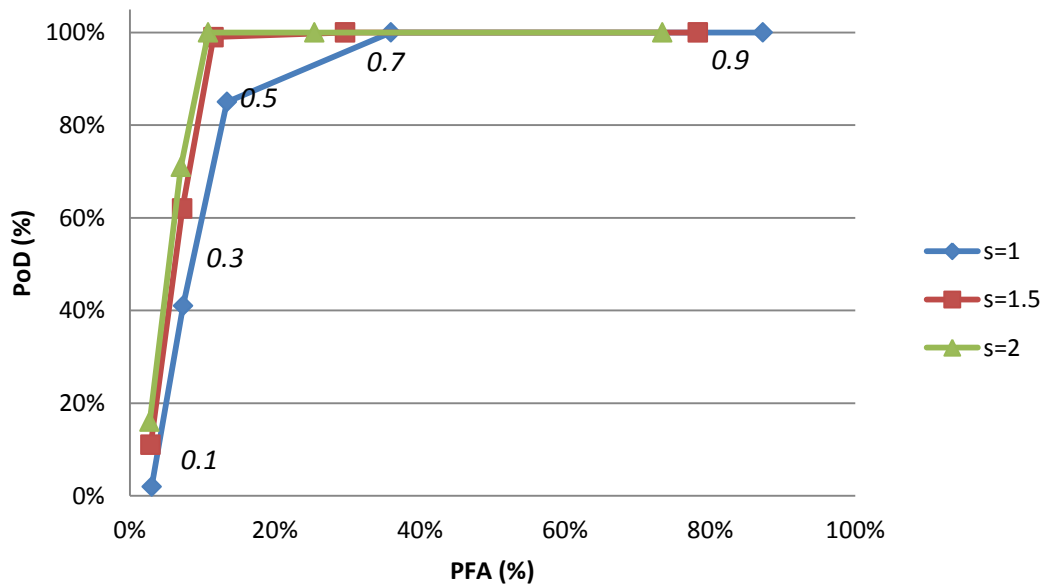
Figure 3.33. ROC for different threshold level, $\alpha=10^{-28}$.

Figure 3.34 shows the PoD and the PFA calculated from two different legitimate reflector locations, one at 30 mm and one at 90 mm, with the noise signal region selected to be close to these legitimate reflector regions. In this case, α was chosen at 10^{-29} and $s = 1.5$. From Figure 3.34 it can be see that though PoD of both regular threshold and frequency dependent threshold are at the same level, PFA is lower if frequency dependent threshold was applied. This indicates that using frequency dependent threshold can further improve the performance of the algorithm.
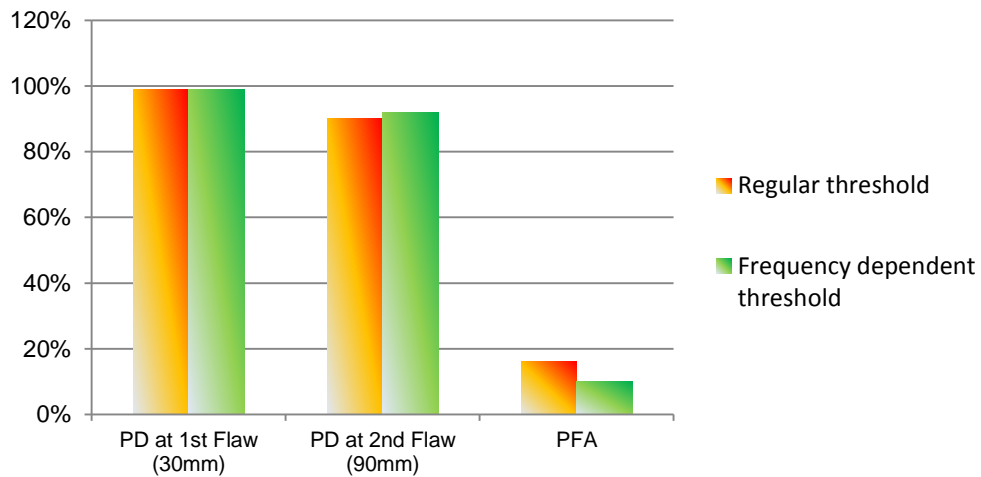
Figure 3.34. PoD and the PFA for regular threshold and frequency dependent threshold.

3.3   Experimental validation

To validate the proposed algorithm, a number of experimentally acquired A-scan traces for three different samples have been used. The austenitic steel sample and the Inconel 617 sample that were described in Section 2.6 are used. The Full Matrix Capture (FMC) dataset was collected using the 5MHz array.

3.3.1   Experimental results

The MB-SSP result for a single A-scan trace for the austenitic steel sample is shown in Figure 3.35(b), with threshold Th set at 0.5. Note the original A-scan is shown in Figure 3.35(a). A traditional SSP result is also presented in Figure 3.35(c), where 10

Gaussian filters with total bandwidth equal to the transducer bandwidth at -6dB (approximately from 3MHz to 6MHz) was used and the recombination algorithm is Polarity Thresholding (PT). The parameter for SSP is a commonly selected based on the transducer bandwidth, when the properties of the test specimens are assumed to be not known. The array was directly placed on the surface of the sample, and the depth of the back wall is 80mm in this case. From Figure 3.35(b) it can be seen that the echo most likely to be a defect (back wall) which is buried in the raw signal remains, while the grain noise around it has been removed. In the SSP A-scan result, the back wall is not positioned correctly and strong artefact signals have been introduced.
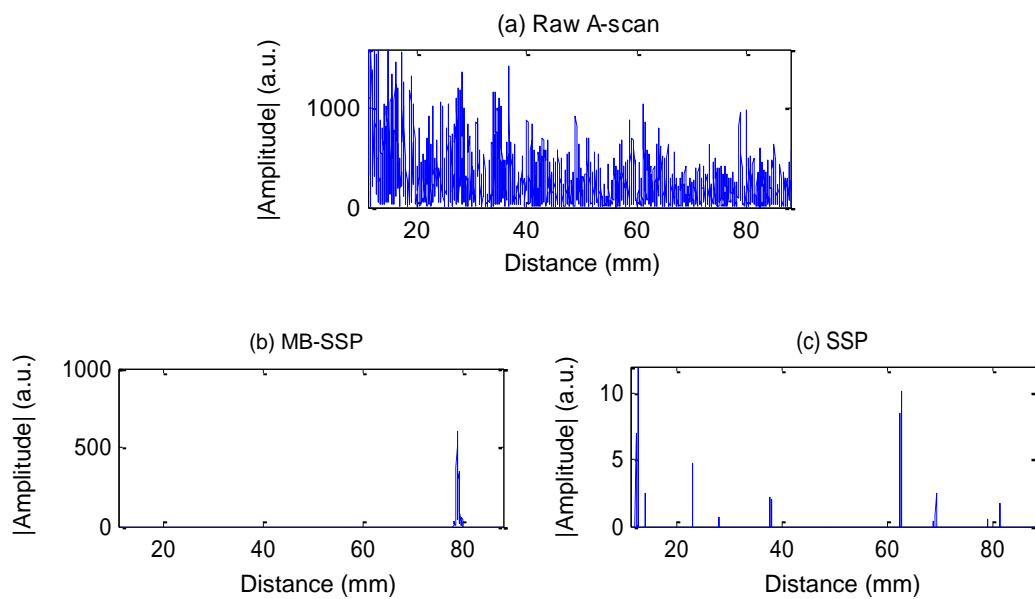
Figure 3.35. Single A-scan of Austenitic steel processed using MB-SSP and SSP

A single A-scan trace for one sample is clearly not enough for the validation purposes. Hence, B-scan images of MB-SSP for both the Inconel 617 sample and the austenitic steel sample are given in Figure 3.36 and Figure 3.37, respectively, as well as the raw data and the SSP results for comparison. All parameter settings remain the same as previously described. Interestingly, in both MB-SSP B-scan images a dark line is visible at around 50mm and 80mm respectively, corresponding to the depth of back wall for each of the two samples. Compared with SSP B-scan images, only the one for the Inconel 617 sample correctly shows a dark line, while the one for the

austenitic sample has failed completely. In both the MPBT and SSP images, there are also many artefacts but the overall image quality from the original B-scan image is significantly improved.
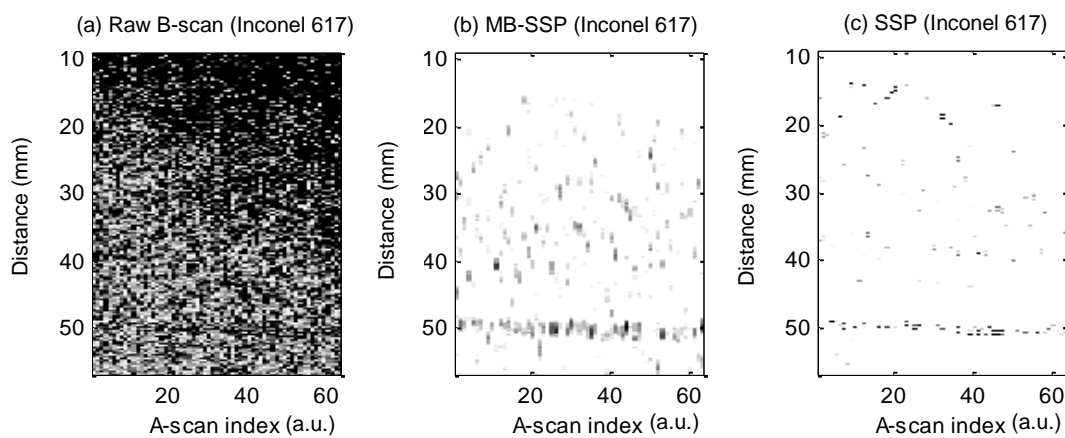
Figure 3.36. B-scan Images of the Inconel 617 sample processed using MB-SSP and SSP.
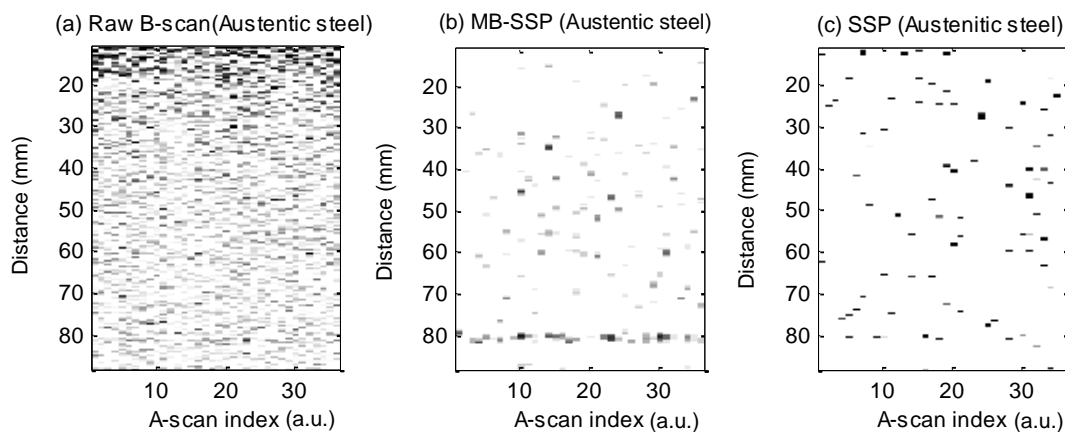
Figure 3.37. B-scan Images of the austenitic steel sample (see Table 2.3) processed using MB-SSP and SSP.

3.3.2 Comparison

Further comparison is now considered to show the robustness of the proposed MB-SSP method. Table 3.1 gives the Signal to Noise Ratio (SNR) of each case in Figure 3.36 and Figure 3.37. The SNR in Figure 3.36 and Figure 3.37 is the average value from all A-scan traces in the B-scan image, calculated by using the peak value of the signal divided by the mean value of noise, in dB. The signal was chosen from the

region of ±3mm around the position of back wall, and the noise was chosen from the region between the array and 10mm above the back wall. From Table 3.1 it can be seen that the proposed MB-SSP algorithm enhances SNR by approximately 16dB for both samples and consequently, defects are more visible compared with SSP images, while SSP is shown to fail on the austenitic steel data, but achieves 14dB SNR enhancement on the Inconel 617 sample data.

Table 3.1. SNRs of images in Figure 3.36 and Figure 3.37

Inconel 617 B-scan images		Austenitic steel B-scan images	
Raw image	7.51dB	Raw image	9.82dB
MB-SSP	22.94dB	MB-SSP	26.50dB
SSP	21.57dB	SSP	-0.97dB

It is considered that SNR is not sufficient to describe the performance since the resolution of the SSP varies as a function of parameter setting. Moreover, both MB-SSP and SSP contain non-linear processing. To further compare the performance of MB-SSP and traditional SSP with different conditions (different materials, different propagation distances and parameters setting etc.), PoD and PFA are used, with each PoD and PFA calculated from 700 A-scan traces. Echoes from the back wall were used for the PoD calculation.

Figure 3.38 shows the robustness of the proposed MB-SSP algorithm in bandwidth selection. MB-SSP is less sensitive to frequency, since it uses a fixed wide bandwidth as default. In Figure 3.38, each column represents specially tuned SSP results, where the maximum indicates PoD and minimum indicates PFA. The parameters setting for all five columns are the same, except the bandwidth selection. Obviously, the performance of SSP is closely related to its bandwidth selection. In this case, the Inconel 617 sample was tested, and the best performance for SSP results appeared when the bandwidth is selected as 50% at -6dB with the centre frequency at 2MHz. For MB-SSP results, the fixed bandwidth avoids this frequency sensitivity while maintained a related higher performance without losing information in the raw signal, since it selects a bandwidth approximately equal to the widest one of SSP case (the leftmost column, 100% bandwidth at -6dB, 5MHz centre frequency),

and its PoD is higher than all SSP cases, while its PFA is only higher than one SSP result. This is because MB-SSP reduces the structural noise for different frequencies respectively before reconstruction.
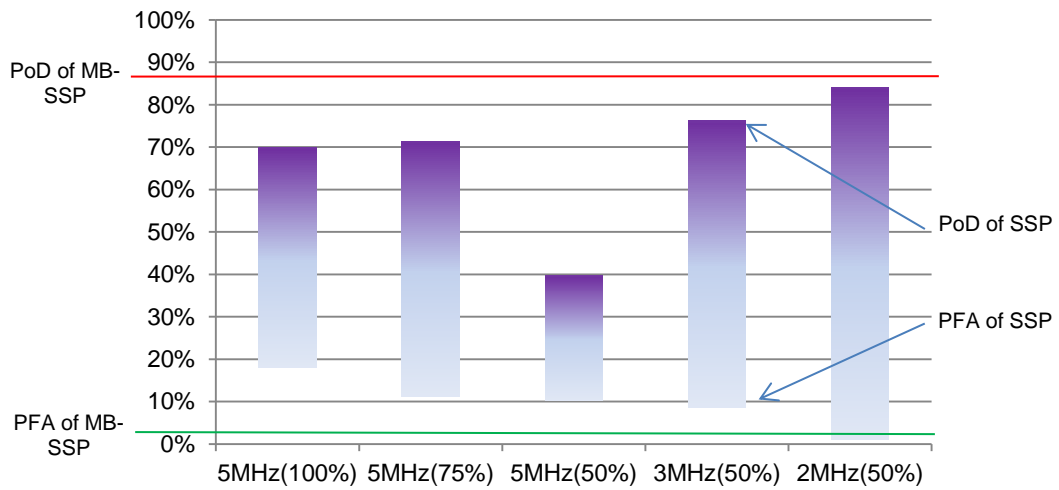
Figure 3.38. PoD and PFA of MB-SSP and SSP with Different Bandwidth Selection. Each bar represent a SSP results, with maximum indicates PoD and minimum indicates PFA. The red line and the green line indicate PoD and PFA of MB-SSP, respectively.

Figure 3.39 shows the performance of MB-SSP using different material properties, as well as SSP for comparison. The parameters set in both Figure 3.39(a) and Figure 3.39(b) are the same, where MB-SSP settings are the same as previously described and SSP settings at 50% bandwidth at -6dB with a 3MHz bandwidth. Figure 3.39(a) shows the performances of the two algorithms at different depths, and Figure 3.39(b) is the result when applied on different materials. For the result of MB-SSP in Figure 3.39(a), The PoD only dropped by 14% when compared the 30mm group to the 50mm group, and the PFA raised by 1%; while in the result of SSP, the PoD dropped by 24% and the PFA raised by 2%. Similarly, as shown in Figure 3.39(b), the PoD difference between the two materials is only 9% for the result of MB-SSP and 41% for the result of SSP; while the PFA difference of the two materials are 2% for MB-SSP and 3% for SSP, respectively. By comparing the PoD and PFA, MB-SSP is more stable when applied to test echoes from different depths or even different materials.

3.4 Summary

This Chapter presents a new spectrum based algorithm, Moving Bandwidth Split Spectrum Processing (MB-SSP), based on A-scan signal processing. It uses the polarity coherence for different frequency components to achieve structural noise reduction and enhanced defect detection.

Figure 3.39. PoD and PFA of MB-SSP and SSP with Different Depth (left) and Different Materials (right). The material tested in (left) is Inconel 617.

Modelled signals were used to analyse the performance and parameters setting of the algorithm. A HDM model was developed to simulate the fact that ultrasonic waves propagating in difficult materials are usually highly frequency dependent. The HDM used here was extended from a widely used analytic model, the main extension is the new model can also simulate the dispersive phase velocity of wave propagation,

97

which is also an important factor for signals acquired from difficult materials. LDM was also introduced as a comparison.

Experimental data from two different samples are also used to validate the proposed MB-SSP algorithm. By comparing the SNR, PoD, and PFA, it has been shown that the proposed algorithm is much less sensitive to material property variation compared with Split Spectrum Processing (with Polarity Thresholding as the reconstruction method), while the performance is maintained.

The main advantage of MB-SSP is its insensitivity to different materials. However, from the results it can be seen that there are still a lot of artefacts on the processed signals. This is because the aim of MB-SSP focuses on the improvement of reliability, hence the noise reduction and legitimate reflector detection ability is not optimised. In the next Chapter, a model based algorithm (using pre-knowledge of the materials) will be introduced. This algorithm will optimise the processing based on *a priori* training signals from the legitimate reflectors. For array applications, an improvement of the algorithm to include the spatial variance of the signal is needed in order to further improve the robustness of the algorithm. This will be further discussed in Chapter 7.

Chapter 4

Advanced A-scan Based De-noising Techniques using Supervised Learning Part I: Classification

Chapter 3 introduced a new algorithm named Moving Bandwidth Split Spectrum Processing (MB-SSP), which aims to enhance the reliability of detection when pre-knowledge of the test material is lacking. Unfortunately, although the performance of MB-SSP is good compared with conventional algorithms, it is not optimised. Hence, if there was pre-acquired knowledge of the material, such as the spectrum distribution of the target echo, statistical based algorithms can then be applied to further improve the detection capability.

In contrast to MB-SSP, statistical based algorithms investigate the stochastic behaviour of the pre-acquired data, to design a specific prototype which can adapt to certain type of materials. For example, it can estimate the spectrum characteristic of the material of interest based on this pre-acquired knowledge, to configure the parameters of the algorithm [134]. Furthermore, the statistical characteristics of the grain noise and the flaw can be observed separately, and used to classify signals into either group based on their similarity.

Recently, a new technique has been developed for target detection and identification in the area of distributed sensor networks [137]. Acoustic and seismic signals have been acquired from different types of vehicles. By analysing the spectra of the collected signals and applying select pattern recognition techniques, these vehicles have been successful detected and classified.

The idea of applying pattern recognition techniques can also be introduced into ultrasound non-destructive inspection. With multiple A-scan traces (acquired by a single transducer or array) as training data, the new echoes with undetermined

information can be characterized by pattern recognition techniques, and as a result, flaw signals and grain noise will be potentially be distinguishable.

The idea of using pattern recognition to classify ultrasound echoes from different types of reflectors has also appeared in the literature [138].

Pattern recognition is considered by some to be nearly synonymous with machine learning in computer science [139], is widely used in applications in the fields of medical, industry and finance. As the core capabilities of artificial intelligence, pattern recognition and machine learning have developed rapidly and their related applications have become ever more popular. This has led to the idea of combining ultrasound de-noising techniques for difficult material inspection with pattern recognition and machine learning. This Chapter will introduce the conventional supervised classification algorithm, and the subsequent two Chapters will then follow this with Artificial Neural Networks (ANN) techniques and unsupervised clustering techniques.

4.1   Pattern recognition / Machine learning techniques

One major field in pattern recognition and machine learning is to analyse, recognize and classify objects. These include images, signals or any measureable objects that need to be classified. These objects are generally identified as a 'pattern'. For example, in handwriting recognition system, each handwriting character is a specific and unique pattern. The system classifies each handwriting character to the related ASCII table using pattern recognition algorithms. Another important application is voice recognition technology. The voice assistant application in the smart phone can extract useful patterns from the input signals acquired from the microphone, and correctly match the voice with words. Importantly, pattern recognition algorithms can classify input patterns with small differences accurately into their related group, if the fundamental characteristic of each group was known *a priori*.

In ultrasonic NDE applications, it is difficult to distinguish target signals from grain noise when inspecting difficult materials. However, there are still differences

between them as discussed in Chapter 2. In particular, the frequency components in the spectra of target signals and grain noise are inherently different.

Like images and voice signals, ultrasound signals can also be treated as patterns. Therefore, the classification issue of different ultrasound signals can potentially be solved by introducing appropriate pattern recognition techniques.

Although non-statistical based algorithms like SSP and MB-SSP can distinguish the target echoes from noise in some cases, it is difficult to set a specific 'threshold' to optimally separate the target and noise due to the variability of their spectral characteristics. For example, target spectra reflected from different distances may have different bandwidth due to the effects of attenuation. However, assuming there is sufficient pre-acquired signals that have already been identified as containing target echoes or only containing grain noise, then pattern recognition algorithms can classify future experimental data signals associated with the material precisely after learning the behaviour from the two groups of pre-acquired signals.

Pattern recognition systems comprise the following aspects when implemented as a classification algorithm: feature extraction, training and classification. The classification algorithm is supervised and sometimes referred as classifier.

Training is the process that allows the classification algorithm to learn the characteristic of the test dataset. For this work, the test data is defined as any input dataset input into the classification algorithm and subsequently, classified to a labelled group. In the case of ultrasound NDE of difficult materials, the labelled groups are the legitimate reflector group and the grain noise group. Importantly, the label of the test data is unknown (or assumed to be unknown) before being input to the classifier. On the contrary, the label of training data must been known *a prior*.

The information in the input data is usually large and redundant. Feature extraction is required to reduce the dimension of raw input and concentrate the information to a higher level.

Details of the implementation of the classification algorithm will be described in Section 4.2.

4.2 Methodology

A new method termed Segment Recognition Classifier (SRC) is developed in this Chapter, and its flowchart is shown in Figure 4.1. The block marked by blue is the standard methodology. Green blocks contain new approaches that are proposed in this Thesis. The red block evaluates several standard classification algorithms to achieve optimum performance in different scenarios.

In this Thesis, a segment or a segmental signal refer to a short period of signal; it usually has the length equal to several wavelengths of the signal. Each aspect of the SRC algorithm will now be discussed.
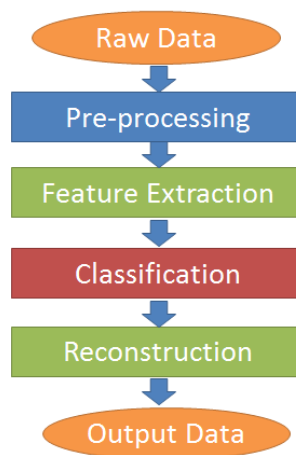
Figure 4.1. Flowchart of Segment Recognition Classifier (SRC).

4.2.1 Pre-processing

Signals collected from the ultrasound probe should be initially pre-processed to produce high fidelity input signals for the SRC system. This step depends on the specific situation, for example a filter can be applied if the original signal contains strong high frequency electronic noise.

As the algorithm requires *a prior* knowledge, training data should be prepared initially. Training is process to 'teach' the algorithm key characteristics of the input data and in this case, the training data must include two groups. One group should

only contain grain noise signals, which usually can be randomly selected from the raw dataset since most of the segmental signals contain only grain noise. The other group contains the legitimate reflector training data. The signals in this group are selected from the locations in the raw dataset where legitimate reflector echoes are known to exist. For example, if the distance of the legitimate reflector is already known, then its training data can be selected according to the distance and wave velocity.

4.2.2   Feature extraction

Once the pre-processing is complete, the algorithm will progress forward to feature extraction, which will be used for both training and classification purposes. In ultrasonic inspection, useful information corresponding to echoes from legitimate reflectors is typically only contained within small segments relative to the entire waveform. Note that the length of these small segments must contain the entire signal length associated with the legitimate reflector echo, to ensure all relevant information is included. Therefore, the size (number of samples) of the segment relies on the acquired signal conditions, e.g. the probe frequency, the sampling rate and length of the emitted signal. Typically, the size of the segment should cover five wavelengths (or five periods in time domain) of the transducer centre frequency. In this way the whole A-scan trace will be divided into small segments and analysed. There are many ways to do this, such as using Short Time Fourier Transform (STFT) or Wavelet Transform (WT). More details about feature extraction will be given in Section 4.3-4.5.

The extracted data can be treated as an M-dimensional vector:

$$V = \{v_1, v_2 \cdots v_M\}$$
(4.1)

where V is the extracted feature vector corresponding to a segment.

4.2.3 Classification

The extracted feature vectors can now be classified using pattern recognition algorithms. For each M-dimensional vector obtained, it must be categorised as a legitimate reflector or grain noise. The first stage to achieve this is to use the segments that have already been clearly identified as a reflector or as grain noise to train the system. After the system has learned the characteristic differences between the two categories, further (unknown) data can be input to the system for classification.

There are many well-developed pattern recognition techniques, such as Naive Bayse (NB) classifier, k-Nearest Neighbor (kNN), and Support Vector Machine (SVM) [140], which will be introduced in Section 4.3.2 – 4.3.4, respectively. The performance of these classifiers will be analysed in the remainder of this Chapter.

4.2.4 Reconstruction

Assuming the legitimate reflector segments is labelled as '1' and noise is labelled as '0'. When every small segment in an A-scan trace has been classified, an indicated signal only consisting of 1 and 0 will be generated. This indicated signal will simply imply the positions of the legitimate reflectors. However, this indicated signal is too dictatorial to clearly identify a segment in the A-scan trace as belonging to a legitimate reflector or noise, as 'false alarm' indications, which can be negligible in the original dataset, may also been displayed as '1', i.e. the same as for a legitimate reflector echo. An improved method is to consider all the segments that contain this point, and average their classification results.

$$p(k) = \frac{\sum_{n=k-L}^{k} C\{V_n\}}{L} \tag{4.2}$$

where $p(k)$ is the probability profile, k is a point in the A-scan trace, V_n is the feature vector of a segment which has a starting point at n and a length of L. C is the classification result of the vector, either '0' or '1'.

As the legitimate reflector will be labelled as '1', the output in Eq. (4.2) can be seen as a probability profile of the original signal, which implies the possibility that the points in the original signal can be a legitimate reflector. This 'detection probability profile' is the core operator of the algorithm and can be further processed, for example to achieve noise reduction as discussed in the experimental results in Section 4.6. Here, the processed A-scan can be calculated by multiply the probability profile signal with the original raw signal.

4.3   Performance analysis: extracting features by STFT

As stated previously, the frequency characteristic of a legitimate reflector and grain noise are different. Therefore, a feature vector can be extracted from the spectrum of a segmental signal that may or may not contain a legitimate reflector. One way to achieve this is to apply the Short Time Fourier Transform (STFT).

Take the austenitic steel sample which introduced in Section 2.6 as an example. Two groups of normalized spectra of segmental signals are shown in Figure 4.2, one is from legitimate reflectors and one is from grain noise. The legitimate reflectors in this case are the back wall signals of the austenitic steel sample. The signals were collected by using a 5MHz array as described in Section 2.6. As can be seen in Figure 4.2, the frequency spectra in the reflector group are more consistent compared to the noise group. In the reflector group, the maximum points appear at around 2MHz in most cases. Although in the higher frequencies region, between 4-8MHz, there is also strong energy peaks which are contributions by grain noise. However, the maximum points in the noise group can be observed as randomly distributed between 3MHz to 8MHz. This phenomenon implies that the reflector echo spectra have common characteristics which are inherently different from the noise spectral characteristics and that the higher order frequency components in the reflector data can be attributed to grain noise.

Obviously, these differences can benefit the classification algorithm approach. Therefore, feature vectors can be assembled using discrete points chosen

equidistantly from the spectral profiles. Importantly, the selected extraction range of frequency should be wider than the transducer bandwidth, in order to get more spectral information.

For example in the case of Figure 4.2, it can be seen that most of the energy is distributed below 10MHz. Hence, 8 points have been extracted from 1MHz to 9MHz equidistantly, to reduce the feature dimensions while maintaining the algorithm accuracy. Importantly, in this way the frequency difference between each point is 1MHz, which is exactly the frequency resolution of STFT when the segment length is selected as 5 periods of the transducer centre frequency. Note that when extracting features using STFT, the segment length is the same with the STFT time window.

In addition, to reduce the effect of attenuation and beam divergence, all spectra are normalized before extracting feature vectors.
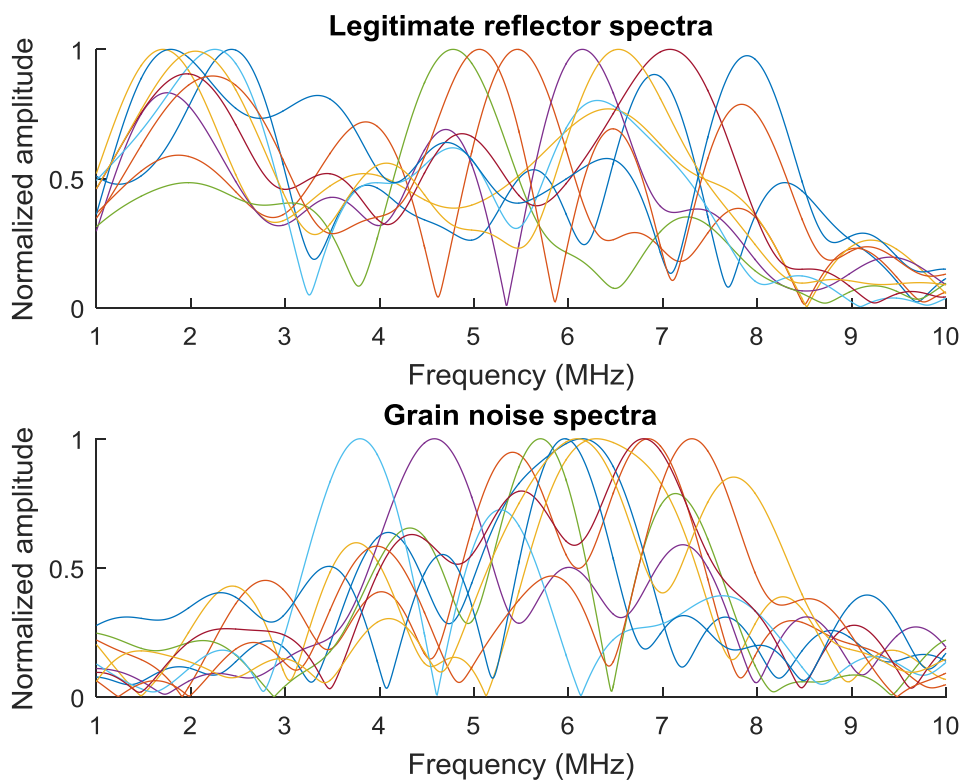
Figure 4.2. Spectra examples of both backwall and grain noise signals from the austenitic steel sample.

4.3.1 Generating simulated signals

A suitable classifier should be chosen to ensure the performance of the algorithm is optimized. For the purpose of analysis, simulated signals are required for this work and the simulation model introduced in Chapter 3 was used. Within the high dispersion model (HDM), the parameters were set as 5MHz centre frequency, 50% transducer bandwidth at -6dB and 100MHz sampling frequency. The attenuation factor a is chosen as $\alpha = 10^{-29}$, and the detect amplitude factor s is chosen as 1.5. Unless otherwise specified, all simulated signals in this Chapter use the above configuration. In the cases where $\alpha = 10^{-30}$, this has been selected to produce closely matched spectra between the legitimate reflector and noise; hence ensuring a more challenging processing scenario for the algorithm. The following Sections (4.3.2-4.3.4) describe three different classification algorithms and uses, where appropriate, the simulated datasets.

4.3.2 Naive Bayes classifier

Let w_1 denote the reflector group and w_2 denote the grain noise group. By learning the stochastic behaviour of the two groups, it is easy to calculate their prior probability $P(w_1)$ and $P(w_2)$,

$$P(w_1) = \frac{N_1}{N}, P(w_2) = \frac{N_2}{N} \tag{4.3}$$

where N is the total number of training samples, N_1 and N_2 are the number of samples in w_1 and w_2.

According to Bayes rule, the posterior probabilities of each class,

$$P(w_i|V) = \frac{P(w_i) \prod P(v_j|w_i)}{\sum P(w_i) \prod P(v_j|w_i)} \tag{4.4}$$

where V is the feature vector of an observation as stated in Eq. (4.1), i is the index of the class, v_j is an element in the feature vector, and j is the index of the element.

The classification result of an observation is based on estimating of the posterior probability for each class. The one with larger posterior probability is more likely to be the class of the observation.

Naive Bayes is a classification algorithm that applies density estimation to the data. It (naively) assumes that the predictors are conditionally independent, hence the name. Although this assumption is usually violated in practice, Naive Bayes has robust performance in many complex situations [140].

The likelihood function $P(v_j|w_i)$ in Eq. (4.4) is usually evaluated by Maximum Likelihood Estimation [140]. However, the type of the probability distribution of $P(v_j|w_i)$ needs to be known in advance in order to estimate their parameters. According to the literature [134], ultrasound signals generally follow a normal distribution. This can be validated using the Kolmogorov-Smirnov test (KS test) [141], with the practical dataset acquired from the austenitic steel sample which described in Section 2.6 with the 5MHz linear array as the evaluation dataset. The one-sample KS test is a nonparametric test of the null hypothesis that the population Cumulative Distribution Function (CDF) of the data is equal to the hypothesized CDF. It quantifies a distance between the Empirical Cumulative Distribution Function (ECDF) of the evaluation dataset and the CDF of the reference hypothesized distribution, as shown in Figure 4.3. In this case, the feature vector is constructed using 8 elements between 2MHz to 9MHz. Each plot in Figure 4.3 shows the ECDF of an individual frequency component, with the standard normal CDF as a comparison.
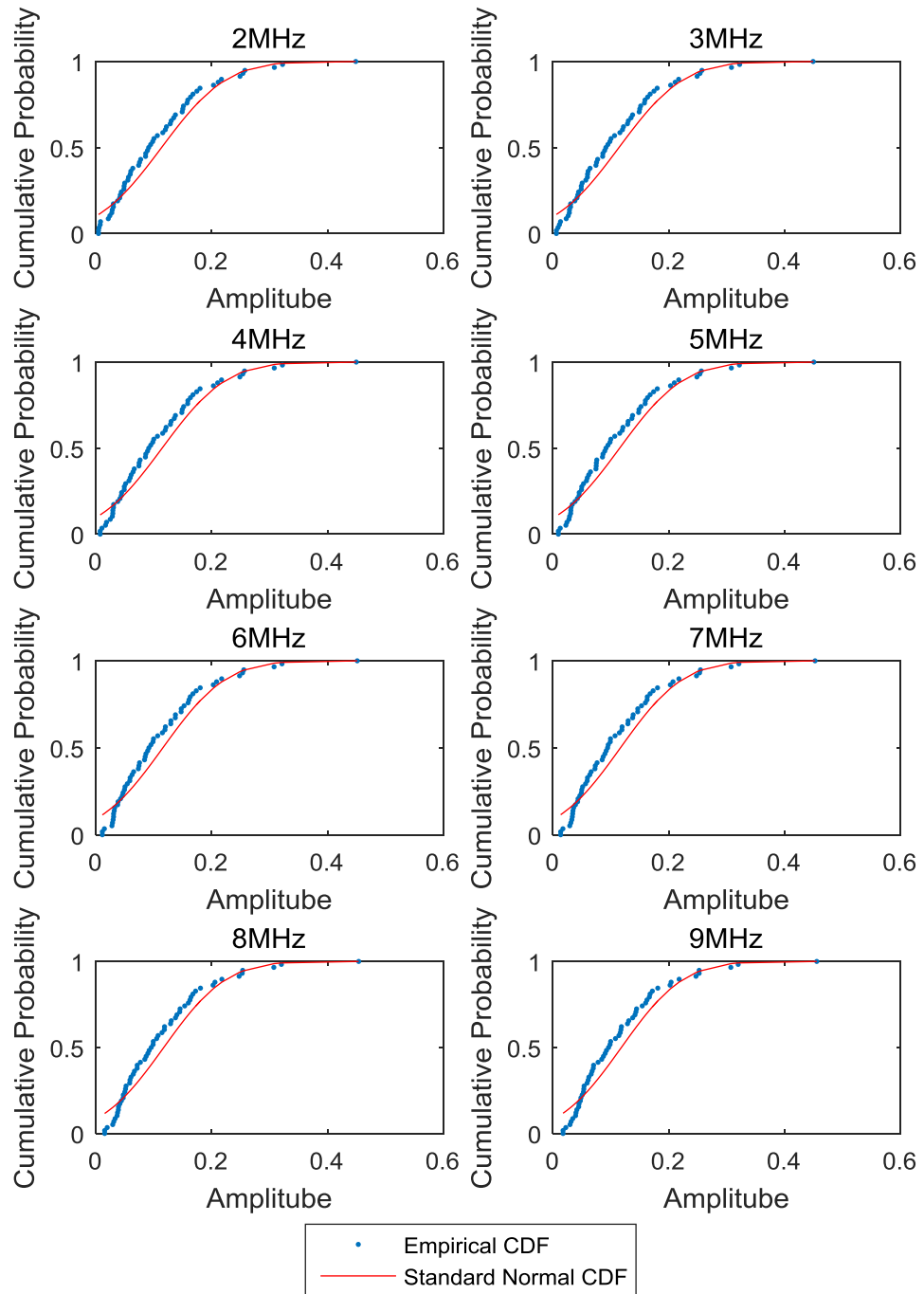
Figure 4.3. KS test of different frequency components of the austenitic steel sample.

The KS test statistic Dn is defined by,

$$Dn = sup_x |G(x) - F(x)|$$

(4.5)

where sup is the supremum of the set of distances. $F(x)$ is the ECDF of the tested data which is empirical measured and define as,

$$F(x) = \frac{number\ of\ elements\ in\ the\ sample\ \leq x}{total\ number}$$

(4.6)

and $G(x)$ is the CDF of the reference distribution,

$$G(x) = \int_{-\infty}^{x} fx(t)dt$$

(4.7)

where $fx(t)$ is the density function of the reference distribution. $G(x)$ can be calculated by the integral of the density function of the reference distribution, which in this case is the normal distribution.

KS test then decides to reject or accept the null hypothesis by interpolation Dn in a table or using an approximation formula [142].

Generally speaking, the smaller distances between the two CDF indicates the distribution of the two data sets are similar. From Figure 4.3 it can be seen that the ECDF and CDF are relatively close and that indicates all the elements of the feature vectors follow normal distributions.

4.3.3 k-Nearest Neighbors

Although it has been shown that the elements in the feature vector follow normal distribution, see Figure 4.3, the likelihood function is however still estimated approximately. In practice, the situation may be more complex, hence the k-Nearest Neighbors (kNN) algorithm is introduced for comparison. The steps of kNN can be expressed as,

● Calculate the distances between the input vector and the vectors in the training sets in close proximity, regardless of class.

- Choose the k vectors in the training sets that have smallest distances to the input vector. In the case of two classes, k should be an odd number.
- Count the number of vectors that belongs to each class respectively, from the chosen k vectors.
- The input vector is then classified to the class with largest number.

The principle of the kNN classifier is straightforward and importantly, it is not concerned about how the training sets are distributed.

Based on the theoretical analysis [140], it is often suggest that kNN has optimised performance when the number of training samples $N \rightarrow \infty$ and $k \rightarrow \infty$. However this is difficult to achieve in practice. A large value of k will significantly increase the computation complexity, and also for most of cases, such a large set with explicit training samples are not available. However, many practical situation are complex and the performance of kNN does not simply enhance with the increased k. In this work, 2000 simulated signals are used to evaluate the most suitable k to adapt the classification for this simulated case.

As can be seen in Figure 4.4, the probability of how many legitimate reflectors are correctly classified (known as true positive rate (TPR) or sensitivity [143]) is increased when k is increased, but has no significant improvement after $k = 7$. While the probability of how many grain noise vectors are correctly classified (known as true negative rate (TNR) or specificity [143]) is decreased after the point when $k = 5$. In addition, since larger values of k require larger computation power, the k parameter used in this work will be selected at $k = 5$.

4.3.4 Support Vector Machine

In recent years, a new classification algorithm named Support Vector Machines (SVM) has been reported. It separates the classes in high dimensional space optimally using a hyperplane. SVM tends to find the largest separation, or margin, between two classes, as shown in Figure 4.5.
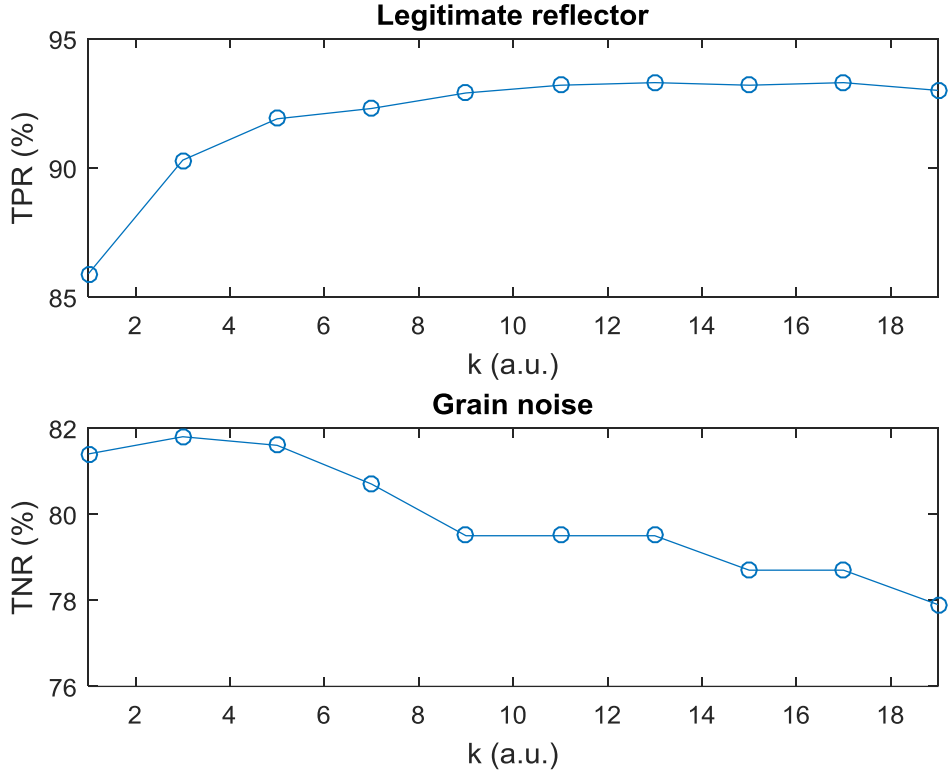
Figure 4.4. Analysis of kNN classification algorithm plotting TPR and TNR as a function of *k*.

The purple line on the figure is the maximum-margin hyperplane. A hyperplane is expressed as,

$$g(x) = W^T V + W_0 = 0 \qquad (4.8)$$

where W and W_0 are the weight and bias vector, respectively, V is the feature vector of an observation.

The optimal solutions of finding the maximum-margin hyperplane can be evaluated by introducing a Lagrange function.

The solutions,

$$W = \sum \lambda_i y_i V_i \qquad (4.9)$$

are the support vectors, i.e. the circled points in Figure 4.5, where λ is the Lagrange multiplier, y_i is a label related to V_i, $y_i = 1$ when V_i belongs to class w_1, $y_i = -1$ when V_i belongs to class w_2, i is the index of the support vector

The maximum-margin hyperplane therefore is:

$$g(x) = \sum \lambda_i y_i V_i^T V + W_0 = 0 \tag{4.10}$$

Traditional SVM is a linear classifier that assumes all data in different classes can be separated by a linear hyperplane, as in the case of Figure 4.5. However in practice, this is not always true. In the case shown in Figure 4.6, there are vectors that cannot be correctly classified no matter how or where the hyperplane is placed.
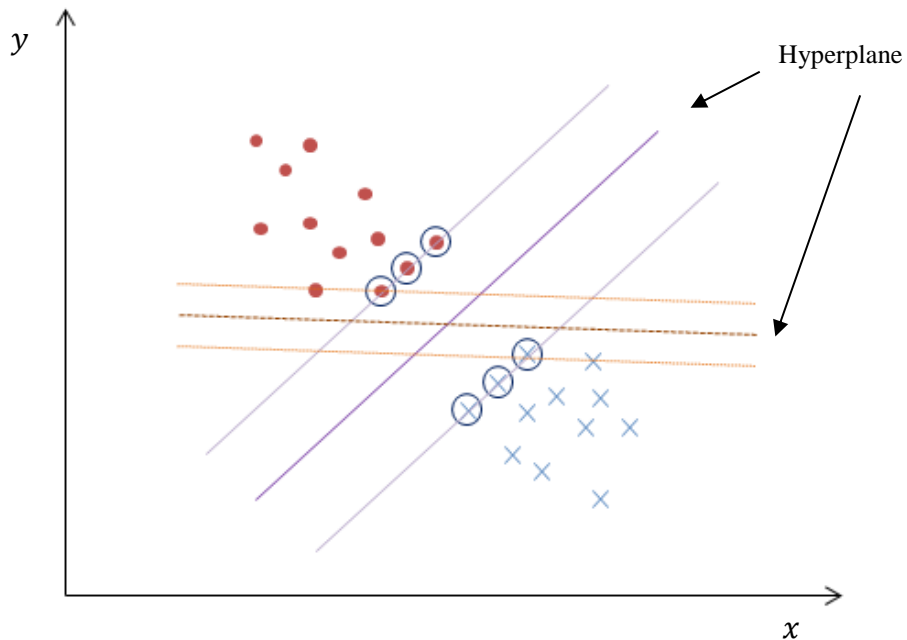
Figure 4.5. Concept of SVM. Dots and crosses in the figure represents two different groups. The hyperplane is used to separate the two groups. SVM tends to determine the hyperplane with largest margins between the two groups. The circles in the figure are the support vectors. They are used to determine the boundary of each group, and hence determine the hyperplane. The axis label x and y represent a two dimensional space.
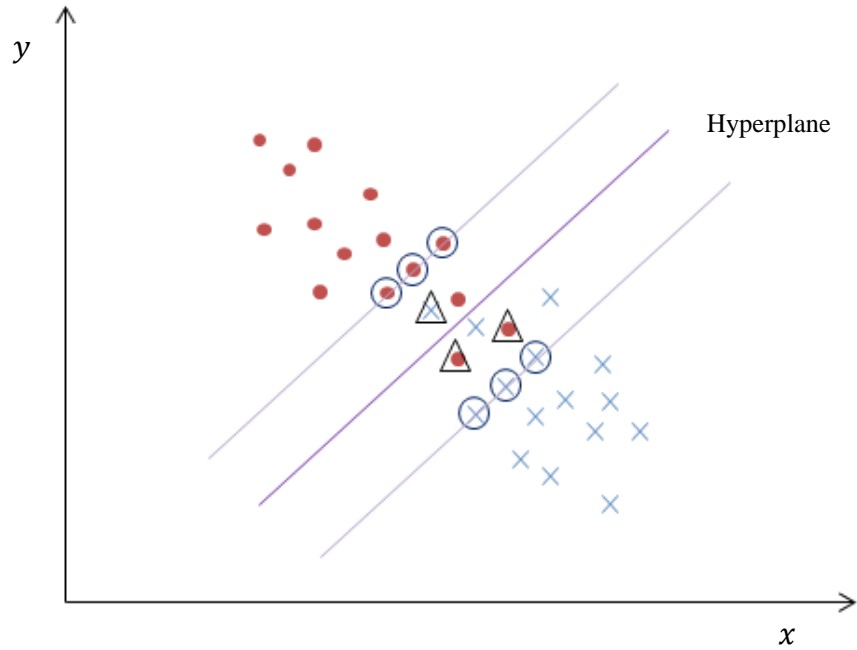
Figure 4.6. Concept of SVM showing that classes that cannot be linearly separated. Linear hyperplane cannot completely separate the two groups, no matter where it is placed. The axis label x and y represent a two dimensional space.

One strength of SVM is that it can easily been expanded to a non-linear classifier without significantly increasing the computational complexity. This is achieved by replaced the inner product $V_i^T V$ in Eq.(4.10) by a kernel function [140].

This allows the algorithm to fit the maximum-margin hyperplane in a transformed higher dimensions feature space. Although the classifier is a linear hyperplane in the transformed feature space, it may be nonlinear in the original input space.

The hyperplane function in the new feature space is,

$$g(x) = \sum \lambda_i y_i \, k(V_i, V) + W_0 = 0 \tag{4.11}$$

where $k(V_i, V)$ denotes the kernel function.

There is an uncertain conclusion of how to choose the kernel function. For this work, the redial basis function (RBF) [140] approach has been chosen as the kernel.

An evaluation of the linear and non-linear SVM approaches is shown in Figure 4.7. Nine groups of simulated data were used to test the performances, where each

contains 2000 samples. It can be seen that though the TPR of legitimate reflectors are fairly close in each simulation, the TNR of grain noise in the non-linear SVM is generally better when compared to the linear SVM case. Therefore, the non-linear SVM is more suitable to be used in the classification of legitimate reflector and grain noise. This also indicate the boundary between the two classes is non-linear.
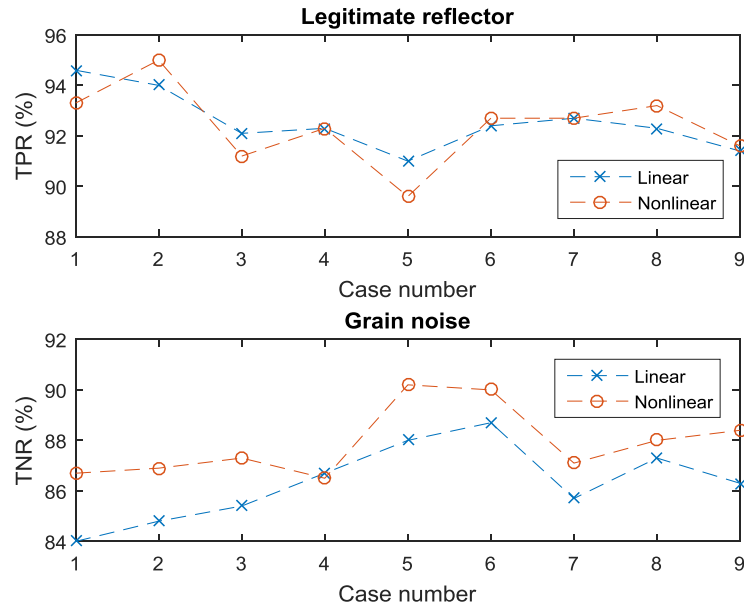
Figure 4.7. TPR and TNR for linear SVM and non-linear SVM .

4.3.5   An example classification result

Prior to evaluating the classifiers on simulation data, described later in Sections 4.3.6 to 4.3.10, an intermediate evaluation was conducted to provide an initial validation of the three proposed classifiers using the practical dataset acquired from the austenitic steel with the 5MHz linear array described in Sections 2.6. As can be seen in Figure 4.8, TPR, TNR and *Accuracy* have been given for the three classifiers respectively, in the form of histograms. The *Accuracy* is the total percentage rate of the output that has been correctly classified to the related class [143], and hence, it indicates the overall performance of the classifier. It can been seen that all the three classifiers have satisfactory performance. Naive Bayes (NB) has the lowest overall percentage rate among the three classifiers, although it still correctly classified for 96.6% of the data. Clearly, SVM has the best performance in this case among the three classifiers.
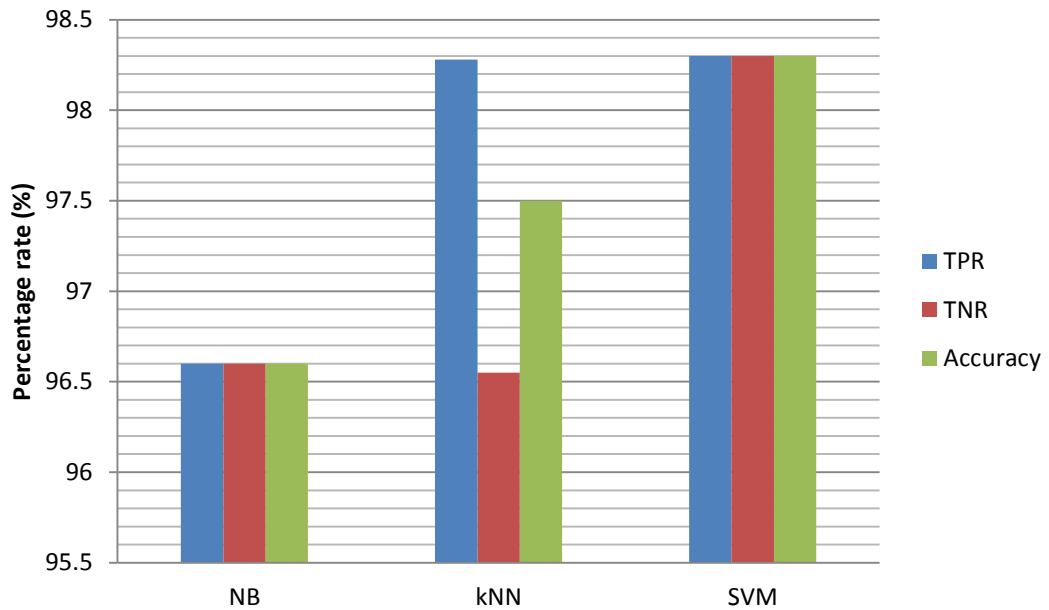
Figure 4.8. TPR, TNR, and *Accuracy* of the classification results using NB, kNN, and SVM for the austenitic steel sample. The legitimate reflectors are back wall echoes at 79mm; the grain noise segments are extracted randomly.

4.3.6 Training data with different characteristics

In practice, the training data that covers echo signals of different types such as echoes from different propagation distances, may not be easy to acquire, even if there are calibration samples which are manufactured from the same material. For example, the training data may be acquired from a shallow side-drilled hole but the flaw is hidden at a much deeper location. Another example is using back wall signals as training data, since back wall signals can be much easier to acquire. For this reason, the effect of training data acquired from different locations are analysed. Simulated signals are generated for three different cases.

- Case 1: All legitimate reflectors are set at 75mm, grain noise segments are extracted from random distances.
- Case 2: All legitimate reflectors are set at 125mm, all grain noise segments are extracted from random distances.

116

- Case 3: legitimate reflectors are set randomly between 75mm to 125mm, grain noise segments is extracted from random distances.

An additional dataset is also simulated for the purpose of evaluation, described as the test data. The test data for all three groups have random distributed legitimate reflectors between 75 mm and 125 mm.

From Figure 4.9, Figure 4.10 and Figure 4.11 it can be seen that case 3 has the highest *Accuracy* for all the three classifiers. This is predictable since the training data in this case mostly closely matches to the test data. Importantly, the *Accuracy* in the other two cases is also reasonably close to case 3. Especially for SVM, where the worst *Accuracy* (case 2, 87.55%) is still considered acceptable as it is only 4% lower than case 3. That means, the idea of using training data with slightly different characteristics is acceptable. Note that in this simulation, SVM has the best overall performance among the three classifiers.
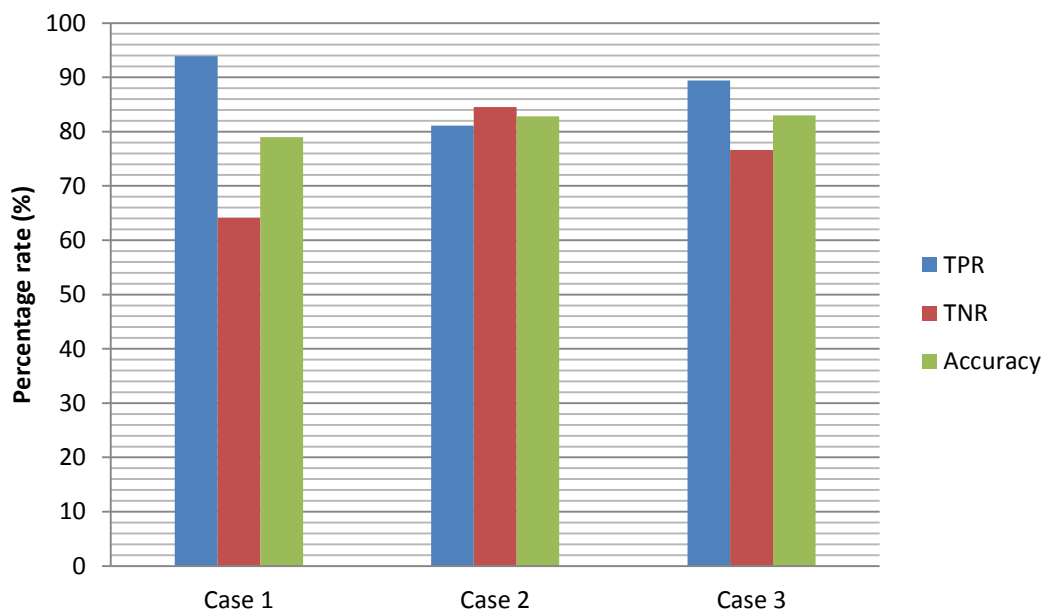
Figure 4.9. TPR, TNR, and *Accuracy* of NB classification results for 2000 simulated A-scans, with legitimate reflector training data collected at different distances. All legitimate reflectors in case 1 are at 75 mm, all legitimate reflectors in case 2 are at 125 mm, and the legitimate reflector in case 3 are randomly distributed between 75 mm and 125 mm. Grain noise training data are collected uniformly between 75 mm and 125 mm for all the three cases. The test data for all three groups are extracted randomly between 75 mm and 125 mm. The data is simulated using the high dispersive model with $\alpha = e^{-29}$, $s = 1.5$, 5MHz centre frequency.
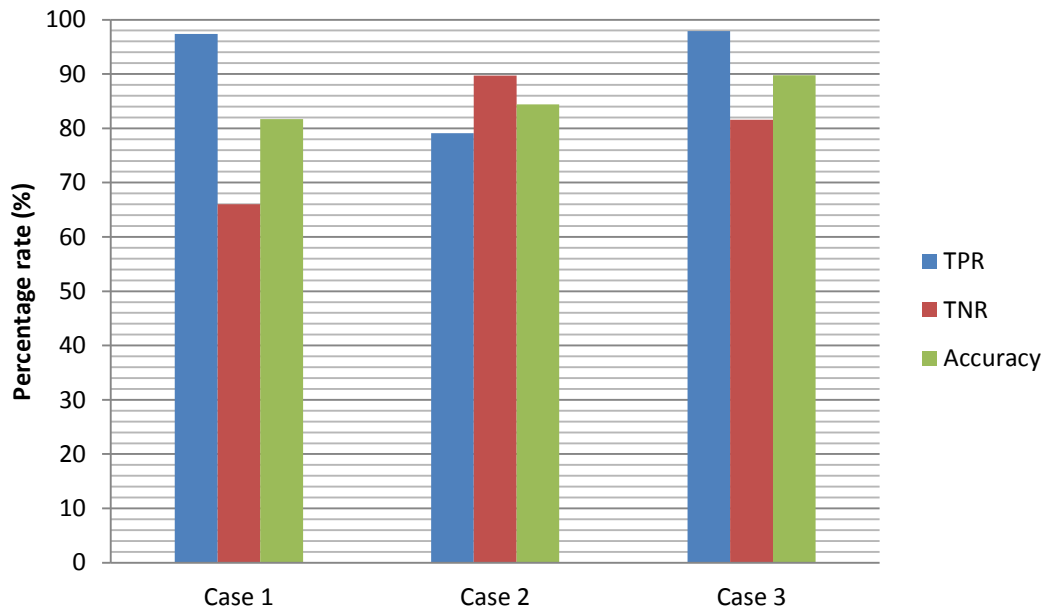
Figure 4.10. TPR, TNR, and *Accuracy* of kNN classification results for 2000 simulated A-scans, with legitimate reflector training data collected at different distances. All legitimate reflectors in case 1 are at 75 mm, all legitimate reflectors in case 2 are at 125 mm, and the legitimate reflector in case 3 are randomly distributed between 75 mm and 125 mm. Grain noise training data are collected uniformly between 75 mm and 125 mm for all the three cases. The test data for all three groups are extracted randomly between 75 mm and 125 mm. The data is simulated using the high dispersive model with $\alpha = e^{-29}, s = 1.5$, 5MHz centre frequency.
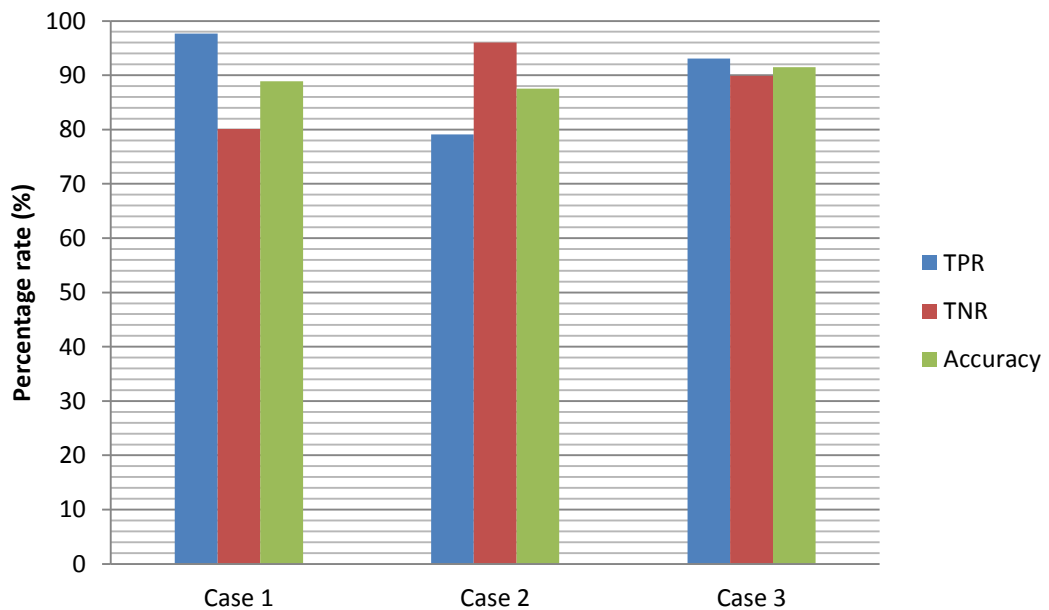
Figure 4.11. TPR, TNR, and *Accuracy* of SVM classification results for 2000 simulated A-scans, with legitimate reflector training data collected at different distances. All legitimate reflectors in case 1 are at 75 mm, all legitimate reflectors in case 2 are at 125 mm, and the legitimate reflector in case 3 are randomly distributed between 75 mm and 125 mm. Grain noise training data are collected uniformly between 75 mm and 125 mm for all the three cases. The test data for all three groups are extracted randomly between 75 mm and 125 mm. The data is simulated using the high dispersive model with $\alpha = e^{-29}, s = 1.5$, 5MHz centre frequency.

4.3.7　Size of the training data

Generally, an increased number of samples can provide more accurate information for a statistical study. This can been seen in Figure 4.12, which shows the TPR, TNR and *Accuracy* for the three classifiers when the size of the training data is modified. The size of training data for each class is increasing from 10 to 1000. The *Accuracy* improves when the total number of training sets increases and becomes stable after ~200. In this example, SVM has the best performance according to Figure 4.12.

4.3.8　Balance between classes

It is generally known that in practice, segmental signals that contains legitimate reflector are much rarer than segments containing grain noise components. An issue is therefore raised: with the limited available legitimate reflector training data, how to choose the appropriate number of training data in the noise class. As discussed in Section 4.3.7, increasing the number of training datasets generally offers an enhanced performance. However, since the number of training data in the reflector class is limited, it is unknown if the imbalance in the two training datasets will cause unexpected problems. Figure 4.13 shows the unbalanced training approach using a fixed number of noise training datasets of 1000 and an increased number of reflector training datasets from 10 to 1000. Compared with Figure 4.12, which illustrated the balanced situation but with a changing size population, the performance of SVM is much better in the region associated with low training numbers, and it almost reaches stable instantly when the training number grows. Therefore, for SVM, selecting extra noise training data will enhance the performance. NB has a similar performance compared with the balanced situation depicted in Figure 4.12. Unfortunately, the unbalanced training approach significantly reduces the performance of kNN, as can be seen in Figure 4.13. This is because kNN searches for the k nearest training vectors and determines the class that most of the vectors belong to. For an unbalanced training scenario, the density of the class with bigger size is naturally larger than the others, hence misleading the kNN classifier. When the number of reflector training datasets is low, almost all test data has been classified into grain noise. Note that kNN becomes very unstable in this case. The two spikes in the Grain

Noise trace in Figure 4.13, at around 250 and 690, are suspected to have been caused by the addition of non-uniform distributed training data.
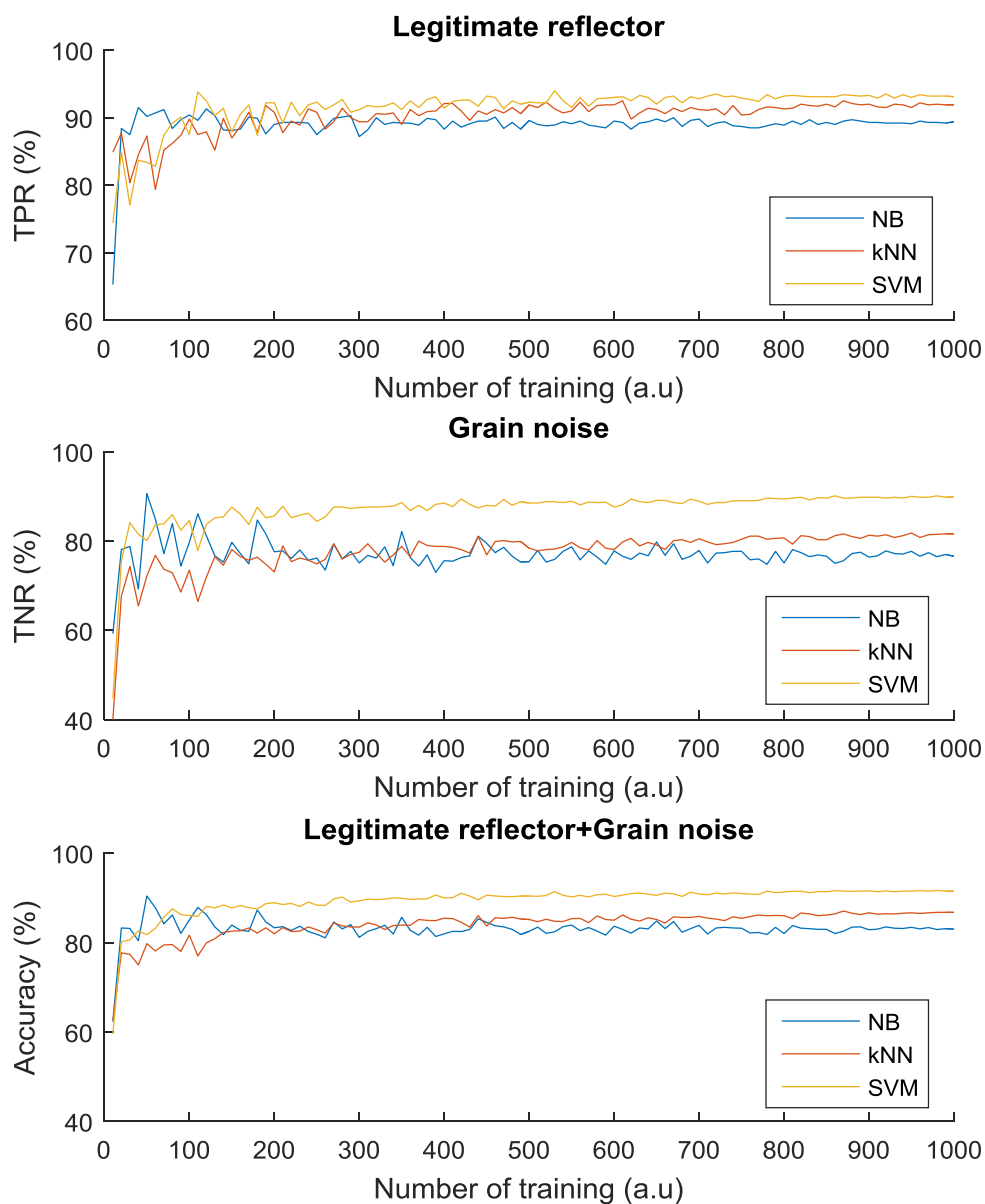
Figure 4.12. TPR, TNR, and *Accuracy* of NB, kNN, and SVM when the size of the training set is changing. The number of observations in both classes is equal, and is increasing from 10 to 1000. The data is simulated using the high dispersive model with $\alpha = e^{-29}$, $s = 1.5$, 5MHz centre frequency.
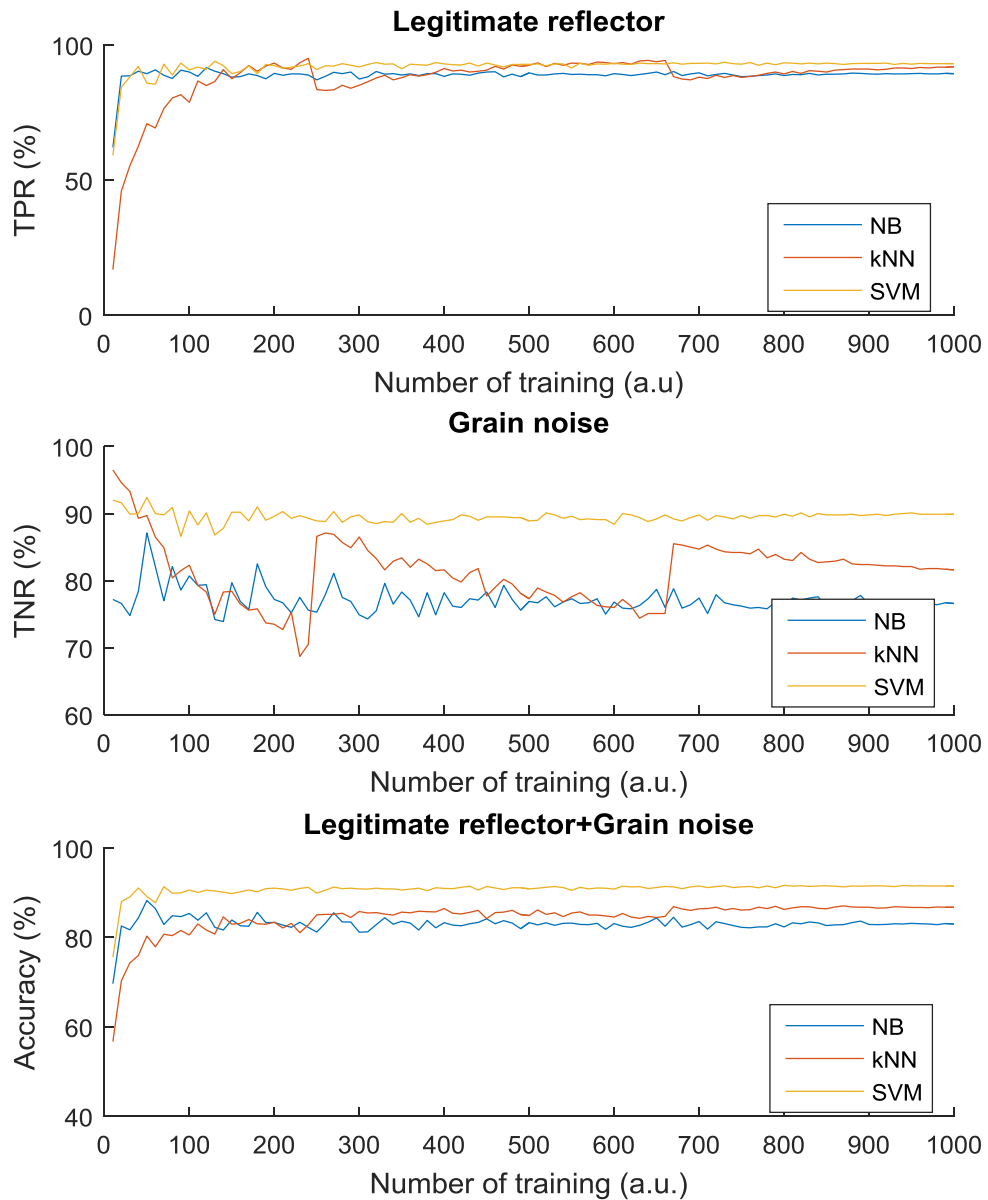
Figure 4.13. TPR, TNR, and *Accuracy* of NB, kNN, and SVM when the sizes of the two classes in the training set are unequal. The number of observations in the grain noise class is fixed at 1000 while the number of observations in the legitimate reflector classes is changing from 10 to 1000. The data is simulated using the high dispersive model with $\alpha = e^{-29}$, $s = 1.5$, 5MHz centre frequency.

Figure 4.14 shows an additional example when the training data is slightly unbalanced. The noise training data is about 20% larger than the corresponding reflector group. It can be seen that this small imbalance does not cause significant detrimental effects compared with Figure 4.12.
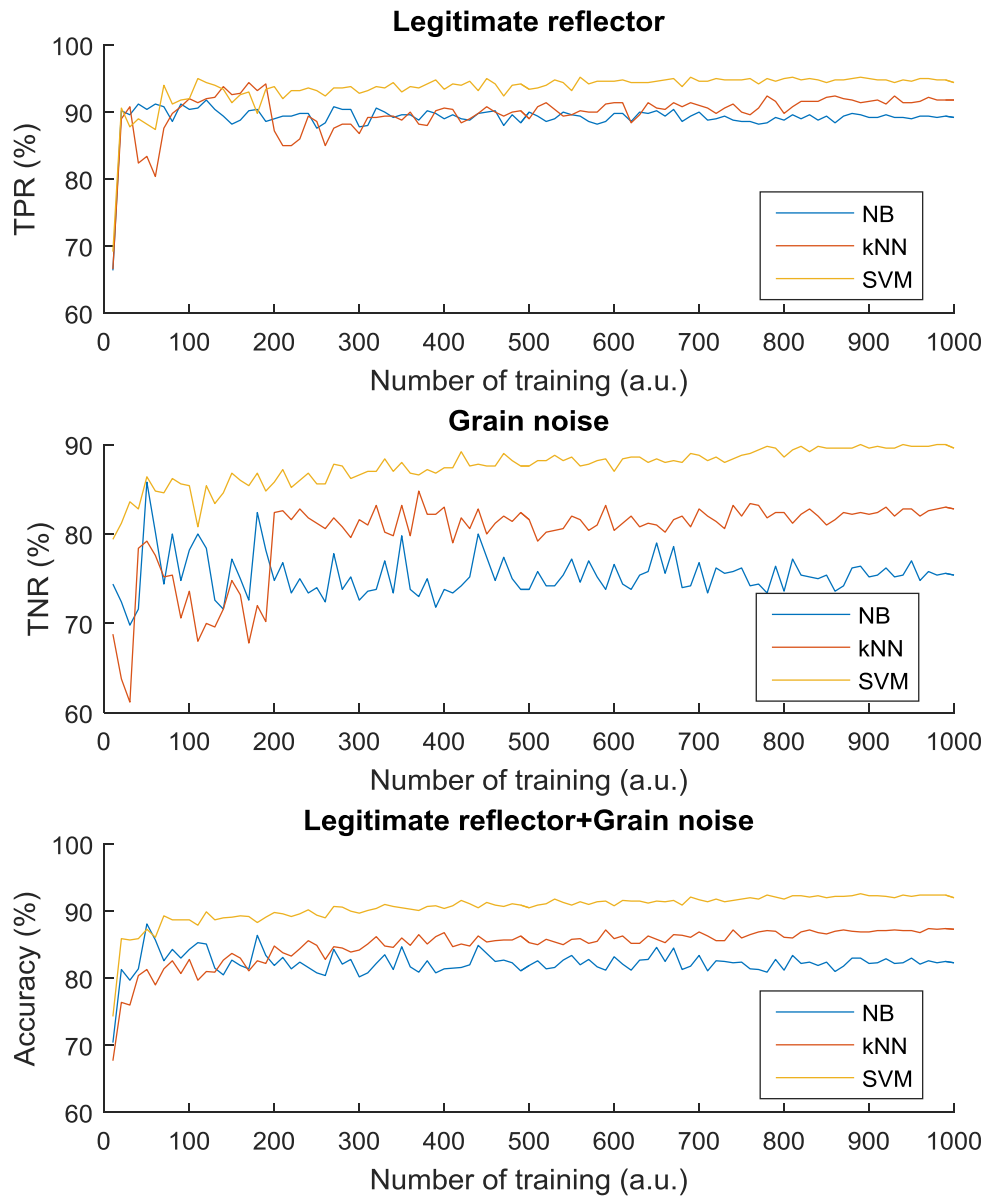
Figure 4.14. TPR, TNR, and *Accuracy* of NB, kNN, and SVM when the sizes of the two classes in the training set are unequal. The number of observations in the grain noise class is 20% larger than the legitimate reflector classes. The size of the reflector training set is increasing from 10 to 1000. The data is simulated using the high dispersive model with $\alpha = e^{-29}$, $s = 1.5$, 5MHz centre frequency.

4.3.9 Inaccurate training

When acquiring training data in practice, noise segments can easily been mixed into the legitimate reflector group by mistake, as the segments containing only a legitimate reflector are difficult to find. Figure 4.15 shows the effect of inaccurate training for the three classifier algorithms. As can be seen in Figure 4.15, at most 50% of the training data of legitimate reflector has been replaced by noise, while the noise group remains the same. Interestingly, the performance of SVM is maintained despite the effective increase in noise.

4.3.10 Effect of similar spectrum characteristic between two classes

In some cases, the characteristic differences between a legitimate reflector spectrum and grain noise is not significant. Since the frequency resolution is limited by the length of segmental signals when applying STFT, the feature vectors of reflectors and noise may be similar. This may increase the difficulty of classification and reduce the accuracy/performance of the algorithm. Figure 4.16 illustrates an example under these conditions. The simulated signals are generated using the HDM model with $a = e^{-30}$, $s = 1.5$, 5MHz centre frequency with 50% bandwidth, and 100MHz bandwidth, as discussed in Section 4.3.1. Again, 2000 signals are simulated to analyse the result. It can be seen in Figure 4.16 that the kNN approach has the best performance among the three classifiers.
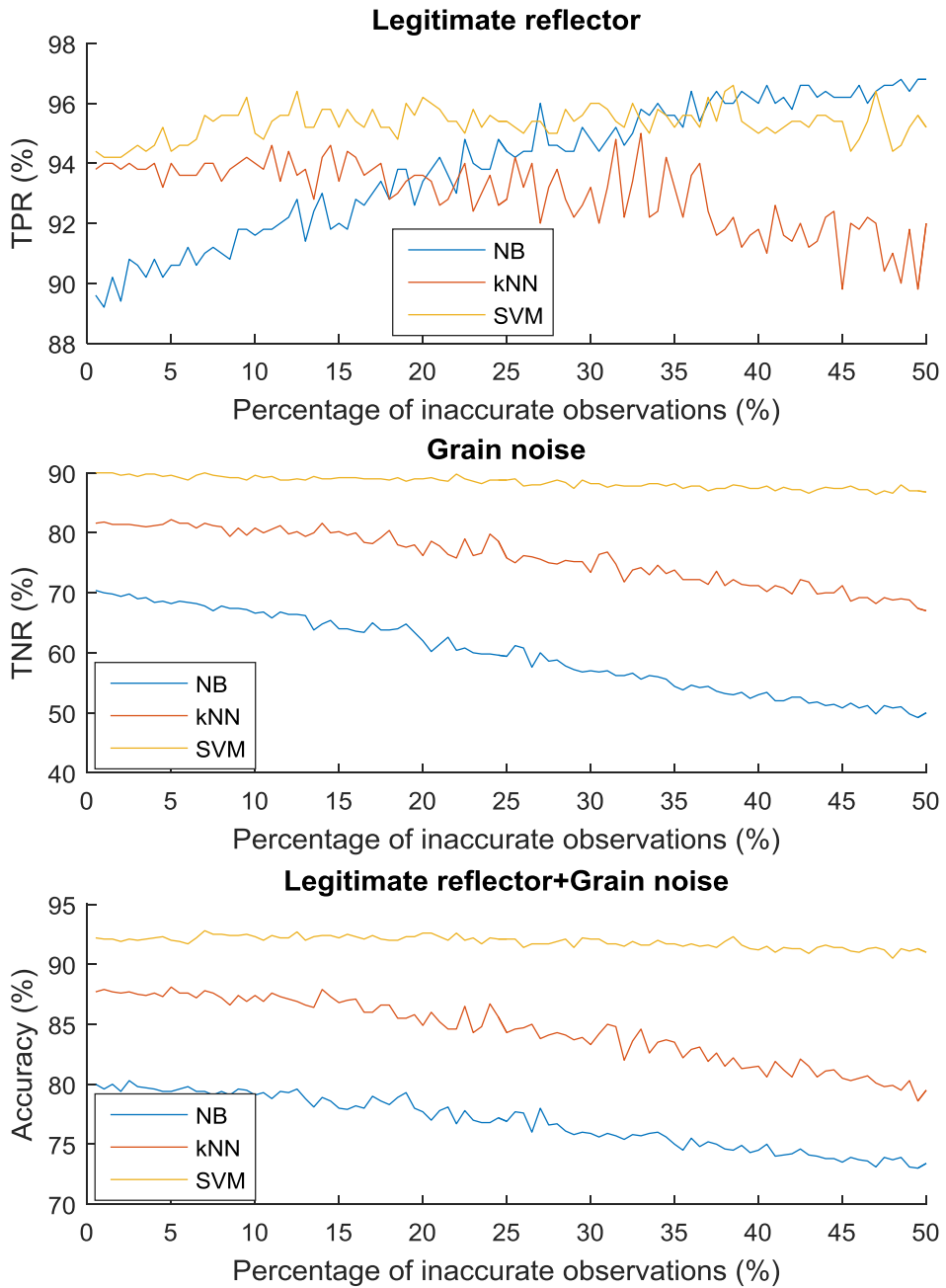
Figure 4.15. TPR, TNR, and *Accuracy* of NB, kNN, and SVM when the legitimate reflector training set is mixed with a certain proportion of grain noise. The data is simulated using the high dispersive model with $\alpha = e^{-29}$, $s = 1.5$, 5MHz centre frequency

Figure 4.16. TPR, TNR, and *Accuracy* of an example classification results using MLP, kNN, and SVM when the spectrum characteristics of legitimate reflector and noise are close. The data is simulated using the high dispersive model with $\alpha = e^{-30}$, $s = 1.5$, 5MHz centre frequency.

4.4 Performance analysis: extracting features by CWT

Since the spectral characteristics are similar between groups in the case of Section 4.3.10 and the frequency resolution is limited by STFT, other extraction methods should be considered. The limitation of frequency resolution is decided by the length of the signal. One way to solve this is, instead of applying STFT, filtering the whole signal into a set of different frequency channels to generate an alternate time-frequency representation. However, this will greatly increase the computation cost, since many frequency channels are needed to increase frequency resolution.

Another way to achieve this is to apply the continuous wavelet transform (CWT) instead of repeatedly filtering the signal. CWT has a higher frequency resolution compared with STFT. Theoretically, using CWT as the feature extraction method can help distinguish between the two classes of interest with a high degree of success.

Unlike STFT, the time-frequency representation of CWT oscillates rapidly along the time axis and selection of feature vectors may be inconsistent. That means, for a

certain time slice, which is chosen to coincide when a legitimate reflector is present, the profile along its scales axis (similar to frequency axis) can still look like a noise. This is particularly true form the oscillatory nature of the CWT close to the zero crossings. Therefore, before extracting feature vectors, moduli and envelopes were initially added, by applied the Hilbert transform, to remove the effect of this oscillation. Otherwise, the data can contain strong nonlinearities.

Figure 4.17 shows an example classification result using CWT as feature extraction method. The dataset used in Figure 4.17 is the same simulation dataset as used in Figure 4.16. The feature vector contains 64 elements in this case, which is also the number of scales in CWT.

All feature vectors should be pre-processed by

$$V_{norm}^{(n)} = \frac{V^{(n)}}{\frac{1}{S_c L} \sum_{i=1}^{S_c} \sum_{n=n-\frac{L}{2}}^{n+\frac{L}{2}} |v_i^{(n)}|} \tag{4.12}$$

to remove the effect of attenuation, where $V_{norm}^{(n)}$ is the processed feature vector, $V^{(n)}$ is the original feature vector, L is the calculation range which is chosen at four times of the wavelength of the centre frequency empirically, S_c is the total number of scales, i is the scale index, and n is the current time instant.

However, the performance when applying CWT is not as good as expected. The *Accuracy* of NB and SVM remains at the same level, but the performance of kNN has significantly dropped. This may be due to the averaging procedure, which also reduces the differences between the reflector and noise components.

4.5   Additional feature: distance

One important factor that affects the spectral characteristic of the echoes is attenuation. For this reason, spectra of legitimate reflectors and grain noise which is detected from different distances may have similar characteristics. Therefore, if the training data of legitimate reflector can be collected from a set of different distances,

then the distances can be treated as an additional feature and can be attached to feature vectors extracted by STFT or CWT.

As can be seen in Figure 4.18, the overall performance of the three classifiers is improved when compared with case 3 shown in Figure 4.9, Figure 4.10 and Figure 4.11, by introducing an additional distance to the STFT implementation.
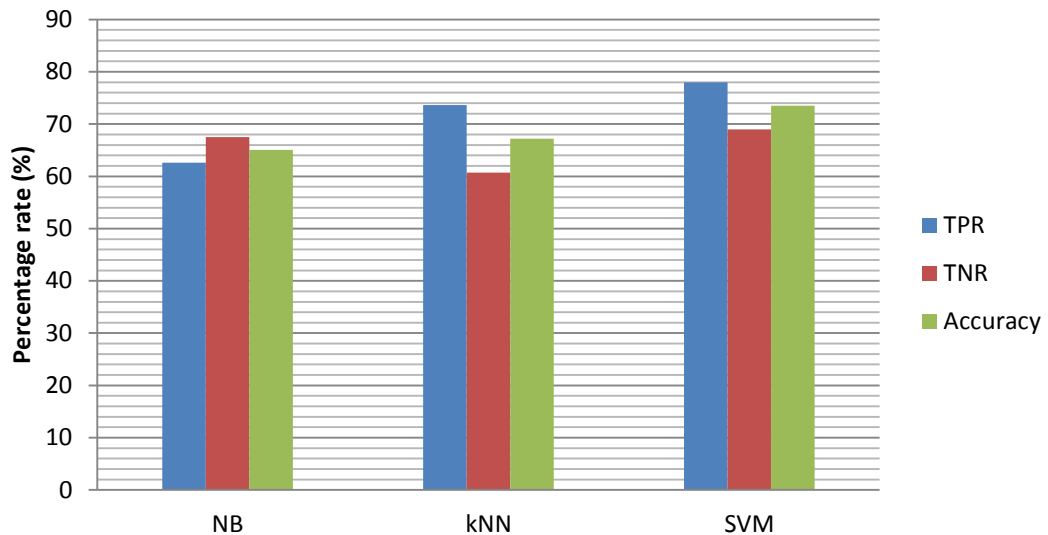
Figure 4.17. TPR, TNR, and *Accuracy* of an example classification results, to compare the performance of NB, kNN, and, SVM, with CWT as the feature extraction method, when the spectrum characteristics of legitimate reflector and noise are close. The data is simulated using the high dispersive model with $\alpha = e^{-30}, s = 1.5,$ 5MHz centre frequency

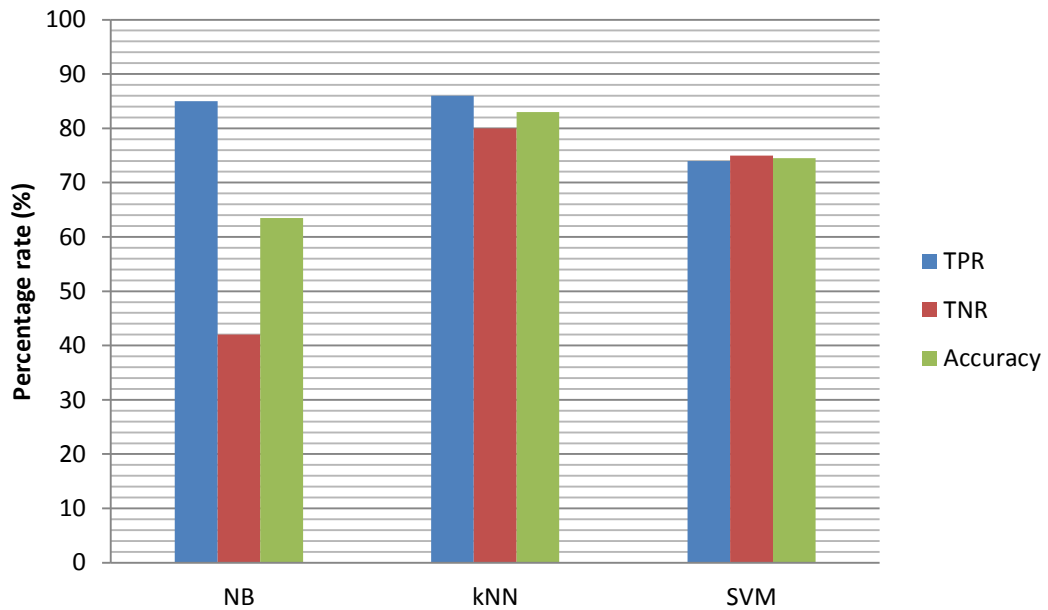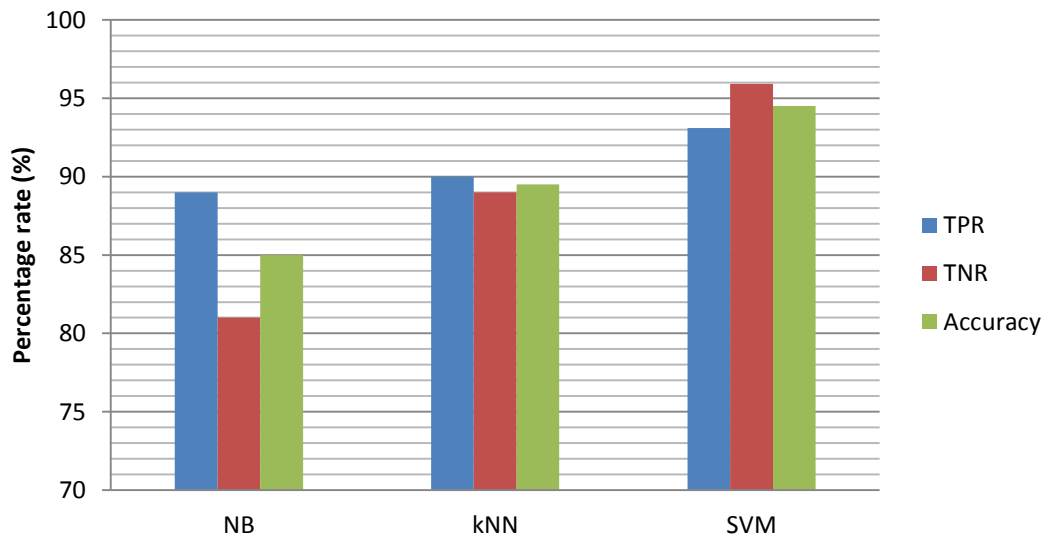Figure 4.18. TPR, TNR, and *Accuracy* of an example classification results, to compare the performance when the propagation distance of the received echo is included as an extra feature. The data is simulated using the high dispersive model with $\alpha = e^{-29}, s = 1.5,$ 5MHz centre frequency

Note that only when the training data of legitimate reflectors covers all the possible distance locations, can this method be used to improve performance, otherwise it may cause an overfitting problem [140] that cannot classify the reflectors properly.

4.6 Classifier evaluation with A-scan and B-scan results

A-scan and B-scan simulations using the same HDM model parameters as described in Section 4.3.1 are presented in this Section to produce more visualised results. Moreover, experimental results using the austenitic steel and the Inconel 617 samples, see Section 2.6, are further used to validate the Segment Recognition Classifier (SRC) algorithm methodology (Section 4.2).

4.6.1 Classifier evaluation: Simulation results

The process through which SRC suppresses grain noise is achieved by assigning points more likely to be a real reflector with a higher value, and reducing points that more closely resemble noise. Figure 4.19 gives an example of how SRC reduces noise in a single A-scan trace. The data is simulated using the HDM model with $\alpha = e^{-29}$, $s = 1.5$, 5MHz centre frequency. After processing using the detection probability profile as stated in Section 4.2.4, the grain noise has been significant reduced and only the positions that are most likely to be a reflector remain, as shown in Figure 4.19. Interestingly, the peak signal appeared at 75mm, corresponding to the depth of back wall. Figure 4.20 shows an image generated by combining 2000 individual A-scans. Each A-scan contains only one legitimate reflector. The location of the legitimate reflector in each A-scan is set uniformly between 75mm and 125mm. The diagonal line in each image in Figure 4.20 is the collection of the legitimate reflector echoes. It can be seen that the original signals have a strong grain noise characteristic. The diagonal line of legitimate reflector echoes is completely hidden by the background noise. By applying the SRC method, the grain noise has been greatly reduced. From Figure 4.20 it can be seen that the B-scan processed by SVM has the lowest background noise, and the one processed by NB has the

strongest noise remaining among the three processed B-scan images. This is in agreement with the analysed results discussed in Section 4.3.6.

Table 4.1 shows the calculated SNR for each image in Figure 4.20.
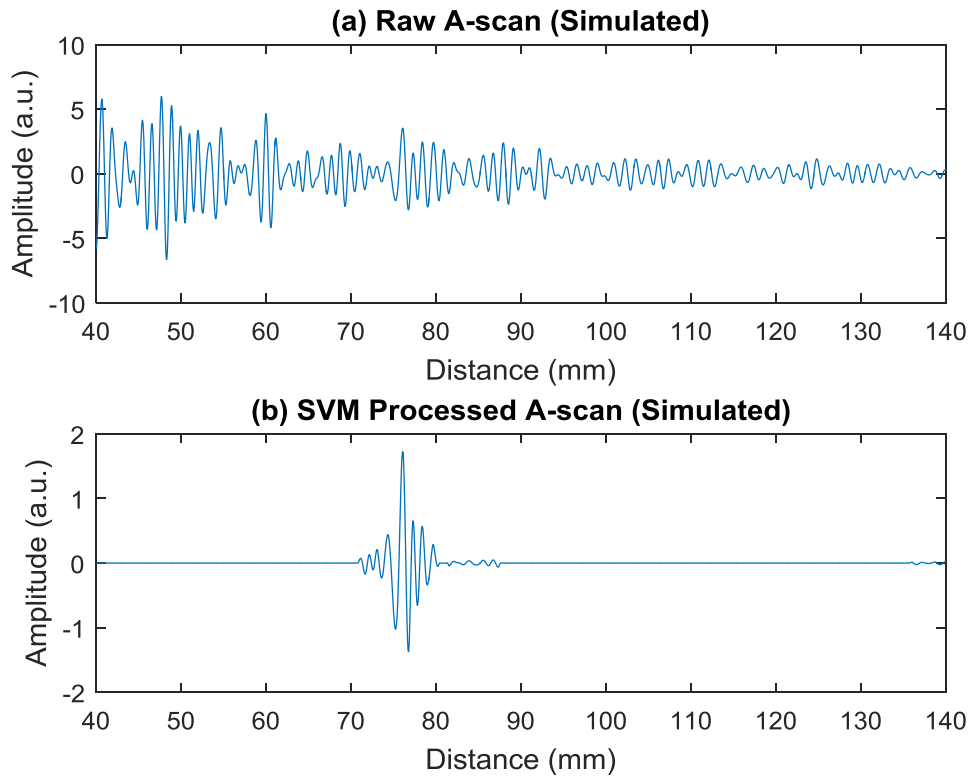
Figure 4.19. A-scans results of the simulated data, with SVM as the classifier, STFT as the feature extraction method. High dispersion model (HDM) was used to simulate the data. The parameters of the HDM model are selected at $\alpha = e^{-29}$, $s = 1.5$, 5MHz centre frequency with 50% bandwidth at -6dB, and 100MHz sampling frequency. A reflector is set at 75mm
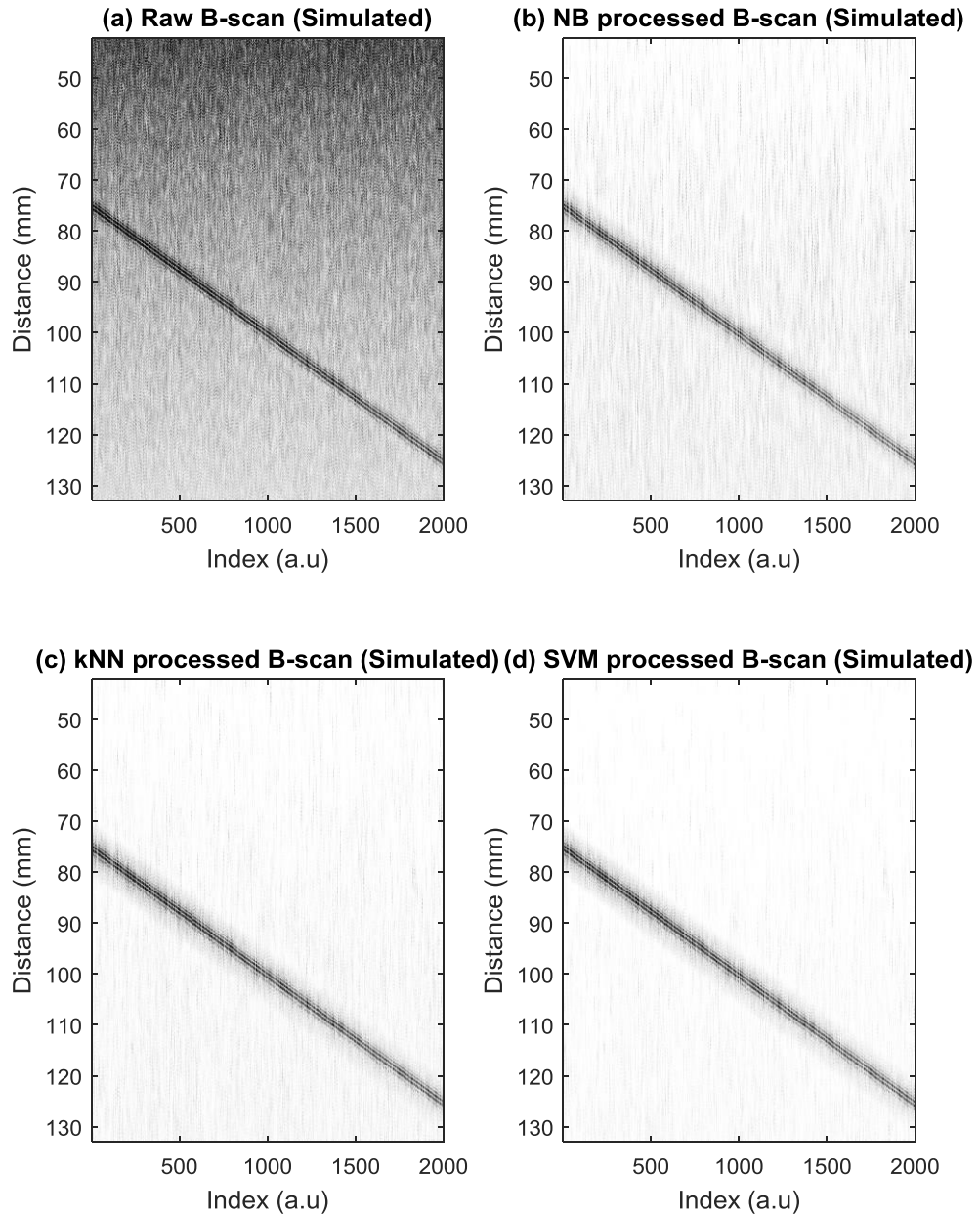
Figure 4.20. B-scans results of the simulated data, (a) Raw B-scan, (b) NB processed B-scan, (c) kNN processed B-scan, (d) SVM processed B-scan. The feature extraction method used is STFT. High dispersion model (HDM) was used to simulate the data. The parameters of the HDM model are selected at $\alpha = e^{-29}$, $s = 1.5$, 5MHz centre frequency with 50% bandwidth at -6dB, and 100MHz sampling frequency. Absolute values of signals is used for all images. The diagonal line in the images are formed by the legitimate reflectors, from 75mm to 125mm.

Table 4.1. SNR for simulated results presented in Figure 4.20.

Raw B-scan	10.08dB
NB processed B-scan	36.20dB
kNN processed B-scan	39.57dB
SVM processed B-scan	41.30dB

4.6.2 Classifier evaluation: Experimental results

An experimental evaluation of the classifier methodology was undertaken on the three difficult material samples described in Section 2.6. For consistency, the 5MHz linear array has been used to acquire data, with sampling frequency of 100MHz. In each experimental measurement, B-scan images have been generated from the raw data and subsequently, processed using SVM. In all cases, the feature extraction method used is STFT.

Austenitic Steel Sample

Figure 4.21 and Figure 4.22 are the processed results from the austenitic steel sample. It can be seen that in the A-scan result, depicted in Figure 4.21, only the back wall signal at 79mm has been detected while the grain noise has been mostly removed. Figure 4.22 is the combination of 40 individual A-scans extracted from an acquired FMC dataset representing the same transmit-receive element pairs. From Figure 4.22 it can be seen that the back wall is originally hidden in strong background noise in the raw A-scan image and is subsequently clearly visible in the processed image. Again, the SNR of image in Figure 4.22 has been calculated and is detailed in Table 4.2.

Table 4.2. SNR for simulated results presented in Figure 4.22.

Raw B-scan	12.20dB
SVM processed B-scan	43.57dB
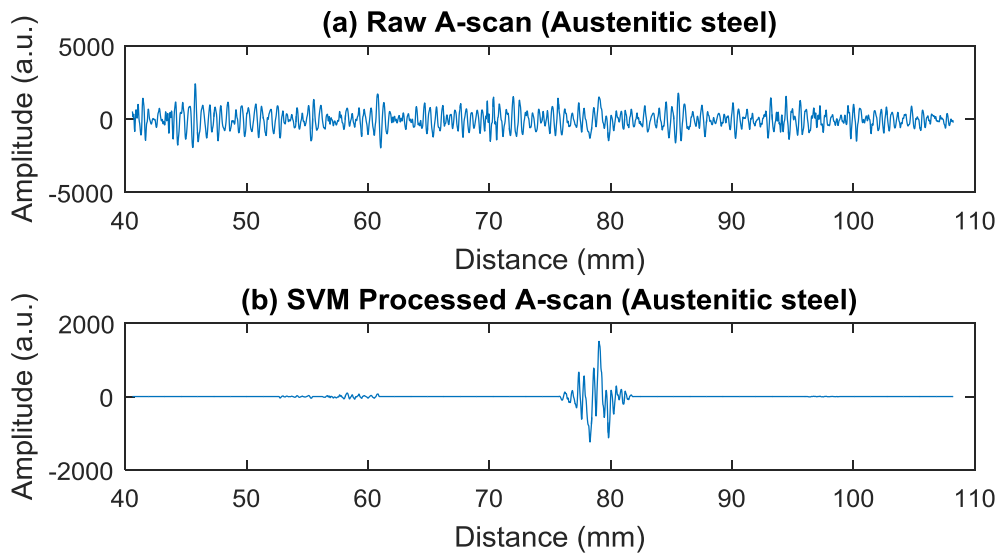
Figure 4.21. A-scans of austenitic steel sample. Data was acquired using 5MHz linear array. A back wall echo is located at 79mm.
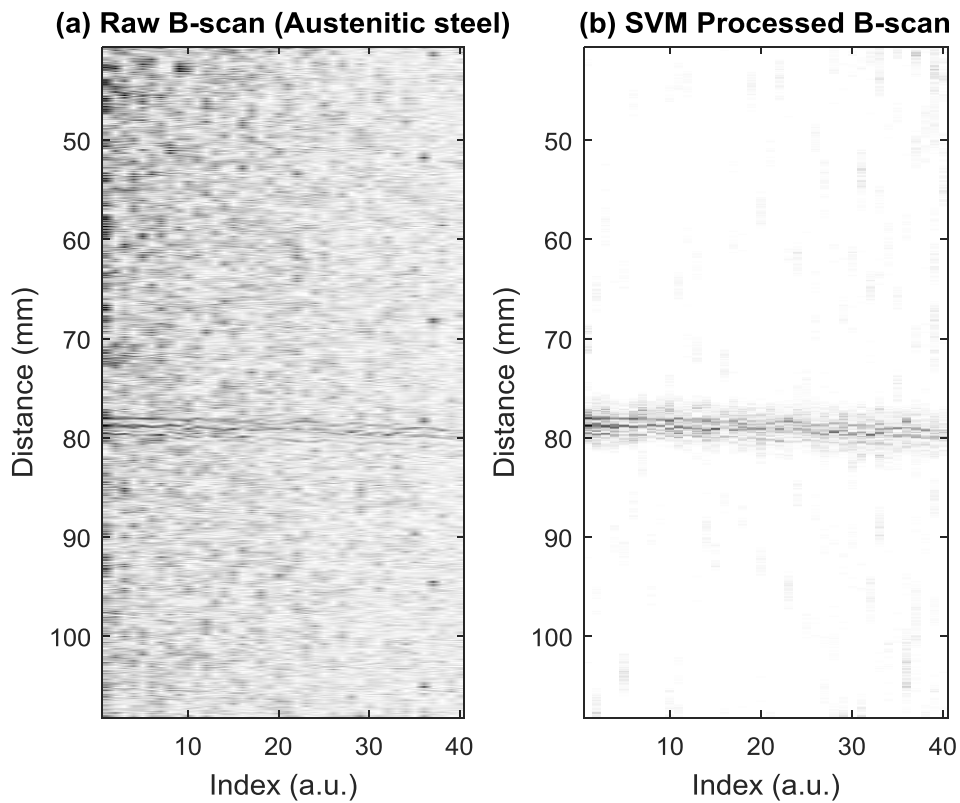
Figure 4.22. B-scan results of the austenitic steel sample, (a) Raw B-scan, (b) SVM processed B-scan. The feature extraction method used is STFT. Data was acquired using 5MHz linear array. Absolute values of signals is used for all images, darker colour represent higher amplitude. The line in the image is the backwall of the sample, at 79mm.

Inconel 617 Sample

Figure 4.23 presents the B-scan images obtained from the Inconel 617 sample, with the resultant SNR figures shown in Table 4.3. Again, the back wall is buried in strong grain noise in the raw B-scan and the processed image has been able to identify the back wall, albeit with some imaging artefacts remaining.
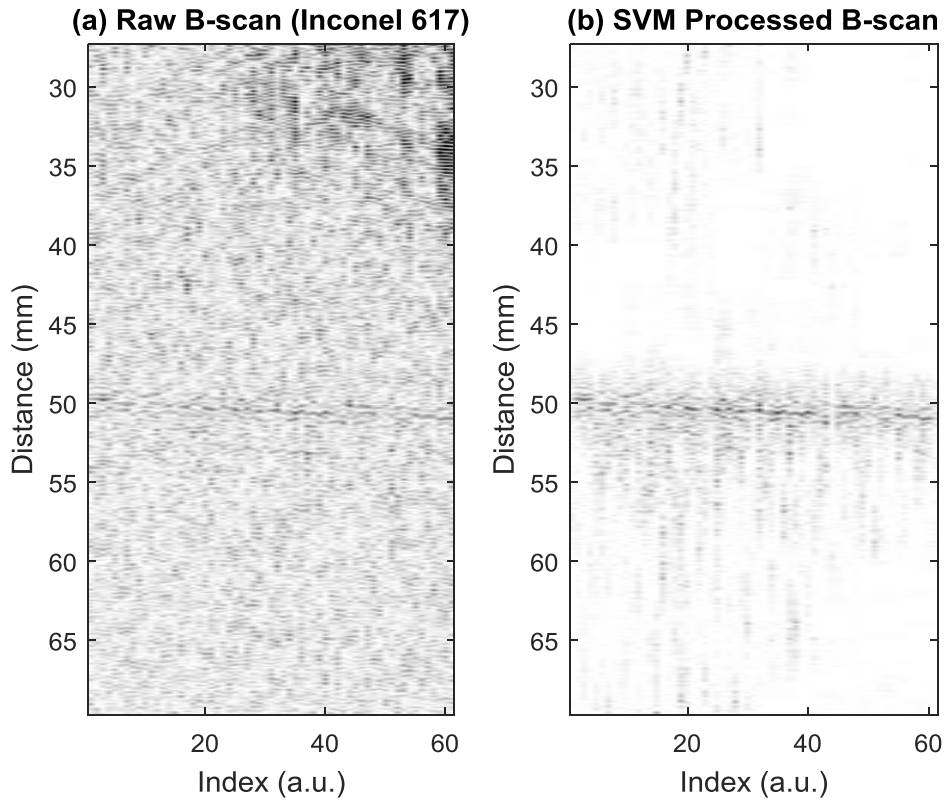
Figure 4.23. B-scan results of the Inconel 617 sample, (a) Raw B-scan, (b) SVM processed B-scan. The feature extraction method used in SVM is STFT. Data was acquired using 5MHz linear array. Absolute values of signals is used for both images, darker colour represent higher amplitude. The line in the images is the back wall of the sample, at 50mm.

Table 4.3. SNR for simulated results presented in Figure 4.23.

Raw B-scan	11.38dB
SVM processed B-scan	37.35dB

Inconel 625 Sample

Figure 4.24 presents the B-scan image from the Inconel 625 sample. The B-scan image comprises 140 individual A-scans which were acquired by placing the sample in a water tank, with a separation distance of 10cm to the transducer, with the spatial distance between each A-scan during the acquisition set at 10mm. The training data was selected from the location on the block corresponding to A-scan's with index 60-80, as shown in Figure 4.24. By applying the SRC algorithm, in addition to the back wall signal of A-scan 60-80 being enhanced, the second reflection of the back wall at 160mm is now also evident. Note that this sample has two different grain size in different regions, which complicates the post-processing as the returning echoes will have different spectra characteristics. Importantly, the proposed SRC has proved its robustness by successfully enhanced these signals. Table 4.4 details the calculated SNR for each of these images.
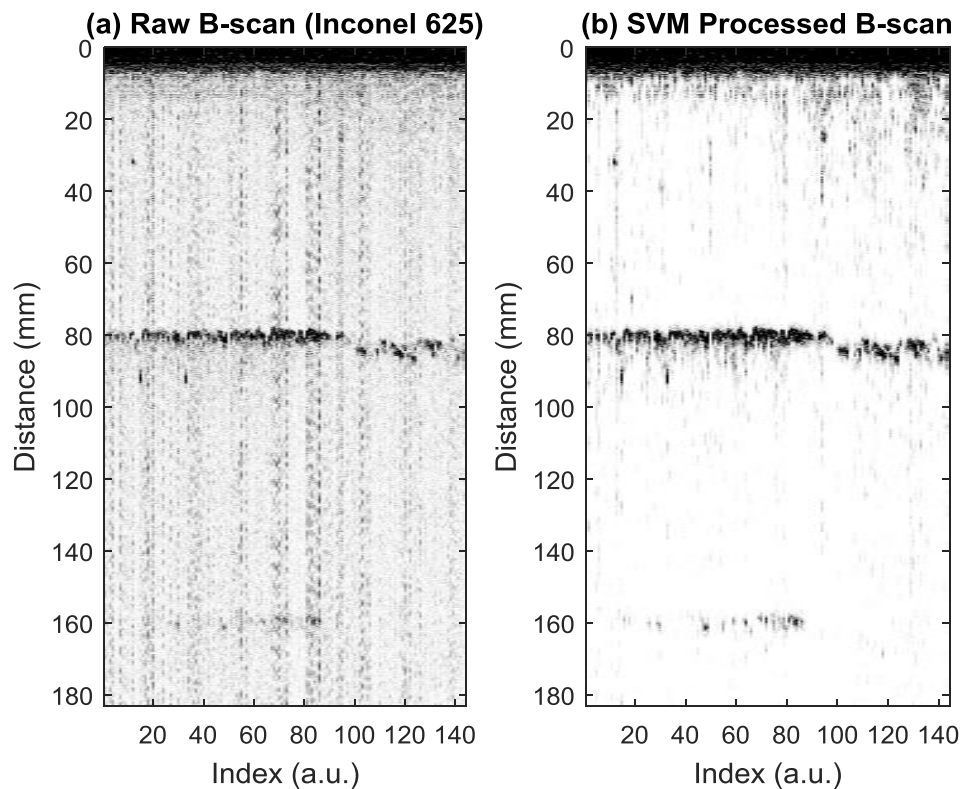
Figure 4.24. B-scan results of the Inconel 625 sample, (a) Raw B-scan, (b) SVM processed B-scan. The feature extraction method used in SVM is STFT. Data was acquired using 5MHz single transducer. Absolute values of signals is used for both images, darker colour represent higher amplitude. Back wall of the sample is at 80mm. The images also slightly shows the second reflection of the back wall at 160mm.

Table 4.4. SNR for simulated results presented in Figure 4.24.

| Raw B-scan	19.46dB
SVM processed B-scan	38.75dB

4.7 Summary

A new method for grain noise reduction using pattern recognition techniques for ultrasonic inspection in NDE has been presented. Segments have been classified using pattern recognition techniques based on the spectral difference between the legitimate reflectors and grain noise.

From the three classifiers evaluated in this work, Support Vector Machine (SVM) has been shown to be the best performer in most of the cases, since it can non-linearly separate the data in a higher dimensional space, without concern for the statistic behaviour of the training data. k-Nearest Neighbors (kNN) can be selected for use in cases that the spectra difference between training classes are close. Although the performance of Naive Bayes (NB) classifier is not distinctive, it can be used in cases where training data is lacking, but the statistical distribution of their spectral characteristics can be estimated. Generally, large training datasets should be used to obtain better performance. Even for the case where legitimate reflector training data is limited, a large number of noise training data should still be used, unless the kNN classifier is selected.

CWT offered the potential to improve the performance of the classifier algorithms since it has higher frequency resolution. However, the results show no improvement. The next Chapter will discuss the application of using CWT to enhance detectability.

The propagation distances of received echoes can also be treated as a feature, if the size of the legitimate reflector training dataset is large and covers a wide range.

Both simulation and experimental results were used to validate the proposed algorithm. Results have shown that the new method is effective for noise reduction

and is promising for legitimate reflector detection in the inspection of difficult materials.

Chapter 5

Advanced A-scan Based De-noising Techniques using Supervised Learning Part II: Artificial Neural Networks

Chapter 4 introduced three grain noise reduction algorithms using pattern recognition techniques: NB, kNN, and SVM. Based on the discussion in Section 4.3.4, the pattern features of ultrasound signals in different classes are generally separated non-linearly. Classifiers with non-linear decision hyperplane, therefore, have more accurate classification capability. With the develop of computer science, an interesting area has become more and more popular in machine learning and pattern recognition named Artificial Neural Network (ANN) [57]. ANNs are a family of models that are inspired by biological neural networks such as the brain. In the past decade, ANNs have achieved great success in many practical areas; it has been proved robust in many non-linear signal classification problems, due to their ability to generate arbitrarily complex decision boundaries [144].

There are examples of using ANNs in both NDE inspection and biomedical ultrasound. Polikar *et al.* [138] has shown the application of using ANN in automated signal classification systems for ultrasound weld inspection. Different types of ultrasound echoes that reflect from cracks, counterbores, and root welds are classified using Multilayer Perceptron (MLP) [57], based on their wavelet extracted feature vectors. A number of other classification issues are also described by Margrave [145] and Liu [146].

ANNs have also been applied to noise reduction and flaw detection techniques in ultrasound NDE. Sun *et al.* [123] proposed an advanced frequency diversity based technique combined with Adaptive Network-based Fuzzy Inference System (ANFIS)

[124]. The features of input signals were extracted using fuzzy logic and the output was calculated by an adaptive network. Pita *et al.* [147] proposed an algorithm to enhance flaw detection capability by using Radial Basis Function Network [148], while Liu [125] and Sun [122] have also demonstrated algorithms with implementations of MLP.

In this Chapter, applications using ANNs to improve the performance of ultrasound grain noise reduction and flaw detection algorithms will be introduced. MPL will be implemented to demonstrate the application of an ANN as the classifier in a Segment Recognition Classifier (SRC) algorithm, as described in Section 4.2. Moreover, an advanced wavelet based filtering technique will be combined with MLP and the concept of Deep Learning networks introduced for ultrasound noise reduction. Throughout the Chapter, a combination of simulation and experimental A-scan and B-scan images will be presented to illustrate the algorithm performance.

5.1 Overview of Artificial Neural Networks

ANNs are modelled using multiple neurons which are interconnected. A neuron is a node which contains a certain activation function. The connections between neurons are weighted, and the neurons can also be biased, acting as the 'memory' of the model. By adjusting the 'memory', i.e. the activation function, the weights and the biases, the ANN model can be treated as an algorithm or a function with a certain logic and can then adapt to a particular practical issue.

Neurons are the basic components of the ANN. Figure 5.1 shows the concept of a neuron. $\{a_1, a_2, \cdots, a_i\}$ are the elements of an input vector, $\{w_1, w_2, \cdots, w_i\}$ are the weights of each input elements, where i is number of elements, and b is the bias. The output of the neuron is,

$$x = f(\sum w_i a_i + b)$$

(5.1)

where f is the activation function of the neuron.
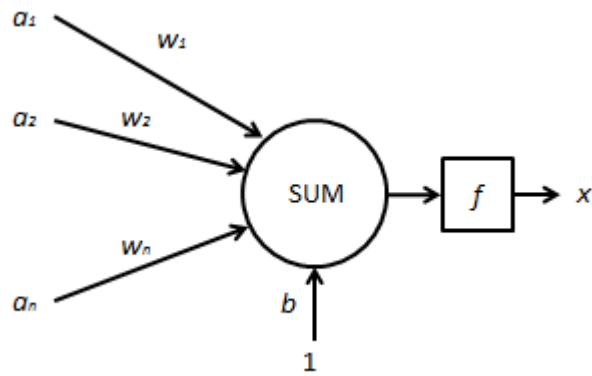
Figure 5.1. Concept diagram of a neuron in ANNs.

ANNs are constructed by several layers of neurons. Figure 5.2 illustrates the structure of a three layer feed-forward ANN, which includes one input layer, one hidden layer, and one output layer. Note that there can be more than one hidden layer in some multilayer ANNs. A feed-forward ANN is that the neurons in each layer can only communicate with the neurons in its previous or next layer, and there is no feedback between layers. The outputs of the neurons in the previous layers can be treated as inputs to the neurons in the next layers until the final output is generated [149, 150].
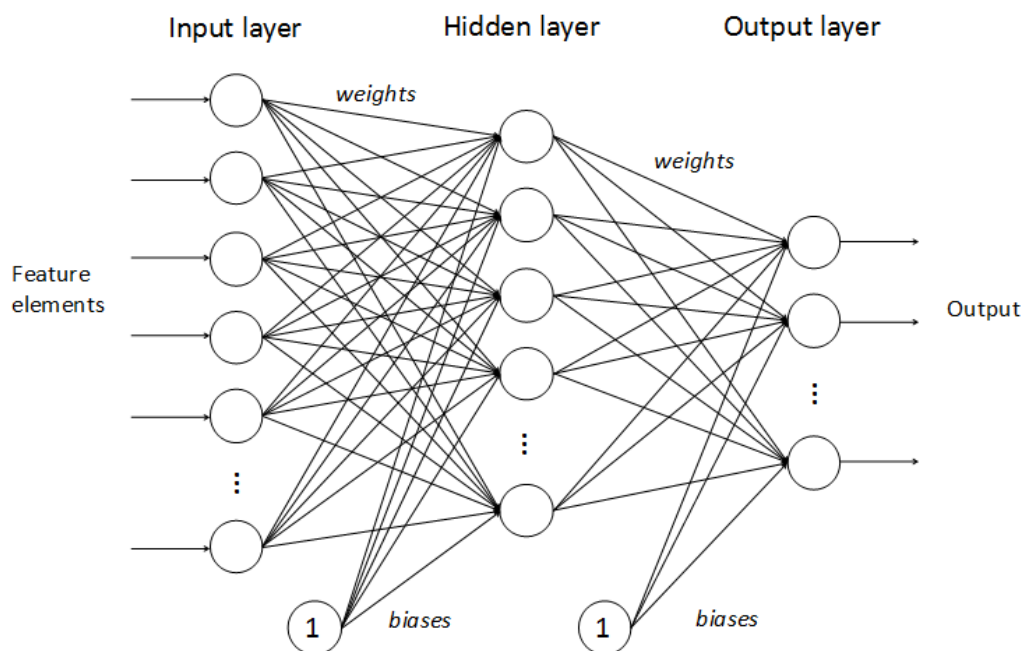
Figure 5.2. Example diagram of a three layer ANN.

The number of neurons in the input and output layers can be easily decided since they are equal to the number of elements in the input feature vector and the number of elements in the desired output. However, there are no specific rules to determine the number of neurons in the hidden layers. It has been reported that the hidden layer size should to be between 50% and 300% of the inputs size [151], with others suggesting an optimal number of hidden neurons is 75% of the number in the input layer [152]. However, neither of these are commonly accepted due to the insufficient theoretical foundation. Therefore, the number of neurons in the hidden layer is usually chosen empirically [153]. Generally, this number should not be too large as it can make the ANN too adaptive to a certain training dataset and should not be too small as the ANN model will not accurately learn the characteristic of the training data.

5.2   Multilayer Perceptron, an example of using ANN classifier
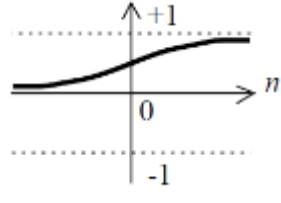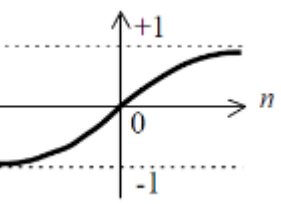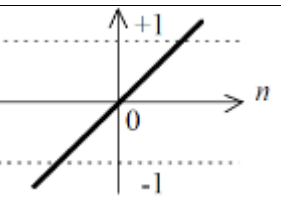
Multilayer perceptron (MLP) is a widely used, simple, yet powerful ANN model. In this Section, MLP has been selected as a demonstration of how ANNs are performed when used as a classifier for ultrasound grain noise reduction and flaw detection applications. Two different ways of extracting features are compared, using Short Time Fourier Transform (STFT) and Continues Wavelet Transform (CWT). MLP and Support Vector Machine (SVM) are compared in each case and also in different training scenarios.

5.2.1   Concept of Multilayer Perceptron

MLP has a typical feed-forward ANN structure as illustrated in Figure 5.2. After selecting an appropriate number of layers and neurons, the network assigns small random values to all weights and biases. The feed forward calculation will then be performed: for each input training vector, multiply its elements with the weights of each neuron in the first hidden layer; summation; and finally, substitute into the

activation function. Typically, log-sigmoid function, tan-sigmoid function, or linear function is chosen as the activation function of MLP, as shown in Table 5.1.

Table 5.1. Commonly used activation functions in ANNs [154].

Log-sigmoid function	$f(n) = \dfrac{1}{1 + e^{-n}}$	
Tan-sigmoid function	$f(n) = \dfrac{2}{1 + e^{-2n}} - 1$	
Linear function	$f(n) = n$	

In this work, the tan-sigmoid function is selected to be implemented and demonstrate the concept. When all neurons outputs in a layer are calculated, they are then used as the inputs to the next layer. This process is repeated until the final output is generated. The output of a neuron in each layer is,

$$x_j^{(l)} = f(\sum_i w_{ji}^{(l)} x_i^{(l-1)} + b_j^{(l)}) \tag{5.2}$$

where l is the index of layers, i is the index of neurons in the previous layer and j is the index of neurons in the current layer. Therefore, w_{ji} denotes the weight of the ith input element for the jth neuron in the current layer, i.e. the connection between the jth neuron in the current layer and the ith neuron in the previous layer.

Obviously, the output of the model, at this stage, is not likely to be the desired result, since all weights and bias parameters are randomly generated. The back propagation algorithm [155] is then used to minimize the error of outputs by adjusting the parameters (weights and biases) of the MLP. The back propagation algorithm applied here acts as a training procedure. It starts at the output layer by feeding the desired result into the network and proceeds back to the first hidden layer.

Let

$$s_j^{(l)} = \sum_i w_{ji}^{(l)} x_i^{(l-1)} + b_j^{(l)} \tag{5.3}$$

The training error of each layer is calculated by

$$\delta_j^{(l)} = [d_j - x_j^{(l)}] f'(s_j^{(l)}) \tag{5.4}$$

for the output layer, and

$$\delta_j^{(l)} = f'(s_j^{(l)}) \sum_k \delta_k^{(l+1)} w_{kj}^{(l+1)} \tag{5.5}$$

for the hidden layers, where δ is the error gradient, d is the desired final output, k is the index of neurons in the next layer. f' is the derivative of f.

After all δ are calculated, the weights and the biases are adjusted by

$$w_{ji}^{(l)}(new) = w_{ji}^{(l)}(current) + \mu \delta_j^{(l)} x_i^{(l-1)}$$
$$+ \eta \left[w_{ji}^{(l)}(current) - w_{ji}^{(l)}(old) \right] \tag{5.6}$$

and

$$b_{ji}^{(l)}(new) = b_{ji}^{(l)}(current) + \mu \delta_j^{(l)} + \eta [b_{ji}^{(l)}(current) - b_{ji}^{(l)}(old)] \tag{5.7}$$

The symbols μ and η are the learning rate and the momentum. Learning rate μ is a constant that decides the convergence rate of the back propagation algorithm. The value of μ must be small enough to ensure the convergence, but cannot be too small

or the convergence rate will be slow [140]. The aim of adding the momentum term is to smooth the oscillation and accelerate the convergence [156].

After all the training data has gone through the above steps, the mean square error (MSE) of the network is calculated by

$$MSE = \frac{1}{2Q} \sum_{1}^{Q} \sum_{j} (d_j - y_j)^2 \qquad (5.8)$$

where Q is the number of training samples, y is the calculated output of the network. The training stops when the MSE value becomes lower than the pre-set threshold or the maximum number of allowable iterations (epoch) is met. Otherwise, it is necessary to repeat Equations (5.2) through to (5.7) until these conditions are satisfied.

5.2.2 Combining with Short Time Fourier Transform

The procedure of using MLP as a classifier to achieve noise reduction for an ultrasound A-scan signal acquired from a difficult material sample is similar to the algorithms described in Chapter 4. One method is to partner MLP with STFT, which is similar to the approach described in Section 4.3.

Segmental signals are first extracted from the pre-acquired A-scan data as the training data and labelled into two groups: a segmented group which contains only grain noise; and the other group which contains legitimate reflectors.

The feature vector of a segmental signal is assembled using discrete points that are extracted from the normalized Fourier spectrum equidistantly. Again, in alignment with the example shown in Section 4.3, 8 points are extracted from 1MHz to 9MHz equidistantly to form an input feature vector, for the data acquired from the austenitic steel sample using the 5MHz array.

The number of nodes in the input layer is equal to the number of elements in the feature vector, which is 8 in this case. A three layer MLP is chosen, and the neurons number in the hidden layer is selected at 10 empirically. An output layer with 2

neurons is used. If the input presents a legitimate reflector, the desired output is {1,0}, and if the input is pure grain noise, the desired output is {0,1}, respectively.

Raw signals can then be input to the algorithm for noise reduction and defect detection after the network is trained. For each time instant t in a raw signal, extract a segment from $(t - L/2)$ to $(t + L/2)$, where L is the length of the segment. For each segment of length, L, apply the STFT and use the extracted feature vector in the frequency domain as the input to the network. The output of the algorithm should be a binary value: 1 denotes a legitimate reflector is present at the given time instant t; and 0 denotes only noise is present. This can be done by comparing the values of the two neurons in the output layer, if the value of the first neuron is larger, then output 1, otherwise output 0.

A binary trace is generated after all time instants in the A-scan have been classified. This binary trace implies the positions where the legitimate reflectors may appear in the raw signal. However, this binary trace is too dictatorial for saying a segment in the raw A-scan belongs to a legitimate reflector or noise hence a smoothed version is designed by averaging the classification result of all the segments that covers a certain time instant, as described in Section 4.2.4.

An example classification result using MLP is shown in the histogram in Figure 5.3, along with the classification result using SVM, as a comparison. The input data was acquired experimentally from the austenitic steel sample using 5MHz array, as described in Section 2.6. From the histogram in Figure 5.3, it can be seen that the performance of MLP is similar to SVM. The True Negative Rate (TNR) which indicates the percentage rate of how many desired grain noise segments have been correctly detected, is 98.3% for both MLP and SVM. The True Positive Rate (TPR) which indicates the percentage rate of how many desired legitimate reflector segments have been correctly detected, is 100% for MLP and 98.3% for SVM. The overall *Accuracy* (percentage rate of how many input segments have been classified into the correct class) of MLP is 99.1% which is slightly higher than SVM (98.3%).

The performances of MLP with STFT under different conditions are analysed and shown in Fig 5.4. 2000 A-scans are simulated for each analysis, using the high

dispersion model (HDM), described in Section 3.2.1. Each A-scan contains a legitimate reflector. The centre frequency is chosen at 5 MHz with 50% transducer bandwidth at -6dB. And the sampling frequency is set at 100 MHz. The attenuation factor α is chosen at 10^{-29}, and the defect amplitude factor is 1.5. Unless otherwise specified, all simulated signals in this Chapter use the above configuration. As stated in Section 4.3.1, there are some cases where $\alpha = 10^{-30}$, this has been selected to produce closely matched spectra between the legitimate reflector and noise; hence ensuring a more challenging processing scenario for the algorithm.

Figure 5.4 shows the TPR, TNR, and *Accuracy* of the classification results of MLP using training data with different legitimate reflectors. Three different cases here, simulate the situation that training data and test data are acquired from various propagation distances, as described in Section 4.3.6. All training data of legitimate reflectors in case 1 are collected at 75 mm, and at a distance of 125 mm in case 2. The training data for a legitimate reflector in case 3 is randomly distributed between 75 mm and 125 mm. The training data of the grain noise for all the three cases are randomly selected since the noise signal from different locations is easier to acquire in practice. The test data for all three groups contains both legitimate reflectors and noise signals and are extracted randomly between 75 mm and 125 mm. The classification results of SVM using the same data are also given in Figure 5.4, as a comparison.

Like the classifiers introduced in Chapter 4, the performance of MLP is optimised when the training data covers segments with a range of different characteristics. It can be seen that the *Accuracy* of MLP in case 3 has the highest percentage rate at 92.4% among all the three cases. Although not optimised, the *Accuracy* of MLP in case 1 and case 2 are still promising which implies that the MLP is capable of identifying legitimate reflectors even when the knowledge of the pre-acquired training data is inconsistent with the reflector data.

From Figure 5.4, it can also be seen that the performance of MLP and SVM is similar; noting that SVM is considered superior to Naive Bayes (NB) and k-Nearest Neighbors (kNN). Figure 5.5 to Figure 5.9 explore the performance of MLP and compares the MLP algorithm with other classifiers for reference.
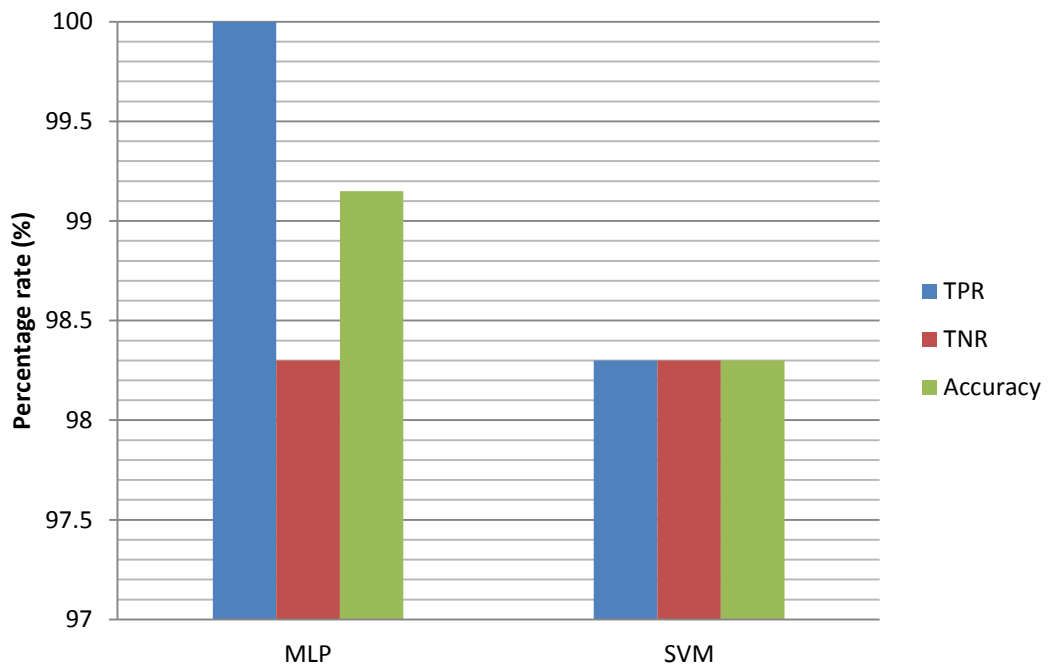
Figure 5.3. TPR, TNR, and *Accuracy* of the classification results using MLP and SVM for the austenitic steel sample. The legitimate reflectors are back wall echoes at 79mm; the grain noise segments are extracted randomly.

Figure 5.5 illustrates a trend diagram of the *Accuracy* of MLP and SVM when the size of the training set is changing. The size of the training set for both classes is increasing from 10 to 1000. It can be seen that the *Accuracy* of both classifiers is growing with the size of the training set since usually large training sets provides more knowledge of the data. The performance of MLP is comparable to SVM when the training set is large. However, when the size of the training set is small, especially when under around 70, the performance of MLP becomes unstable. This is because the parameters of MLP are initialised randomly; if the training is insufficient, then the performance of the trained network will be variable. The insufficiently trained network is underfitted and it is not able to capture the differences between classes accurately.
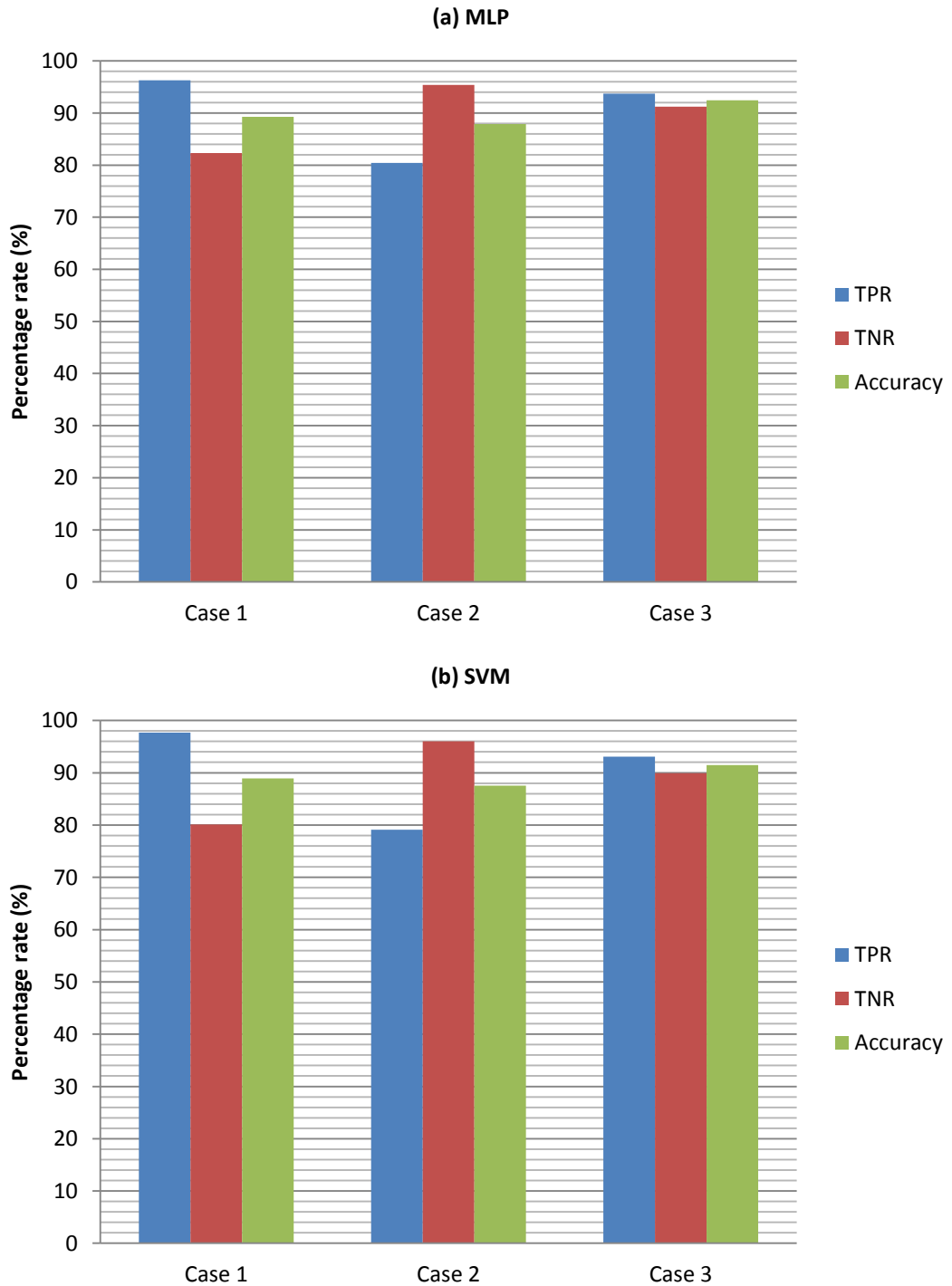
Figure 5.4. TPR, TNR, and *Accuracy* of (a) MLP and (b) SVM classification results for 2000 simulated A-scans, with legitimate reflector training data collected at different distances. All legitimate reflectors in case 1 are at 75 mm, all legitimate reflectors in case 2 are at 125 mm, and the legitimate reflector in case 3 are randomly distributed between 75 mm and 125 mm. Grain noise training data are collected uniformly between 75 mm and 125 mm for all the three cases. The test data for all three groups are extracted randomly between 75 mm and 125 mm. The data is simulated using the high dispersive model with $\alpha = e^{-29}$, $s = 1.5$, 5MHz centre frequency.

147

Figure 5.5. *Accuracy* of MLP and SVM when the size of the training set is changing. The number of observations in both classes is equal, and is increasing from 10 to 1000. The data is simulated using the high dispersive model with $\alpha = e^{-29}$, $s = 1.5$, 5MHz centre frequency.

Figure 5.6 and Figure 5.7 show the effect of unequal size of the two classes in the training set to the MLP algorithm performance. In Figure 5.6 the size of the grain noise training set is about 20% larger than the legitimate reflector training set. Like the previous results shown in Figure 5.5, the performances of MLP and SVM are similar, although MLP is not stable when the size of the training set is small.

Figure 5.6. *Accuracy* of MLP and SVM when the sizes of the two classes in the training set are unequal. The number of observations in the grain noise class is 20% larger than the legitimate reflector classes. The size of the reflector training set is increasing from 10 to 1000. The data is simulated using the high dispersive model with $\alpha = e^{-29}$, $s = 1.5$, 5MHz centre frequency.

Figure 5.7 shows the TPR, TNR, and *Accuracy* of MLP and SVM using simulated data. Here, the size of legitimate reflector training set has been varied between 10 to 1000 and the size of grain noise training set fixed at 1000, to replicate the fact that the grain noise training data is much easier to collect in practice. It can be observed

from Figure 5.7 that the performance of MLP is poor when the size of the legitimate reflector training set is small, although the two classifiers have similar performance when the size of the reflector training set is large. As can be seen in Figure 5.7(c), the *Accuracy* of MLP is low especially when the size of the reflector training set is lower than 100. Comparing Figure 5.7(a) and Figure 5.7(b), the TPR is at a significantly low level while TNR is nearly 100%. These indicate that the MLP network cannot capture the characteristic of the legitimate reflector as the training data is significantly weighted towards grain noise.

Figure 5.8 shows the situation when the training set contains errors. The grain noise training set is unaffected while a certain proportion of grain noise data has been mixed into the legitimate reflector training set. At most, 50% of the training data for the legitimate reflector has been replaced by noise. The MLP used in Figure 5.8(a) has 50 neurons in its hidden layer as described in Figure 5.2. From Figure 5.8(a) it can be seen that the *Accuracy* of MLP and SVM are close when the error in the training set is small. However, the *Accuracy* of MLP decreases when the proportion of the grain noise observed in the reflector group increases. Both classifiers were trained by using 1000 training data per group. MLP has strong nonlinearity, hence it reduces its generalization capability, especially when the size of the network is large. If the training set contains errors, the strong nonlinearity may cause the network to adapt to the noise and not generalize. The MLP used in Figure 5.8(b) has 10 neurons in its hidden layer. Compared with Figure 5.8(a), the *Accuracy* of MLP is slightly increased when the proportion of mixed grain noise is high since it has a smaller network size. However, the performance of SVM is still superior.

Usually, the nonlinearity of the network can benefit the classification process when the training set strongly represents the test set. However, strong nonlinearity along with an inaccurate training set data will lead the network start to learn the potential characteristic differences between the sub-groups of noise, hence, it will generate poor prediction results when classifying new data. Additionally, strong nonlinearity may cause the network to adapt to the training set, which is usually referred to as an overfitting problem.
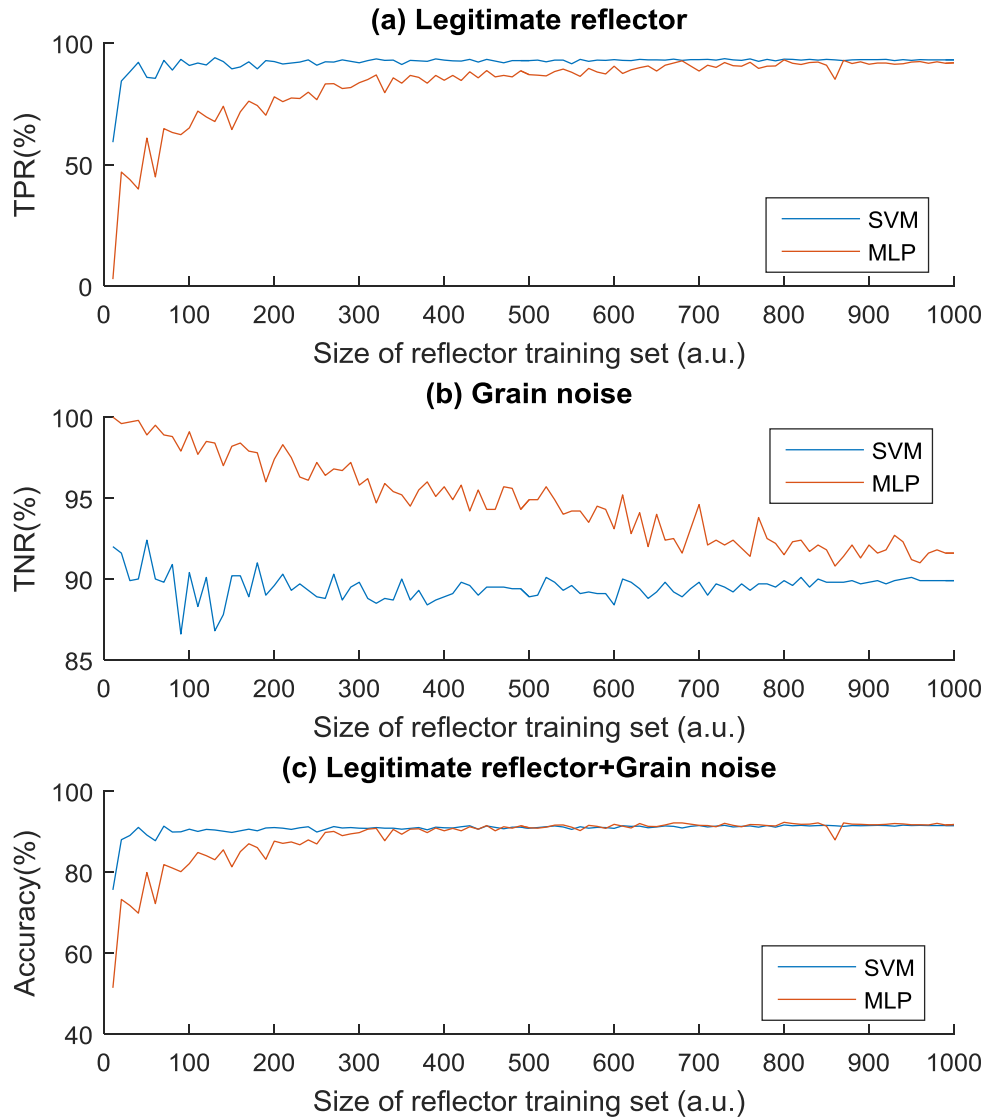
Figure 5.7. TPR, TNR, and *Accuracy* of MLP and SVM when the sizes of the two classes in the training set are unequal. The number of observations in the grain noise class is fixed at 1000 while the number of observations in the legitimate reflector classes is changing from 10 to 1000. The data is simulated using the high dispersive model with $\alpha = e^{-29}$, $s = 1.5$, 5MHz centre frequency.

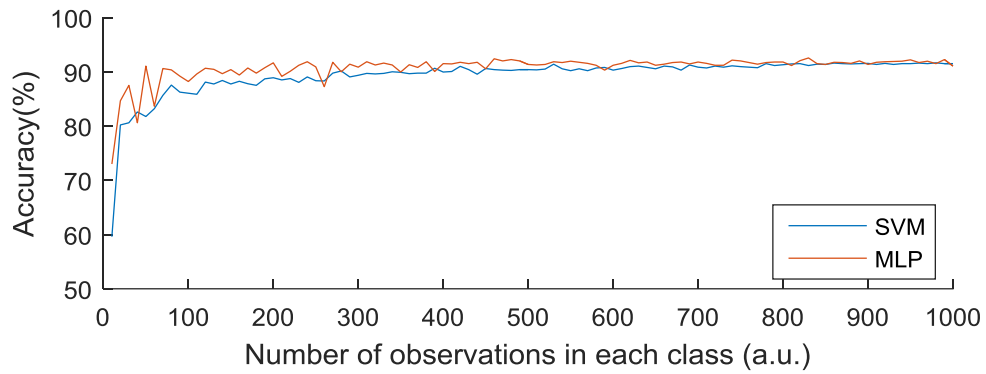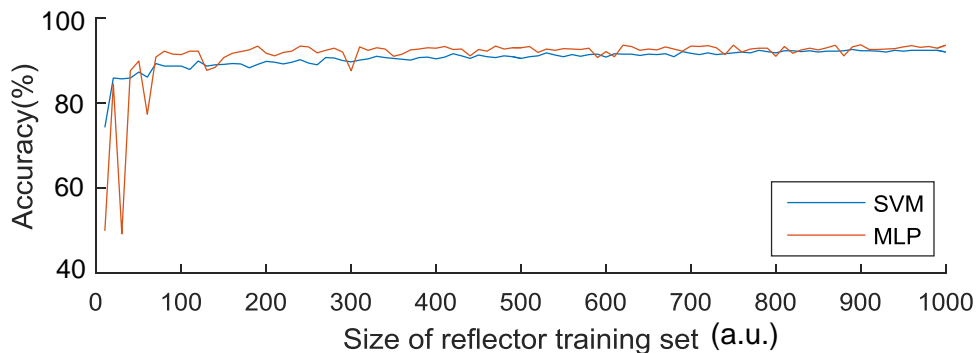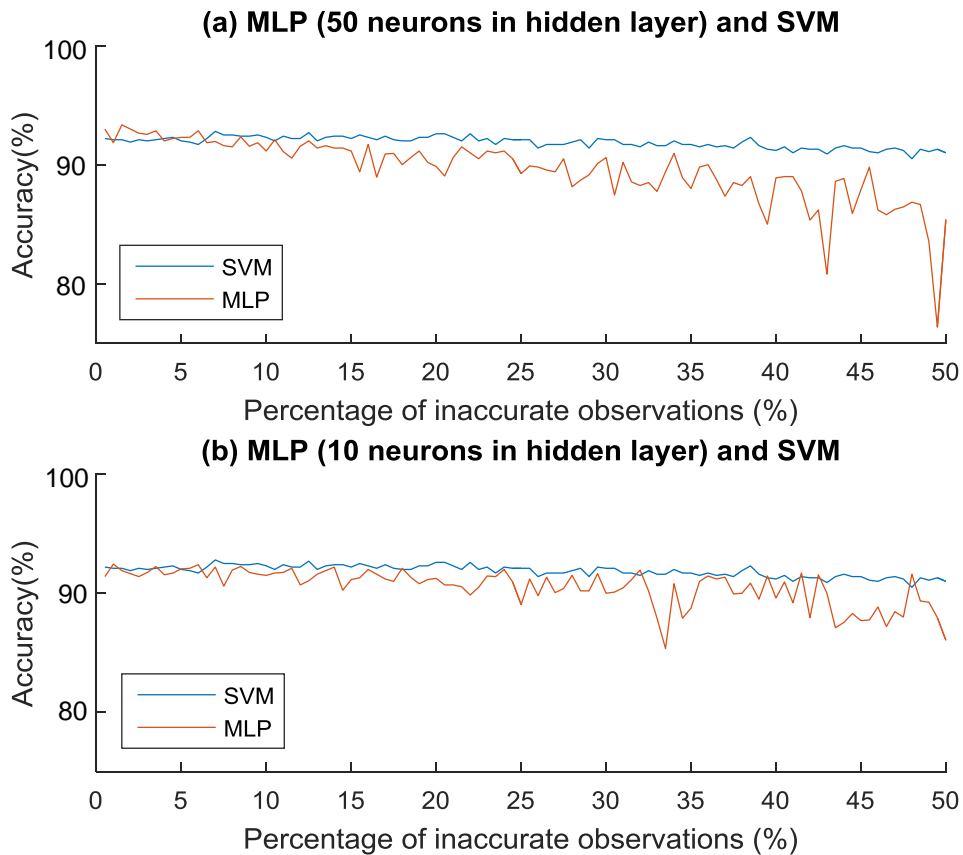Figure 5.8. *Accuracy* of MLP and SVM when the legitimate reflector training set is mixed with a certain proportion of grain noise. (a) MLP has 50 neurons in the hidden layer, and (b) MLP has 10 neurons in the hidden layer. The data is simulated using the high dispersive model with $\alpha = e^{-29}$, $s = 1.5$, 5MHz centre frequency.

Overfitting occurs when the number of free parameters in the network is excessive (e.g. the neuron number of hidden layers is large), the training set is too large or the training set cannot represent the test data precisely. If the training set cannot represent the test set precisely, like the examples presented in Figure 5.8, or sometimes it is only a subset of the required training set and cannot teach the network all the characteristics of the test set, then the network will have a poor generalization. In this case, an overfitted network can accurately classify an input observation from the training set, but the probability of correctly classifying an input observation from other data sets may be low.

Similarly to Section 4.3.10, the performance of MLP in the case where the spectrum characteristics of the legitimate reflector and grain noise are similar, and cannot be easily distinguished by STFT, have been analysed and presented in Figure 5.9. Again the simulation parameter settings are $\alpha = e^{-30}$, $s = 1.5$, 5MHz centre frequency. The results of SVM and kNN are also given as comparisons. It can be seen that the *Accuracy* of MLP is slightly higher than SVM, but lower than kNN ,which was also the best classifier in the earlier work presented in Section 4.3.10.
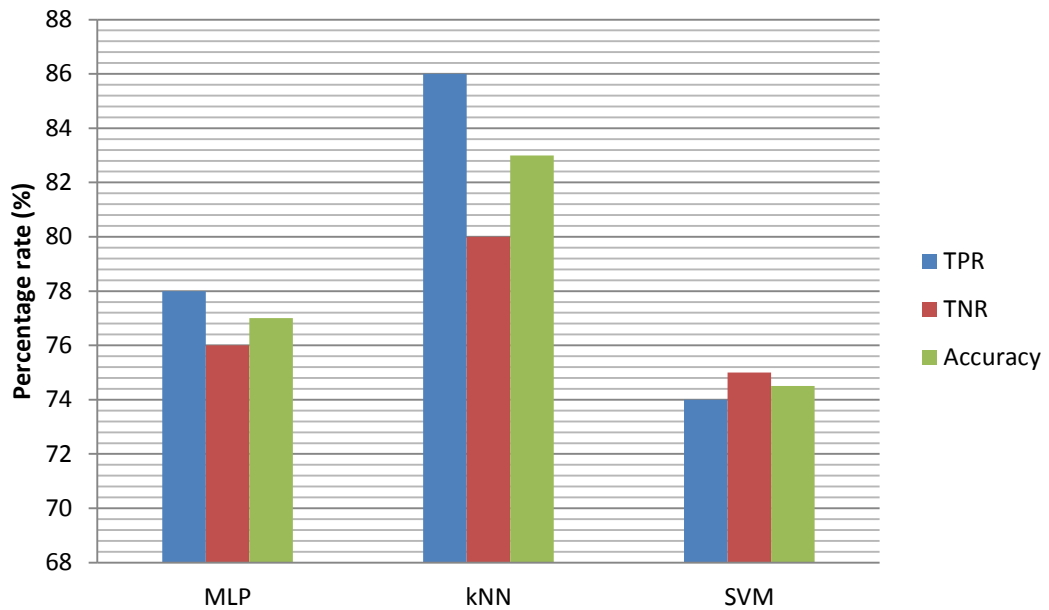
Figure 5.9. TPR, TNR, and *Accuracy* of an example classification results using MLP, kNN, and SVM when the spectrum characteristics of legitimate reflector and noise are close. The data is simulated using the high dispersive model with $\alpha = e^{-30}$, $s = 1.5$, 5MHz centre frequency.

5.2.3 Combining with Continuous Wavelet Transform

Another way to extract features is to apply the Continuous Wavelet Transform (CWT), as described in Section 4.4. This option is considered as CWT offers a better time-frequency resolution and ability to distinguish more detailed differences between legitimate reflectors and grain noise, compared to STFT. However, the classification results using CWT as the feature extraction method is not always as

promising as expected, as discussed in Section 4.4, due to the envelopes of the transformed 2-D signals losing detail compared with the raw transformed 2-D signals.

The combination of SVM and CWT demonstrates better performance compared with NB and kNN, yet its *Accuracy* is still lower than kNN with STFT when the spectrum characteristics of reflector and noise are similar. Figure 5.10 shows the classification result of MLP with the same conditions. The dataset is simulated by high dispersive model (HDM) using $\alpha = e^{-30}$, $s = 1.5$, 5MHz centre frequency, as applied in Section 4.4 and in Figure 5.9.

CWT is initially applied to each raw A-scan to generate the 2-D time-frequency signal. The mother wavelet used in this work is the Morlet wavelet, and 64 scales are chosen linearly from 10 to 55. Hilbert transform is then applied to each scale of the transformed signal, and the absolute value is taken to smooth the oscillation between peaks. For each time instant, all scales are extracted and formed as the feature vector. In this case, 64 scales are calculated; therefore, the input layer of the MLP has 64 neurons. A three layer MLP is selected here, and 100 neurons are used in its hidden layer, as determined empirically. The output layer contains two neurons, {1,0} as the legitimate reflector and {0,1} as the grain noise. The final output of the algorithm is binary and depends on which of the two neurons is larger: '1' if the first neuron is greater; otherwise '0'.

Figure 5.10 gives the results of the combination of MLP and CWT, together with the combination of SVM and CWT, and the combination of kNN and STFT as the base comparison. The training set for all the three cases is identical. It can be seen that though the *Accuracy* of MLP with CWT is higher than SVM with CWT, its *Accuracy* is still slightly lower than kNN with STFT. The same reasoning holds that the envelope generated by the Hilbert Transform has removed key details of the CWT transformed signal.

As described in Section 4.4, modulus and envelopes were added when extracting the feature vectors to reduce the nonlinearity, since otherwise the data is too complex. One benefits of MLP is its strong nonlinearity performance, especially when the size of the network is large. Figure 5.11 shows the classification results of the MLP –

153

CWT combination when using the feature vector directly into the network without applying the Hilbert Transform or taking the modulus. The results of kNN – STFT combination and SVM – CWT are also given as a comparison. Again, the HDM is used to simulate the data, using $\alpha = e^{-30}$, $s = 1.5$, 5MHz centre frequency. Without the restriction of the envelopes and the modulus, more details of the feature vectors have been acquired by the network. It can be seen in Figure 5.11 that the TPR, TNR, and *Accuracy* of the MLP – CWT combination are close to that of the Knn – STFT combination, with only 1.2%, 0.5%, and 0.3% differences, respectively.
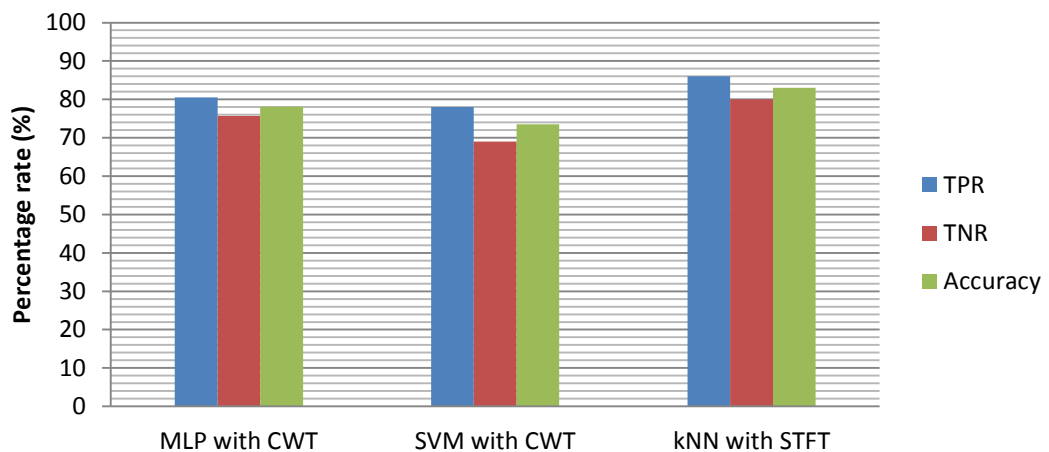
Figure 5.10. TPR, TNR, and *Accuracy* to compare the performance of MLP with CWT, SVM with CWT, and kNN with STFT, with simlar spectrum characteristics for legitimate reflector and noise. Data is simulated using the high dispersive model with $\alpha = e^{-30}$, $s = 1.5$, 5MHz centre frequency.
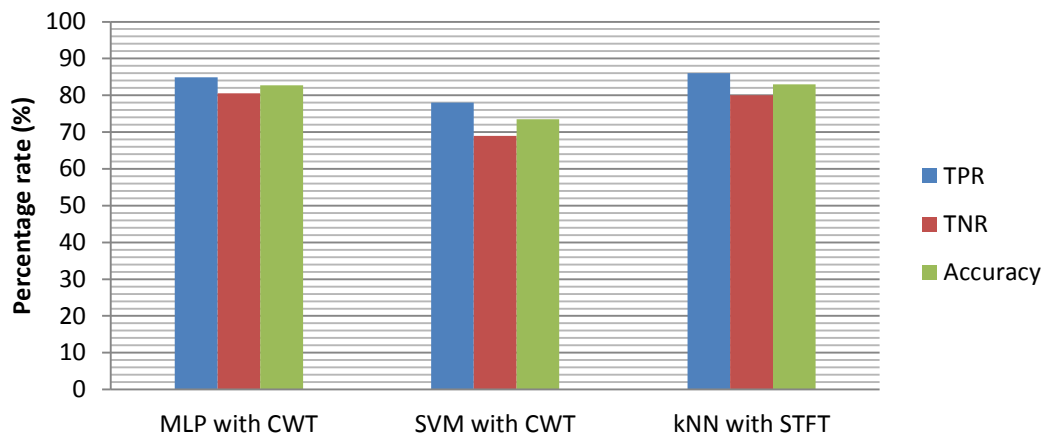
Figure 5.11. TPR, TNR, and *Accuracy* to compare the performance of MLP with CWT, SVM with CWT, and kNN with STFT, with simlar spectrum characteristics for legitimate reflector and noise. The feature vectors used in MLP are the original values, without been enveloped. Data is simulated using the high dispersive model with $\alpha = e^{-30}$, $s = 1.5$, 5MHz centre frequency.

Although the strong nonlinearity of MLP has benefited the classification result, it may also lead the network to be overfitted to a particular training set and hence can have a poor generalization. As a result, MLP is good for the case when the training set and the test set have similar characteristics, but not suitable to be used to classify when those characteristics vary significantly.

5.3 Wavelet based filtering de-noising algorithm pruning by Artificial Neural Network

The initial motivation for applying the continuous wavelet transform (CWT) as the feature extraction method is to use the advantage of its higher time-frequency resolution, to obtain more detailed differences between the legitimate reflector and the grain noise. However, as discussed in Section 4.4 and Section 5.2.3, using CWT as the feature extraction method does not improve the classification results, unless the training set is perfectly selected. CWT has also been shown to offer a generally worse performance than using STFT with kNN when the spectrum differences of the legitimate reflectors and the grain noise are close, although the CWT – MLP combination performed well. Moreover, for the purpose of extracting more details, a larger number of scales are used in CWT to assemble a feature vector compared with STFT, which takes more computational power.

The Wavelet Transform has already been widely used as a filtering technique for ultrasound signal noise reduction [22, 66, 120, 121, 157], in addition to also being used as a feature extraction method. In general, these filtering techniques can be summarised as follows:

- Filtering the raw A-scan input signal into a series of channels (usually referred as coefficients) with different 'pseudo-frequencies' (e.g. with different scales for the case of CWT).
- Processing these channels using pruning (only retain a set of particular channels that most likely contains a legitimate reflector) and/or thresholding

(all channels whose modulus is smaller than the pre-defined threshold are discarded).

- Reconstructing the output signal using the pruned/thresholded channels by the inverse wavelet transform.

The purpose of the pruning and thresholding is to eliminate or suppress channels that have little contribution to the legitimate reflectors. Many rules have been suggested for the method of pruning/thresholding [66, 158-160]. However, most of the rules only involve the acquisition configuration parameters, like the centre frequency and bandwidth of the transducer; few have considered the information of the energy distribution of the legitimate reflectors and the grain noise, or only have used it empirically.

An advanced method of pruning/thresholding rule is proposed in this work, using the pre-acquired training set to locate the wavelet coefficients with larger contributions to the legitimate reflectors accurately. On the other hand, this can be treated as a feature reduction issue of choosing the most effective features among all feature elements. In ANNs, this can be achieved by evaluating the weights that connect each neuron. Generally, a larger weight denotes that the connection is highly activated, and the connected neurons have more contribution to the classification. Therefore, let's take the MLP as an example, the proposed method can be achieved by the following steps:

- Filtering the raw A-scan signal that contains the training set into a series of coefficients $W_{co}(i,t)$ with different 'pseudo-frequencies', where i is the index of scales, t is the time instant.
- Selecting coefficients from certain time instants to assemble the training set, then train the network. Each coefficient trace is related to an input neuron.
- For each input neuron i, calculate the average value of all weight moduli that connect to it, noted as S_i.
- Record the value of the *(N+1)th* largest S_i as Sp. *N* scales will be selected by pruning the wavelet coefficients using:

$$W_{cp}(i, t) = \begin{cases} 0; & for\ S_i \leq Sp \\ W_{co}(i, t) * (S_i - Sp); & for\ S_i > Sp \end{cases} \qquad (5.9)$$

- Setting a threshold level T. T should be a fractional number between 0 to 1. Thresholding the pruned coefficients by:

$$W_{ct}(i, t) = \begin{cases} 0; & for\ |W_{cp}(i, t)| \leq T * |W_{cp}(i, t)| \\ W_{cp}(i, t) - T * W_{cp}(i, t); & \\ & for\ |W_{cp}(i, t)| > T * |W_{cp}(i, t)| \end{cases} \qquad (5.10)$$

- Reconstructing the output result using the processed wavelet coefficients $W_{ct}(i, t)$ using the inverse wavelet transform.

Different from the de-noising techniques that use classification, using ANNs to prune/threshold the wavelet coefficient is an easier and faster algorithm since the network is only involved once for the pruning/thresholding step and is then no longer required for the calculation of each time instant in the output signal. It is suitable for the case that no significant spectrum characteristic distortion has been observed in the dataset (e.g. no strong frequency dependent attenuation or highly inhomogeneous material property). Further discussion and results will be given in Section 5.5.

5.4   Automatic feature extraction using the stacked autoencoders

Automatically extract features from ultrasound segmental signals using a Deep Learning network is discussed in this Section.

Based on the analysis from the above sections, the MLP approach has no significant advantage compared with other classifiers when the network only has three layers. Raising the numbers of layers may enhance the performance, but it will increase the complexity of training, and can easily cause overfitting.

Another reason that may potentially limit the algorithm performance is the selection of features. Feature extraction is an important part of machine learning, as a precise and efficient representation of the pattern is essential for the accuracy of classification. In practice, this is usually done manually based on pre-acquired

knowledge and expertise. Whether appropriate features can be extracted or not mainly depends on experience. For example, the centre frequency and the bandwidth of the transducer are required to help to decide the extraction range for using both STFT and CWT; and the scales number of CWT is selected empirically. It is therefore considered that an automatic feature extraction method could potentially benefit the classification process.

5.4.1 Background of Deep Learning

In recent years, a field of research named Deep Learning has become popular and been widely used. Deep Learning can be treated as an extension of traditional ANNs. It is part of a broader family of machine learning methods based on learning representations of data [161] and was inspired by the mechanism of the brain. By studying the brains of cats, Hubel *et al*. [162] has discovered that the processing of visual signals in the brain is a series of abstraction and iteration. In other words, the information processing of the visual system is layered. Started from the lowest layer (pixels) the features of images are extracted step by step. The more abstract the feature is, the easier it can be classified by the brain.

Like the visual system of the brain, the Deep Learning technique creates features using a layered approach. Let's assume a Deep Learning system has a cascade of layers and by adjusting the parameters in each layer to make the output of the system equal to the input (i.e. the ideal scenario), then the output of each layer can be treated as a series of different features of the input, where each feature is an alternative expression of the original information. The main idea of Deep Learning is to use a cascade of many layers of nonlinear processing units for automatic feature extraction and transformation, where each successive layer uses the output from the previous layer as input.

Compared with traditional shallow learning like SVM and the three layer MLP, which have been introduced in this work, Hinton *et al.* [163] has highlighted that networks with many layers have extraordinary learning ability. The features created by these networks are a more natural representation of the original information and are more beneficial for visualisation or classification. To overcome the difficulty of

training for multilayer networks, the Deep Learning approach uses a layer-wise pre-training mechanism which is very different when compared to the traditional training methods.

5.4.2 Principle of stacked autoencoders

Stacked autoencoders (SAE) is a network that is targeted for learning efficient coding [164] and is a simple model in terms of Deep Learning. The function of an autoencoder is to learn a representation of a dataset. Typically the autoencoder is used for the dimensionality reduction. SAE contains a cascade of autoencoders and the principle of the approach is now described.

    i.   *Unsupervised learning of the autoencoder.*

Feed the data in the training set into a three layer network without supplying the accompanying input labels. Set the number of neurons in the output layer equal to those in the input layer, and assume the number of neurons in the hidden layer is less than those in the input layer, as illustrated in Figure 5.12. The situations when the number of neurons in the hidden layer is larger than the input layer (sparse autoencoder [165]) will not be discussed in this work. Train the network using the back propagation algorithm methodology, to make the outputs and the inputs as equal as possible. Since the number of neurons in the hidden layer is less than the input layer, it forces the network to compress the input data and abstract the hidden structure inside. The values of the neurons in the hidden layer can be seen as an abstracted feature of the raw data. The hidden layer in the network can be considered as the encoder, and the output layer as the decoder.
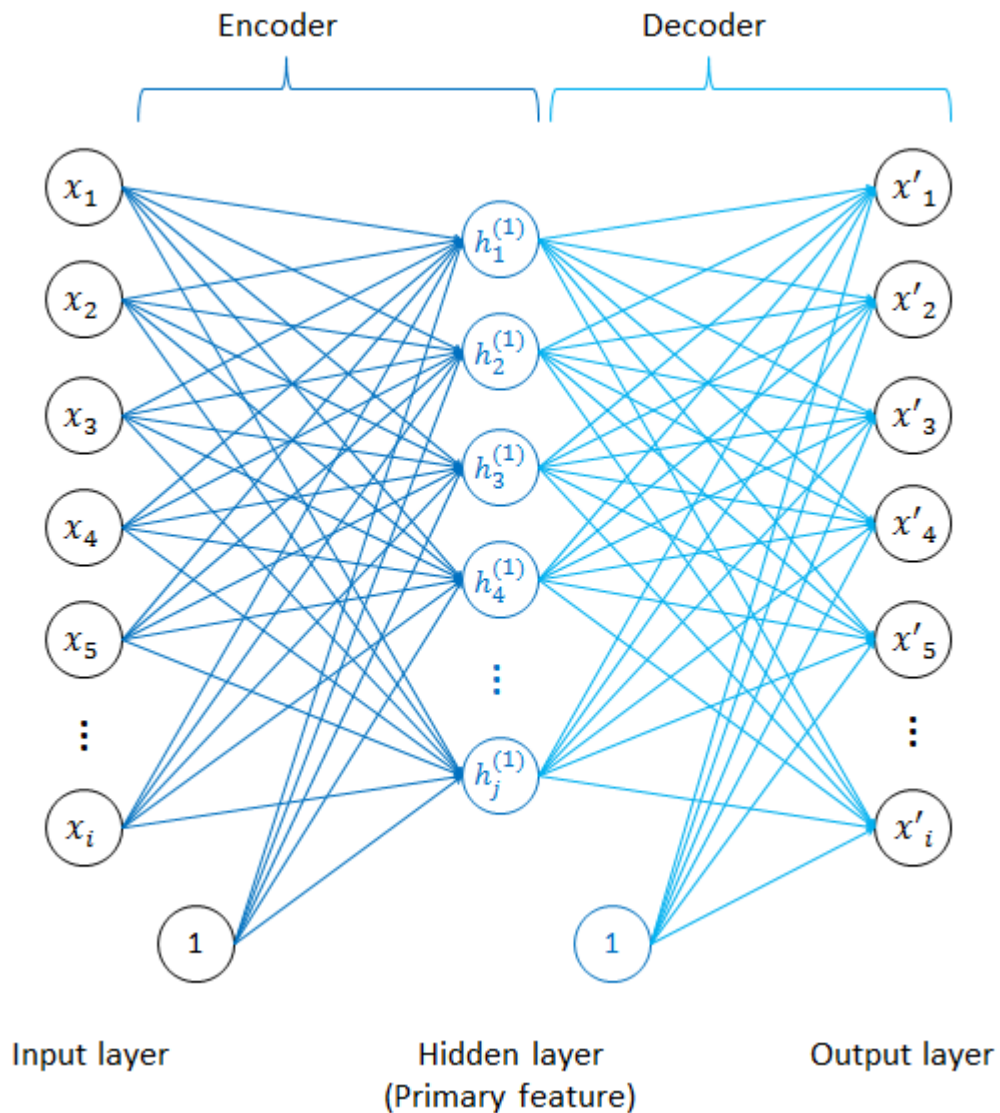
Figure 5.12. Concept diagram of an autoencoder. i is the neuron index in the input / output layer and j is the neuron index in the hidden layer, $i > j$. The outputs of the autoencoder network are expected to be the same with the inputs. The values of the neurons in the hidden layer can be seen as the primary features of the raw input.

ii.   Layer based training.

Using the values of the hidden layer neurons in Figure 5.12 as inputs, the methodology then creates a new three layer network. Train the network by letting the outputs equal to the inputs, and set the number of neurons in the hidden layer to be smaller than those in the input layer, to get the secondary features, as shown in Figure 5.13. Repeating this procedure will train the autoencoder layer by layer, until the pre-set layer number is reached.
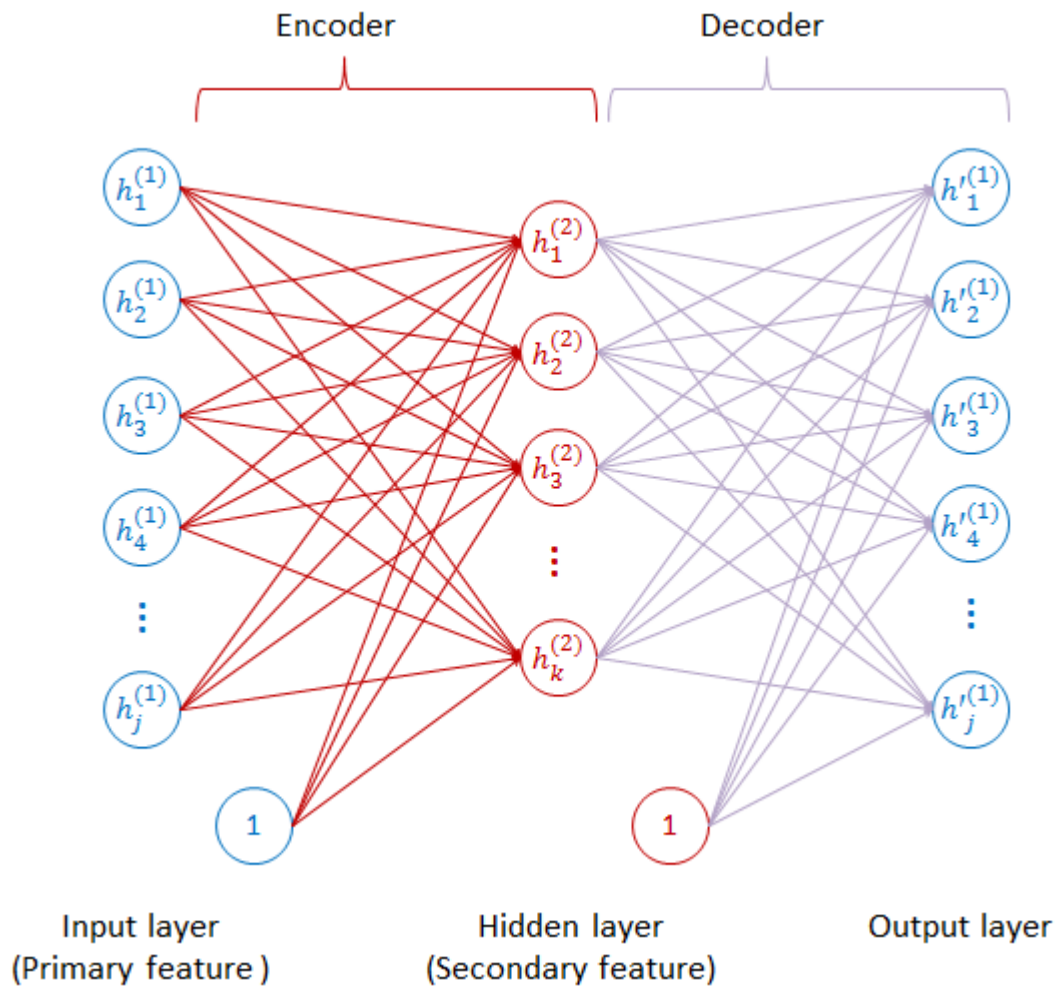
Figure 5.13. An autoencoder network with pre-calculated primary features fed in as inputs. The values of the neurons in the hidden layer are the secondary features of the raw inputs. j is the neuron index in the input / output layer and $\boldsymbol{k}$ is the neuron index in the hidden layer, $j > k$.

iii.   Supervised learning.

Stacking all the hidden layers of the trained autoencoders into one network. The stacked autoencoders now have the ability to learn from the raw data and to abstract a good feature representation. However, it cannot be used directly to classify the raw data since it has no information of the class label yet. There are two ways to modify it. One is to use the output of the network in the form of the extracted feature vectors and feed into a classifier, then applying supervised training. The other way is to connect a classifier at the end of the network and subsequently tune the entire network finely by supervised training. The latter one is preferable if the size of the

training set is sufficiently large. A full view of the SAE network after all layers are connected is shown in Figure 5.14.
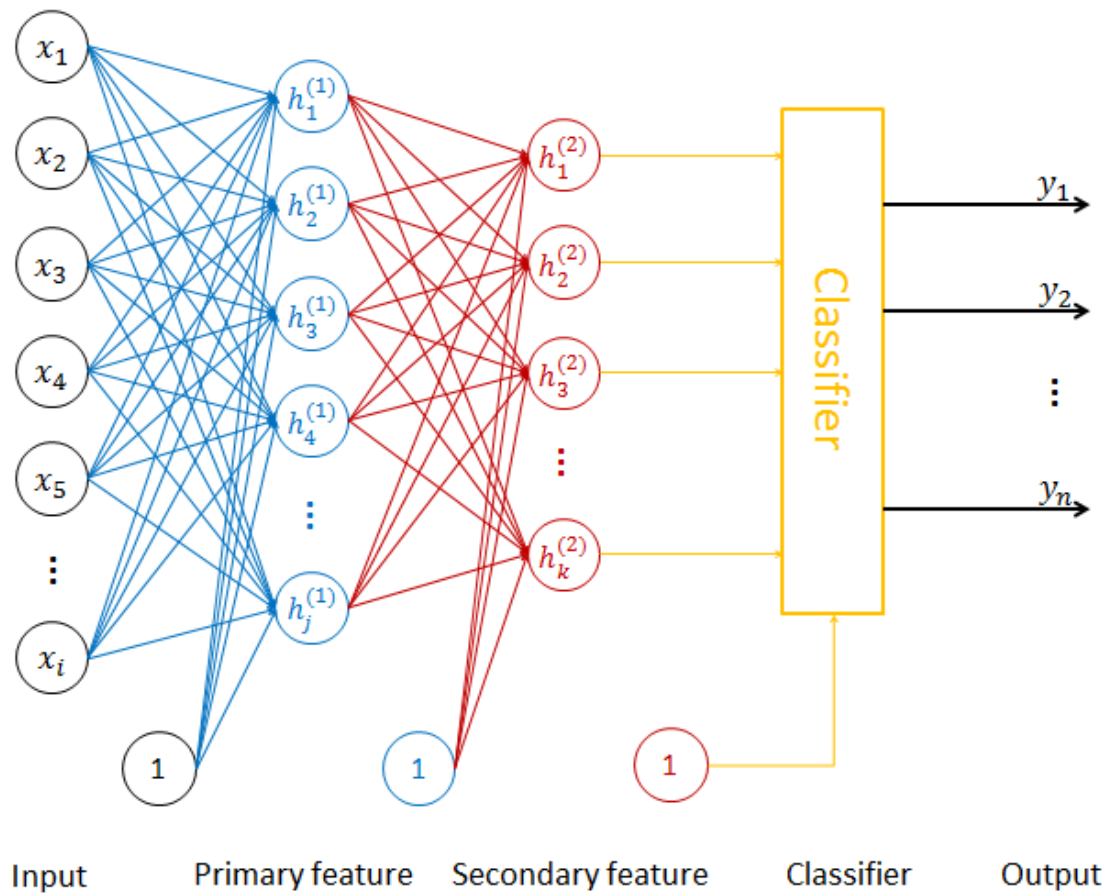
Figure 5.14. Concept diagram of stacked autoencoders (SAE). Each hidden layer is pre-trained and a classifier is attached at the end of the network.

5.4.3 Performance analysis of classification using features extracted by stacked autoencoders

Unlike other classifiers, SAE extracts features automatically. Therefore, the input of the SAE network is the segmental signals segregated from raw A-scans. In this work, the length of the segmental signal is chosen at 100, to match the empirically chosen 100 neurons input layer. Note that this length has been selected to match the time duration of the signal of interest associated with the A-scans collected in this work and would have to be modified if a different acquisition sampling rate was used. The

segmental signals should first be normalised to remove the effect of attenuation. Three encoders are stacked for the purpose of feature extraction, with the number of neurons in the three encoders being 50, 25 and 12 respectively. An additional layer is attached at the end of the network to simply perform the classification function. The classification layer is the output layer of the network which contains two neurons. As discussed previously for the MLP model in Section 5.2.2, the expected output of the SAE network is {1,0} for a legitimate reflector observation and {0,1} for a grain noise.

Simulated data is again used in this Section to analyse the performance of SAE, with the high dispersion model (HDM) used to generate data. Unless otherwise specified, the parameters of the HDM model used for this aspect of the Thesis are $\alpha = e^{-29}$, $s = 1.5$, 5MHz centre frequency with 50% bandwidth at -6dB, 100MHz sampling frequency. The same training and test data set up described in Section 4.3.6 and used in Figure 5.4 was used again to evaluate the SAE algorithm.

Figure 5.15 illustrates the classification performance of SAE using training sets acquired at different depths, along with MLP and SVM for comparison. The feature extraction method used in MLP and SVM is STFT.

SAE has accurately classified the segments into related classes in all three cases, with *Accuracy* at 97.4% for case 1, 97% for case 2, and 97.95% for case 3. As can be seen in Figure 5.15, the *Accuracy* of SAE is highest in case 3 which uses a training set covering segments from a range of different depths. Like the other classifiers, SAE has a better performance when the training set is perfectly matched with the test set. The *Accuracy* of SAE is better than SVM and MLP as shown in Figure 5.15, implying that the automatically extracted features have well represented the input segmental signals.
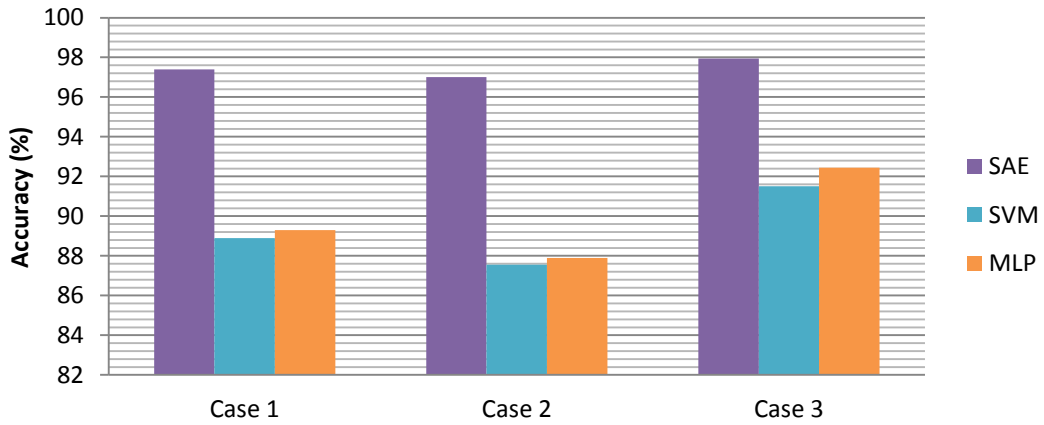
Figure 5.15. *Accuracy* of SAE, SVM, and MLP classification results for 2000 simulated A-scans, with legitimate reflector training data collected at different distances. All legitimate reflectors in case 1 are at 75 mm, and at 125 mm for case 2 and randomly distributed between 75 mm and 125 mm for case 3. Grain noise training data was collected uniformly between 75 mm and 125 mm for all the three cases. The test data for all three groups are extracted randomly between 75 mm and 125 mm. The data is simulated using the high dispersive model with $\alpha = e^{-29}$, $s = 1.5$, 5MHz centre frequency.

As shown in Figure 5.16, the *Accuracy* of SAE is slightly larger than SVM for all sizes of training sets. Similar to the MLP results in Figure 5.5, SAE may be underfitted when the training set is small and this manifests as significant fluctuations, as can been seen in Figure 5.16 when the number of observations in less than 200.
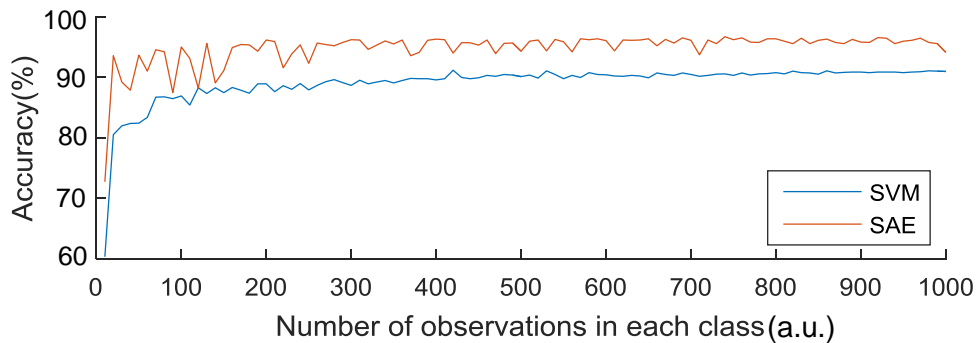
Figure 5.16. *Accuracy* of SAE and SVM when the size of the training set is changing. The number of observations in both classes is equal, and is increasing from 10 to 1000. The data is simulated using the high dispersive model with $\alpha = e^{-29}$, $s = 1.5$, 5MHz centre frequency.

The comparison of SAE and SVM when the numbers of legitimate reflectors and grain noise in the training set are unequal is given in Figure 5.17. Figure 5.17(a)

164

shows the case when the size of the grain noise class in the training set is slightly larger (by 10%) compared to that of the legitimate reflector; and Figure 5.17(b) shows the case when the size of the two classes is significantly disproportionate: here the size of legitimate reflector class is variant from 10 to 1000, while the size of grain noise class is fixed at 1000. The *Accuracy* of SAE is higher than SVM in both scenarios when the size of the training set is large. It can be seen that the *Accuracy* of SAE is low and fluctuating in Figure 5.17(a) only when the size of the training set is small, as discussed previously like the situation in Figure 5.16. However, the performance of SAE is significantly unstable when the size of the two classes in the training set is greatly unbalanced, as can be seen in Figure 5.17(b), the *Accuracy* fluctuates heavily when the size of the reflector training set is less than half of the noise training set.
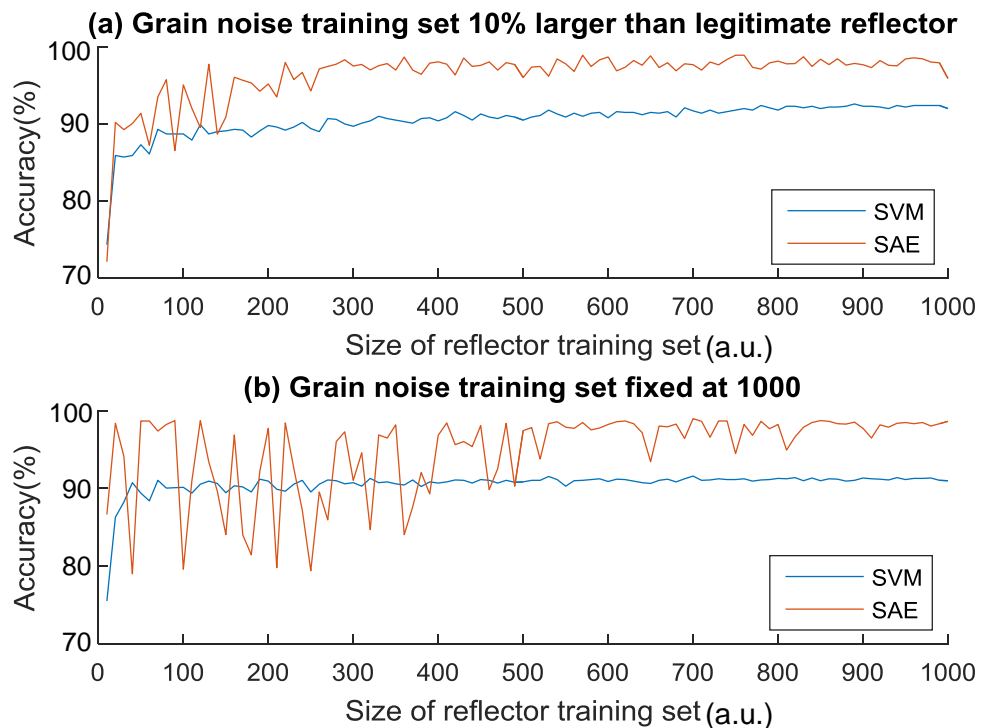
Figure 5.17. *Accuracy* of SAE and SVM when the sizes of the two classes in the training set are unequal. (a) The number of observations in the grain noise class is 20% larger than the legitimate reflector classes, (b) the number of observations in the grain noise class is fixed at 1000. The size of the reflector training set is increasing from 10 to 1000. The data is simulated using the high dispersive model with $\alpha = e^{-29}$, $s = 1.5$, 5MHz centre frequency.

The *Accuracy* of SAE when the training set of a legitimate reflector is mixed with a certain proportion of grain noise has also been considered and Figure 5.18 presents these results along with the *Accuracy* of SVM. The grain noise training set is unaffected. The overall trend of *Accuracy* of SAE has only dropped slightly when the proportion of mixed noise is high and generally outperforms SVM. Although the inaccurate training data does not reduce the *Accuracy* significantly as observed for MLP in Figure 5.18, the *Accuracy* profile of SAE is increasingly fluctuated, implying that the mixed grain noise training makes the performance of SAE unstable.

Figure 5.19 shows the classification results of SAE when the spectrum characteristics of legitimate reflectors and grain noise are similar. As was discussed for Figure 5.9, results for SVM and kNN approaches, using STFT as the feature extraction method, are also given for comparison. Interestingly, the *Accuracy* of SAE remains at a very high level compared to the other two techniques, which is in agreement with the earlier results shown in Figure 5.15.
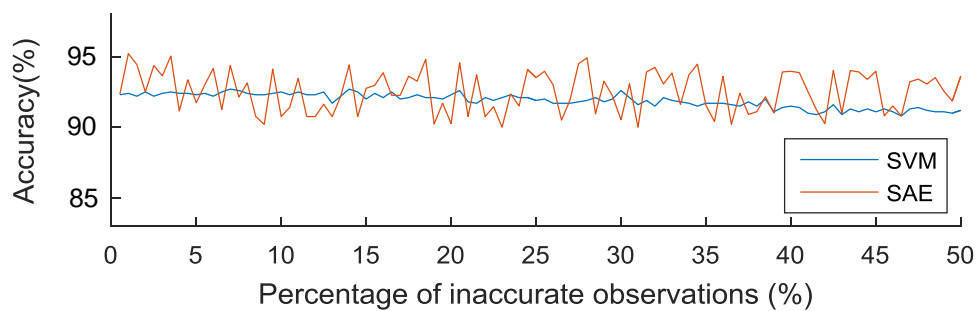
Figure 5.18. *Accuracy* of SAE and SVM when the legitimate reflector training set is mixed with a certain proportion of grain noise. The data is simulated using the high dispersive model with $\alpha = e^{-29}$, $s = 1.5$, 5MHz centre frequency.
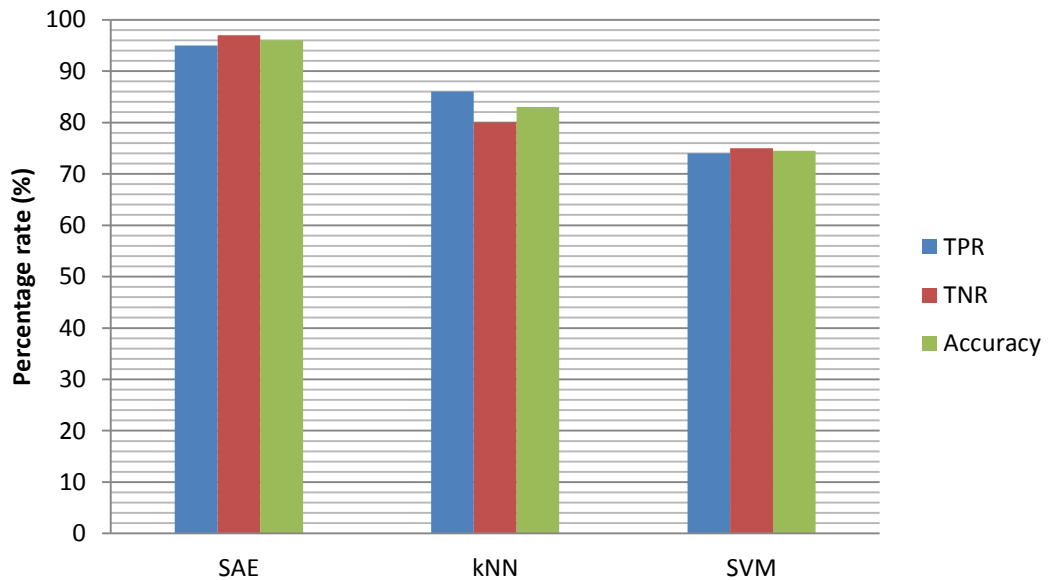
Figure 5.19. TPR, TNR, and *Accuracy* of an example classification results using SAE, kNN, and SVM when the spectrum characteristics of legitimate reflector and noise are close. The data is simulated using the high dispersive model with $\alpha = e^{-30}$, $s = 1.5$, 5MHz centre frequency.

Another factor that may affect the performance of SAE is the position(s) of reflector echoes in the training segmental signals. In order to correctly detect the distance of a legitimate reflector, its echo peak should be at the centre of the range of the training segment, as shown in Figure 5.20(a). However, the echo of a legitimate reflector is easily distorted by grain noise in practice, making it difficult to select an accurate extraction range for the training segment. Usually, the segments that are to be used for the training datasets can be extracted based on the knowledge of the sound speed of the test material and the distance to the flaw or back wall, for example. However, the speed of the test material could vary in an inhomogeneous material, making the position of the legitimate reflector echo peak in the training segments unpredictable. The classification results will not be significantly affected if the position of the legitimate reflector echoes are distributed randomly but mostly focused at the centre as shown in Figure 5.20(b). The same philosophy can be applied when using the features that are extracted by STFT. If the positions of the legitimate reflectors echoes are all on one side of the training segments as shown in Figure 5.20(c), it is still possible to get a correct result using STFT, as the spectrum of the segmental signal will not be distorted as long as the segmental signal contains the legitimate

reflector. However, this can strongly affect the result when using SAE. The distance of the legitimate reflectors in the output results will be shifted since the input data using this training set is completely different compared with the training set extracted using the correct range. Details will be discussed further in Section 5.5.1.

5.5   A-scan and B-scan Results

Both simulation and experimental A-scan and B-scan results are presented in this Section to validate the algorithms discussed earlier in this Chapter.

5.5.1   Results of classification algorithms

Figure 5.21 shows the B-scan results of MLP and SAE, using simulated data. The B-scan images of the raw signal and SVM are also given as comparisons. The feature extraction method used in both SVM and MLP is STFT. The data was simulated using the high dispersion model (HDM), using the following parameters: $\alpha = e^{-29}$, $s = 1.5$, 5MHz centre frequency with 50% bandwidth at -6dB, 100MHz sampling frequency. Each B-scan image is formed by 2000 A-scans and each A-scan contains a legitimate reflector. The locations of these legitimate reflectors are distributed uniformly from 75mm to 125mm. As shown in Figure 5.21(a), the dark oblique line is assembled by the legitimate reflectors of each A-scan. Absolute values of the signals are used in all images, and darker colour in a B-scan image refers to higher amplitude in the related A-scan representation.
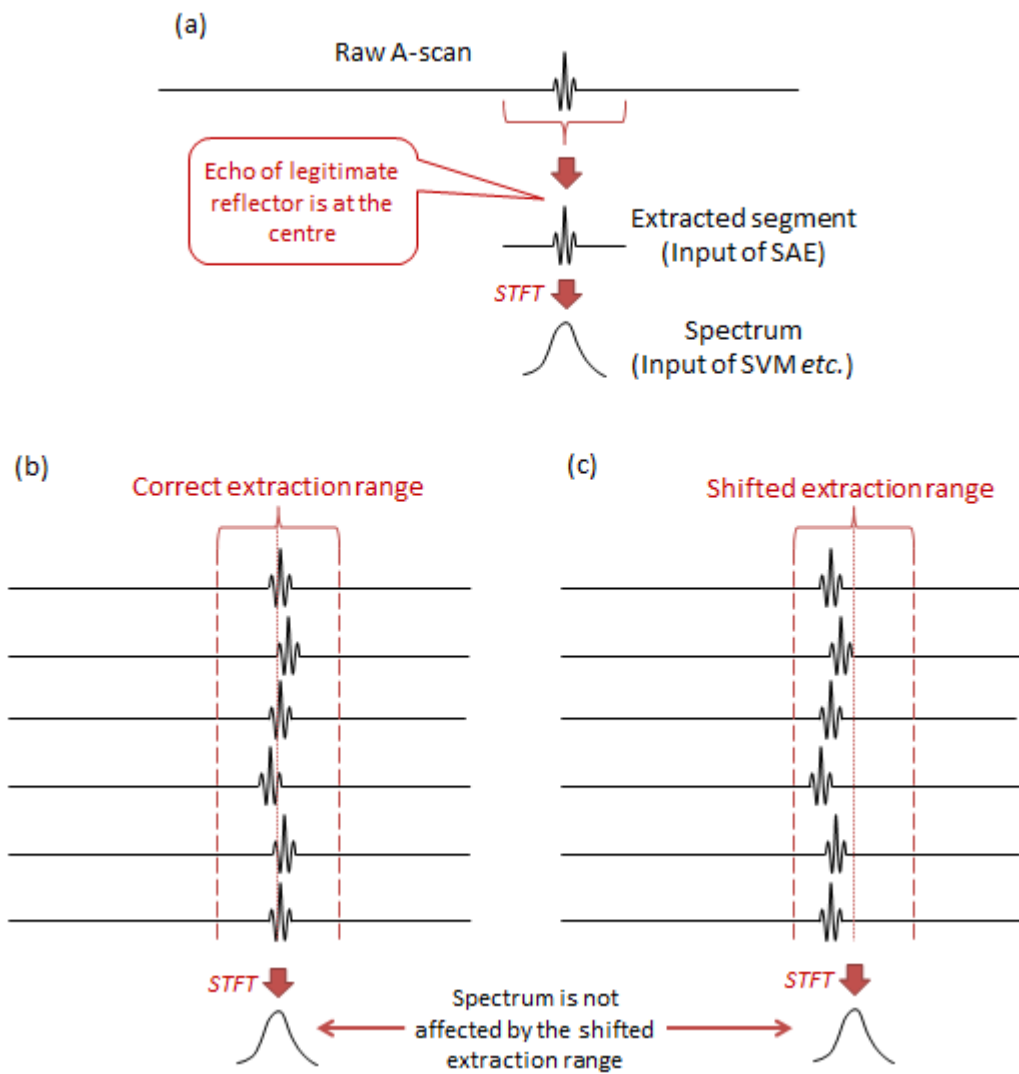
Figure 5.20. Segmental signal extracted from different ranges and its spectrum. (a) Echo of the legitimate reflector is at the centre of the segment, (b) acceptable extractions when the echoes are distributed around the centre, and (c) improper extraction range when echoes are not distributed around the centre.

(a) Raw B-scan (Simulated)

(b) SVM processed B-scan

(c) MLP processed B-scan

(d) SAE processed B-scan

Figure 5.21. B-scans results of the simulated data, (a) Raw B-scan, (b) SVM processed B-scan, (c) MLP processed B-scan, (d) SAE processed B-scan. The feature extraction method used in SVM and MLP is STFT. High dispersion model (HDM) was used to simulate the data. The parameters of the HDM model are selected at $\alpha = e^{-29}$, $s = 1.5$, 5MHz centre frequency with 50% bandwidth at -6dB, and 100MHz sampling frequency. Absolute values of signals is used for all images, darker colour represent higher amplitude. The dark line in the images are formed by the legitimate reflectors, from 75mm to 125mm.

As can be seen in Figure 5.21, the noise level is greatly reduced, and the visibility/clarity of the legitimate reflector line is enhanced after the image has been processed by MLP or SAE. Table 5.2 shows the SNR calculated for each image.

The SNR in each B-scan image is the average of the SNR of all A-scan traces, calculated using the peak value of the legitimate reflector echo divided by the mean value of noise, in dB.

Compared with the raw B-scan image (Figure 5.21(a)), the images processed by MLP (Figure 5.21(c)) and SAE (Figure 5.21(d)) have significantly improved the SNR by 31.11dB and 38.59dB respectively. Interestingly, the SNR predicted for MLP is similar to that determined for SVM. Whereas the SAE algorithm has outperformed all other methodologies, which is consistent with the analysis shown in Figure 5.4 and Figure 5.15.

Table 5.2. SNR for simulated results presented in Figure 5.21.

Raw B-scan	10.08dB
SVM processed B-scan	41.30dB
MLP processed B-scan	41.91dB
SAE processed B-scan	48.67dB

Figure 5.22 presents the experimental B-scan results from an austenitic steel sample for an image generated using the raw acquired data and three processed B-scans. Forty A-scans are shown in each B-scan and each one contains a back wall echo. The data was acquired using a 5MHz linear array, and sampling at 100MHz. The backwall of the sample is located at 79mm. In addition to the B-scan image, Table 5.3 details the calculated SNR for each image. In all three cases, using a feature extraction method, the processed B-Scan is able to discern the backwall signal in the image, with SNR improvements of 31.37dB, 32.82dB and 41.07dB for SVM, MLP and SAE, respectively. Importantly, similar to the simulated data analysis, SAE has outperformed the other methodologies.
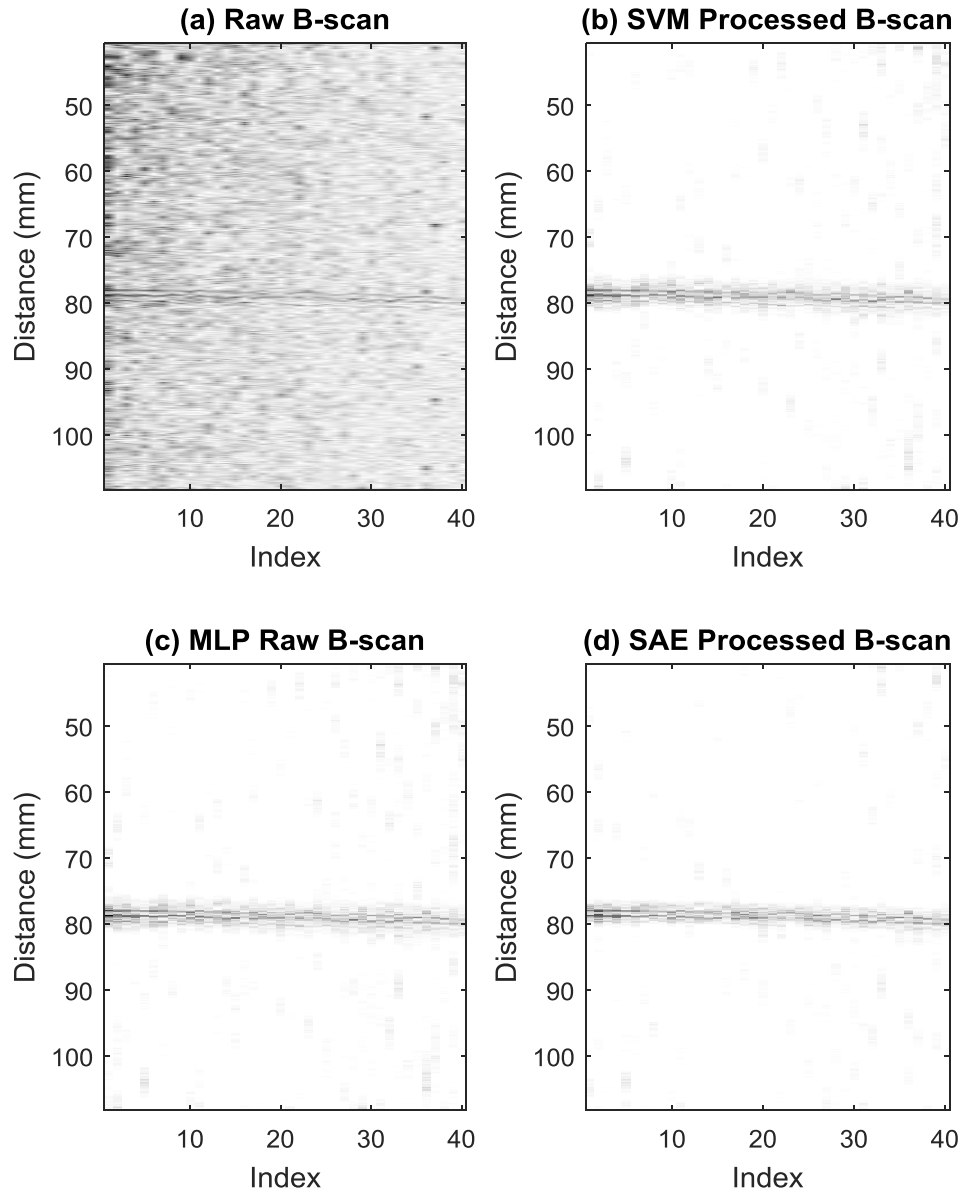
Figure 5.22. B-scan results of the austenitic steel sample, (a) Raw B-scan, (b) SVM processed B-scan, (c) MLP processed B-scan, (d) SAE processed B-scan. The feature extraction method used in SVM and MLP is STFT. Data was acquired using 5MHz linear array. Absolute values of signals is used for all images; darker colour represents higher amplitude. The dark line in the images is the back wall of the sample, at 79mm.

Table 5.3. SNR for B-scan images presented in Figure 5.22.

Raw B-scan	12.20dB
SVM processed B-scan	43.57dB
MLP processed B-scan	45.02dB
SAE processed B-scan	53.27dB

172

As discussed in Section 5.4.3, the echo position of the legitimate reflector when selecting the training segmental signals for SAE could be critical to its performance. Figure 5.23 shows two different ways of selecting the legitimate reflector training segments. The positions of reflector echoes are distributed randomly, and mostly at the centre of the segments within the correct extraction range, while the positions of the reflector echoes are all located at the upper part of the segments with a shifted extraction range.
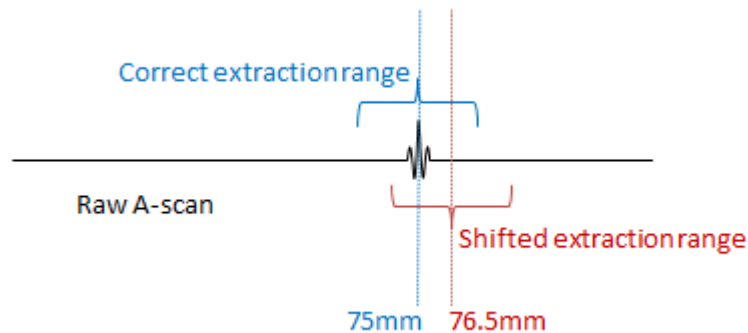
Figure 5.23. Echo position of legitimate reflectors when selecting the segmental signals for training.

Figure 5.24 shows the SAE B-scan results using the two different training sets related to the scenarios illustrated in Figure 5.23. 2000 A-scans are simulated using the high dispersion model (HDM), and all parameters are consistent with those used in Figure 5.21. The legitimate reflectors in all A-scans are located at 75mm. Figure 5.24(b) illustrates the result related to the correct extraction range as shown in Figure 5.23 and Figure 5.24(c) relates to the shifted extraction range. Although the legitimate reflectors (dark lines in the images around 75mm) are clearly shown in both SAE B-scans in Figure 5.24(b) and Figure 5.24(c) compared with the raw B-scan, there is a significantly spatial shifting of the legitimate reflectors in Figure 5.24(c) from 75mm to around 76.5mm due to the inappropriate selection of the training segments.

(a) raw B-scan   **(b) SAE**   **(c) SAE with shifted training**

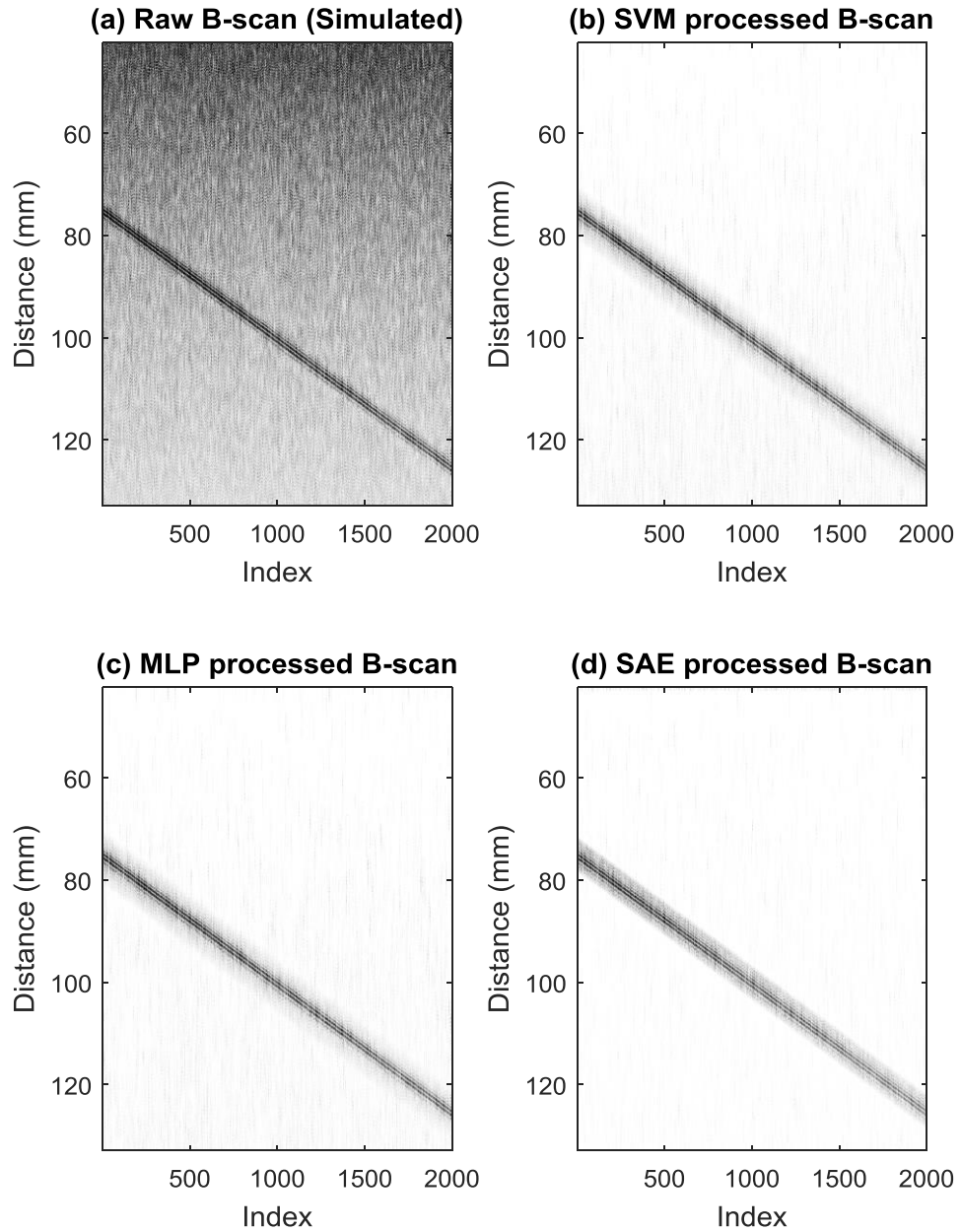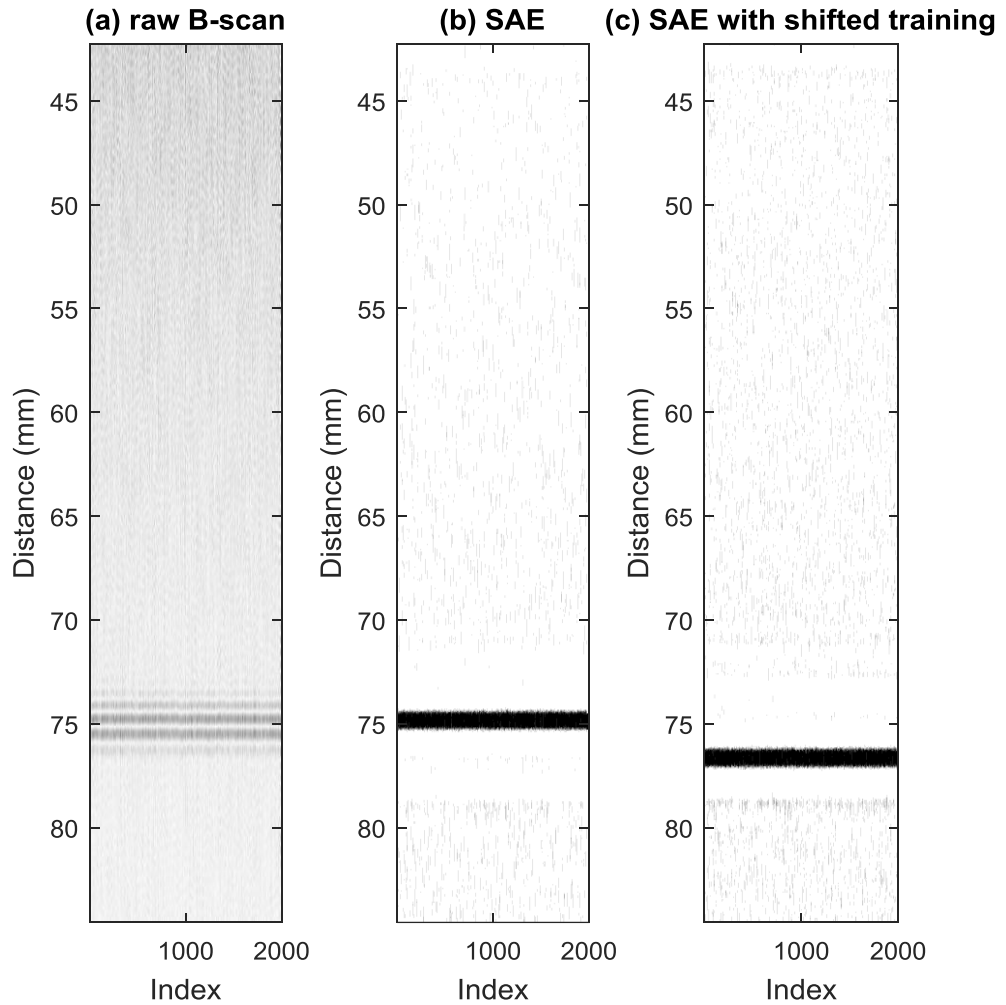Figure 5.24. B-scans results of the simulated data, (a) Raw B-scan, (b) SAE processed B-scan, (c) SAE processed B-scan when the legitimate reflector echo in its training set are all shifted to one side. (b) and (c) are the binary output results of SAE that have not been smoothed. High dispersion model (HDM) was used to simulate the data. The parameters of the HDM model are selected at $\alpha = e^{-29}$, $s = 1.5$, 5MHz centre frequency with 50% bandwidth at -6dB, and 100MHz sampling frequency. Absolute values of signals is used for all images, darker colour represent higher amplitude. The dark lines in the images are formed by the legitimate reflectors, at 75mm. There is a clear shifting of the legitimate reflectors in (c).

5.5.2   Results of wavelet based filtering algorithm

A simulated A-scan result is shown first to demonstrate the process of wavelet based filtering. HDM is then used to generate the simulation data, using $\alpha = e^{-30}$, $s = 1.5$, 5MHz centre frequency with 50% bandwidth at -6dB, and 100MHz sampling frequency. A flaw echo is simulated at 75mm and it is masked by the strong grain noise, as can be seen in Figure 5.25(a). The contour plot of the modulus CWT coefficients of the raw A-scan signal is also shown in Figure 5.25(b). Morlet wavelet

[66] is chosen as the mother wavelet and 64 scales is used with a linear interval. The scales of the CWT are converted into pseudo-frequencies in Figure 5.25(b) to make it more visual.

Considering the energy lost in higher frequency range due to the frequency dependent attenuation, the main energy of the signal should be distributed slightly below 5MHz, which is consistent with the energy distribution shown in the contour plot in Figure 5.25(b), the area with the highest energy has moved from 5MHz to 4.5MHz. A conventional way to de-noise the signal using CWT is to filter the signal by pruning and thresholding based on this area [66]. Figure 5.26 shows the pruned and thresholded CWT coefficients using the following equations:

$$W_{cp}(i,t) = \begin{cases} 0; & for\ i < i_1 \\ W_{co}(i,t); & for\ i_1 < i \le i_2 \\ 0; & for\ i > i_2 \end{cases} \tag{5.11}$$

$$W_{ct}(i,t) = \begin{cases} 0; & for\ |W_{cp}(i,t)| \le T * \max |W_{cp}(i,t)| \\ W_{cp}(i,t) - T * \max |W_{cp}(i,t)|; \\ & for\ W_{cp}(i,t) > T * \max |W_{cp}(i,t)| \\ W_{cp}(i,t) + T * \max |W_{cp}(i,t)|; \\ & for\ W_{cp}(i,t) < -T * \max |W_{cp}(i,t)| \end{cases} \tag{5.12}$$

where i_1 and i_2 are the pruning range, and 'max' is the abbreviation of 'maximum'. In this case, i_1 and i_2 are the 8th scales and the 16th scales, which relate to 3.9MHz and 5.6MHz respectively in their pseudo-frequency. The pseudo-frequency is a way to approximately convert wavelet scales to frequency, using the centre frequencies of related daughter wavelets. T, the Threshold is chosen as 0.5 empirically for the remaining processing in this Chapter. An inverse CWT is then performed to reconstruct the signal.

As can be seen in Figure 5.26, although there is energy distributed around 75mm, there are several areas that contains stronger energy, especially at around 47mm and 61mm. This will cause the processed A-scan to incorrectly identify the flaw location as shown in Figure 5.28(a), where strong noise remains at 47mm, 61mm, and 117mm.

Figure 5.28(b) is the reconstructed signal using the proposed new wavelet filtering algorithm from Section 5.3. The flaw echo at 75mm is successfully detected, and the

grain noise is greatly suppressed. As can be seen from the CWT contour plot in Figure 5.27, the scales with the largest contribution for distinguishing the flaw and the grain noise have been selected by MLP. Eight scales have been selected from the original 64 scales. Compared with Figure 5.25(b), the scales which have the highest energies are focused around 75mm are identified, with a 2MHz to 3MHz pseudo-frequency, which is consistent with the pruned wavelet in Figure 5.27. Note that although it looks like most remaining scales are locating at around 7MHz to 8MHz, there are only two scales in that area. The confused appearance is caused by the non-linear frequency resolution of the wavelet transform. The frequency resolution decreases when the pseudo-frequency increases.
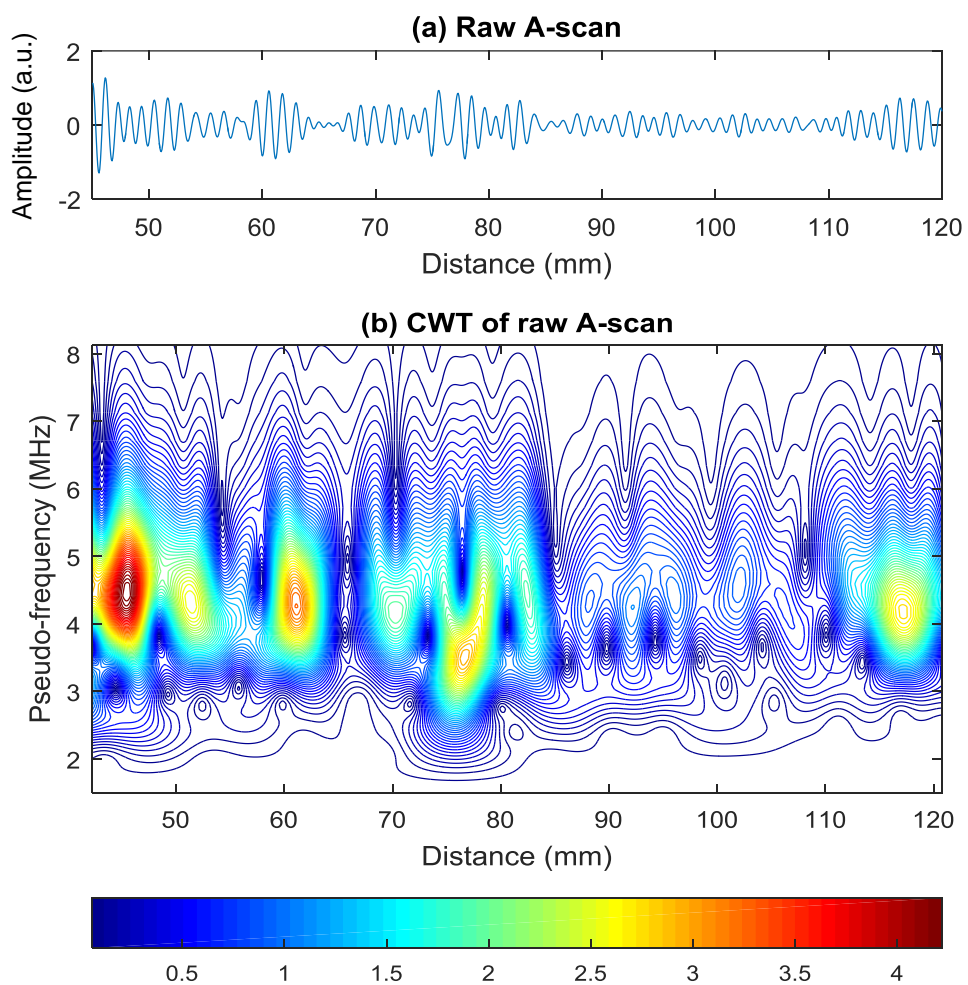
Figure 5.25. Raw A-scan and its modulus CWT contour plot. The data is simulated using the high dispersive model with $\alpha = e^{-30}$, $s = 1.5$, 5MHz centre frequency. The legitimate reflector is located at 75mm.

Pruned CWT (conventional)
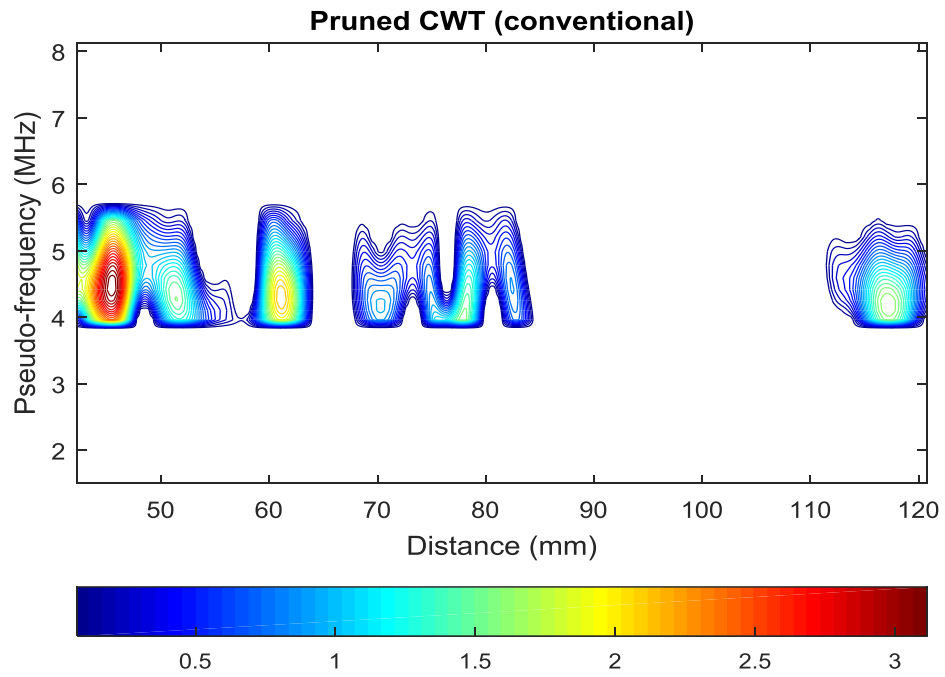
Figure 5.26. Contour plot of pruned and thresholded CWT of the A-scan in Figure 5.25, using a conventional method introduced in [66]. The threshold level is at 0.5.
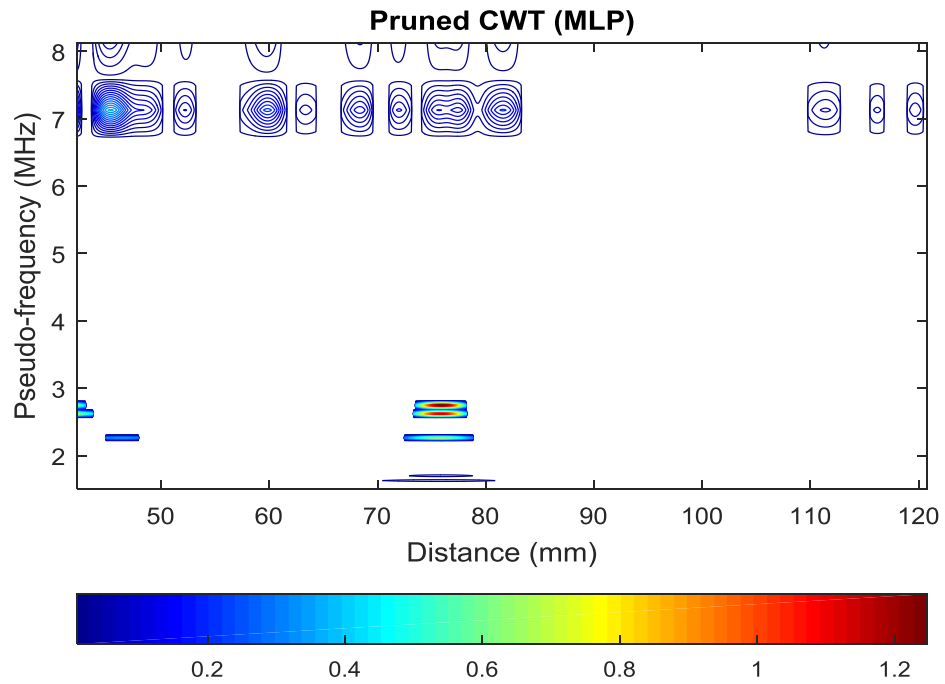
Pruned CWT (MLP)

Figure 5.27. Contour plot of pruned and thresholded CWT of the A-scan in Figure 5.25, using the proposed new method which combined with MLP. The threshold level is at 0.5.
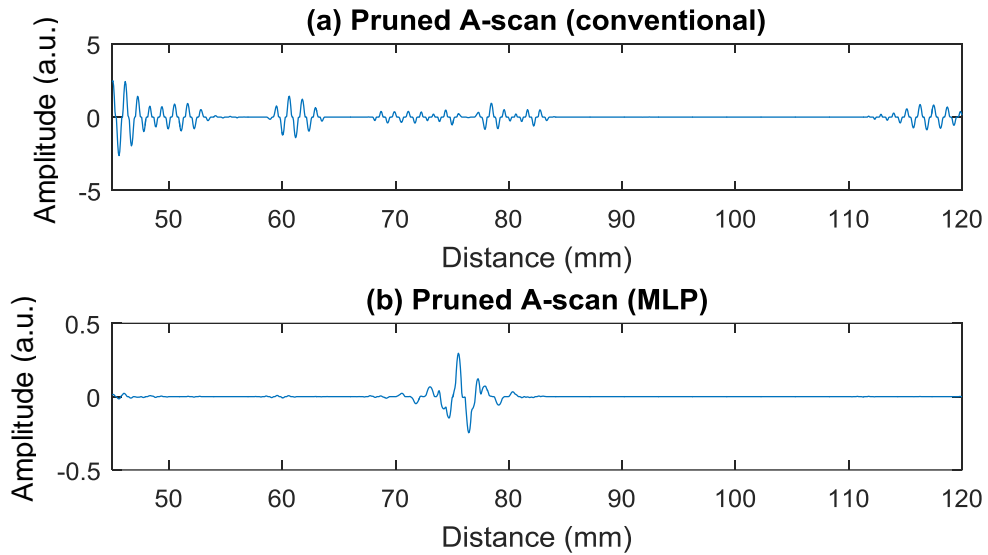
Figure 5.28. Reconstructed A-scans, (a) using the pruned CWT coefficients in Figure 5.26, and (b) using the pruned CWT coefficients in Figure 5.27. The legitimate reflector is located at 75mm.

Figure 5.29 shows the B-scan images of simulated signals, using the same parameter settings as used in Figure 5.25. Compared with the raw B-scan, the pruned B-scan with the help of MLP has a more visible feature at 75mm as can be seen in Figure 5.29(c), which is formed by the flaw echoes in each A-scan. Although the line of flaw echoes can also be observed in Figure 5.29(b), which has been formed using the conventional method, this has a lower SNR and many flaw echoes have not been successfully detected. The SNR calculations for these images are given in Table 5.4.

Experimental data is also used to demonstrate the performance of the proposed algorithms. Figure 5.30 presents the results of CWT filtering of data acquired from the austenitic steel sample. The data was acquired by a 5MHz linear array, at 100MHz sampling frequency. Again, the back wall of the sample is at 79mm. Comparing Figure 5.30(a) and Figure 5.30(c), it can be seen that the back wall becomes more visible after been processed using wavelet filtering, while the conventional method fails to show the location of the back wall. The SNR calculations for the three images are shown in Table 5.5. Although the CWT filtered B-scan with the help of MLP has reduced the noise compared with the raw B-scan,

its SNR is lower than the B-scans processed by Segment Recognition Classifier (SRC), as presented in Figure 5.22 and Table 5.3.
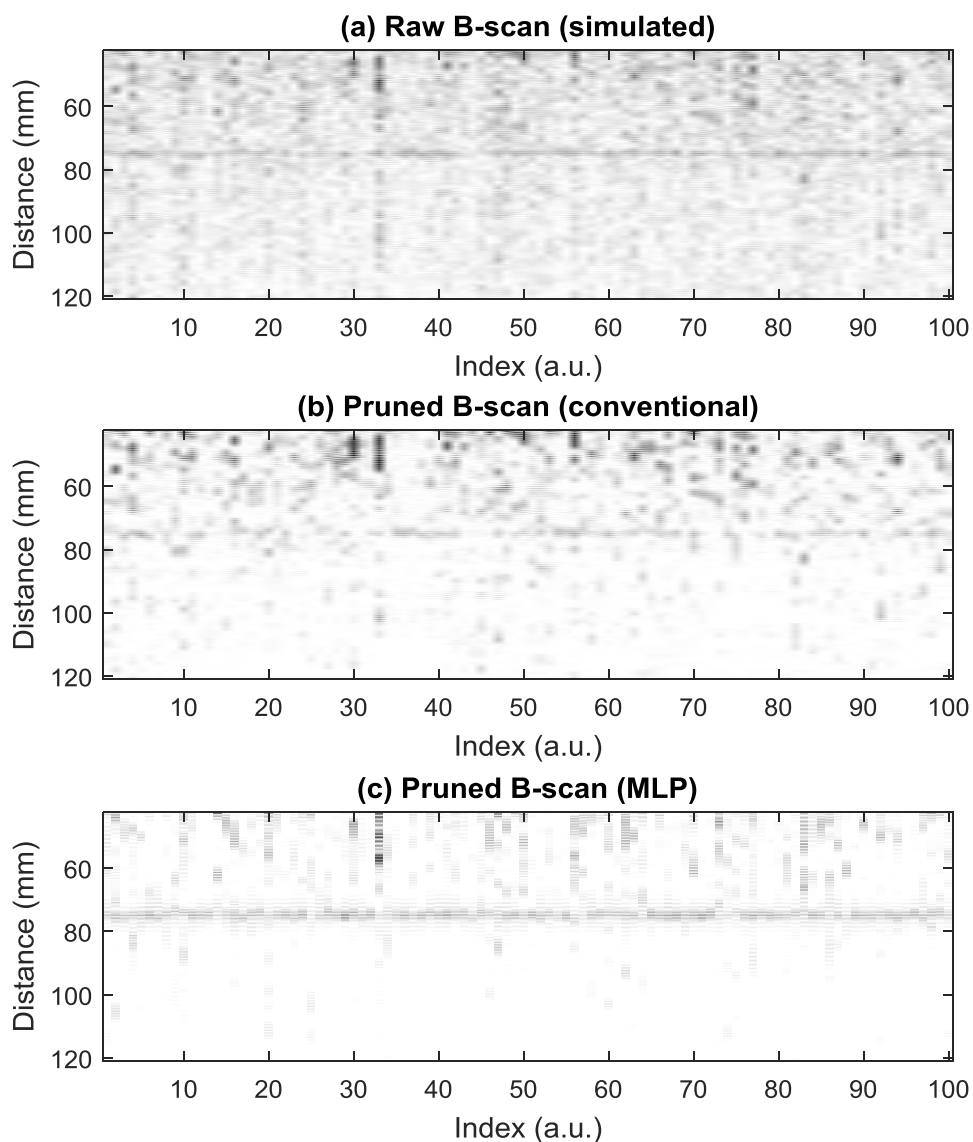
Figure 5.29. B-scan images simulated using the same settings used in Figure 5.25. Each A-scan contains a legitimate reflector at 75mm. (a) Raw B-scan, (b) processed B-scan using the conventional wavelet filtering, and (c) processed B-scan using the proposed wavelet filtering. All images are shown in modulus. Darker colour indicates higher amplitude.

Table 5.4. SNR calculations for B-can images presented in Figure 5.29

Raw B-scan	9.00dB
SVM processed B-scan	10.22dB
MLP processed B-scan	23.61dB

(a) Raw B-scan (austenitic steel)

(b) Pruned B-scan (conventional)

(c) Pruned B-scan (MLP)
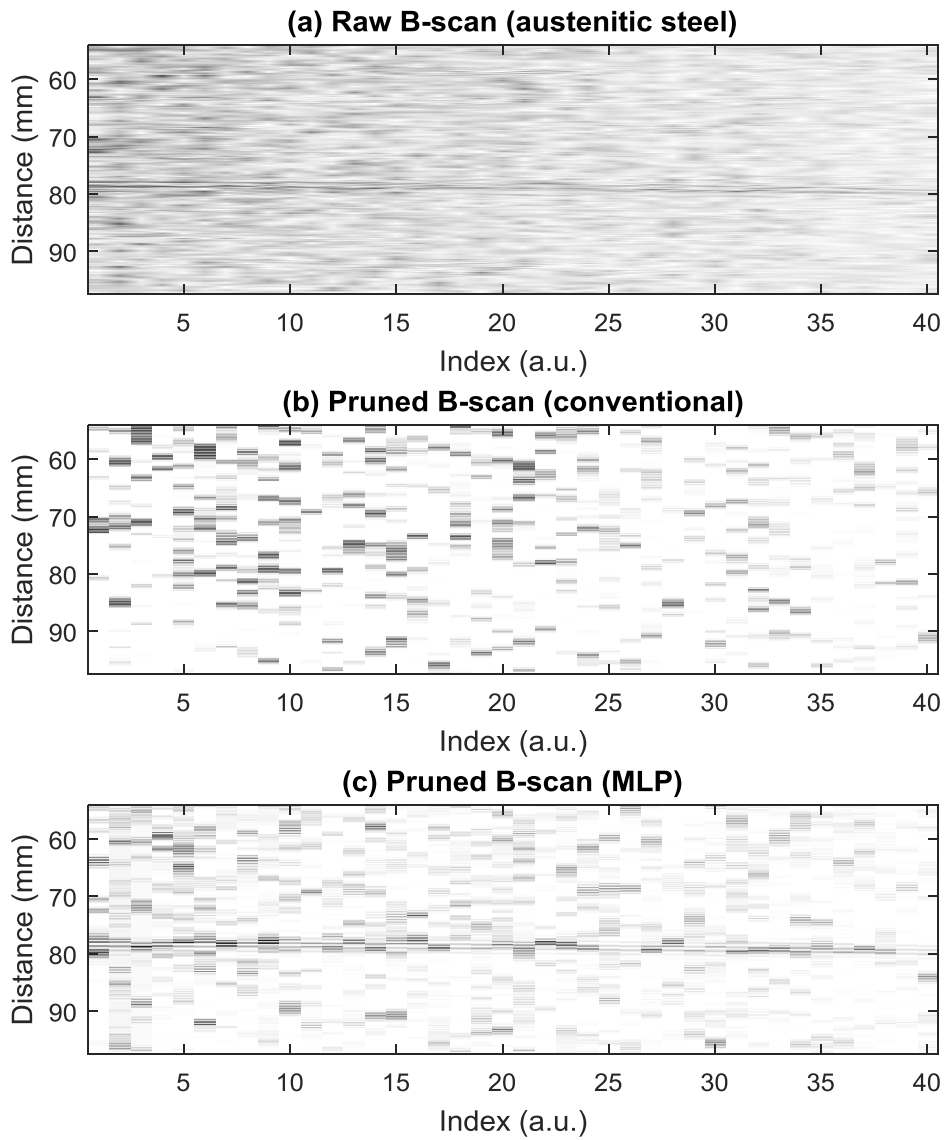
Figure 5.30. B-scan images of the austenitic steel sample. Each A-scan contains a back wall echo at 79mm. (a) Raw B-scan, (b) processed B-scan using the conventional wavelet filtering, and (c) processed B-scan using the proposed wavelet filtering. All images are shown in modulus. Darker colour indicates higher amplitude.

180

Table 5.5. SNRs calculations for B-scan images presented in Figure 5.30

Raw B-scan	12.20dB
Pruned B-scan (conventional)	4.85dB
Pruned B-scan (MLP)	22.66dB

Figure 5.32 illustrates another example of processed experimental B-scan imaging. The data was acquired from the Inconel 617 sample with a 5MHz linear array. The schematic of the array and the sample is shown in Figure 5.31. Different from the results in Figure 5.30, both conventional and the wavelet filtering algorithms have reduced the noise level and successfully detected the back wall echoes (oblique dark lines in the images). However, the back ground (noise level) of Figure 5.32(c) is much clearer compared with Figure 5.32(b). The corresponding SNR calculations show that Figure 5.32(c) has a superior SNR compared to Figure 5.32(b). This SNR data is detailed in Table 5.6.
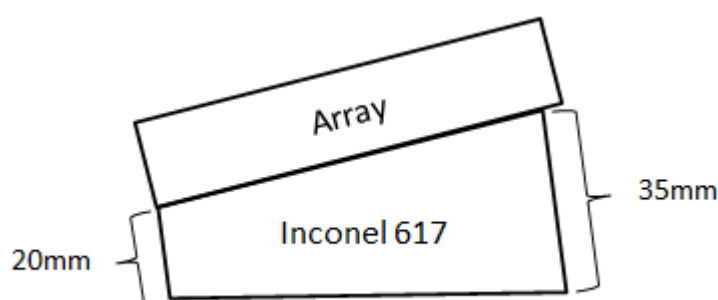
Figure 5.31. Schematic plots of the array and the Inconel 617 sample geometry.

Table 5.6. SNR calculations for B-scan images presented in Figure 5.32

Raw B-scan	16.33dB
SVM processed B-scan	20.70dB
MLP processed B-scan	30.26dB

(a) Raw B-scan (Inconel 617)

(b) Pruned B-scan (conventional)

(c) Pruned B-scan (MLP)
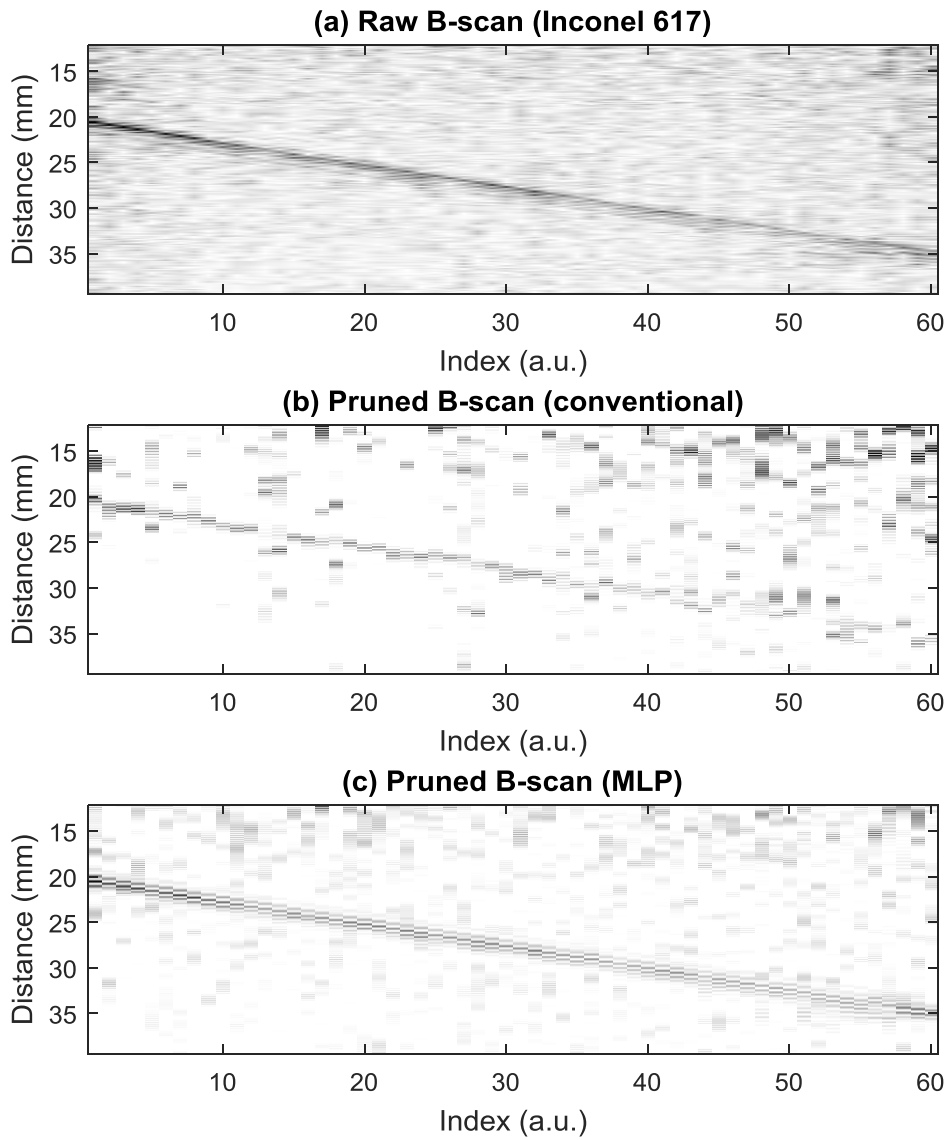
Figure 5.32. B-scan images of the Inconel 617 sample. Each A-scan contains a back wall echo, distributed between 20mm to 35mm. (a) Raw B-scan, (b) processed B-scan using the conventional wavelet filtering, and (c) processed B-scan using the proposed wavelet filtering. All images are shown in modulus. Darker colour indicates higher amplitude.

5.6 Summary

This Chapter has developed the benefits of applying supervised machine learning and pattern recognition into ultrasound time domain signal de-noising techniques. A number of different artificial neural network (ANN) applications have been introduced and combined with appropriate signal processing techniques.

Multilayer perceptron (MLP) has been chosen as an example of traditional ANNs. The classification performance of ultrasound segmental A-scan signals is generally similar to that of SVM. However, underfitting and overfitting problems could occur when the size of the training set is either too small or too large. Small training datasets may cause the performance of the MLP to be unstable; while large, inaccurate training sets may lead the MLP to start fitting to the unwanted noise characteristics of the signals. Like other classifiers, the features used by MLP can be extracted using either STFT or CWT. Although MLP has better performance using the features extracted by CWT compared with other classifiers based on its high nonlinearity, there is no significant improvement compared with those using STFT as its feature extraction method.

A good way to combine ANNs and the wavelet transform is to use ANNs to search the wavelet coefficients that can best represent the differences between legitimate reflectors and grain noise, then prune the wavelet to filter the raw signal. Usually, these coefficients should have higher SNR than the other approches. A three layer MLP has been chosen as an example. By summing up the weights of all neurons in the hidden layer after training, the coefficients that have larger contributions can be pruned from the raw CWT coefficients matrix. Initial results show that the proposed algorithm can successfully detect the legitimate reflectors and has higher SNR improvement compared with a conventional method.

Deep learning is an effective way to extract features automatically. The results of stacked autoencoders (SAE) are shown as an example of using Deep Learning as an ultrasound A-scan de-noising technique. The performance of SAE is promising, but inappropriate selecting of the training segmental signals may cause the detected legitimate reflector to be shifted. The automatic feature extraction function of SAE is

very similar to the well-known principal component analysis (PCA) [166]. However, experiences show that PCA is difficult to identify the difference between the legitimate reflector and grain noise when the SNR is low. The raw input is mainly represented by the first principal component and the second principal component after been processed by PCA since the levels of further components are significantly attenuated compared with the first two. This may not be enough to distinguish the noise and reflector groups due to their strong nonlinear boundary. Besides, Theodoridis and Koutroumbas [140] have shown that the first principle component is not always the best feature to represent the difference between two classes, as illustrated in Figure 5.33. Additionally, compared with PCA, the parameters of SAE are much easier to tune after being attached to a classifier.
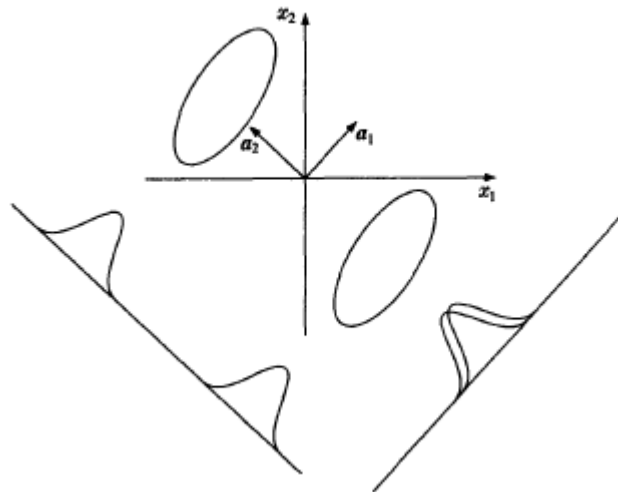
Figure 5.33. An example that shows the first principle component is not always the best one for classification. a_1 is the first principle component as the dataset has the largest projection on it. Apprently, the second principle component a_2 is more suitable for classification as the projection of the two classes along a_1 is overlapped [140].

Comparing all the proposed algorithms that use supervised learning in this Chapter and Chapter 4, SVM with STFT extracted features is suitable for most of the cases. SAE can also shown promise to further improve the SNR if the segmental signals in the training set are extracted properly. Although the noise reduction capability of the wavelet filtering algorithm is less optimal compared with classification algorithms, the wavelet filtering algorithm is much faster since it needs less computational power. Therefore, it is a good choice for the cases where the SNR of the raw signals is high.

Chapter 6

Unsupervised clustering in ultrasound A-scan processing

As discussed extensively in literature, traditional Split Spectrum Processing (SSP) algorithms are highly sensitive to their parameter tuning [112], which may result in the legitimate reflectors like flaws or backwall echoes not being detected, or even result in scattering noise not being fully eliminated and hence becoming classified as an artefact. Chapter 3 introduced an advanced frequency diversity based algorithm, Moving Bandwidth Split Spectrum Processing (MB-SSP), which was developed to avoid the parameter sensitivity problems of SSP. While the MB-SSP algorithm has a higher reliability in flaw detection, there are still many artefacts remaining in the processed signals, since the aim of MB-SSP was more focused on enhancing reliability rather than optimising noise reduction capability.

To improve noise reduction and flaw detection capability, Chapters 4 and 5 have discussed algorithms using supervised pattern recognition techniques. These prototype based algorithms provide more accurate performance since they are able to self-regulate using the training process by adapting the signals acquired from samples with different properties. However, high-quality training data is not easy to be acquired. Consequently, the performance of prototype based algorithms may be less when compared with traditional techniques, if the training is inappropriate.

To address these reasons, this Chapter presents a new algorithm named Potential Real Defect Miner (PRDM). Here, the term *real defect* refers to the legitimate reflector. The algorithm was inspired by the supervised classification algorithms that were introduced in Chapters 4 and 5. It uses an unsupervised clustering algorithm to help to remove artefacts in the signals that are introduced by A-scan based noise reduction techniques like MB-SSP, and improve the accuracy of the detection

without acquiring any advanced training data. It can also be used to accurately select training data for the classification algorithms described in Chapter 4 and Chapter 5.

6.1 Concept of using unsupervised clustering in ultrasound A-scan de-noising processing

The classification algorithms used in Chapters 4 and 5 are supervised and trained by labelled training data, to recognise whether a segmental signal contains a legitimate reflector or not. This labelled training data is critical when classifying observations into a related class; but unfortunately it is not always available. However, the characteristic differences between the legitimate reflector and grain noise exist independently of the label. These characteristic differences can be used by certain algorithms to gather such observations into groups. These algorithms are known as clustering analysis and are categorised as unsupervised learning algorithms. The aim of clustering analysis is to group similar observations together, without any concern for what label the group has. Importantly, the observations in a clustered group (sometimes referred as a cluster) are more similar to each other than to those in other groups.

The characteristic differences of legitimate reflector and noise cannot be used to label the legitimate reflector echoes in the raw signals. However, this characteristic difference can be used to cluster segments of the raw signals into groups. As the segments containing legitimate reflectors are more similar to each other compared to those contain only grain noise, they will gather into one (or sometimes more) group. This cannot immediately benefit the de-noising methodology as the legitimate reflector group is unknown. However, since segments that contain legitimate reflectors are much rarer than segments that contain only grain noise, then the percentage of clustered groups within the whole dataset identified as containing a legitimate reflector is typically very low.

Typically, the total number of segments within the entire dataset is usually large. This will force each clustered group to contain a large number of segments when the

number of groups is kept small. Since most of the segments in raw A-scans only contain noise, the significant imbalance between noise and legitimate reflectors will cause the legitimate reflector segments to be easily mismatched with one of the noise groups. If the number of groups is large, then the process of finding similar segments for each group will be too complex.

Therefore, the idea of using clustering to find the legitimate reflector directly from the raw dataset is hard to achieve.

However, assume the raw signals have already been processed by another A-scan based defect detection algorithm, and the processed signals show the location of the legitimate reflectors along with a few artefacts. Now, the clustering algorithm can be used to simply divide the segments that contain those echoes into several groups and pick out the specific group that contains only legitimate reflectors by comparing how many segments in the raw dataset have similar characteristic to the segments in this group.

Another application of clustering is to use it to support the classification based algorithms (Chapters 4 and 5) to accurately locate the segments that contain legitimate reflector echoes for their use in training. As the legitimate reflector echoes are often buried by strong grain noise and the wave speed in inhomogeneous materials varies for different paths, it is difficult to accurate locate the position of legitimate reflector echoes even when the distance of the reflectors and the wave speed are known *a priori*. Hence, only an approximate range can be calculated. With the help of clustering, all segments inside this range can be regrouped based on their spectral characteristic similarity. Since the locations of legitimate reflector echoes in the adjacent A-scans are typically close, the legitimate reflector echoes of a group of A-scans that are acquired continuously in the same area in practice will form a consecutive line. If the segments in one of the clustered groups are distributed in this pattern, then the locations associated with those segments represent the most likely location of the legitimate reflectors.

6.2 k-means clustering

There are many different ways to achieve clustering, for example sequential clustering algorithm [167], hierarchical clustering algorithms [168, 169] and algorithms based on cost function optimization [170, 171]. In this work, an algorithm named *k-means* which belongs to the latter category has been selected to illustrate the concept of clustering. *k-means* is one of the most widely used and well-known clustering algorithms [172-174]. It clusters the raw dataset by minimising the overall distance J between each observation and the centre of its related group,

$$J(c_1, \cdots, c_M) = \sum_{j=1}^{M} \sum_{i=1}^{N} \left\| x_i^{(j)} - c_j \right\|^2 \tag{6.1}$$

where $c_1, \cdots, c_M$ are the centroids of each group, $x_i^{(j)}$ is an observation that belongs to group j. J is termed the within-cluster sum of squares (WCSS) function. In other words, the objective of *k-means* is finding the solution of $(c_1, \cdots, c_M)$ when J is minimized.

The *k-means* clustering can be achieved through the following steps,

1) Randomly select M observations as the initial centroids of M groups,
2) Assign an observation to the group whose centroid has the smallest Euclidean distance to it. Repeat this for all the observations.
3) Update the centroid of each group by calculating the arithmetic mean of all observations in that group.
4) Repeat steps 2 and 3 until the assignment is no longer changing (i.e. J reaches a minimum value).

6.3 Artefact noise echoes removal

The procedure of using a clustering algorithm to remove artefacts in the processed A-scans can be achieved in six steps, as illustrated in the flowchart presented in Figure 6.1.
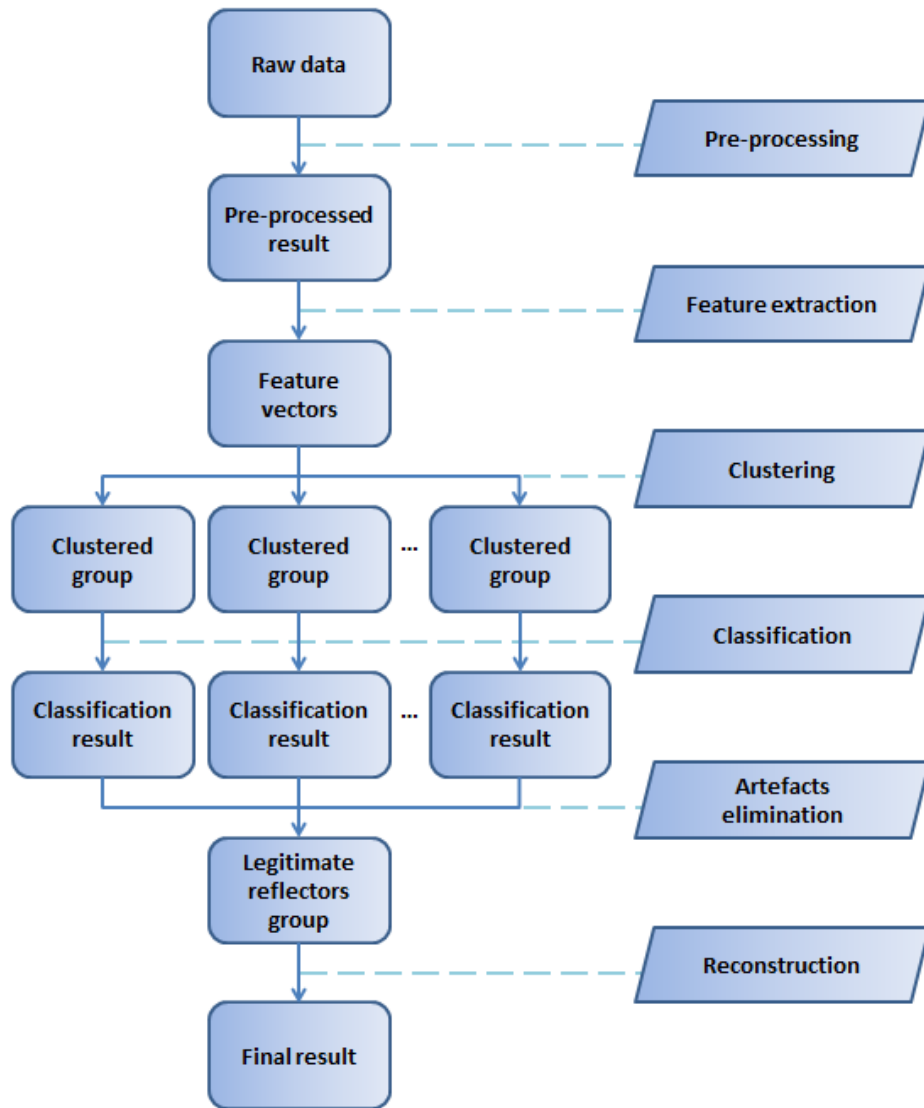
Figure 6.1. Flowchart of Potential Real Defect Miner (PRDM) when used to remove artefact noise echoes in processed A-scan signals.

6.3.1 Pre-processing

As discussed in Section 6.1, clustering algorithms are unsupervised and hence cannot classify the input data based on *a priori* knowledge. It can only divide the data into groups with similar characteristics. Therefore, raw A-scans are not suitable to be directly processed by the proposed algorithm and pre-processing is required using other A-scan based defect detection techniques, such as SSP and MB-SSP. This removes the majority of grain noise and only keeps echoes containing legitimate reflectors along with some remaining artefacts.

6.3.2 Feature extraction

As with the feature extraction method used in Section 4.2.2, after the raw A-scans have been processed, segmental signals will be selected from all the locations which potentially to contain a flaw. Feature vectors can then be extracted from these segments using a range of different methods. A common way to achieve this is to apply a Short Time Fourier Transform (STFT). Extracted features can be treated as an N-dimensional vector, as described by Eq. (4.1).

6.3.3 Clustering

The aim of clustering is to regroup all the selected segmental signals into several groups, using their extracted feature vectors. Each group contains segmental signals with similar characteristics. Experience gained in this area suggests that to ensure the segments that contain real flaw signals will be separate from the artefact signals, the total number of groups should be greater than 10.

6.3.4 Classification

The clustered results can now be further processed using a classification algorithm. Unlike clustering algorithms, classification algorithms are supervised which requires pre-acquired data from each category to train the algorithms. In this case, there are two categories, segments which contain a legitimate reflector and segments containing grain noise. Since the legitimate reflector echoes should be contained in one (or more) clustered groups and in the pulse-echo mode, the majority part of the received signal contains no flaw echo. Hence, the training data required for these two categories can be selected from the clustered segments and the remaining part of the raw signal. In other words, a large set of segments randomly selected from different signals and different locations can be trained as the 'noise' category, and then a group can be chosen that was clustered in the previous step to be trained as a 'reflector'. The entire raw dataset can then be classified using the trained data and repeated for all clustered groups.

190

Most of the supervised classification algorithms that were introduced in Chapters 4 and 5 are suitable for this application.

6.3.5   Artefacts elimination

For each group, if only a small number of segments in the raw dataset have been classified as a 'reflector', then the selected group contains the real flaw signals: this group should be labelled as 'legitimate reflector'; otherwise, label it as 'artefact'. The decision of a classified 'reflector' group is small and is determined on the detection rate of the pre-processed algorithm. The detection rate is defined as,

$$P_{detect} = \frac{count\ of\ detected\ segments}{all\ segments} \times 100\% \tag{6.2}$$

Since the proposed algorithm aims to remove artefacts from the pre-processed results, the count of classified 'reflectors' should not exceed the count of detected segments in the pre-processed results. Hence, if the percentage rate of classified 'reflectors' over all segments in raw data is larger than P_{detect}, then this group is most likely to belong to 'legitimate reflector'. If more the one group has been labelled as 'legitimate reflector', these groups should be combined and repeat step 'classification' and step 'artefacts elimination'.

6.3.6   Reconstruction

The classified 'legitimate reflector' is labelled as 1 and noise as 0. Hence, after every segment in an A-scan signal has been classified, a binary signal will be generated. This binary signal can be used to imply the position of the legitimate reflectors. However, this binary signal is too dictatorial for saying a fragment in the A-scan trace belongs to a legitimate reflector or noise. An improved method is to consider all the segments that contain this point and average their classification results, same as described previously by Eq. (4.2) in Section 4.2.4:

After the binary signal has been smoothed, it can be used to reduce the artefact noise by weighting the raw signal. This will indicate the location of legitimate reflectors

while maintaining their original information, like amplitude and spectral characteristic.

6.4 Accurately extracting training data

As discussed in Section 6.1, clustering algorithms can also be used to identify training segments containing legitimate reflector echoes for the supervised classification algorithms that were introduced in Chapters 4 and 5. The concept of locating training segments is similar to that of artefact removal and the flowchart presented in Figure 6.2 illustrates this concept. There are six key procedures which are now described in more detail.

6.4.1 Locating the area

Based on the distance to a known structural feature (e.g. back wall) and knowledge of the appropriate wave speed, locating the range in each A-scan which should contain the legitimate reflector segment can be calculated. Aligning these ranges for every A-scan can form an area of interest. This area should slightly wider than the length of a segment (around three times of the length of a segment), to ensure all legitimate reflectors are captured. This area can then be sub-divided into a set of segments, as shown in Figure 6.2.

6.4.2 Feature extraction, clustering, and classification

After the signals in the area of interest have been divided into segments, extracting feature vectors from them and performing clustering, similar to those of the artefact removal algorithms described through Section 6.3.2 to Section 6.3.4, will be applied. A classification stage will then classify the segments in each area of interest using each clustered group as the 'legitimate reflector' training set and the randomly selected noise segments outside the area as the 'grain noise' training set.
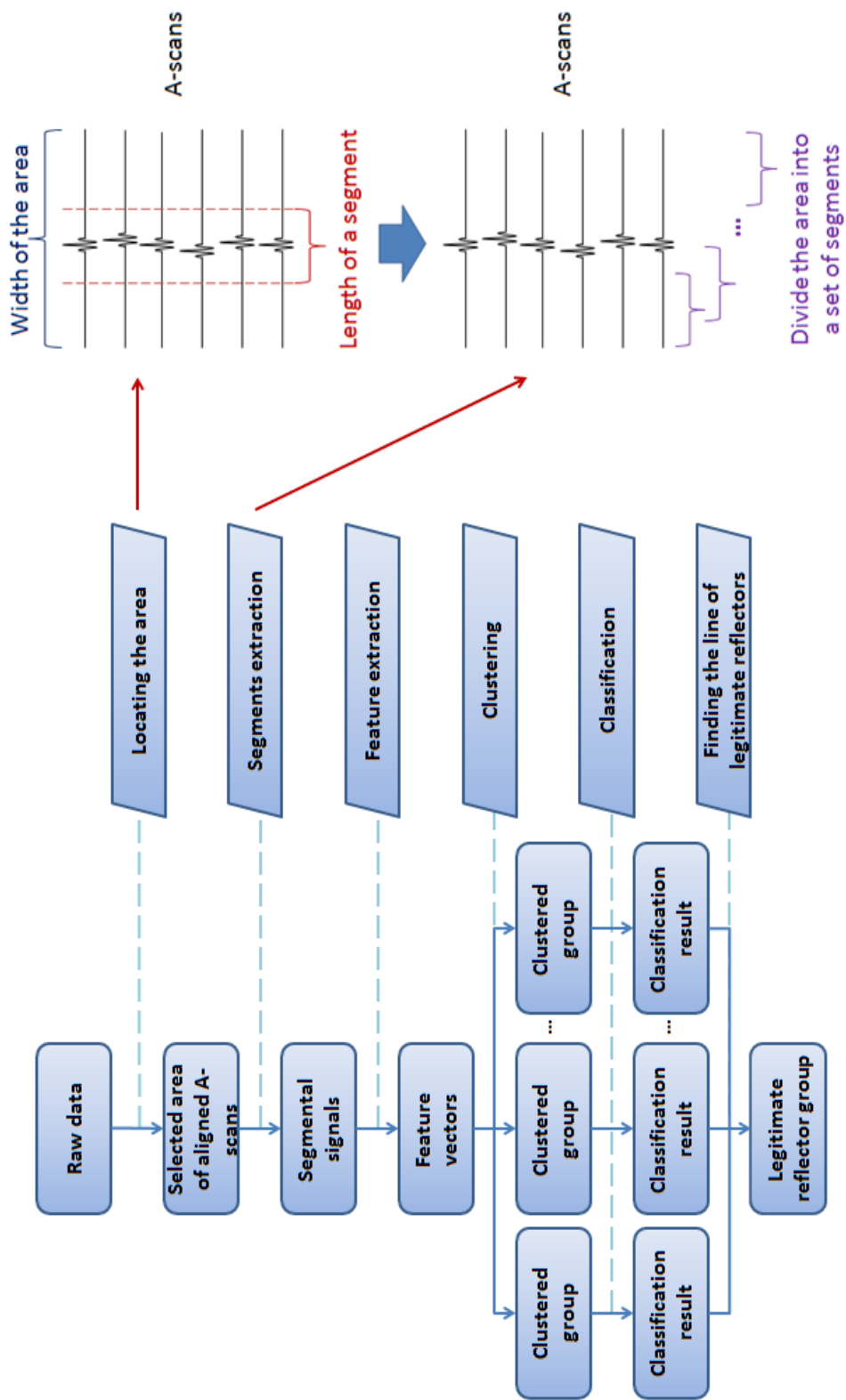
Figure 6.2. Flowchart of PRDM when used to locate the training segmental signals of legitimate reflectors.

193

6.4.3   Finding the line of legitimate reflectors

Assign each 'legitimate reflector' segment in the area of interest as '1' and each grain noise segment as '0'. Then use Eq. (4.2) to reconstruct the area of interest for each clustered group and produce an image of the reconstructed area for each clustered group. If the 'legitimate reflectors' in an image are distributed randomly, indicating no meaningful pattern, then the related cluster should be the noise cluster. If the image shows a clear identifiable feature, then the related cluster should contain the real legitimate reflector, and the position of the feature indicates where the training segments of legitimate reflector should be extracted.

6.5   Advanced centroids initialising by genetic algorithm

One of the important issues for *k-means* clustering is the selection of the group centroids. The initial centroid positions will directly affect the performance of the clustering as the algorithm may sometimes be limited to a less optimised local best solution during the convergence. A simple and traditional way to solve this issue is by repeatedly running the algorithm using different selections of centroids, and then searching for the best one. However, this search process is random in nature and this Section will address this issue by introducing an alternate method to search for an optimised solution by introducing a genetic algorithm (GA) approach [175].

GA was first inspired by Darwin's natural selection theory [176]. It searches the optimised solution of a function by simulating the process of natural evolution. To achieve this, GA abstracts the candidate solutions (called individuals) as 'chromosomes' and produces a new generation (prediction) which is more adaptive to the condition by heredity, mutation, and selection. Unlike the traditional methods that optimise the solution by processing a single initial solution iteratively, which is easy to stop at a locally optimised solution, GA has a group of initial solutions (population) that covers a broad range and hence, the approach is strong at searching for global optimised solutions.

6.5.1 Advanced centroids methodology

In this work, an advanced algorithm is introduced that searches the optimised centroids positions in conjunction with GA, as illustrated in the flowchart presented in Figure 6.3. The following sub-sections provide details on the key process components identified in this flowchart.
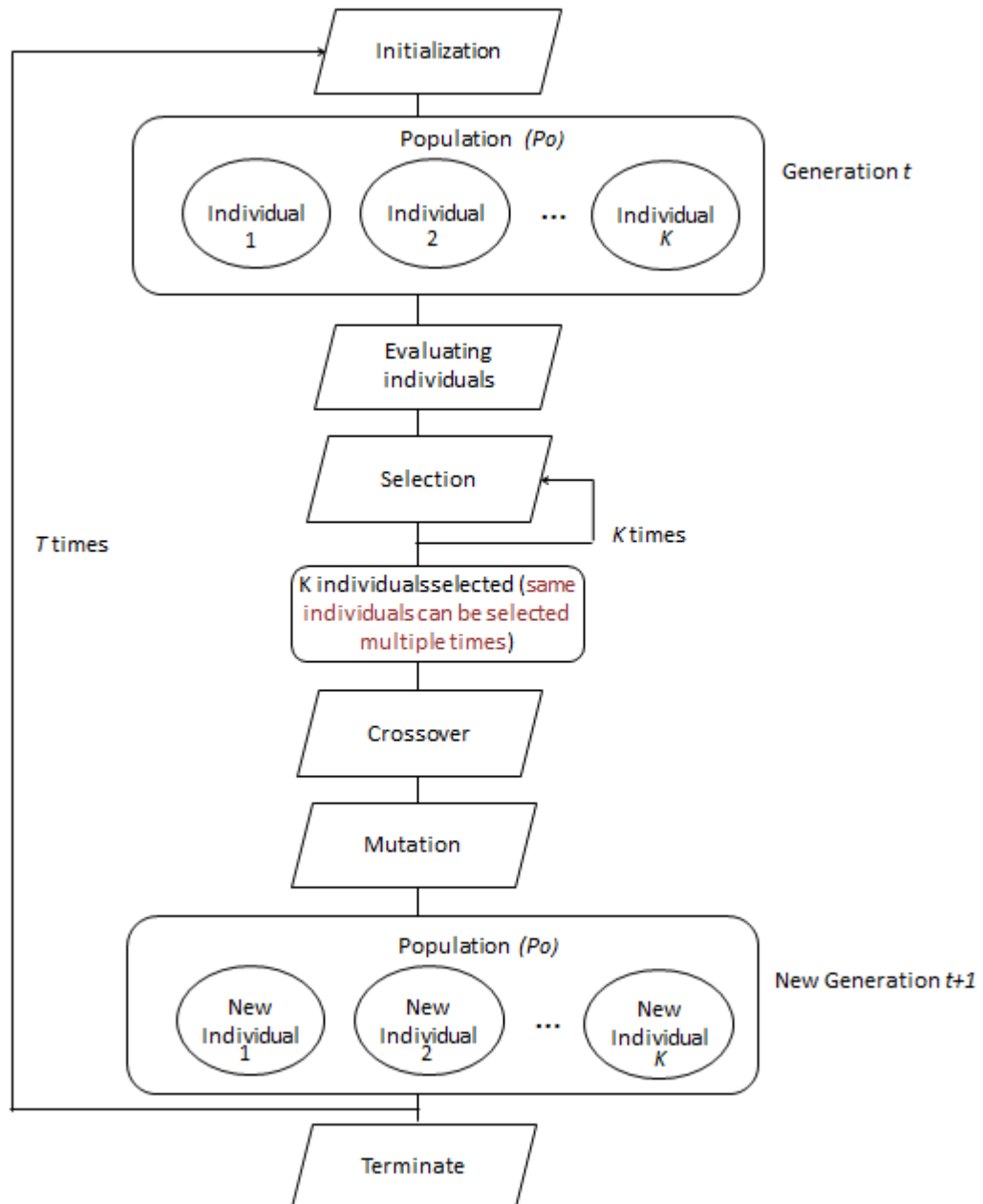
Figure 6.3. Flowchart of enhanced Genetic Algorithm (GA).

First, randomly select K combinations of M feature vectors from the dataset to be clustered as individuals of the first generation $Po(t), t = 1$, where Po denotes the population and t is the order of generation. K is the population size and M is the number of clusters. These individuals assemble the first generation and each individual will be treated as an initial group of centroids. It is then necessary to encode each individual to simulate the concept of a chromosome, which can be achieved by encoding the individual using an array of binary numbers [177], as shown in Figure 6.4.
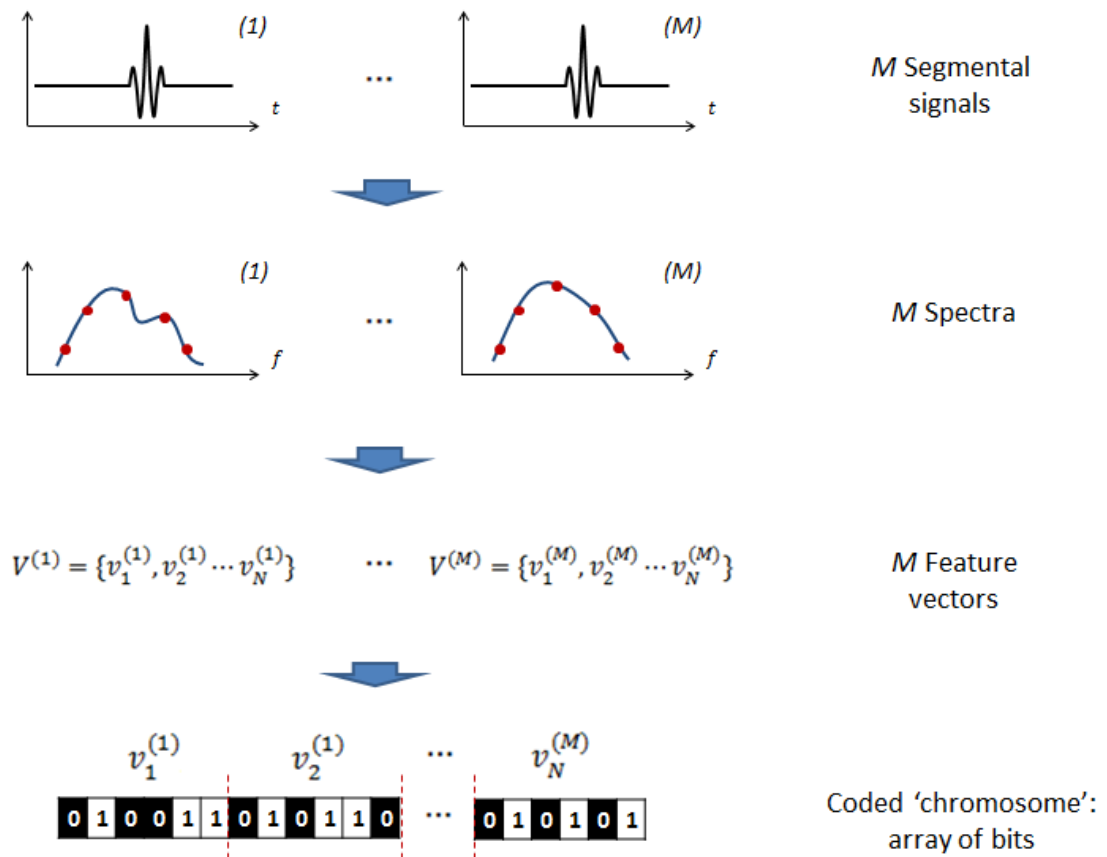
Figure 6.4. Encoding a feature vector using an array of binary number.

ii.   Evaluating individuals

It is appropriate to calculate how much each individual will adapt to the conditions. The more adaptive an individual is, the higher chance its 'gene' will pass onto next generation. The function to measure this is called a fitness function [175]. In this work, the fitness function is defined as,

$$S_f(x) = \frac{K+1}{K} \times \max[all\ J(x')\ in\ the\ current\ generation] - J(x') \qquad (6.3)$$

where x is the coded chromosome of an individual (a group of centroids), J is the within-cluster sum of squares (WCSS) function, K is the size of the population, $\max[J]$ denotes the max value of J in the current generation, x' is the chromosome of the centroids after been processed by the *k-means* algorithm, S_f is called the fitness score.

iii.   Selection

Replace the initial centroids x with x', as the new individuals of the population. Select an individual from the population based on the fitness score, where individuals with a higher fitness score are more likely to be selected. A common method that is used to select an individual is based on roulette wheel selection [178]. It assigns each individual to a slice of the wheel, with the size of the slice based on the fitness score, as shown in Figure 6.5. To select an individual, spin the wheel and pick the one selected by the needle. Repeat this process until K individuals are selected.

iv.   Crossover

This process pairs the selected individuals and then exchange (crossover) part of their chromosomes between each other, to produce two new individuals. Crossover is an important step of GA and is the major way to generate new individuals. In this work the crossover is taken at a randomly chosen point along the arrays of bits of the selected individual pair, which depends on a crossover rate. This operation is shown in Figure 6.6.
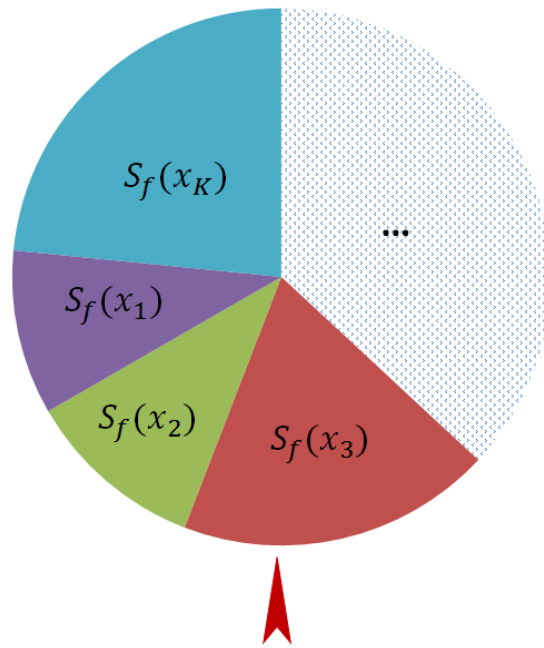
Figure 6.5. The concept of a roulette wheel. The size of each slice is based on the related fitness score.
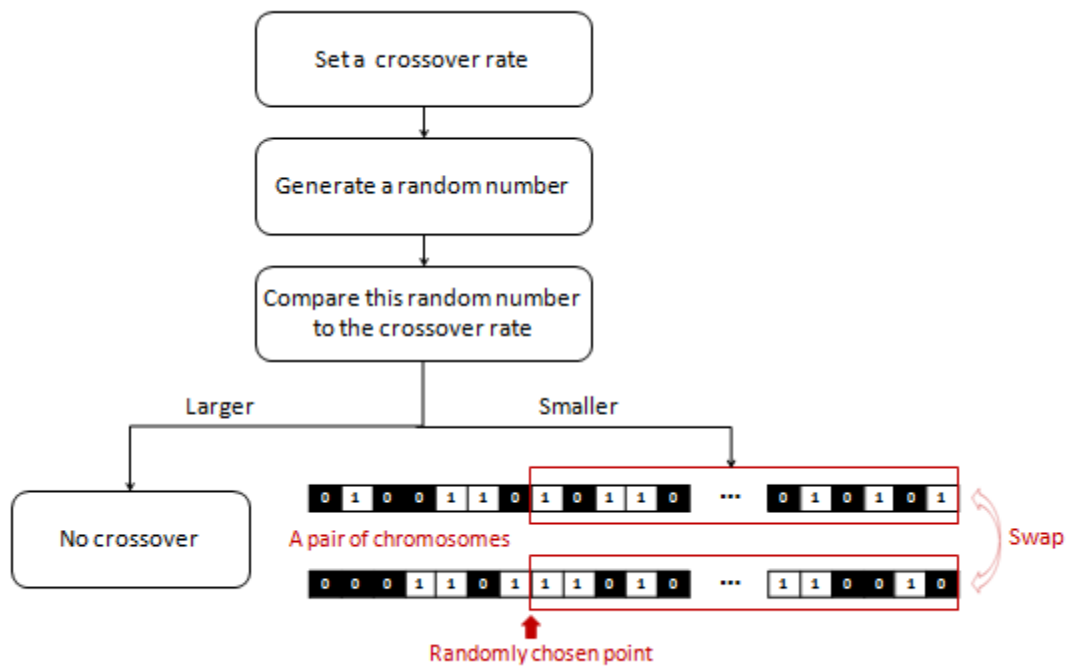
Figure 6.6. The concept of crossover. The two matched individuals will swap part of their array of bits at a randomly chosen point based on a crossover rate.

v. *Mutation*

Based on a mutation rate, certain bits in the array of bits will be flipped, to generate new individuals. Mutation can enhance the capability of searching optimised solutions in a small area, while keeping the genetic diversity of the population. Figure 6.7 shows the concept of mutation. In this work, only one point in the array of bits may be flipped. The new generation $Po(t+1)$ is produced after all the above steps are performed.
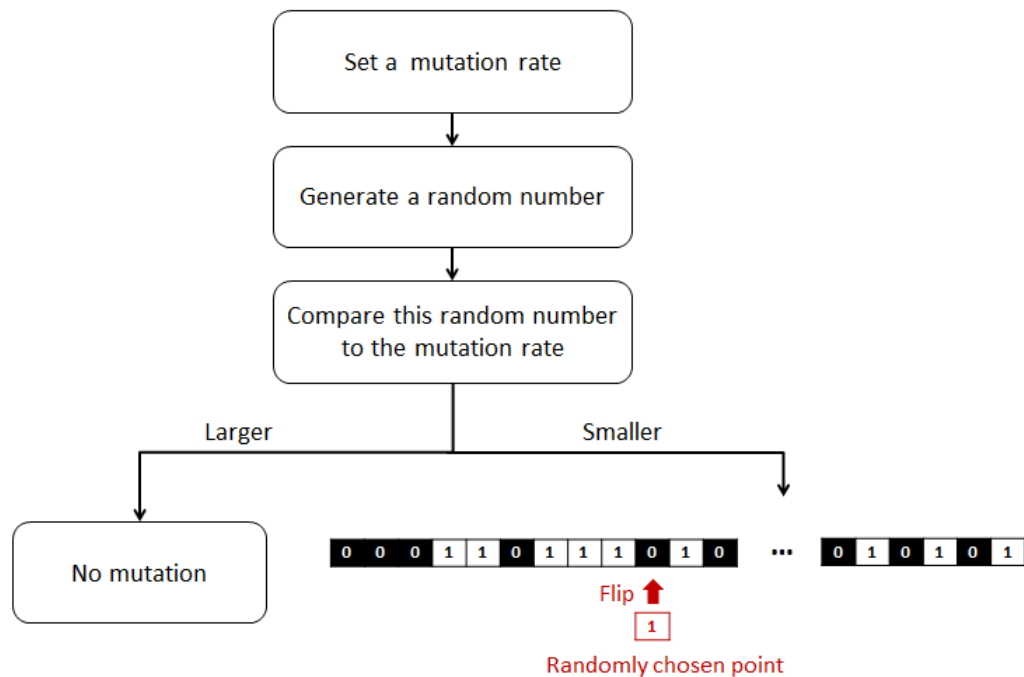
Figure 6.7. The concept of mutation. One bit in the chromosome of an individual will be flipped based on a mutation rate.

vi. *Terminate condition*

Repeat *steps i* to *v* until *t* reaches the pre-set value T. T is the total number of generations and should be chosen large enough to ensure the GA algorithm converges, noting that a larger T is more computation expensive. In this work, T is chosen at 60. Output the individual with the minimum J value for all generations as the optimised solution and the centroids of each clusters.

6.5.2   Performance analysis

Figure 6.8(a) and Figure 6.8(b) show the trend associated with the within-cluster sum of squares (WCSS) distance (i.e. J in Eq. (6.1)) of the traditional method and the enhanced GA method illustrated in Figure 6.3. Both cases have used a dataset that contains 6000 segmental signals, which was extracted from MB-SSP processed A-scans, as described in Section 3.3.1. The raw A-scans were acquired from the austenitic steel sample using a 5MHz linear array. The population size of GA in Figure 6.8(b) is 30, and there are 60 generations. Each individual in the population is constructed by 20 feature vectors as centroids of clusters. Figure 6.8(b) gives the individual with the smallest WCSS distance for each generation. To make a fair comparison, the iteration times of the traditional method has been set to 1800 times (30×60); i.e. for every 30 iterations, the smallest WCSS distance is recorded. In both cases the iteration times of *k-means* clustering is 100. The vertical axis, WCSS distance, in both Figure 6.8is the summation of distance from all observations to their related centroids; where smaller distances are indicative of more compact groups and signify highly suitable centroids. From Figure 6.8(a) it can be seen that the WCSS distance is randomly changing when using the traditional method. Although the WCSS distance also fluctuates before the 30th generation, the overall trend then shows consistency and a gradual decrease, eventually becoming flat, as illustrated in Figure 6.8(b). Compared with the random approach, GA is stronger at finding an optimal solution. Although the traditional method can also find a relatively optimal solution, it is uncertain when the optimised solution will appear due to the randomness of the output. As shown in Figure 6.8(a), the lowest WCSS distance appeared in the second last group (59). Importantly, in this example, the lowest WCSS distance recorded by the traditional method ($J = 1186.6$) is still slightly higher than the GA enhanced method ($J = 1186.3$). Note that the most optimised J in theory should still have a large value (around 1186 based on personal experience), since the total number of observations (i.e. feature vectors of segments) is large (6000) and there are inherent differences in the distances between them and the centroids.
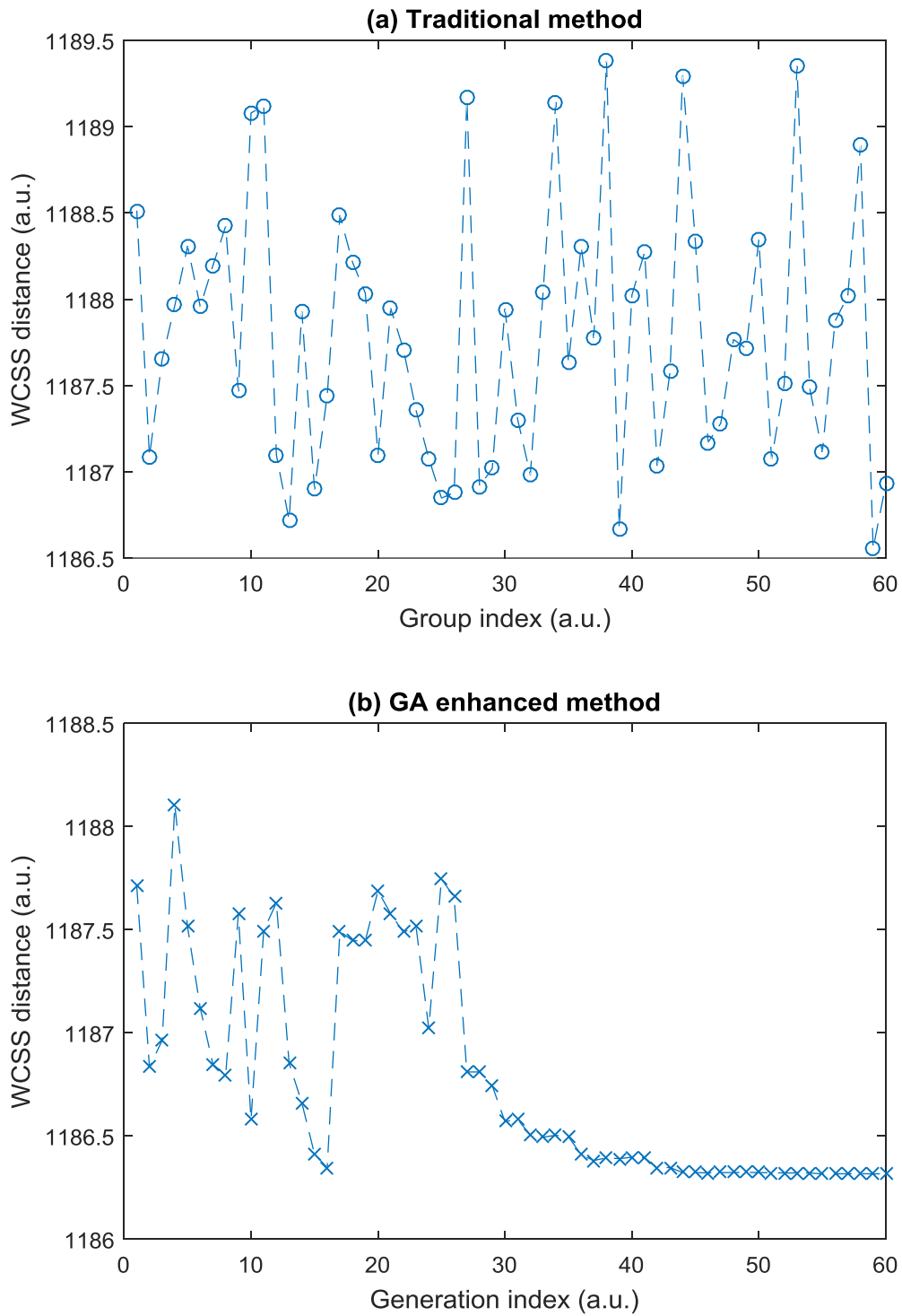
Figure 6.8. Comparison of the WCSS distance trend for the traditional method and the enhanced GA method. (a) The traditional method, the overall iteration is 1800 and been divided into 60 groups. The case with minimum WCSS distance is shown for each group. (b) Enhanced GA method. The population size is 30, and the total generation is 60. The k-means used in both figures have 100 iterations.

6.6 Results

To validate PRDM, experimental data was acquired from two different samples: the Inconel 617 sample with a 46 mm back wall and the austenitic steel sample with a 79 mm back wall. A-scan data was acquired by a 5MHz linear array. In addition, simulation data was generated using the high dispersive model (HDM), introduced in Chapter 3, where the centre frequency is chosen at 5 MHz with 50% transducer bandwidth at -6dB; the sampling frequency is 100 MHz; the attenuation factor α is chosen at 10^{-29}; and the defect amplitude factor is 1.5.

6.6.1 Spectral analysis

Segmental signals were acquired from the austenitic steel sample. After being processed by the MB-SSP algorithm, all segmental signals that contain echo peaks (could be either a legitimate reflector or artefact noise) were selected. STFT was used here to extract features from these test segmental signals. The lowest feature extraction frequency point was to be chosen at 1MHz and the highest frequency point was chosen at 9 MHz, to ensure that more features can be extracted from the spectrum. Initially, spectra are normalised to remove the influence of attenuation. Feature vectors are constructed by points that are extracted equidistantly from the spectra of segments.

Figure 6.9 presents the normalised spectra from 6 different groups after clustering, with 10 individual spectra illustrated from each group. It can be easily seen that the spectra in each group have a similar characteristic, which is varies between the different groups. Table 6.1 gives the percentage of segmental signals in the raw data that been classified as a 'reflector' within each group and this is compared to the detection rate (P_{detect} in Eq. (6.3)) using MB-SSP. Only Group 4 has a significantly small percentage rate compared with the detection rate of MB-SSP, which indicates it should be the only group which belongs to the legitimate reflector.
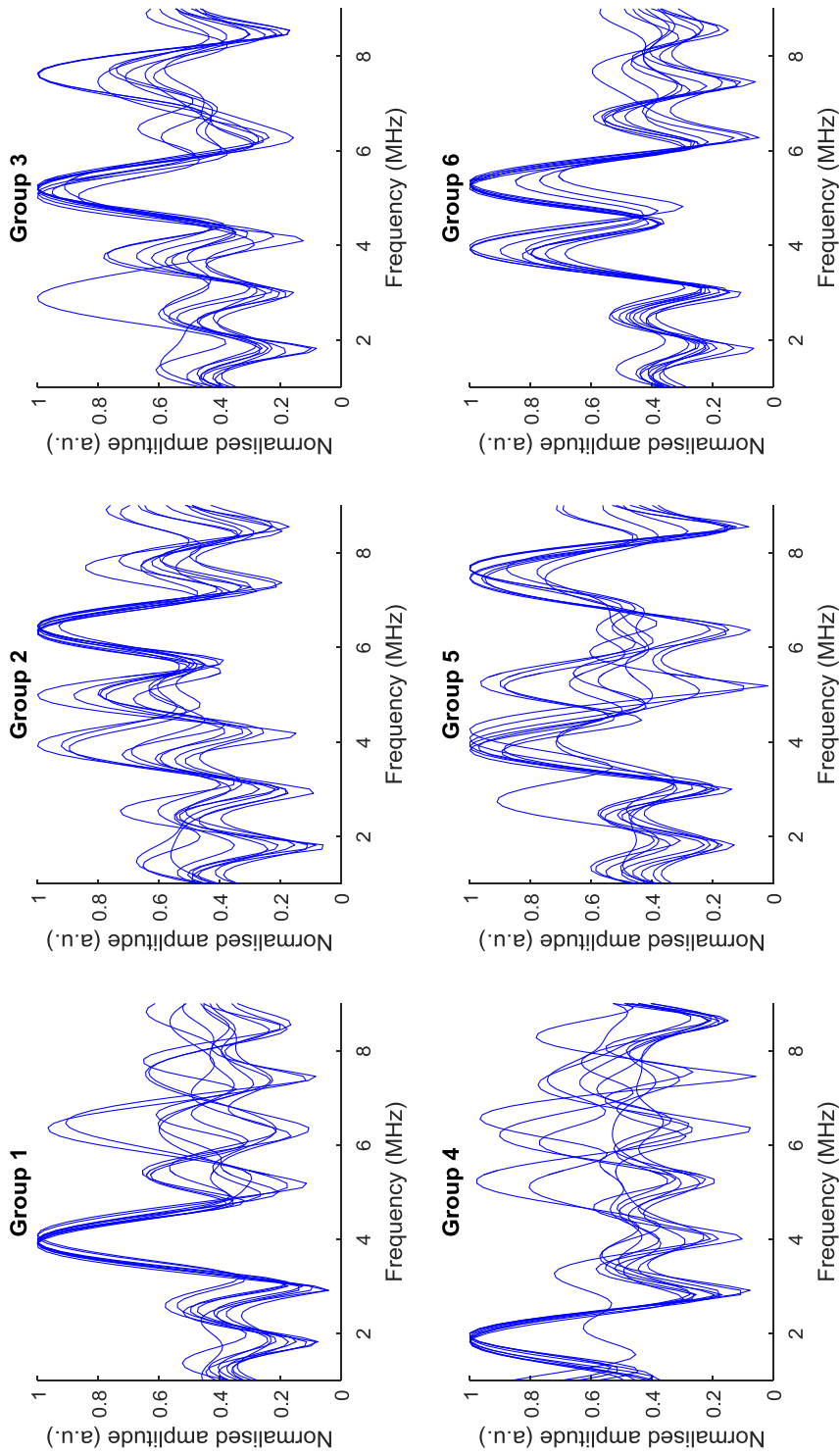
Figure 6.9. Spectra of 6 different clustered groups. All spectra are normalized and 10 spectra are chosen from each group. The raw data were acquired from the austenitic steel sample using a 5MHz linear array.

Table 6.1. Detection rate for the clustered groups presented in Figure 6.9. Group 4 has a significantly small percentage rate compared with the detection rate of MB-SSP, which indicates it should belongs to the legitimate reflector

Detection rate of MB-SSP	24%
Group 1	76.4%
Group 2	49.1%
Group 3	63.8%
Group 4	9.3%
Group 5	65.6 %
Group 6	54.7%

6.6.2   Results of artefact removal algorithm

This Section describes the result of the artefact removal algorithm, using an experimental dataset acquired from the austenitic steel sample (experiment 1) and the Inconel 617 sample (experiment 2). The pre-processing algorithm used in experiment 1 is the MB-SSP algorithm and for experiment 2 the traditional SSP with Minimization algorithm is used.

i.   Experiment 1: austenitic steel

As discussed in Section 6.6.1, Group 4 from Figure 6.9 has the smallest percentage rate and it is most likely to belong to the legitimate reflector. A PRDM processed A-scan example is shown in Figure 6.10(c), together with the raw A-scan signal, Figure 6.10(a), and the corresponding MB-SSP results in Figure 6.10(b).

Although MB-SSP has greatly eliminated the grain noise from the raw signal and correctly shows the location of the back wall at ~79 mm, many artefacts have been retained. It can be easily seen that after further processing by PRDM, most artefacts in the MB-SSP result have been removed, while the 79 mm back wall echo has been retained. Note that the echo signal of the back wall is slightly distorted because of the strong phase dispersion effect in this difficult material. In addition, the sound

velocity of the material is not a constant value, therefore the measurement of the echo peak is not exactly located at 79 mm.

Figure 6.10. A-scan examples of the austenitic steel sample. (a) Raw A-scan. (b) MB-SSP processed A-scan. (c) PRDM processed A-scan. The back wall echo is at 79mm.

Figure 6.11 shows the B-scan images from raw signals, MB-SSP results and PRDM results. Each B-scan image contains 32 parallel placed A-scans. As can be seen in Figure 6.11(b) and Figure 6.11(c), the B-scan images are consistent with the A-scan results in Figure 6.10. The B-scan image from MB-SSP processing still contains many artefacts, while most of them have been removed after processing using PRDM.

(a) Raw B-scan (austenitic steel)

(b) MBPT processed B-scan **(c) PRDM processed B-scan**

Figure 6.11. B-scan images of the austenitic steel sample. (a) Raw B-scan. (b) MB-SSP processed B-scan. (c) PRDM processed B-scan. The darker colour in the images refers to a higher amplitude. The back wall of the sample is at 79mm.

The Probability of Detection (PoD) and Probability of False Alarm (PFA) of MB-SSP and the proposed PRDM algorithm are given in Table 6.2, to quantify and

compare their performance. As stated in Chapter 3, PoD is the likelihood that an algorithm has correctly identified a legitimate reflector, while the PFA is the likelihood that an algorithm has incorrectly classified a noise peak as a defect. Interestingly, the PoD for both MB-SSP and PRDM are similar, but importantly the PFA for PRDM is significantly less when compared to the MB-SSP algorithm.

Table 6.2. PoD and PFA calcualted for the MB-SSP and PRDM results presented in Figure 6.11

	Austenitic steel	
	MB-SSP	PRDM
PoD	95.0%	97.5%
PFA	12.4%	4.0%

ii. *Experiment 2: Inconel 617*

Figure 6.12 and Figure 6.13 provide additional experimental results using the Inconel 617 sample and pre-processed using the Minimization algorithm. Interestingly, when compared with Figure 6.11, the proposed algorithm not only reduces the artefacts but also greatly enhances the visibility of the back wall. As can be seen in Figure 6.12(b), the echo peak of the back wall at around 46 mm is smaller in comparison to the noise peak in the data/signal preceding it, with the PRDM methodology producing a single back wall indication, as illustrated in Figure 6.12(c). Accordingly, the back wall feature presented in the B-scan image in Figure 6.13(c) is much clearer than that observed in Figure 6.13(b). As a comparison of the performance, PoD and PFA are given in Table 6.3 and in this case, PRDM outperforms Minimization in terms of both PoD and PFA.
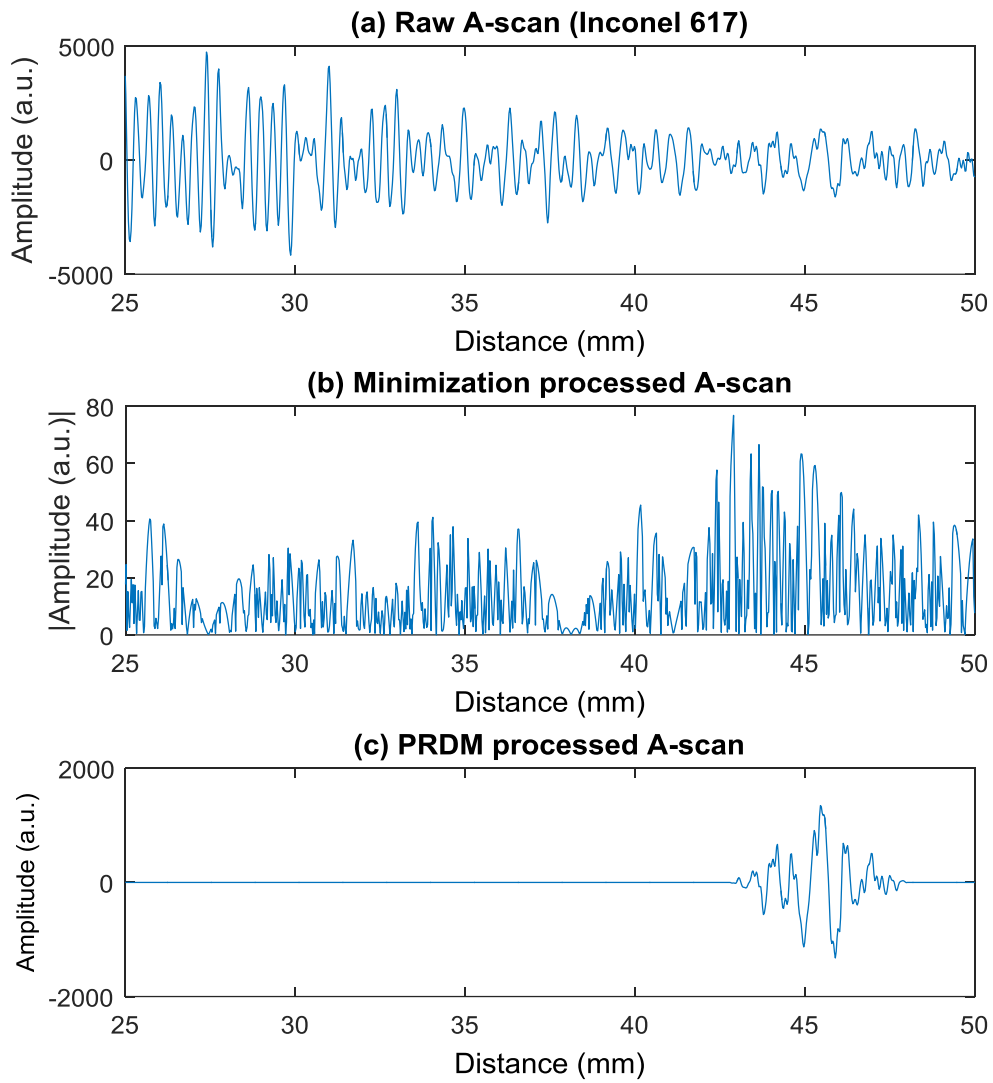
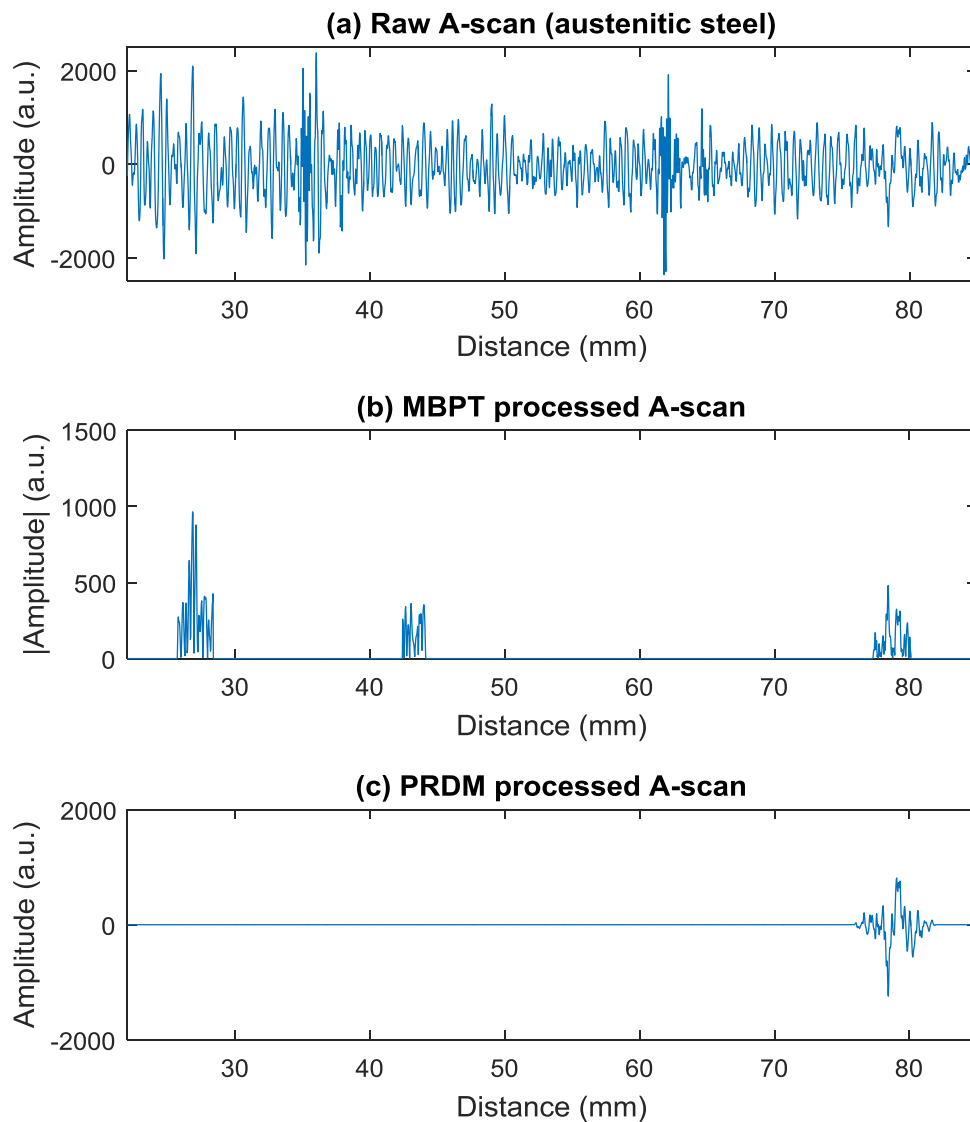Figure 6.12. A-scan examples of the Inconel 617 sample. (a) Raw A-scan. (b) Minimization processed A-scan. (c) PRDM processed A-scan. The back wall echo is at 46mm.
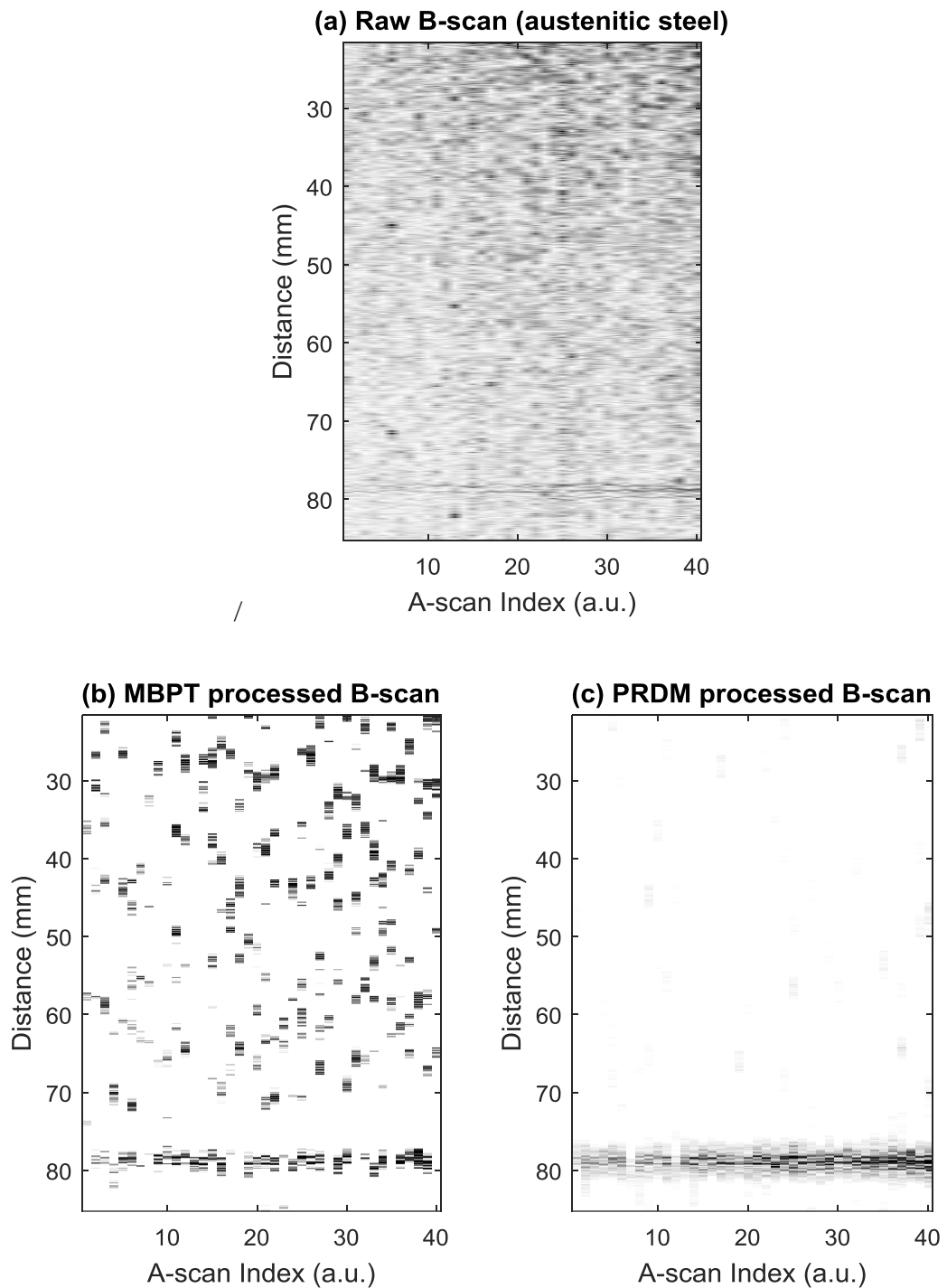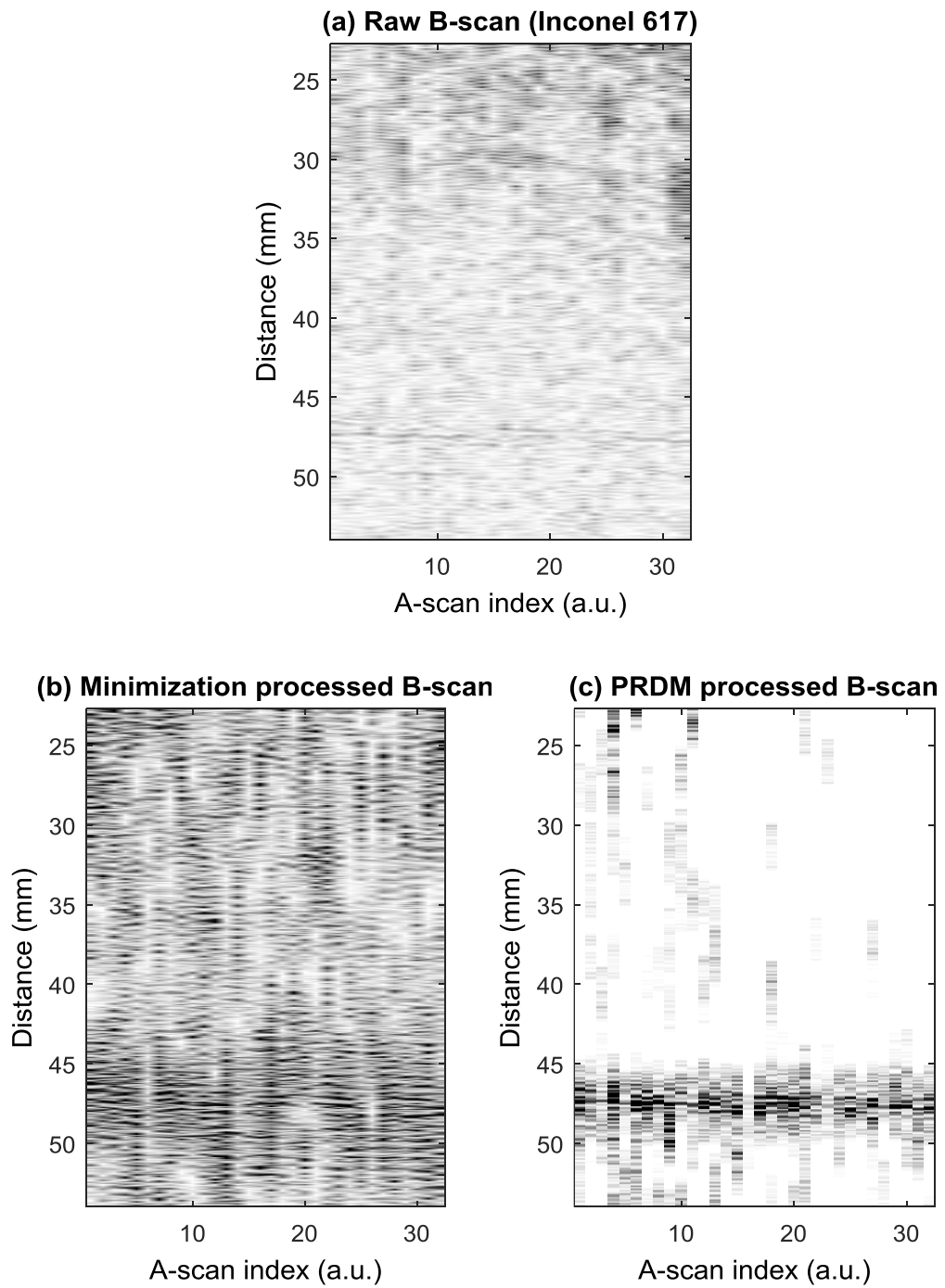
Figure 6.13. B-scan images of the Inconel 617 sample. (a) Raw B-scan. (b) Minimization processed B-scan. (c) PRDM processed B-scan. The darker colour in the images refers to a higher amplitude. The back wall of the sample is at 46mm.

Table 6.3. PoD and PFA calcualted for the Minimization and PRDM results presented in Figure 6.13

	Inconel 617	
	Minimization	**PRDM**
PoD	87.5%	94.3%
PFA	19.6%	8.9%

6.6.3 Results of training data extraction algorithm

This Section shows the experimental and simulation results demonstrating how clustering can be used to help to extract training data for classification algorithms. Figure 6.14 illustrates the areas of B-scan images that contains a back wall feature. The data was acquired from the austenitic steel sample and both B-scan images in Figure 6.14 are formed from 120 A-scans. Figure 6.14(a) is the raw image and Figure 6.14(b) is one of the processed images which clearly shows an indication. Comparing the two B-scan images it can be seen that there is a clear indication in Figure 6.14(b) at the correct location of the back wall, which can only be faintly seen in the raw image in Figure 6.14(a). Importantly, this Figure is only used to indicate the best area to select training data and is not the image of de-noised reflector echoes.

Simulation data is also used to validate the proposed algorithm, in the case that the echo location of the legitimate reflector in each A-scan is slightly different, which inhibits the direct observation of the flaw / back wall indication in the raw image. The data was simulated using the high dispersive model (HDM) with $\alpha = e^{-29}$, $s = 1.5$, 5MHz centre frequency. Figure 6.15(a) gives an example that the echo peak of the legitimate reflector in each A-scan is distributed randomly between 74mm and 76mm. It can be seen that the legitimate reflectors indication in the raw image is completely hidden, which make the extraction of training segment difficult. After processing using the PRDM algorithm, the B-scan image shows a distinct feature at around 75mm, Figure 6.15(b), which is very likely to be the line of the legitimate reflectors and hence, can be used to guide the training segment extraction.
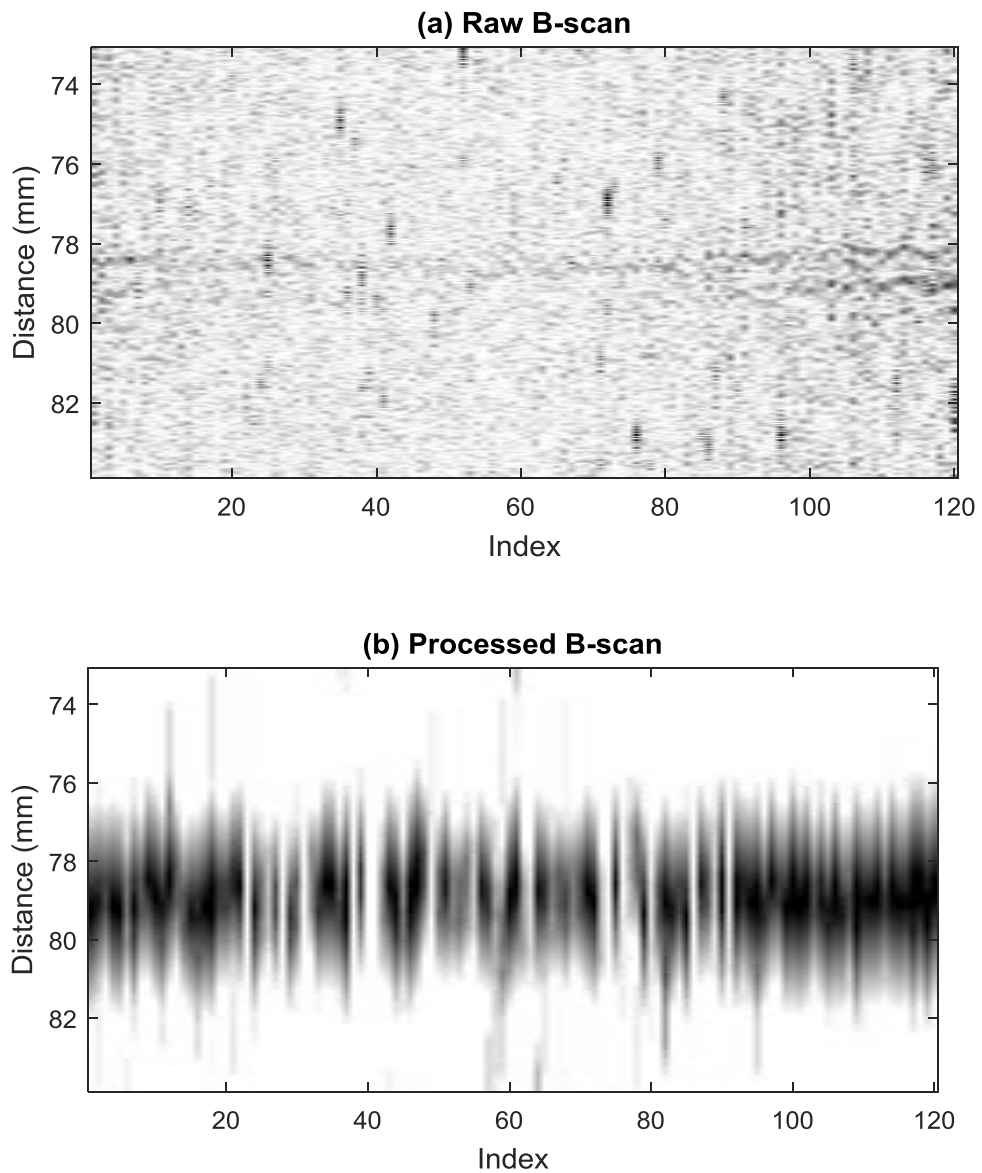
Figure 6.14. Using PRDM to find the training segments of the legitimate reflector. The data was acquired in the austenitic steel sample. (a) Raw B-scan image contains 120 A-scans. (b) One of the processed B-scan image using PRDM. The darker colour indicates higher amplitudes. The back wall echoes can be seen in the raw B-scan image in (a) at around 79mm, since their peaks aligned as a dark line. The processed B-scan in (b) correctly shows this distance.

6.7 Summary

This Chapter has discussed how unsupervised clustering algorithms can be used to support ultrasound A-scan signal processing to improve image clarity for difficult material inspections. With the help of clustering algorithms, segmental signals that

211

have similar characteristics can be grouped together and combined with classification algorithms to further eliminate artefact signals that typically remain from the A-scan signals processed by other algorithms. It can also be used to assist in accurately locating training segmental signals for the classification algorithms, which can feed into the work previously introduced in Chapters 4 and 5.
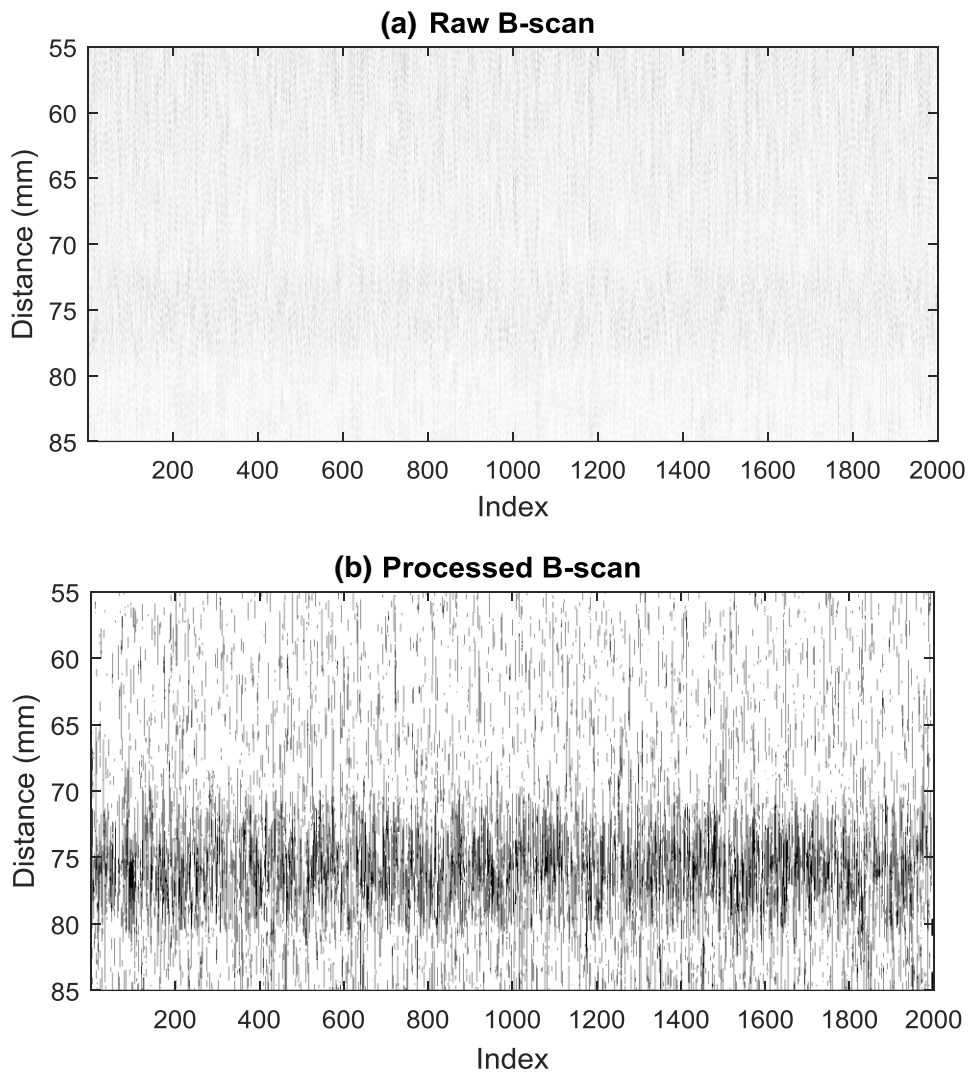
Figure 6.15. Using PRDM to find the training segments of the legitimate reflector. The data was simulated using the high dispersive model with $\alpha = e^{-29}$, $s = 1.5$, 5MHz centre frequency. (a) Raw B-scan image contains 2000 A-scans. (b) One of the processed B-scan image using PRDM. The darker colour indicates higher amplitudes. The legitimate reflector echoes are randomly distributed between 74mm to 76mm which are hidden in the raw image (a). The processed B-scan in (b) shows the location of the legitimate reflectors line.

k-means clustering was used as an example technique in this Chapter to demonstrate the proposed concept as it is one of the most well-known and commonly used clustering algorithms. *k-means* is simple and straightforward to be applied, but its performance relies on the initial location of the centroids of each cluster, with the initial location chosen randomly. Conventionally, an optimal location of centroids can be selected by trial-and-error. Here, an advanced method has been described which combines clustering with a genetic algorithm approach. Initial result shows that with the help of GA, an optimised centroids location is more easily found.

Another issue that may affect the performance of *k-means* in this application is the number of clusters. As every test dataset is different, the best number of clusters is hard to determine. Ball and Hall have proposed an advanced algorithm based on *k-means* named Iterative Self-Organizing Data Analysis Technique (ISODATA) [179], which can automatically decide the number of clusters by merging or splitting during the calculation. However, this requires presetting a threshold which is based on the expected density of each cluster. As the pre-knowledge of the test dataset is usually lacking for applications involving difficult material, this would difficult to implement for such NDE inspections. Experience suggests that the clusters should be not less than 10 in order to separate the legitimate reflector segments from grain noise segments.

Experimental results demonstrated that the PRDM algorithm can further remove artefact noise signals by comparing the PoD and PFA to other approaches: MB-SSP and SSP algorithm (with Minimization as the reconstruction method). Overall, PRDM has outperformed both of these other techniques in terms of PoD and PFA, although the austenitic steel sample produced relatively close results for PoD from both MB-SSP and PRDM approaches.

An addition benefit of the PRDM approach is for supporting the extraction of appropriate training data sets which are then used to train the classification algorithms. The PRDM algorithm was shown using both experimental and simulation data that is can be used to improve extremely low SNR raw B-scan images and support the identification of legitimate reflector echoes.

Chapter 7

A-scan based noise reduction techniques in array imaging

Chapters 3 to 6 introduced several different A-scan based defect detection techniques. These techniques are all frequency diversity (or using other spectrum-based characteristics such as wavelet) based algorithms. In recent years, phased array transducers have become more commonly used in industry. Phased array transducers have by their nature an advantage to include spatial diversity since they observe targets from different orientations. As introduced in Chapter 2, structural noise in coarse-grained materials is not only frequency sensitive, but also spatial sensitive. The influence of grain noise can be reduced by observing from different angles and positions, with an appropriate time delay introduced for each observation. The concept of spatial diversity is not new to array applications, with algorithms such as Synthetic Aperture Focusing Techniques (SAFT) widely used. With the possibility of different combinations of array elements, many array based imaging techniques have been developed and outclass the performance of SAFT, such as the classic focused B-scan which is also widely used in industry, and the golden standard imaging algorithm Total Focusing Method (TFM) [27]. Many advanced spatial diversity based algorithms have also been proposed recently, such as Spatially Averaged Sub-Array Correlation Imaging (SASACI) [89] and Correlation for Adaptively Focused Imaging (CAFI) [90].

Based on array imaging applications, there are also advanced techniques using both spatial and frequency diversity that have been developed, such as Spectral Distribution Similarity Analysis (SDSA) [126] and Phase Coherence Imaging (PCI) [10]. SDSA calculates the spectrum similarity of A-scan segments across different transmitting-receiving pairs of array elements, while PCI uses the concept that grain

noise has a more random distributed phase compared with a target flaw across different A-scans.

Since phased array probes are increasingly being used in many applications and importantly, the spatial diversity approach can potentially be applied to the A-scan data. This Chapter will investigate extending the A-scan based algorithms that have been introduced in Chapters 3-6 into phased array imaging techniques.

7.1 Analytical modelling of 1-D linear phased array

Before introducing and evaluating the array imaging algorithms, the frequency domain based analytical model that was introduced in Chapter 3 should be modified to adapt to the phased array configuration. Figure 7.1 shows a slice of an inspection medium attached to a 1-D phased array. A Cartesian coordinate system is implied, where x and z represent locations in the lateral and axial directions, respectively. The zero reference point $(0,0)$ is assumed at the centre of the array. Figure 7.1 illustrates the ultrasound wave path from a transmit element tx at $(x_{tx}, 0)$ to a point reflector (a legitimate reflector or a scatterer) at (x_k, z_k), and reflected back to a receive element rx at $(x_{rx}, 0)$.
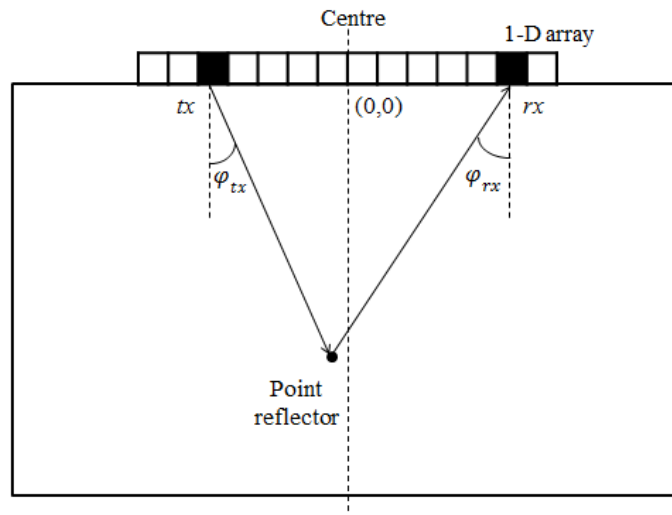
Figure 7.1. Schematic diagram of a 1-D linear array and the wave propagation path for a point reflector.

Building on the discussion in Section 3.1, the frequency response of an echo $R(\omega)$ from a distant reflector can be expressed as,

$$R(\omega) = \sigma H_{tran}(\omega) H_{refl}(\omega) e^{-i\omega\tau}$$
(7.1)

where , σ is the reflection coefficient, $H_{refl}(\omega)$ refers to the frequency response of the material, $H_{tran}(\omega)$ now contains the frequency response of the transmit and receive array elements, hence will be replaced as the product $H_{tx}(\omega)$ and $H_{rx}(\omega)$. τ is the total wave propagation time from the transmit element to the point reflector and then to the receive element, which can be calculated as

$$\tau = \frac{d}{v} = \frac{d_{tx} + d_{rx}}{v}$$
(7.2)

where

$$d_{tx} = \sqrt{(x_{tx} - x_k)^2 + z_k^2}$$
(7.3)

is the distance between the transmit element tx and the point reflector,

$$d_{rx} = \sqrt{(x_{rx} - x_k)^2 + z_k^2}$$
(7.4)

is the distance between the point reflector and the receive element rx, and v is the wave speed.

A single element transducer is usually directional and has a relatively focused beam, whereas for array elements the energy distribution of the waves has a wider characteristic. For this reason, the model should include two additional factors, the directivity function, and the divergence factor to include the effect of beam directivity and beam spread, respectively [27]. According to McNab and Stumpf [180] and assuming the length of an element is much longer than the width, the directivity function of a single rectangular element in a 2-D model can be defined as

$$P_{tx} = \text{sinc}\left(\frac{\pi w \sin \varphi_{tx}}{\lambda}\right)$$
(7.5)

and

216

$$P_{rx} = \text{sinc}\left(\frac{\pi w \sin \varphi_{rx}}{\lambda}\right) \tag{7.6}$$

where w is the width of an element, and λ is the wavelength of the ultrasonic wave. φ_{tx} and φ_{rx} are the angles between the element normal and the wave path, for the transmit element and the receive element, respectively.

The beam spread effect that reduces the wave energy at the location of a reflector can be simply estimated using the following equation,

$$E_{tr} = \frac{1}{\sqrt{d_{tx}d_{rx}}} \tag{7.7}$$

for the entire propagation distance of the ultrasonic wave. Here d_{tx} and d_{rx} are the distances between the transmit element and the receive element to the reflector, as shown in Eq. (7.3) and (7.4), respectively.

Therefore, the spectrum of a legitimate reflector $R_{Sig,tx,rx}(\omega)$ and the spectrum from grain noise $R_{Noi,tx,rx}(\omega)$ for each tx-rx pair can be simulated as

$$R_{Sig,tx,rx}(\omega) = sP_{tx}P_{rx}E_{tr}H_{tx}(\omega)H_{rx}(\omega)H_{refl}(\omega)e^{-i\omega\tau} \tag{7.8}$$

and

$$R_{Noi,tx,rx}(\omega) = H_{tx}(\omega)H_{rx}(\omega)\sum_{k=1}^{K}\sigma_k P_{tx}P_{rx}E_{tr}H_{refl}(\omega)e^{-i\omega\tau} \tag{7.9}$$

respectively, where k is the index of a scatterer and K is the total number of the scatterers in the model. Again, the reflection coefficient σ in Eq. (3.7) is removed, since it is a constant number for a legitimate reflector signal. s is the defect amplitude factor which is used to adjust the ratio between the legitimate reflector echo amplitude and the noise level, after both has been normalised.

After substituting the material frequency response, Eq. (3.18), the scatterer frequency response, Eq. (3.19), and the Nearly Local model, Eq. (3.20), into Eq. (7.8) and Eq. (7.9), an inverse Fourier transform is applied to complete the array high dispersion model (AHDM). The process of converting the low dispersion model (LDM) to the

array application is similar. In this Chapter, only the AHDM is used to evaluate the imaging algorithms.

7.2 Array imaging using processed FMC

A simple and direct way to combine the A-scan based noise reduction techniques to array imaging is by processing each raw A-scan individually before applying the imaging algorithm. This can be achieved by processing each raw A-scan in the FMC dataset and applying a post-processing algorithm, such as TFM, which will be used as the reference example in this Chapter.

The first example combines MB-SSP (Chapter 3) and SRC (Chapter 4) processing of the individual A-scans in the FMC dataset with the TFM imaging algorithm. The FMC dataset was simulated using the AHDM model, with the centre frequency set at 5MHz with 50% transducer bandwidth at -6dB. The sampling frequency is 100MHz. The attenuation factor α is chosen at 10^{-29}. A point reflector is simulated at 75mm depth, directly below the centre of the 1-D linear array, with a defect amplitude factor s at 1.5, as defined by Eq. (3.22). The density of the scatterer field is simulated at 5 scatterers/wavelength^2 to simulate Rayleigh distributed grain noise [41]. The array configuration is simulated with 64 elements, each with a 0.7mm element size. A representative schematic diagram is presented in Figure 7.2.

As can be seen in Figure 7.3, the point reflector observed in the raw TFM image can be easily confused with grain noise. The intensity of the grain noise is close to that produced by the point reflector. Figure 7.4 is the TFM image after the FMC is processed by the MB-SSP. It can be seen that the noise level is lower than the raw TFM, and subsequently, the point reflector is more visible. Figure 7.5 is the TFM image after the FMC dataset has been processed by the SRC. The back ground noise in this image has been further reduced compared with Figure 7.4 since the SRC has a better noise reduction capability compared with the MB-SSP, as discussed in Chapters 3 and 4. Table 7.1 gives the calculated SNR for each of the three images in Figure 7.3-Figure 7.5.
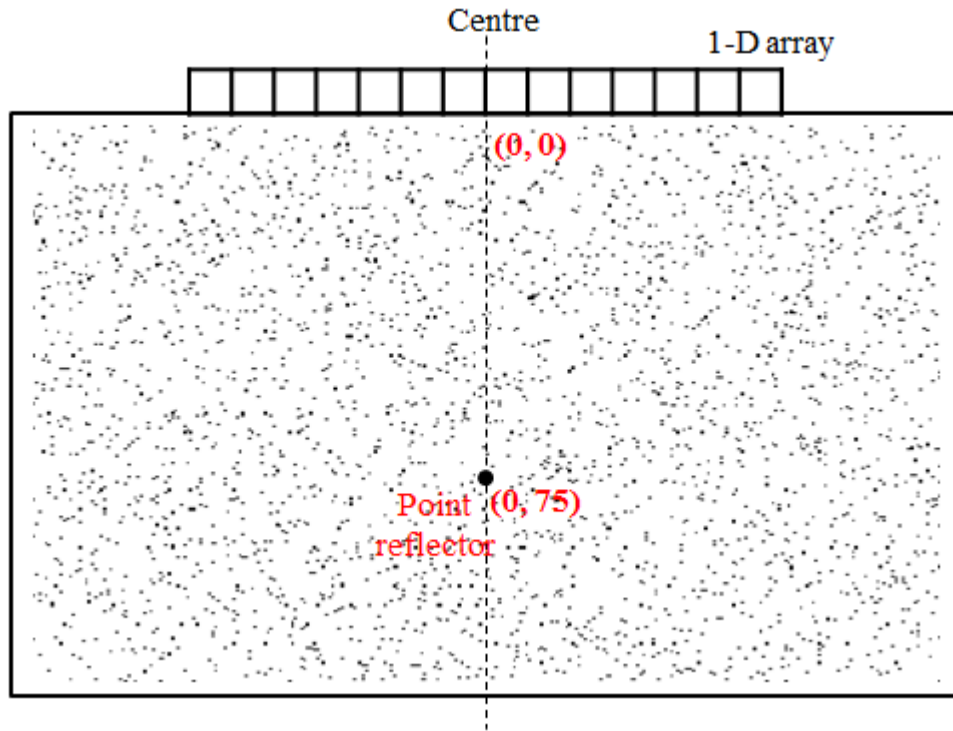
Figure 7.2. Schematic diagram of the simulation model. A point reflector is set at (0mm, 75mm), and surrounded by scatterers with a density of 5 scatterers/wavelength^2.
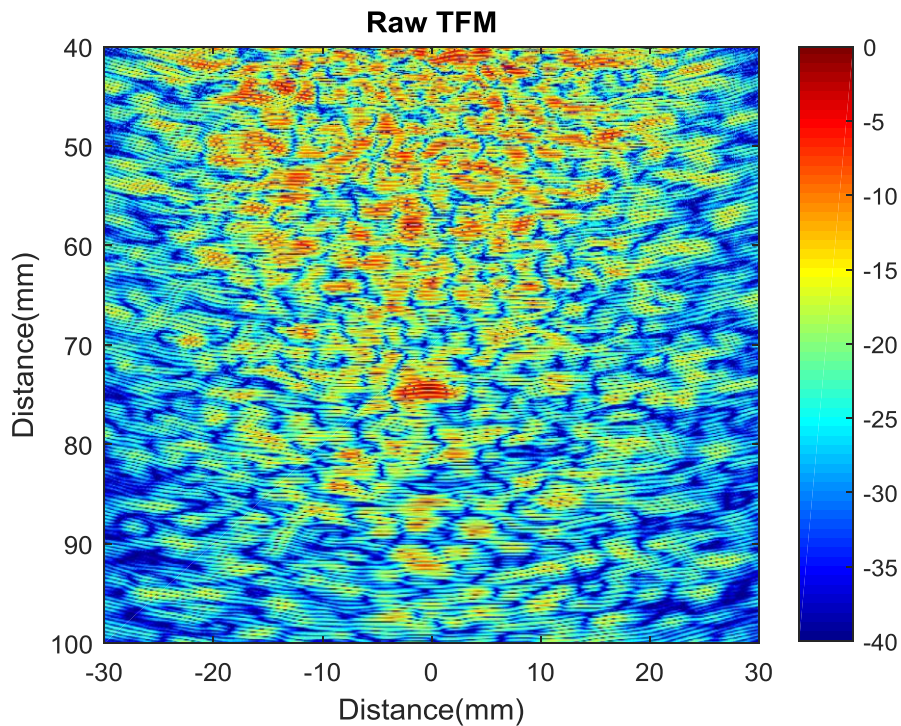
Figure 7.3. Raw TFM image generated by the simulated FMC. The FMC is simulated using the high dispersive model with $\alpha = e^{-29}$, $s = 1.5$, 5MHz centre frequency. The array parameters are set at 64 elements, 0.7mm element size.
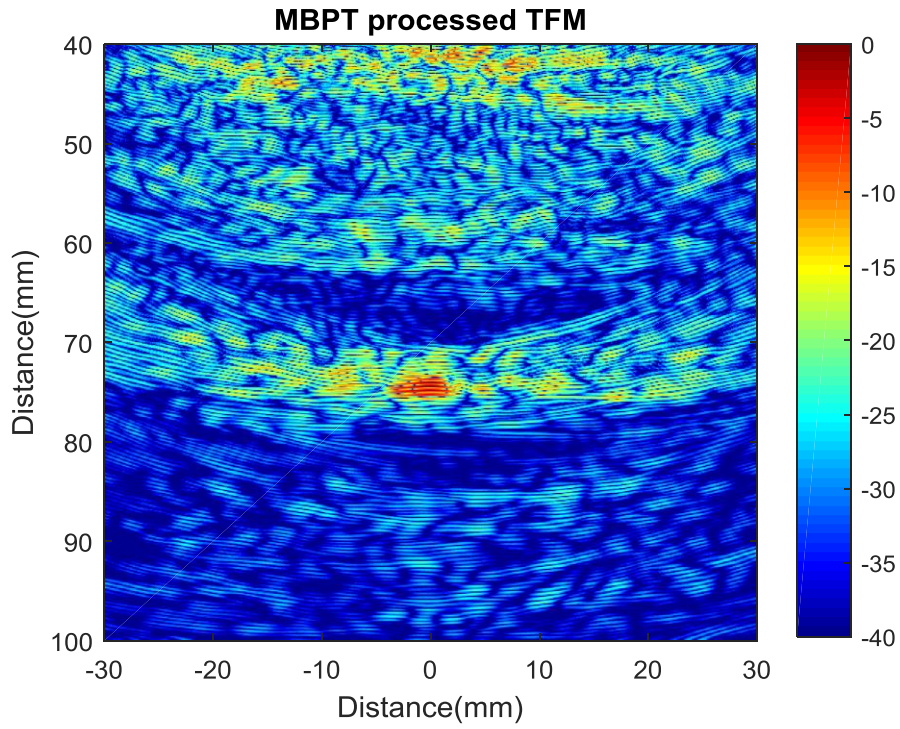
Figure 7.4. MB-SSP processed TFM image generated by the simulated FMC. The FMC is the same one that was used in Figure 7.3 and pre-processed by MB-SSP before imaged using TFM.
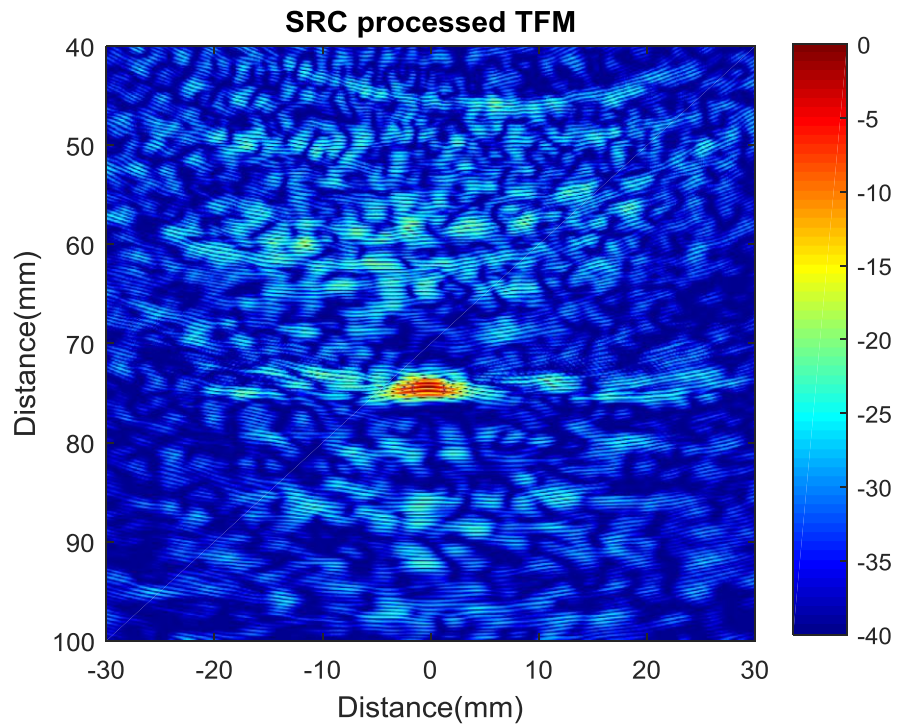
Figure 7.5. SRC processed TFM image generated by the simulated FMC. The FMC is the same one that was used in Figure 7.3 and pre-processed by SRC before imaged using TFM.

Table 7.1. SNR of images in Figure 7.3, Figure 7.4, and Figure 7.5. The SNR of FSPC image in Figure 7.8 is also given in this table for comparison.

Raw TFM	10 dB
MB-SSP processed TFM	26 dB
SRC processed TFM	35 dB
FSPC	49 dB

The TFM algorithm and other traditional array imaging techniques can reduce grain noise and enhance legitimate reflectors since a legitimate reflector has a more coincident phase distribution among A-scans of different transmitter-receiver pairs compared to grain noise. The intensity of a point in the image where only grain noise is present would be counteracted when superposing the amplitude of the related points in each A-scan, as illustrated in Figure 7.7.6. However, this mechanism and the processed-FMC approach, using A-scan based noise reduction techniques, cannot fully benefit each other when producing images. The FMC still contains a few artefact echoes after processing by the A-scan based noise reduction techniques, and these artefacts are sometimes difficult to be reduced since the related point in other A-scans are zeros, as shown in Figure 7.7.6.

Although the reduced noise in A-scans does improve the SNR in the related image, the background noise can still be clearly observed, as illustrated in the images shown in Figure 7.3 – Figure 7.5.
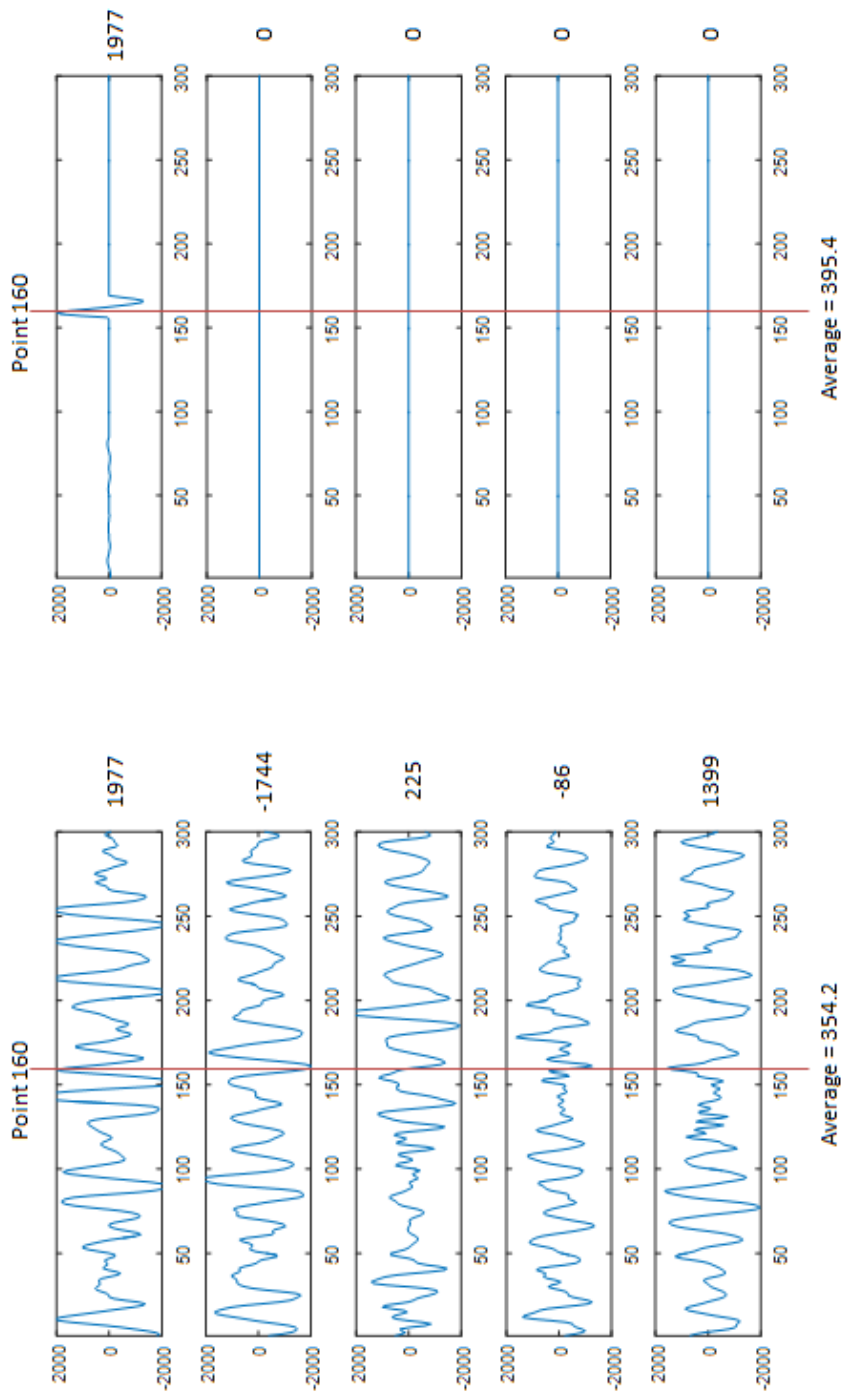
Figure 7.7.6. Noise counteracting for A-scans after focal law is applied. The five A-scans on the left is the raw signals and the five A-scans on the right is processed by noise reduction techniques. The top right A-scan has an artefact noise echo remains. The number next to each A-scan is the amplitude of the sample point 160 of it. The artefact noise has no other echoes to counteract it as the noise at the same position in other signal has all been removed. This causes the average in the right hand side group are even higher than the raw signal group.

7.3 Frequency-spatial polarity coherence

An alternative way to combine the MB-SSP technique with the array imaging is now introduced in this Section. As shown in Figure 7.4, although the MB-SSP processed TFM has an improved SNR, the background noise in the image is still strong. Another issue is the strong lateral noise near the point reflector. The high energy of this noise is leaked from the point reflector and is caused by the off-axis effect when imaging. Therefore, to further improve the image quality, a new algorithm named Frequency-Spatial Polarity Coherence (FSPC) has been developed that takes benefit of both spatial and frequency information. The FSPC achieves grain noise reduction in images by applying both frequency and spatial diversity. The entire procedure can be described in five steps, as illustrated in the flowchart presented in Figure 7.7.

- Step 1: Partition each A-scan in the full matrix capture into a serial of overlapped frequency bands;
- Step 2: Check the polarity coincidence inside each frequency band;
- Step 3: Apply a focal law to generate a coefficient matrix within each frequency band;
- Step 4: Combine all coefficient matrix to generate weighting matrix;
- Step 5: Use the weighting matrix to reconstruct the final output image.

Further details of each step in the FSPC algorithm will now be presented.

7.3.1 FSPC Methodology

i. Spectrum partition approach

Like MB-SSP, for all A-scan traces in the acquired Full Matrix Capture (FMC) dataset, FSPC firstly divides the A-scan data into a set of sub-signals which contain different frequency bands. This is achieved by bandpass filtering the raw signal or applying a window function to its spectrum. The reason to divide the spectra of the raw signals into these sub-bands is that the attenuation and scattering of the transmitted ultrasound wave are highly frequency dependent. That means the energy of the target flaw can only partly dominate the frequency range of the received echo

spectrum. The aim of this spectrum partitioning is to determine the most effective frequency range to process.

To avoid the possibility of failing to detect a flaw, there should be an overlap of at least 50% between adjacent filters/windows. Moreover, to enhance information from the raw A-scan signals, the spectral range of total processed bandwidth which contains all filters or windows, should be chosen as wide as possible: typically around 100% bandwidth of the transducer centre frequency. These sub-signals will be denoted as $Y_j(n)$, where n is the time delay and j is the index of filter or window.
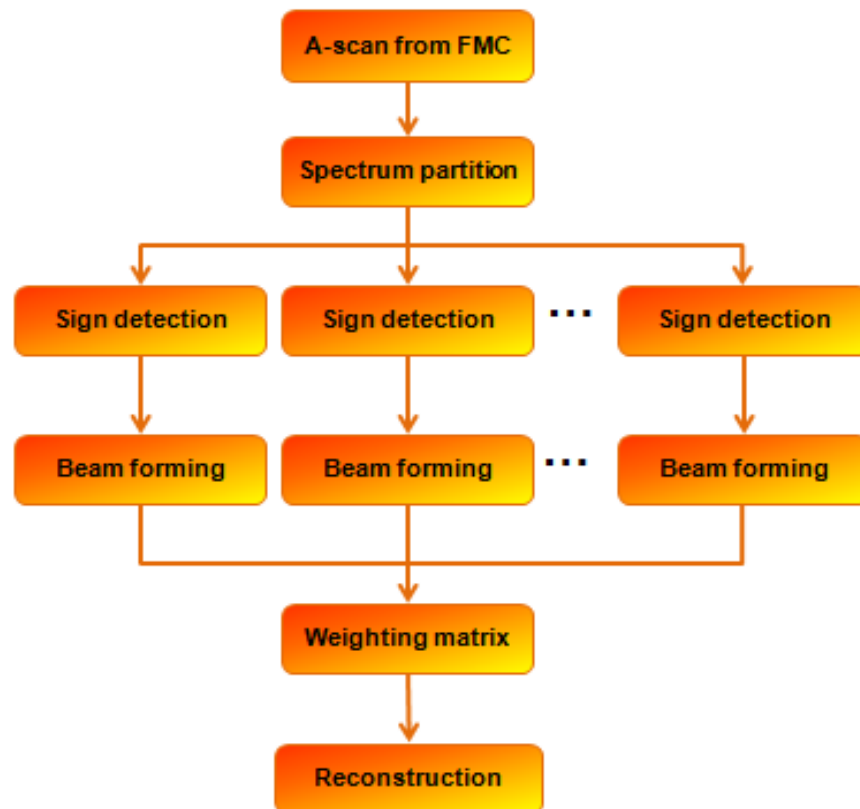
Figure 7.7. Flow chart of Frequency-Spatial Polarity Coherence (FSPC)

ii.   *Sign detection in localised spectrum*

For each sub-signal, $Y_j(n)$, there is the possibility that the spectrum energy of the target flaw could fully dominate the bandwidth of $Y_j(n)$. Hence, the potential location of the target flaw can be detected by applying frequency diversity inside

$Y_j(n)$ itself. This is achieved by checking the polarity coincidence across different frequency channels inside $Y_j(n)$: further splitting $Y_j(n)$ into several channels within its own bandwidth. During this process, if all channels are positive/negative at a specific time delay, then this point is denoted by '1' or '-1' as a potential flaw location, otherwise a '0' is recorded, as shown below:

$$Z_j(n) = \begin{cases} 1, & if \ all \ C_m(n) > 0 \\ -1, & if \ all \ C_m(n) < 0 \\ 0, & otherwise \end{cases} \quad (7.10)$$

where $C_m(n)$ refers to a channel filtered by a Gaussian window, m is the index of channels.

Based on the principle that the spectrum of a legitimate reflector (flaw, back wall, etc.) is generally wider than the spectrum of grain noise, the bandwidth of $Y_j(n)$ needs to be wide enough to ensure that the algorithm can distinguish the legitimate reflector from grain noise. However, for a coarse-grained material, if the bandwidth of $Y_j(n)$ is too wide, the spectrum of the legitimate reflector may become inconsecutive and hence will no longer predominate. This will cause a loss of detection capability. In this case, the bandwidth of the filters/windows in the previous step is critical for the algorithm performance and typically, this should be around 80% fractional bandwidth of the transducer centre frequency.

iii.   Beamforming in localised spectrum

After all A-scans in the FMC have been processed, a set of coefficient matrices will be generated using all processed $Z_j(n)$ values. Each coefficient matrix represents the polarity coherence of a certain frequency range.

Generally, the echoes from a legitimate reflector have a more consistent phase across the A-scans received by different array elements after the focal law has been applied, while structural noise have a more random distributed phase.

Ideally, the location of a flaw in the matrix will be enhanced due to the sign coincidence across different A-scans, while the grain noise will be suppressed.

iv.   Weighting matrix generation

When all coefficient matrices have been calculated, a weighting matrix will then be synthesized through compounding of the different frequency bands. This can be achieved in many different ways. A simple way to do this is by averaging all coefficient matrices and setting a suitable threshold. Alternative ways, including order statistics and scaled polarity thresholding, can also be considered and may provide benefits under certain conditions.

Due to the scattering property of the coarse-grained material, the attenuation is highly frequency dependent. Hence, for the region close to the array, more coefficient matrices should be used to increase the imaging resolution, and for the region far from the array, only coefficient matrices in low-frequency bands should be included to maintain detection capability. The number of coefficient matrices included for a certain depth depends on the frequency of transmitted signals and the material attenuation property. In this work, the number of coefficient matrices was chosen empirically.

v.   Reconstruction

A weighting matrix can be used directly to indicate the defect locations, but this does not contain information on the amplitude associated with the defect response. Multiplying the weighting matrix with an image generated using the same focal law conditions, on the same datasets, will reduce the background grain noise while not compromising the important flaw information.

7.3.2   Simulation result

Figure 7.8 shows the FSPC image generated using the same FMC data used previously for Figures Figure 7.3-Figure 7.5. Compared with the MB-SSP and the SRC images, the FSPC image presents a lower background noise level and a higher SNR, as detailed in Table 7.1. Importantly, the lateral noise around the point reflector in the FSPC image is much lower, especially when compared with the MB-SSP image in Figure 7.4.
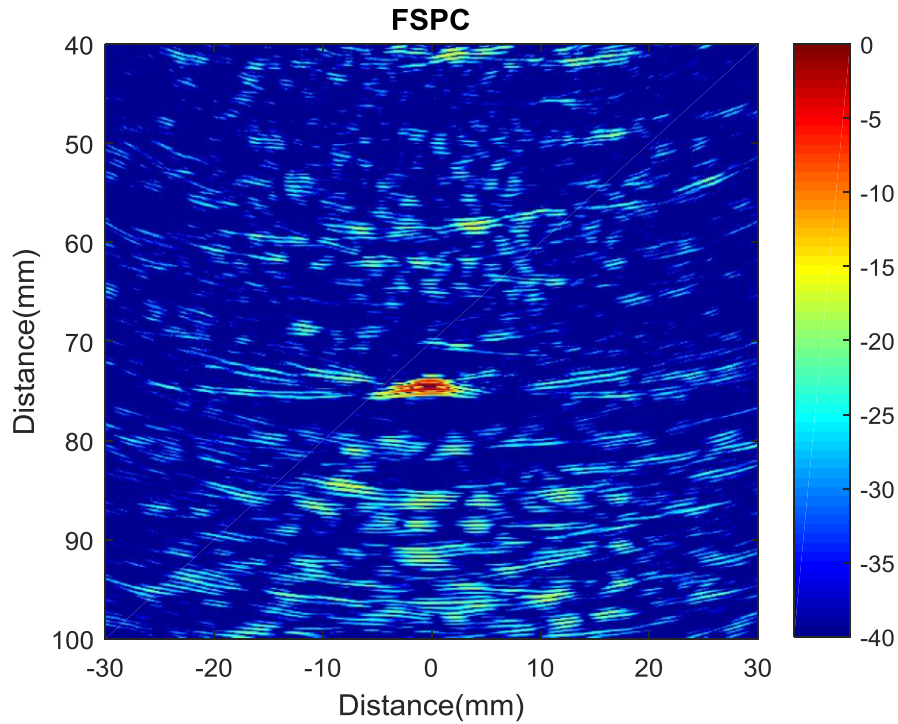
Figure 7.8. FSPC image generated by the TFM algorithm from simulated FMC data. The FMC dataset is the same one that was used in Figure 7.3.

7.4 Experimental evaluation of array imaging approaches

Experimentally acquired FMC datasets are used in this Section to validate the various algorithms developed in this Thesis. Two different samples have been used, the austenitic steel sample and the Inconel 625 sample, using a 5MHz 1-D linear array. The Dynaray phased array controller was used to capture the FMC datasets. Details of the experimental configuration are stated in Chapter 2.

7.4.1 Experiment 1: SRC result of the austenitic steel

As discussed in Section 7.2, after processing every A-scan in a FMC dataset, the revised FMC dataset can be further processed with imaging algorithms like the focused B-scan, TFM, etc. to achieve noise reduction in the resultant images. TFM results of the sample block have been used as a reference for comparison in this

Section. As shown in Figure 7.9, the array was put on the top of the sample block. At this position, the depth of the back wall is 52mm.
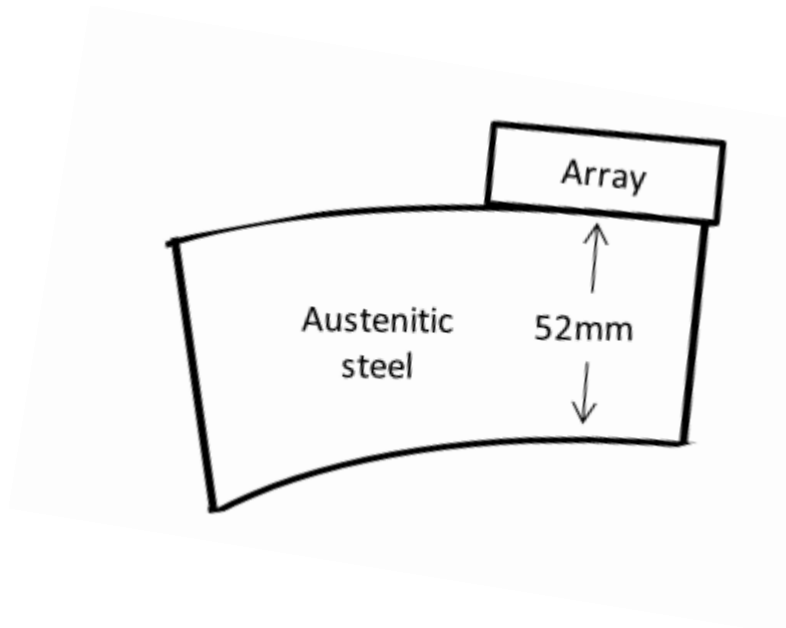
Figure 7.9. Schematic plots of the array and the austenitic sample.

Figure 7.10(a) presents the TFM image of the first back wall using all 64 array elements. Compared with the SRC result, the back ground grain noise has been suppressed in the SRC image shown in Figure 7.10(b). To evaluate the performance of the algorithm, the SNR has been defined as the average of noise area subtracted from the average of signal area; noting that the image is portrayed in dB. The signal area was chosen from the back wall location and the noise is attributed to a large area above the back wall. Importantly, the SNR of the SRC is approximately 20 dB higher than the original TFM image. Note that the noise near the back wall is not completely removed and is caused by the off-axis effects, similar to the lateral noise around the point reflector in Figure 7.4 and Figure 7.5. This effect is less significant for small legitimate reflectors (flaws, side-drilled holes, etc.) in the SRC processed images as can be seen in Figure 7.5, but is not negligible for strong reflectors such as the back wall.
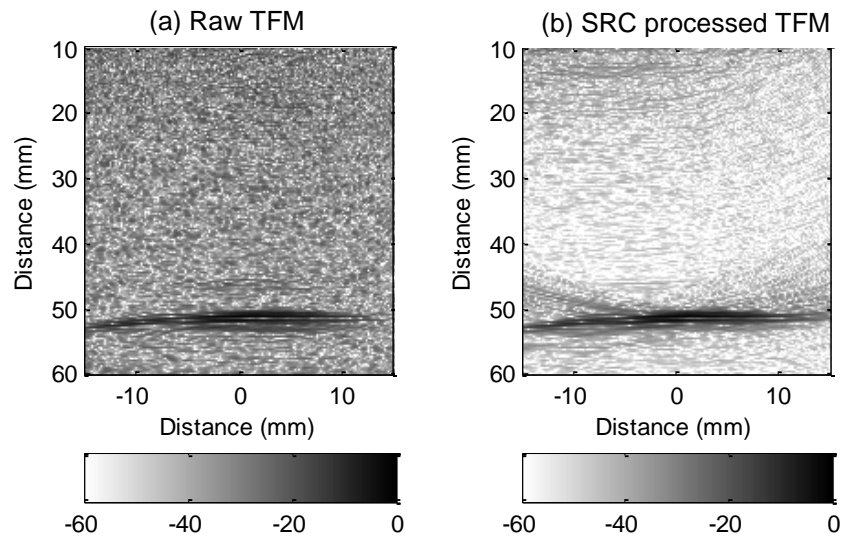
Figure 7.10. TFM and SRC processed images of the austenicit steel sample, using 64 array elements. The back wall is at 52mm. Colourbar represents scale in dB.

Figure 7.11 presents another pair of TFM and SRC images and shows the third reflection of the back wall generated by FMC data with 32 array elements, to demonstrate the performance of SRC in an extreme scenario. In this case, the SNR has been enhanced by 3dB. Although the SNR improvement is not significant, the SRC result clearly indicates the actual location of the feature (at around 156mm) among the artefact shadows.
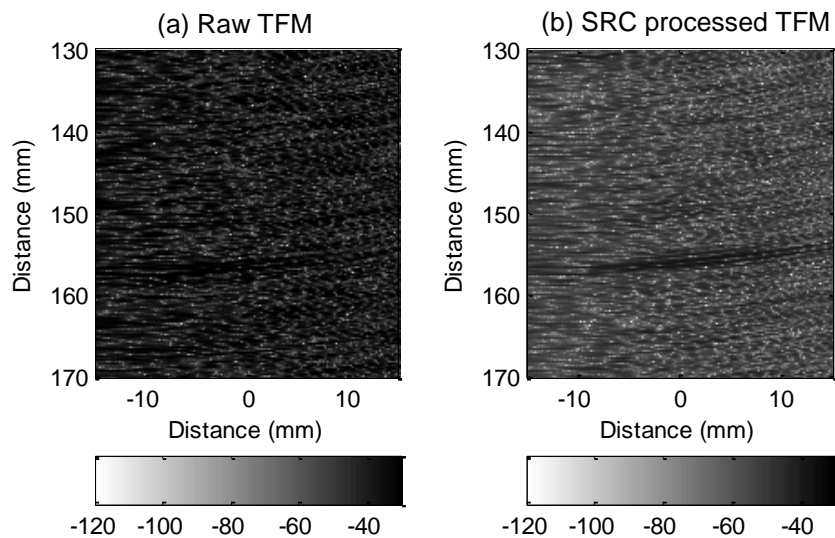
Figure 7.11. TFM and SRC processed images of the austenicit steel sample, using 64 array elements. The images show the third reflection of the back wall at 156mm, to demostrate an extreme scnario.

7.4.2　Experiment 2: FSPC result on the austenitic steel sample

Figure 7.13 presents the FSPC image, and a classic focused B-scan image for comparison, from the austenitic steel sample taken from the opposite and thicker section of the sample as shown in Figure 7.12. The images are 140 mm in depth and contain two reflections of the back wall (located at 57 mm as shown in Figure 7.12) in the sample. The B-scan images were generated by the middle 64 elements of the array, with an aperture size of 16 elements. It can be easily seen that the sample contains strong grain noise, which reduces the visibility of the first reflection of the back wall and buries the second reflection in the classic focused B-scan. By applying FSPC, both reflections of the back wall are clearly evident and importantly, grain noise has been significantly reduced, and SNR is increased by 23dB, as shown in Table 7.2.

Figure 7.14 shows the processed A-scan examples using the classic focused B-scan and the equivalent FSPC techniques (i.e. one of the vertical scan-lines from the images in Figure 7.13). Two back wall echoes are successfully detected for the FSPC while only the first reflection of the back wall can be observed in the focused B-scan.
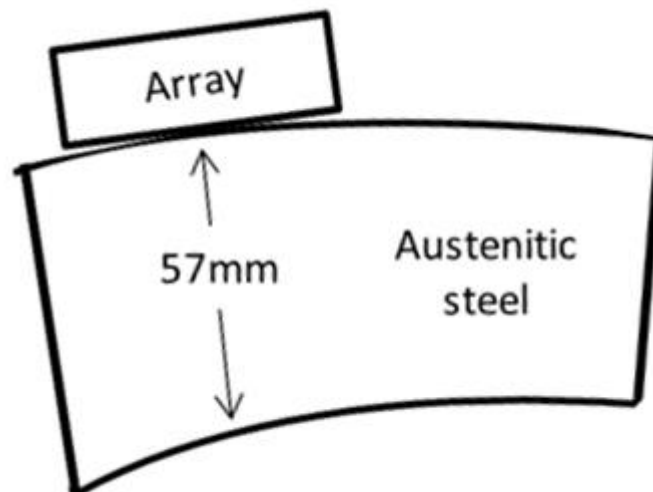
Figure 7.12. Schematic plots of the array and the austenitic sample.
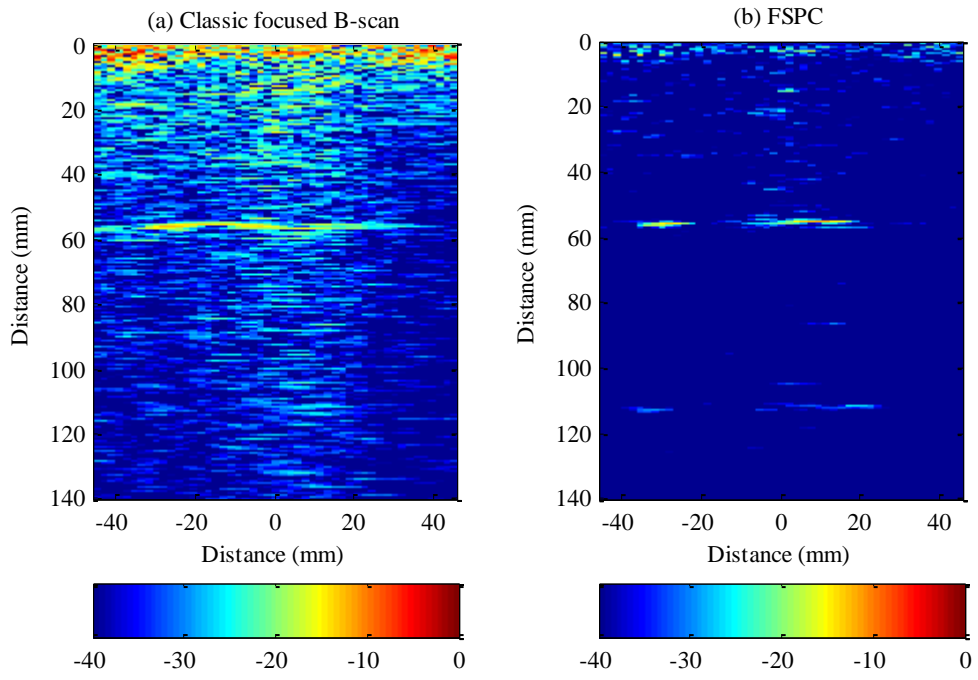
Figure 7.13. Focused B-scan and FSPC images of the austenitic steel sample. 64 elements with an aperture size of 16 used. Two reflections of the back wall are shown in the images, at 57mm and 114mm.
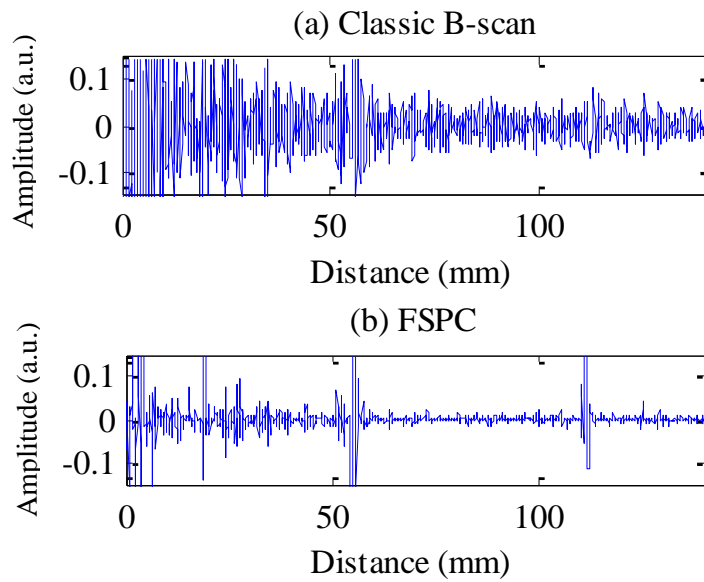
Figure 7.14. Improvement in A-scan noise components when data processed using FSPC

7.4.3 Experiment 3: FSPC result of the Inconel 625

Another experiment which compares the performance between TFM and FSPC algorithms is presented in Figure 7.16, using the Inconel 625 sample. The Inconel 625 sample is 160mm thick and contains 3 side drilled holes (SDHs), with depth around of 7mm, 60mm and 110mm respectively, as illustrated in Figure 7.15. For this experiment, a 64 element aperture has been used to capture to FMC dataset from the 5MHz array. It can be clearly seen in Figure 7.16(b) that the background grain noise is predominantly removed, and the three SDHs and the back wall become clearer. Moreover, to show the performance and improvement of FSPC for these experimental results, the related SNR are given in Table 7.2.
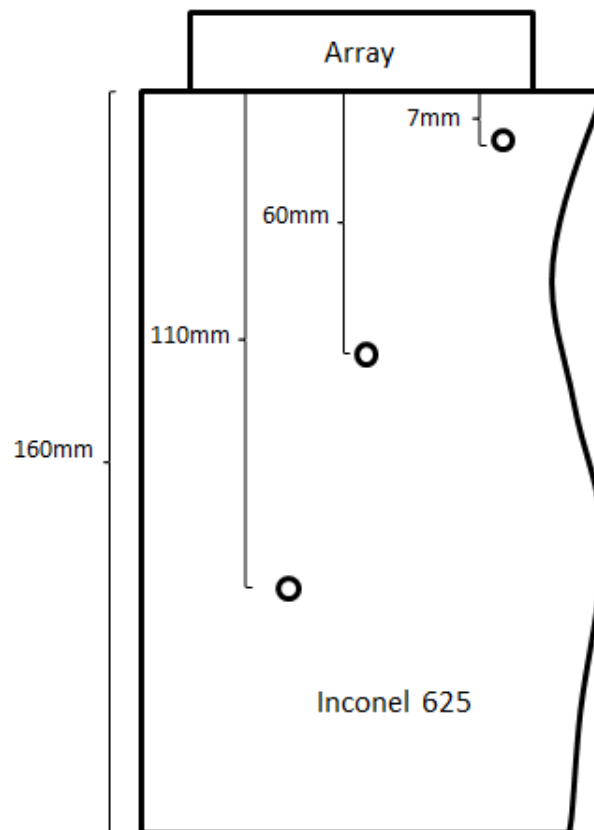
Figure 7.15. Schematic plots of the array and the Inconel 625 sample.
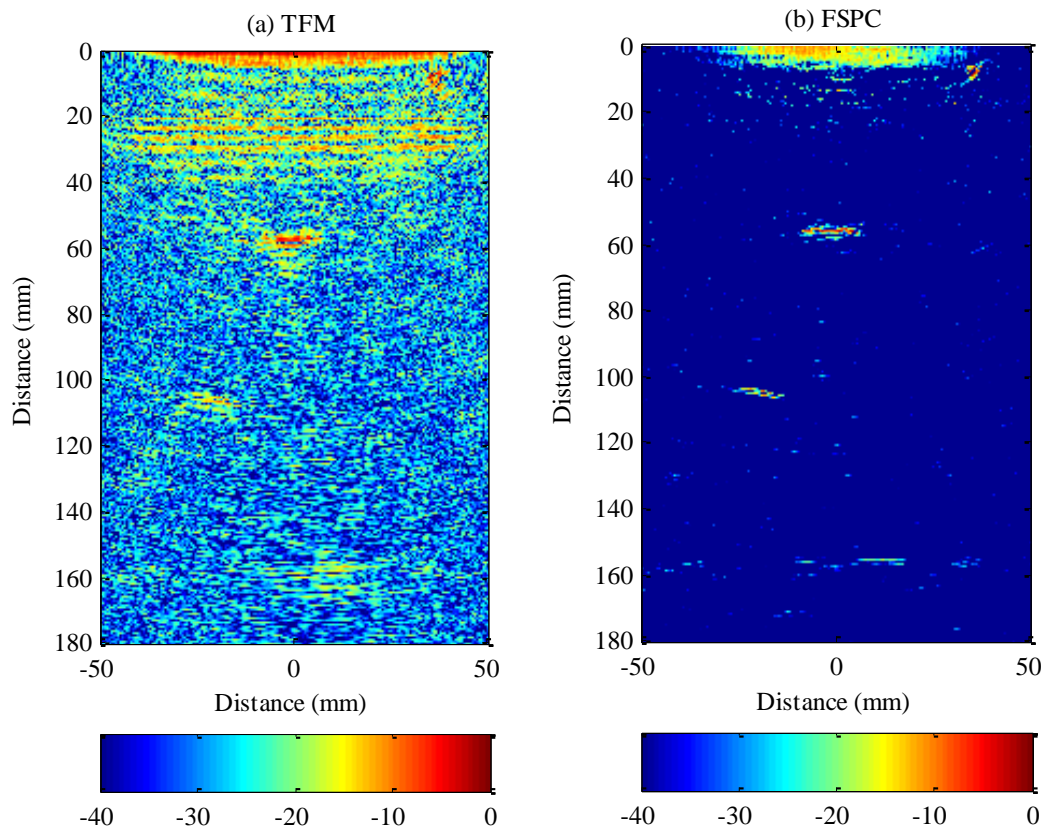
Figure 7.16. TFM and FSPC processed images of the austenicit steel sample, using 64 array elements. The back wall is at 160mm, and three SDHs at 7mm, 60mm, 110mm depth, respectively.

Table 7.2. SNR calculated from the images presented in Figure 7.15 and Figure 7.16

	SNR(dB)	
Sample	Austenitic steel	Inconel 625
Focused B-scan / TFM	19	12
FSPC	42	62

7.4.4 Influence of frequency dependent attenuation in FSPC

In course grained materials, the high frequency ultrasound components are more easily scattered and absorbed. Hence, for an imaging region near the array, a wider frequency range could be used for the coefficient matrix to improve the imaging

resolution. Figure 7.17 shows how the resolution increases as the processed frequency range is increased. The horizontal axis refers to the total included frequency range, e.g. 3MHz means all coefficient matrices from 0.5MHz to 3MHz are used to generate image. The vertical axis is the number of pixels above -6dB, where a lower value refers to a higher resolution. The test target is the 7mm deep SDH, with a 5mm diameter, as shown in Figure 7.15. Through the inclusion of higher frequencies, the processed images will have higher resolution and detection capability in the region near to the array. In Figure 7.17 the resolution stops increasing at around 4MHz due to frequencies higher than 4MHz being significant attenuated for this material. Hence, coefficient matrices higher than that 4MHz did not provide much helpful information.
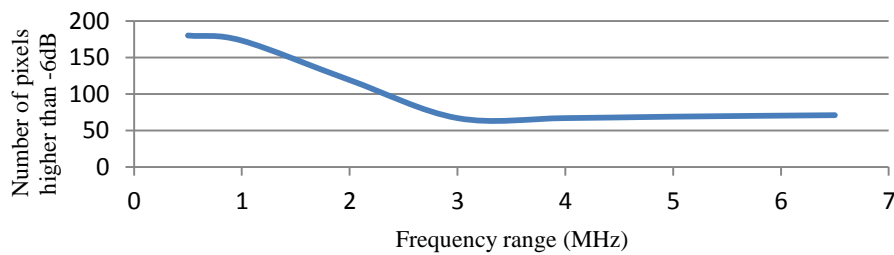
Figure 7.17. The effect of total processed frequency range.

Figure 7.18 gives in indication of this resolution improvement. It shows the normalized weighting matrix combined using two different set of coefficient matrices. The dark regions in the images refer to the pixels which have a value larger than 0.3: this is an arbitrary threshold chosen to illustrate the influence of the frequency band selection on the performance of the imaging algorithm. Figure 7.18(a) only includes a coefficient matrix with the lowest frequency band (0.5MHz-2MHz), and Figure 7.18(b) uses all coefficient matrices from 0.5MHz to 6.5MHz. It can be seen that in Figure 7.18(b) the flaw size is closer to 5mm compared with Figure 7.18(a) (as marked on the images), and importantly, its shape more closely resembles the spherical surface of the SDH.

For imaging regions far from array, only coefficient matrices with lower frequencies should be used, to increase detection capability. Figure 7.19 compares the images of

the 160mm back wall of the Inconel 625 sample. The coefficient matrices used in Figure 7.19(a) is 0.5MHz-3MHz while in Figure 7.19(b) it is 1MHz-4MHz. It can be clearly seen that the visibility/clarity of the back wall is decreased significantly when higher frequencies are included in the FPSC algorithm.
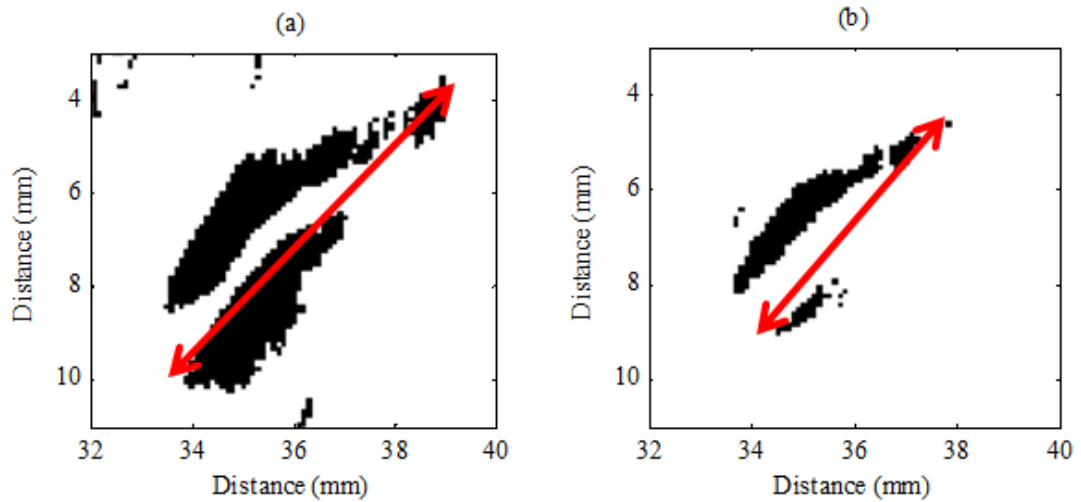
Figure 7.18. Normalized weighting matrices of a SDH with a threshold of 0.3. (a) with frequency range from 0.5MHz to 2MHz, (b) with frequency range from 0.5MHz to 6.5MHz
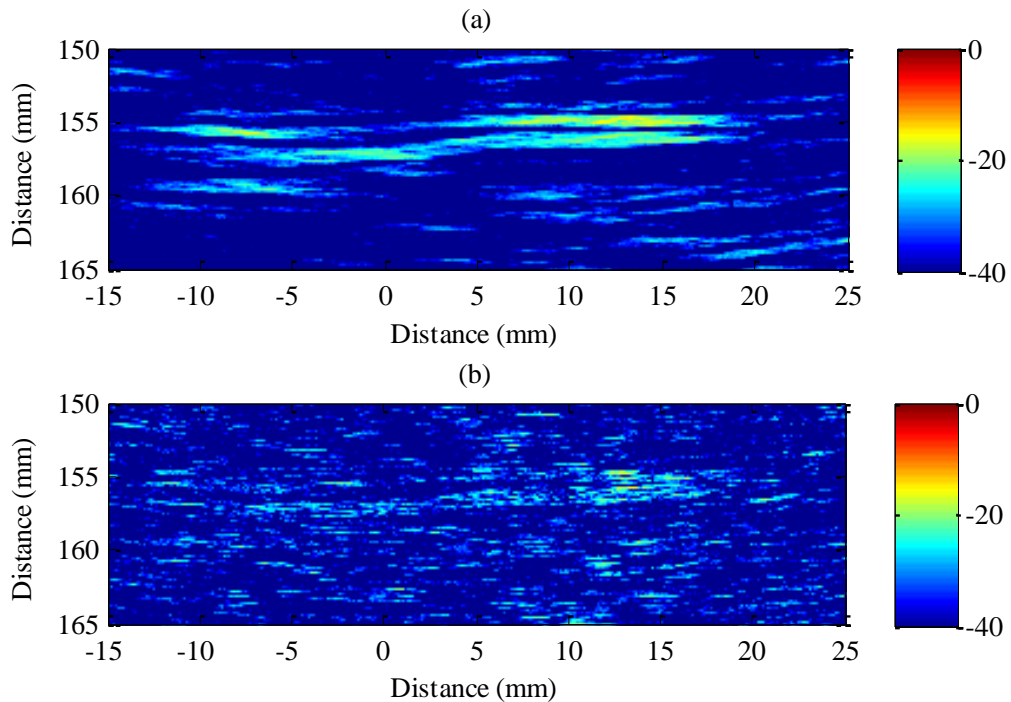
Figure 7.19. FSPC images of back wall of the Inconel 625 sample. (a) with frequency range from 0.5MHz to 3MHz, (b) with frequency range from 1MHz to 4MHz

7.5 Summary

This Chapter has discussed the application of A-scan based grain noise reduction techniques in array imaging, which can be achieved in many different ways. The A-scan based techniques can be used to process the raw signals first and the imaging algorithm can then directly be applied to the processed dataset. Thus, the extension of the MB-SSP and SRC algorithms into array imaging has been introduced. Both the simulation and the experimental results have shown that the back ground grain noise in the image is reduced when the FMC dataset is pre-processed by either the MB-SSP or SRC, with the SRC image demonstrating a higher SNR improvement. However, as the MB-SSP or SRC processed FMC dataset cannot fully benefit from the noise counteracting mechanism in the traditional imaging algorithms, like focused B-scan and TFM, and the back ground noise reduction in the image is therefore limited.

An advanced spatial-frequency diversity based algorithm has also been proposed for array imaging applications, named Frequency Spatial Polarity Coherence (FSPC). The algorithm explores the polarity coherence among different frequency bands and different A-scan traces, to reduce grain noise in the image. Like MB-SSP, the FSPC is less sensitive to material properties compared with conventional frequency diversity based techniques. The focal law used to generate the coefficient matrix is the same as used with a conventional imaging algorithm; hence it can be adapted to many imaging applications. In this work, both focused B-scan and TFM have been used to validate the algorithm. It shows that the FSPC has significantly improved image clarity and compared with the MB-SSP and SRC results, the noise level has also been reduced.

Chapter 8

Conclusion and Future Works

This Chapter will firstly review the research highlights from this Thesis, and then will discuss potential future work in this area.

8.1 Thesis summary

The extensive use of difficult materials in industrial applications demands highly accurate and reliable NDE measurements. This Thesis has introduced a number of novel methodologies based on a range of signal/image processing and statistical techniques.

Chapters 4 and 5 applied supervised classification techniques to improve ultrasound A-scan based noise reduction and subsequent defect detection. Supervised classification techniques can 'memorise' the characteristics of the dataset during a training process, and then classify the input data into related groups according to the pre-knowledge it has learned. In ultrasound inspection of difficult materials, if pre-knowledge of the material can be obtained, the classifier can learn the difference between legitimate reflectors and grain noise.

A new algorithm named Segment Recognition Classifier (SRC) was introduced, with five different classifiers (Naïve Bayes (NB), k-Nearest Neighbors (kNN), Support Vector Machine (SVM), Multilayer Perceptron (MLP), and Stacked Autoencoder (SAE)) applied in the SRC and analysed to assess their performance in grain noise reduction. Generally speaking, SVM has the most satisfied performance over all five classifiers. Although SAE can classify the noise and reflectors more accurately and potentially generate better results, its performance is highly dependent on the fidelity

of training data. MLP has a similar performance when compared with SVM in most of cases. However, underfitting and overfitting problems may occur for MLP, when the size of the training set is either too small or too large. kNN, on the other hand, should be selected for use in the cases where the spectral differences between training classes are minimal.

Although using the classification algorithm to pick out legitimate reflectors from grain noise has shown promising results, the computational power required is usually large. For the scenario in which the grain structure of a material does not vary significantly, an advanced wavelet filtering technique can be used for efficient computation. Moreover, MLP is applied to prune and threshold the wavelet coefficient.

It must be stated that training data is not always available in ultrasound inspection. For cases in which the pre-knowledge of the material is not known, Moving Bandwidth Split Spectrum Processing (MB-SSP) has been developed to improve the algorithm reliability. The advantage of MB-SSP is that it is less sensitive to parameter tuning when testing an unknown material, compared with traditional Split Spectrum Processing (SSP) techniques. Although, there is a minor SNR improvement for MB-SSP when compared with SSP, there are still many noise artefacts left remaining in the processed signals.

By introduced unsupervised clustering, these artefact noise signals in the MB-SSP results can be further reduced through a new algorithm called Potential Real Defect Miner (PRDM). PRDM can also process the results of other techniques like SSP. One disadvantage of the PRDM is that the pre-processed input which generated by other algorithm must be reliable, or the PRDM result may fail.

The classification and clustering algorithms considered in this Thesis were initially developed for application on A-scan signals. The concluding work presented in this Thesis then extended the application of these algorithms for use with phased array imaging. In addition, an advanced array imaging algorithm named Frequency Spatial Polarity Coherence (FSPC) was evaluated. FSPC demonstrated images with a good SNR, since it reduces grain noise using both frequency diversity and spatial diversity.

However, it requires large computation power to generate images, since it generates a set of sub-images before producing the final output.

8.2   Overall conclusion

This Thesis has presented an evolution of a suite of advanced signal processing algorithms and techniques to improve the SNR associated with ultrasonic inspection of difficult materials. The initial concept was to use spectrum based algorithms to reduce grain noise and improve the challenging ultrasonic inspection associated with difficult materials. The important factor in developing these algorithms is the difference in spectral characteristics between features of interest in a sample and grain noise. The features of interest were considered as legitimate reflectors and could include geometric features, for example the sample back wall, and defects/flaws. Interestingly, the high frequency dependent attenuation associated with difficult materials will modify the spectral characteristics depending on the propagation path and hence, is an additional parameter which influences the spectral characteristics on which the developed algorithms are designed to operate.

The Thesis has presented grain noise reduction algorithms based on split spectrum techniques, pattern recognition and clustering. They all have demonstrated improvements over conventional imaging produced from the raw A-scan signals in terms of SNR, PoD and PFA. Albeit, their performance has varied depending on the material under inspection and the quality of training sets used to instruct the algorithms on the differences between legitimate reflectors and grain noise. An important factor to improve the performance of several of these algorithms is the combination of techniques and the application of the developed algorithms to improve the data quality for the training sets used to distinguish the key features in the A-scan signals.

The extension of the noise reduction approaches to array imaging was an important output from this Thesis, as it translated the improvements demonstrated on conventional ultrasonic systems to the modern phased array system configurations. It

is clear that there is an excellent scope for improving array based capabilities for imaging in difficult materials when combining conventional array imaging approaches with these newly developed grain noise reduction techniques. The principal obstacle for implementing these techniques for array imaging is the computational demands associated with the noise reduction algorithms, which are currently only appropriate for off-line post-processing. Note that this issue is also relevant to conventional imaging approaches using a single transducer system, albeit with a lower impact on the system performance.

Overall, the choice of noise reduction algorithm relates to a few key parameters and the quality of available training data. For inspection scenarios when the material properties are relatively well known and there are good quality training sets then SRC provides good results for both single element and array inspections. If the material properties are highly dispersive, in terms of either velocity or phase, then this is challenging for array imaging using FSPC to remove the grain noise. Although, the SRC algorithm would still be appropriate for use with such materials. Alternatively, when the quality of training datasets is poor it is recommended to use MPBT with a single transducer and FSPC with an array transducer system. Moreover, PRDM can be used with both of these to enhance SNR by removing additional noise artifacts.

8.3 Future work

One common issue of the algorithms proposed in this Thesis is their computational expense. Currently, all algorithms are implemented in MATLAB and typically take time to generate results. This limits the practical implementation of these algorithms. Fortunately, all these algorithms can be computed in a parallel way, as the processing of the data is repetitive. Therefore, parallel computing should be considered to accelerate the algorithms, and make them more computationally efficient.

8.3.1 Segment Recognition Classifier (SRC)

Different training scenarios with simulation data have been analysed in the Thesis, along with the validation of experimental data. However, only back wall data has been employed in this work. It therefore would be obvious to extend the performance of SRC to practical defect types, such as cracks, slots, holes etc. Feature extraction methods other than STFT and CWT should also be investigated.

When applied with array imaging, the SRC approach currently can only process spectrum features. Spatial information should also been included in addition to frequency information since many important features of the legitimate reflector are hidden spatially in different A-scan traces of different transmitter-receiver pairs.

8.3.2 Deep Learning networks

The type of the Deep Learning network can be further studied to make the classification performance more stable. In addition, Deep Learning should also been used to extract 2-D feature in array imaging. One of the well-known Deep Learning network named Convolutional Neural Network (CNN) can concentrate features in a high level from a significantly high dimensional input data. This can be used to automatically extract information of interest from a volume of FMC dataset when generating images.

8.3.3 Wavelet filtering

MLP has been used as an example to demonstrate the idea of using neural networks to select coefficients when applying wavelet filtering. Other networks may be more suitable for the coefficients selection and therefore should be further explored. One benefit of using wavelet filtering is that it can choose an arbitrary wave as mother wavelet. Future work would include the use different mother wavelets to adapt to the specific test material.

CWT used in this work is a redundant transform. Its inverse transform is difficult to calculate and hence, limited the selection of mother wavelet. Combining ANNs with other wavelet techniques like the wavelet package should also been considered.

8.3.4   Potential Real Defect Miner (PRDM)

Future works for PRDM include applying the clustering algorithm in array applications using the spatial information, to improve the quality of the array imaging algorithm. Other clustering algorithms should also be involved, like sequential clustering algorithms and hierarchical clustering algorithms. However, there are known difficulties of applying these algorithms. For sequential clustering algorithms, the difficulty is similar to ISODATA: it requires a pre-set threshold which is hard to determine. For hierarchical clustering algorithms, it is difficult to decide when to stop the merging (for agglomerative algorithms) or splitting (for divisive algorithms), as the process is irreversible while the best clustering may appear in an earlier hierarchy.

8.3.5   Moving Bandwidth Split Spectrum Processing (MB-SSP) and Frequency Spatial Polarity Coherence (FSPC)

As discussed in the Thesis, due to the frequency dependent attenuation property of difficult materials, the number of coefficient matrices for FSPC should be changed based on the wave propagation distance. This is currently done manually which required a trial-and-error process. A more general rule should be developed to better guide the inspection.

Parametric studies of MB-SSP and FSPC should be carried out in the inspection of a wide range of materials and flaw characteristics. Although the performance for each individual parameter has been discussed in the Thesis, the conjunction effect between each parameter should be further analysed. The optimal number of filter channels for FSPC should also be exploited.

The reconstruction of the weighting matrix is by a simple averaging of all the coefficient matrices. There are other comparison methods that may potentially

improve the performance of algorithm which can also been investigated, including order statistics, scaled polarity thresholding, and Best Linear Unbiased Estimator (BLUE) techniques.

References

[1]   K. Goebbels, "State of the art and short term development tendencies in nondestructive surface defect detection and evaluation," in *12th World Conference on Non-Destructive Testing*, Amsterdam, The Netherlands, 1989, pp. 3-8.

[2]   P. Roscoe, C. Waites, and M. J. Whittle, "Cost-Effective Inspection Quilification," in *Proceedings of the 13. international conference on NDE in the nuclear and pressure vessel industries*, Kyoto, 1995, pp. 195-165.

[3]   *Basic Principles of Ultrasonic Testing*. Available: https://www.nde-ed.org/EducationResources/CommunityCollege/Ultrasonics/Introduction/description.htm

[4]   F. Masuyama, "History of Power Plants and Progress in Heat Resistant Steels," *ISIJ International,* vol. 41, no. 6, pp. 612-625, 2001.

[5]   A. Diboine and A. Pineau, "Creep Crack Initiation and Growth in Inconel 718 Alloy at 650c," *Fatigue & Fracture of Engineering Materials & Structures,* vol. 10, pp. 141-151, 1987.

[6]   H. G. Jiang, M. L. Lau, and E. J. Lavernia, "Grain growth behavior of nanocrystalline Inconel 718 and Ni powders and coatings," *Nanostructured Materials,* vol. 10, pp. 169-178, 1998.

[7]   B. Xiao, "Methodologies for Enhancing Ultrasonic NDE of Coarse-Grained Materials," PhD, University of Strathclyde, 2016.

[8]   W. Li, S. D. Sharples, R. J. Smith, M. Clark, and M. G. Somekh, "Determination of crystallo graphic orientation of large grain metals with surface acoustic waves," *The Journal of the Acoustical Society of America,* vol. 132, 2012.

[9]   D. N. Alleyne and P. Cawley, "Optimization of lamb wave inspection techniques," *NDT & E International,* vol. 25, no. 1, pp. 11-22, 1992.

[10]   J. Camacho and C. Fritsch, "Phase coherence imaging of grained materials," (in eng), *IEEE Transations on Ultrasonics, Ferroelectrics and Freqency Control,* vol. 58, no. 5, pp. 1006-1015, May 2011.

[11]   Transducer, "Concise Oxford English Dictionary: Eleventh edition.," 11th revised edition ed: Oxford: OUP Oxford, 2006.

[12]   F. L. Thurstone, N. I. Kjosnes, and W. M. McKinney, "Ultrasonic Scanning of Biologic Tissue by a New Technique," *Science,* vol. 149, pp. 302-303, 16 July 1965.

[13]   G. L. Gooberman, *Ultrasonics: Theory and Application.* Hart Publishing Company, 1969.

[14]   A. A. Vives, *Piezoelectric Transducers and Applications*. Springer Science & Business Media, 2013.

[15]   A. Fukumoto, M. Kawabuchi, and J.-I. Sato, "Design of ultrasound transducers using new piezoelectric ceramic materials," *Ultrasound in Medicine & Biology,* vol. 7, no. 3, pp. 275-281, 1981.

[16]   S. N. Ramadas *et al.*, "Tapered transmission line technique based graded matching layers for thickness mode piezoelectric transducers," in *IEEE International Ultrasonics Symposium (IUS)*, Rome, 2009, pp. 1695-1698: IEEE.

[17]   A. J. Mulholland *et al.*, "Enhancing the performance of piezoelectric ultrasound transducers by the use of multiple matching layers," *IMA Journal of Applied Mathematics,* vol. 73, no. 6, pp. 936-949, 01 December 2008.

[18]   A. Troge, R. L. O'Leary, G. Hayward, R. A. Pethrick, and A. J. Mullholland, "Properties of photocured epoxy resin materials for application in piezoelectric ultrasonic transducer matching layers," (in eng), *The Journal of the Acoustical Society of America,* vol. 128, no. 5, pp. 2704-2714, November 2010.

[19]   F. Simonetti, "Multiple scattering: The key to unravel the subwavelength world from the far-field pattern of a scattered wave," *Physical Review E,* vol. 73, no. 3, p. 036619, 24 Mar 2006.

[20]   *Ring-down time / definition of ring-down time by Medical dictionary*. Available: http://medical-dictionary.thefreedictionary.com/ring-down+time

[21]   A. Nowicki, I. Trots, P. A. Lewin, W. Secomski, and R. Tymkiewicz, "Influence of the ultrasound transducer bandwidth on selection of the complementary Golay bit code length," vol. 47, no. 1-4, pp. 64–73, December 2007.

[22]   J. C. Lázaro, J. L. San Emeterio, A. Ramos, and J. L. Fernández-Marrón, "Influence of thresholding procedures in ultrasonic grain noise reduction using wavelets," *Ultrasonics,* vol. 40, no. Issues 1–8, pp. 263–267, May 2002.

[23]   E. Buddemeyer, "The physics of diagnostic ultrasound," *Radiologic clinics of North America,* vol. 13, no. 3, pp. 391-402, 30 Nov 1975.

[24]   B. W. Drinkwater and P. D. Wilcox, "Ultrasonic arrays for non-destructive evaluation: A review," vol. 39, no. 7, pp. 525–541, October 2006.

[25]   *Grating Lobes and Side Lobes / Olympus IMS*. Available: http://www.olympus-ims.com/en/ndt-tutorials/transducers/lobes/

[26]   *Phased array tutorial*. Available: http://www.olympus-ims.com/en/ndt-tutorials/phased-array/

[27]   C. Holmes, B. W. Drinkwater, and P. D. Wilcox, "Post-processing of the full matrix of ultrasonic transmit-receive array data for non-destructive evaluation," (in English), *NDT and E International,* vol. 38, no. 8, 1 December 2005.

[28]   *Introduction to Ultrasonic Testing*. Available: https://www.nde-ed.org/EducationResources/CommunityCollege/Ultrasonics/EquipmentTrans/DataPres.htm

[29]   *What is NDT?* Available: http://www.bindt.org/What-is-NDT/Index-of-acronyms/

[30]   *UT-Weld-1*.   Available: http://www.structuralinsights.com/SI/DEV/admin/data/upimages/ut-weld-1.jpg

[31]   S. P. Kelly, "An air-coupled ultrasonic array scanning system for rapid through transmission NDT," Ph.D, University of Strathclyde, 2000.

[32]   J. D. Owens, D. Luebke, N. Govindaraju, M. Harris, J. Kruger, Lefohn, Aaron E., and T. Purcell, "A Survey of General-Purpose Computation on Graphics Hardware," *Computation on Graphics Hardware,* vol. 26, no. 1, pp. 80-113, 2007.

[33]   T. Lardner, "New Algorithms for Ultrasonic Non-Destructive Evaluation," PhD, University of Strathclyde, 2016.

[34]   J. Dziewierz, "2D Ultrasonic Phased Arrays for Quantitative Characterisation of Complex Defects," PhD, University of Strathclyde, 2015.

[35]   K. Mayer, R. Marklein, K. J. Langenberg, and T. Kreutter, "Three-dimensional imaging system based on Fourier transform synthetic aperture focusing technique," *Ultrasonics,* vol. 28, no. 4, pp. 241-255, 2016.

[36]   Y. Ozaki, H. Sumitani, T. Tomoda, and M. Tanaka, "A new system for real-time synthetic aperture ultrasonic imaging," *IEEE Trans Ultrason Ferroelectr Freq Control,* vol. 35, no. 6, pp. 828-838, 1988.

[37]   A. Chahbaz and R. Sicard, "Comparative evaluation between ultrasonic phased array and synthetic aperture focusing techniques," presented at the Review of Progress in Quantitative Nondestructive Evaluation, Bellingham, WA, 2003.

[38]   Y. Li, V. L. Newhouse, P. M. Shankar, and P. Karpur, "Speckle Reduction in Ultrasonic SAFT Images in Coarse Grained Material Through Split Spectrum Processing," in *Review of Progress in Quantitative Nondestructive Evaluation*, 1989, pp. 727-734.

[39]   S. Chatillon, S. Mahaut, and P. Dubois, "Simulation of Advanced UT Phased Array Techniques with Matrix Probes and Dynamic Settings for Complex Component Inspections," in *Review of Progress in Quantitative Nondestructive Evaluation*, Chicago, 2009, vol. 1091, pp. 864-871: AIP Publishing.

[40]   F. W. Kremkau, *Diagnostic Ultrasound: Principles and Instruments*. W B Saunders Co, 1997.

[41]   J. Zhang, B. W. Drinkwater, and P. D. Wilcox, "Comparison of Ultrasonic Array Imaging Algorithms for Nondestructive Evaluation," *IEEE Transactions on ultrasounics Ferroelectrics and Frequency Control,,* vol. 60, no. 8, pp. 1732-1745, August 2013.

[42]   P. D. Wilcox, C. Holmes, and B. W. Drinkwater, "Advanced Reflector Characterization with Ultrasonic Phased Arrays in NDE Applications," *IEEE Transactions on Ultrasonics, Ferroelectrics, and Frequency Control,* vol. 54, no. 8, pp. 1541-1550, Aug 2007.

[43]   J. Zhang, B. W. Drinkwater, P. D. Wilcox, and A. J. Hunter, "Defect detection using ultrasonic arrays: The multi-mode total focusing method," *NDT & E International,* vol. 43, no. 2, pp. 123–133, March 2010.

[44]   J. Zhang, B. Drinkwater, and P. Wilcox, "Efficient immersion imaging of components with nonplanar surfaces," *IEEE Trans Ultrason Ferroelectr Freq Control,* vol. 61, no. 8, pp. 1284-1295, Aug 2014.

[45]   C. Fan, M. Caleap, M. Pan, and B. W. Drinkwater, "A comparison between ultrasonic array beamforming and super resolution imaging algorithms for

non-destructive evaluation," *Ultrasonics,* vol. 54, no. 7, pp. 1842–1850, September 2014.

[46] S. K. Lehman and A. J. Devaney, "Transmission mode time-reversal super-resolution imaging," *The Journal of the Acoustical Society of America,* vol. 113, no. 5, pp. 2742-2753, May 2003.

[47] F. K. Gruber, E. A. Marengo, and A. J. Devaney, "Time-reversal imaging with multiple signal classification considering multiple scattering between the targets," *The Journal of the Acoustical Society of America,* vol. 115, no. 6, pp. 3042-3047, 2004.

[48] M. O'Donnell and S. W. Flax, "Phase-aberration correction using signals from point reflectors and diffuse scatterers: measurements," *IEEE Trans Ultrason Ferroelectr Freq Control,* vol. 35, no. 6, pp. 768-74, 1988.

[49] S. W. Flax and M. O'Donnell, "Phase-aberration correction using signals from point reflectors and diffuse scatterers: basic principles," *IEEE Trans Ultrason Ferroelectr Freq Control,* vol. 35, no. 6, pp. 758-767, 1988.

[50] B. Beardsley, M. Peterson, and J. D. Achenbacn, "A simple scheme for self-focusing of an array," *Journal of Nondestructive Evaluation,* vol. 132, pp. 738-745, Aug 1995.

[51] N. Chakroun, M. A. Fink, and F. Wu, "Time Reversal Processing in Ultrasonic Nondestructive Testing," *IEEE Trans Ultrason Ferroelectr Freq Control,* vol. 42, pp. 1087-1098, 1995.

[52] M. Fink, "Time reversal of ultrasonic fields. I. Basic principles," *IEEE Trans Ultrason Ferroelectr Freq Control,* vol. 39, no. 5, pp. 555-566, 1992.

[53] C. Prada, E. Kerbrat, D. Cassereau, and M. Fink, "Time reversal techniques in ultrasonic nondestructive testing of scattering media," *Inverse Problems,* vol. 18, pp. 1761-1773, 2002.

[54] G. Zhang, C. Zhang, and D. M. Harvey, "Sparse signal representation and its applications in ultrasonic NDE," vol. 52, no. 3, pp. 351–363, March 2012.

[55] K. M. M. Tant, A. J. Mulholland, and A. Gachagan, "An analytical approach to objectively sizing cracks using ultrasonic phased array data," in *54th Annual British Conference of Non-Destructive Testing, NDT 2015*, 2017.

[56] J. Zhang, P. Yu, and T. Gang, "Measurement of the ultrasonic scattering matrices of near-surface defects using ultrasonic arrays," *Nondestructive Testing and Evaluation,* vol. 31, pp. 303-318, 2016.

[57] S. S. Haykin, *Neural Networks and Learning Machines*. India: Prentice Hall, 2009.

[58] Y. Chen, H.-W. Ma, and G.-M. Zhang, "A support vector machine approach for classification of welding defects from ultrasonic signals," *Nondestructive Testing and Evaluation,* research-article vol. 29, no. 3, pp. 243-254, Jun 2014.

[59] A. V. Pamel, C. R. Brett, and M. J. S. Lowe, "A methodology for evaluating detection performance of ultrasonic array imaging algorithms for coarse-grained materials - IEEE Xplore Document," *IEEE Transactions on Ultrasonics, Ferroelectrics, and Frequency Control,* vol. 61, no. 12, pp. 2042-2053, 2014.

[60] G.-M. Zhang and D. M. Harvey, "Contemporary ultrasonic signal processing approaches for nondestructive evaluation of multilayered structures," *Nondestructive Testing and Evaluation,* research-article vol. 27, no. 1, pp. 1-27, Feb 2012.

[61]   R. Bracewell, *The Fourier Transform and Its Applications*, 3 ed. McGraw-Hill Science/Engineering/Math, 1999.

[62]   T. Butz, *Fourier Transformation for Pedestrians*. Springer Science & Business Media, 2017, p. 202.

[63]   C. Roads, *Microsound*. MIT Press, 2002.

[64]   M. Misiti, Y. Misiti, G. Oppenheim, and J.-M. Poggi, *Wavelet Toolbox User's Guide*. The MathWorks, Inc., 1996.

[65]   C. Zhang, "Application of Multi - Wavelet Analysis in Image Compression," *Rev. T éc. Ing. Univ. Zulia,* vol. 39, no. 3, pp. 76-82, 2016.

[66]   A. Abbate, J. Koay, and J. Frankel, "Signal detection and noise suppression using a wavelet transform signal processor: Application to ultrasonic flaw detection," *IEEE Transactions on Ultrasonics, Ferroelectrics, and Frequency Control,* vol. 44, no. 1, pp. 14-26, January 1997.

[67]   I. Daubechies, "The wavelet transform, time-frequency localization and signal analysis," *IEEE Transactions on Information Theory,* vol. 36, no. 5, pp. 961-1005, 1990.

[68]   C. F. Chen and C. H. Hsiao, "Haar wavelet method for solving lumped and distributed-parameter systems," *IEE Proceedings - Control Theory and Applications,* vol. 144, no. 1, pp. 87-94, 1997.

[69]   I. Daubechies, *Ten Lectures on Wavelets* (CBMS-NSF Regional Conference Series in Applied Mathematics). Society for Industrial and Applied Mathematics, 1992.

[70]   L. G. Weiss, "Wavelets and wideband correlation processing," *IEEE Signal Processing Magazine,* vol. 11, no. 1, pp. 13-32, 1994.

[71]   (2016). *Inverse Continuous Wavelet Transform - MATLAB & Simulink - MathWorks United Kingdom.* Available: http://uk.mathworks.com/help/wavelet/gs/inverse-continuous-wavelet-transform.html

[72]   S. G. Mallat, "A Theory for Multiresolution Signal Decomposition: The Wavelet Representation," *IEEE Transactions on Pattern Analysis and Machine Intelligence,* vol. 11, no. 7, pp. 674-693, July 1989.

[73]   M. V. Wickerhauser, "Lectures on Wavelet Packet Algorithms," in *Lecture notes, INRIA*, 1991.

[74]   G. S. Kino, *Acoustic Waves: Devices, Imaging and Analog Signal Processing*. Prentice Hall, 1987.

[75]   M. Ali, D. Magee, and U. Dasgupta, "Signal processing overview of ultrasound systems for medical imaging," Texas Instruments2008.

[76]   M. Li and Y. Lu, "Source bearing and steering-vector estimation using partially calibrated arrays," *IEEE Transactions on Aerospace and Electronic Systems,* vol. 45, no. 4, pp. 1361-1372, 2009.

[77]   M. Li and Y. Lu, "Maximum likelihood DOA estimation in unknown colored noise fields," *IEEE Transactions on Aerospace and Electronic Systems,* vol. 44, no. 3, pp. 1079-1090, 2008.

[78]   B. He, Y. Liang, X. Feng, T. Y. R. Nian, M. Li, and S. Zhang, "AUV SLAM and Experiments Using a Mechanical Scanning Forward-Looking Sonar," *Sensors,* vol. 12, pp. 9386-9410, 2012.

[79]   M. Li and Y. Lu, "Angle-of-arrival estimation for localization and communication in wireless networks," in *Proceedings of the 16th European*

Signal Processing Conference (EUSIPCO 2008), Lausanne, Switzerland, 2008.

[80] M. Li and Y. Lu, "A refined genetic algorithm for accurate and reliable DOA estimation with a sensor array," *Wireless Personal Communications,* vol. 43, no. 2, pp. 533-547, 2007.

[81] M. Li and Y. Lu, "Dimension reduction for array processing with robust interference cancellation," *IEEE Transactions on Aerospace and Electronic Systems,* vol. 42, no. 1, pp. 103-112, 2006.

[82] V. schmitz and K. Goebbels, "Improvement of Signal-To-Noise Ratio for the Ultrasonic Testing of Coarse Grained Materials by Digital RF-Signal Averaging," in *Proc. IEEE Ultrasonics Symp*, 1982, pp. 950-953.

[83] M. K. Murali and K. neelakantan, "Improved ultrasonic flaw detection technique for austenitic stainless steel welds," *NDT International,* vol. 14, no. 6, pp. 321-324, 1981.

[84] R. S. C. Cobbold, *Foundations of Biomedical Ultrasound*. Oxford University, 2007.

[85] P. M. Shankar, "Speckle reduction in ultrasound B-scans using weighted averaging in spatial compounding," *IEEE Trans Ultrason Ferroelectr Freq Control,* vol. 33, no. 6, pp. 754-8, 1986.

[86] J. E. Wilhjelm, M. S. Jensen, S. K. Jespersen, B. Sahl, and E. Falk, "Visual and quantitative evaluation of selected image combination schemes in ultrasound spatial compound scanning," *IEEE Trans Med Imaging,* vol. 23, no. 2, pp. 181-90, Feb 2004.

[87] C. H. Seo and J. T. Yen, "Sidelobe suppression in ultrasound imaging using dual apodization with cross-correlation," *IEEE Trans Ultrason Ferroelectr Freq Control,* vol. 55, no. 10, pp. 2198-210, Oct 2008.

[88] J. Shin and J. Yen, "Synergistic enhancements of ultrasound image contrast with a combination of phase aberration correction and dual apodization with cross-correlation," *IEEE Trans Ultrason Ferroelectr Freq Control,* vol. 59, no. 9, pp. 2089-101, Sep 2012.

[89] T. Lardner, M. Li, R. Gongzhang, and A. Gachagan, "A New Speckle Noise Suppression Technique Using Cross-correlation of Array Sub-apertures in Ultrasonic NDE of Coarse Grain Materials," in *Review of Progress in Quantitative Nondestructive Evaluation*, Denver, CO, 2013, vol. 1511, pp. 865-871: AIP Conference Proceedings.

[90] T. Lardner, M. Li, and A. Gachagan, "Using Phase Information to Enhance Speckle Noise Reduction in Ultrasonic NDE of Coarse Grain Materials," in *Review of Progress in Quantitative Nondestructive Evaluation*, Baltimore, MA, 2014, vol. 1581, pp. 1061-1068: AIP Conference Proceedings.

[91] M. Li and G. Hayward, "Ultrasound Nondestructive Evaluation (NDE) Imaging with Transducer Arrays and Adaptive Processing," *Sensors,* vol. 12, no. 1, pp. 42-54, December 2011.

[92] J. Camacho, M. Parrilla, and C. Fritsch, "Phase coherence imaging," *IEEE Trans Ultrason Ferroelectr Freq Control,* vol. 56, no. 5, pp. 958-74, May 2009.

[93] J. F. Cruza, J. Camecho, and C. Fritsch, "Plane-wave phase-coherence imaging for NDE," *NDT & E International,* vol. 87, pp. 31–37, April 2017.

[94]   N. M. Bilgutay, R. Murthy, and U. Bencharit, "Spatial processing for coherent noise reduction in ultrasonic imaging   " *The Journal of the Acoustic Society of America,* vol. 87, no. 2, February 1990.

[95]   G. E. Traney, J. W. Alison, S. W. Smith, and O. T. von Ramm, "A quantitative approach to speckle reduction via frequency compounding," *Ultrasonic Imaging,* vol. 8, no. 3, pp. 151-164, 1986.

[96]   N. M. Bilgutay, J.Saniie, E. S. Furgason, and V.L.Newhouse, "Flaw-to-grain echo enhancement," in *Ultrasonics International 1979*, Austria, 1979, pp. 152-157.

[97]   V. L. Newhouse, N. M. Bilgutay, and J. F. Saniie, E. S., "Flaw-to-grain echo enhancement by split-spectrum processing," *Ultrasonic,* vol. 20, no. 2, pp. 59-68, 1982.

[98]   K. K. Yau, "Split-Spectrum Processing for Nondestructive Testing," *NDT.net,* vol. 2, no. 08, Aug 1997.

[99]   J. D. Aussel, "Split-spectrum processing with finite impulse response filters of constant frequency-to-bandwidth ratio," *Ultrasonic,* vol. 28, no. 4, pp. 229-240, 1990.

[100]   P. Karpur, P. M. Shankar, Rose, J. L., and V. L. Newhouse, "Split spectrum processing: optimizing the processing parameters using minimization," *Ultrasonics,* vol. 25, no. 4, pp. 204-208, July 1987.

[101]   P. M. Shankar, P. Karpur, V. L. Newhouse, and J. L. Rose, "Split-spectrum processing: analysis of polarity threshold algorithm for improvement of signal-to-noise ratio and detectability in ultrasonic signals," *IEEE Transactions on Ultrasonics, Ferroelectrics, and Frequency Control,* vol. 36, no. 1, pp. 101-108, 1989.

[102]   V. L. Newhouse, G. Yu, and Y. Li, *A Split Spectrum Processing Method of Scatterer Density Estimation* (NATO ASI Series). Springer Berlin Heidelberg, 1988, pp. 49-69.

[103]   J. Saniie, D. T. Nagle, and K. D. Donohue, "Analysis of order statistic filters applied to ultrasonic flaw detection using split-spectrum processing," *IEEE Trans Ultrason Ferroelectr Freq Control,* vol. 38, no. 2, pp. 133-40, 1991.

[104]   A. Rodriguez, R. Miralles, I. Bosch, and L. Vergara, "New analysis and extensions of split-spectrum processing algorithms," *NDT & E International,* vol. 45, no. 1, pp. 141–147, January 2012.

[105]   M. Karaojuizt, N. Bilgutay, T. Akgul, and S. Popovics, "Defect detection in concrete using split spectrum processing," in *Proc. IEEE Ultrasonics Symp*, Philadelphia, PA, 1998, pp. 843-846.

[106]   A. Rodriguez, A. Salazar, and L. Vergara, "Analysis of split-spectrum algorithms in an automatic detection framework," *Signal Processing,* vol. 92, no. 9, pp. 2293–2307, September 2012.

[107]   I. Bosch and L. Vergara, "Normalized split-spectrum: A detection approach," vol. 48, no. 1, pp. 56–65, March 2008.

[108]   P. Rubbers and C. J. Pritchard, "An overview of Split Spectrum Processing," *NDT.net,* vol. 8, no. 08, Aug 2003.

[109]   Y. Li and V. L. Newhouse, Shankar, P. M., "Speckle reduction in ultrasonic synthetic aperture images," *Ultrasonics,* vol. 30, no. 4, pp. 233-237, 1992.

[110] R. G. Dantas and E. T. Costa, "Ultrasound speckle reduction using modified Gabor filters," *IEEE Trans Ultrason Ferroelectr Freq Control,* vol. 54, no. 3, pp. 530-8, Mar 2007.

[111] J. R. Sanchez and M. L. Oelze, "An ultrasonic imaging speckle-suppression and contrast-enhancement technique by means of frequency compounding and coded excitation," *IEEE Trans Ultrason Ferroelectr Freq Control,* vol. 56, no. 7, pp. 1327-39, Jul 2009.

[112] M. G. Gustafsson, "Nonlinear clutter suppression using split spectrum processing and optimal detection," *IEEE Transactions on Ultrasonics, Ferroelectrics, and Frequency Control,* vol. 43, no. 1, pp. 109-124, 1996.

[113] X. Li, N. M. Bilgutay, R. Murthy, and J. Saniie, "Spectral histogram and its application to flaw detection," in *Proc. IEEE Ultrasonics Symp*, Philadelphia, PA, 1988, pp. 915-918: IEEE.

[114] Q. Tian and N. M. Bilgutay, "Statistical analysis of split spectrum processing for multiple target detection," *IEEE Trans Ultrason Ferroelectr Freq Control,* vol. 45, no. 1, pp. 251-6, 1998.

[115] L. Ericsson and T. Stepinski, "Cut spectrum processing: a novel signal processing algorithm for ultrasonic flaw detection," *NDT & E International,* vol. 25, no. 2, pp. 59-64, 1992.

[116] K. Yuan, Z. Pan, and S. Ma, "Consecutive Polarity Coincidence Based Split-spectrum Processing in Ultrasonic Testing of Coarse Materials," in *Electronic Measurement and Instruments, 2007. ICEMI '07. 8th International Conference on*, 2007, pp. 591-594: IEEE.

[117] M. A. Izquierdo, M. G. Hernandez, J. J. Anaya, and O. Martinez, "Speckle reduction by energy time-frequency filtering," *Ultrasonics,* vol. 42, no. 1-9, pp. 843-6, Apr 2004.

[118] G. Zhang, D. M. Harvey, and D. R. Braden, "Signal denoising and ultrasonic flaw detection via overcomplete and sparse representations," *The Journal of the Acoustical Society of America,* vol. 124, no. 5, pp. 2963-2972, Nov 2008.

[119] S. Song and P. Que, "Wavelet based noise suppression technique and its application to ultrasonic flaw detection," *Ultrasonics,* vol. 44, no. 2, pp. 188–193, February 2006.

[120] E. Pardo, J. L. San Emeterio, M. A. Rodriguez, and A. Ramos, "Noise reduction in ultrasonic NDT using undecimated wavelet transforms," *Ultrasonics,* vol. 44, pp. e1063–e1067, 22 December 2006.

[121] V. Matz, R. Smid, S. Starman, and M. Kreidl, "Signal-to-noise ratio enhancement based on wavelet filtering in ultrasonic testing," *Ultrasonics,* vol. 49, no. 8, pp. 752–759, December 2009.

[122] H. C. Sun and J. Saniie, "Nonlinear signal processing for ultrasonic target detection," in *IEEE Ultrasonics Symposium*, Sendai, 1998, vol. 1, pp. 855-858.

[123] H. C. Sun and J. Saniie, "Ultrasonic flaw detection using split-spectrum processing combined with adaptive-network-based fuzzy inference system," in *IEEE Ultrasonics Symposium*, Caesars Tahoe, NV, 1999, vol. 1, pp. 801-804: IEEE.

[124] J. S. R. Jang, "ANFIS: adaptive-network-based fuzzy inference system," (in English), *IEEE Transactions on Systems, Man, and Cybernetics,* vol. 23, no. 3, pp. 665-685, May/Jun 1993.

[125] Z. Liu, M. Lu, and M. Wei, "Structure noise reduction of ultrasonic signals using artificial neural network adaptive filtering," vol. 35, no. 4, pp. 325–328, June 1997.

[126] B. Xiao, M. Li, R. Gongzhang, R. O'Leary, and A. Gachagan, "Image denoising via spectral distribution similarity analysis for ultrasonic nondestructive evaluation," in *Review of Progress in Quantitative Nondestructive Evaluation*, Baltimore, MA, 2014, vol. 1581, pp. 1041-1047: AIP Conference Proceedings.

[127] E. Menthe, A. Bulak, J. Olfe, A. Zimmermann, and K. T. Rie, "Improvement of the mechanical properties of austenitic stainless steel after plasma nitriding," *Surface and Coatings Technology,* vol. 133–134, pp. 259–263, November 2000.

[128] P. Ganesan, G. D. Smith, and D. H. Yates, "Performance of Inconel Alloy 617 in Actual and Simulated Gas Turbine Environments," *Materials and Manufacturing Processes,* pp. 925-938, 8 Apr 2009.

[129] *INCONEL alloy 617*. Available: http://www.specialmetalswiggin.co.uk/products/inconel-alloy-617

[130] *Inconel 625 Tech Data*. Available: http://www.hightempmetals.com/techdata/hitempInconel625data.php

[131] *NVIDIA Developer*. Available: https://developer.nvidia.com/

[132] J. Dziewierz, T. Lardner, and A. Gachagan, "A Design Methodology for 2D Sparse NDE Arrays using an Efficient Implementation of Refracted-Ray TFM," in *IEEE International Ultrasonics Symposium (IUS)*, Prague, 2013, pp. 136-138.

[133] M. Grevillot, C. Cudel, J. J. Meyer, and S. Jacquey, "Two approaches to multiple specular echo detection using split spectrum processing: moving bandwidth minimization and mathematical morphology," *Ultrasonics,* vol. 37, no. 6, pp. 417–422, September 1999.

[134] M. G. Gustafsson and T. Stepinski, "Studies of split spectrum processing, optimal detection, and maximum likelihood amplitude estimation using a simple clutter model," *Ultrasonics,* vol. 35, no. 1, pp. 31-52, February 1997.

[135] C. S. Ting and W. Sachse, "Measurement of ultrasonic dispersion by phase comparison of continuous harmonic waves," *The Journal of the Acoustical Society of America,* vol. 64, no. 3, pp. 851-857, 09 1978.

[136] P. He, "Simulation of ultrasound pulse propagation in lossy media obeying a frequency power law," *IEEE Transactions on Ultrasonics, Ferroelectrics, and Frequency Control,* vol. 45, no. 1, pp. 114-125, January 1998.

[137] D. Li, K. D. Wong, Y. H. Hu, and A. M. Sayeed, "Detection, classification, and tracking of targets - IEEE Xplore Document," vol. 19, no. 2, pp. 17-29, Mar 2002.

[138] R. Polikar, L. Udpa, S. S. Udpa, and T. Taylor, "Frequency invariant classification of ultrasonic weld inspection signals," *IEEE Transactions on Ultrasonics, Ferroelectrics, and Frequency Control,* vol. 45, no. 3, pp. 614-625, May 1998.

[139] C. M. Bishop, *Pattern Recognition and Machine Learning*. Singapore: Springer, 2006.

[140] S. Theodoridis and K. Koutroumbas, *Pattern Recognition*. USA: Academic Press, 2009.

[141] F. Massey, "The Kolmogorov-Smirnov Test for Goodness of Fit," *Journal of the American Statistical Association,* vol. 46, no. 253, pp. 68-78, Mar 1951.

[142] S. Facchinetti, "A procedure to find exact critical values of Kolmogorov-Smirnov test," *Statistica Applicata - Italian Journal of Applied Statistics* vol. 21, pp. 337-359, 2009.

[143] T. Fawcett, "An introduction to ROC analysis," *Pattern Recognition Letters,* vol. 27, no. 8, pp. 861-874, June 2006.

[144] R. Lippmann, "An introduction to computing with neural nets," (in English), *IEEE ASSP Magazine,* vol. 4, no. 2, pp. 4-22, April 1987.

[145] F. W. Margrave, K. Rigas, D. A. Bradley, and P. Barrowcliffe, "The use of neural networks in ultrasonic flaw detection," *Measurement,* vol. 25, no. 2, pp. 143–154, March 1999.

[146] S. W. Liu, J. H. Huang, J. C. Sung, and C. C. Lee, "Detection of cracks using neural networks and computational mechanics," vol. 191, no. Issues 25–26, pp. 2831–2845, 12 April 2002.

[147] R. G. Pita, R. Vicen, M. Rosa, M. P. Jarabo, P. Verab, and J. Curpian, "Ultrasonic flaw detection using radial basis function networks (RBFNs)," *Ultrasonics,* vol. 42, no. Issues 1–9, pp. 361–365, April 2004.

[148] Purnawansyah and Haviluddin, "Comparing performance of Backpropagation and RBF neural network models for predicting daily network traffic," in *2014 Makassar International Conference on Electrical Engineering and Informatics*, Makassar, South Sulawesi, Indonesia, 2014, pp. 166-169.

[149] D. Svozil, V. Kvasnicka, and J. Pospichal, "Introduction to multi-layer feed-forward neural networks," vol. 39, no. 1, pp. 43–62, November 1997.

[150] G. Hosseini, D. Luo, and K. J. Reynolds, "The comparison of different feed forward neural network architectures for ECG signal diagnosis," vol. 28, no. 4, pp. 372–378, May 2006.

[151] J. O. Katz, "Developing Neural Network Forecasters For Trading," *Technical Analysis of Stocks and Commodities,* pp. 58-70, April 1992.

[152] D. Bailey and D. M. Thompson, "Developing Neural Network Applications," *Al Expert,* pp. 34-41, September 1990.

[153] l. Kaastra and M. Boyd, "Designing a neural network for forecasting financial and economic time series," *Neurocomputing,* vol. 10, no. 3, pp. 215-236, April 1996.

[154] M. Dorofki, A. H. Elshafie, and O. Jaafar, "Comparison of Artificial Neural Network Transfer Functions Abilities to Simulate Extreme Runoff Data," *International Proceedings of Chemical, Biological & Environmenta,* vol. Vol. 33, pp. 39–44, April 2012.

[155] P. J. Werbos, "Beyond regression: New tools for prediction and analysis in the behavioral sciences," PhD, Harvard University, Cambridge, MA, 1974.

[156] F. M. Silva and L. B. Almeida, "Acceleration Techniques for the Backpropagation Algorithm," in *Proceedings of the EURASIP Workshop 1990 on Neural Networks*, 1990, pp. 110-119: Springer-Verlag.

[157] F. Bettayeb, S. Haciane, and S. Aoudia, "Improving the time resolution and signal noise ratio of ultrasonic testing of welds by the wavelet packet," *NDT & E International,* vol. 38, no. 6, pp. 478–484, September 2005.

[158] A. Van Nevel, B. DeFacio, and S. P. Neal, "An Application of Wavelet Signal Processing to Ultrasonic Nondestructive Evaluation," in *Review of*

Progress in Quantitative Nondestructive Evaluation, 2016, pp. 733-740: Springer US.

[159] D. L. Donoho, "De-noising by soft-thresholding," *IEEE Transactions on Information Theory,* vol. 41, no. 3, pp. 613-627, May 1995.

[160] B.-J. Yoon and P. P. Vaidyanathan, "Wavelet-based denoising by customized thresholding," in *Acoustics, Speech, and Signal Processing, 2004. (ICASSP '04). IEEE International Conference on*, Montreal, Canada, 2004, vol. 2, pp. ii-925-8.

[161] L. Deng and D. Yu, "Deep Learning: Methods and Applications," *Foundations and Trends in Signal Processing,* vol. 7, pp. 197-387, 30 Jun 2014.

[162] D. H. Hubel and T. N. Wiesel, "Receptive fields of single neurones in the cat's striate cortex," (in en), *The Journal of Physiology,* vol. 148, no. 3, pp. 574-591, 1 October 1959.

[163] G. E. Hinton and R. R. Salakhutdinov, "Reducing the dimensionality of data with neural networks," (in eng), *Science,* vol. 313, no. 5786, pp. 504-7, Jul 28 2006.

[164] C.-Y. Liou, W.-C. Cheng, and J.-W. Liou, Liou, Daw-Ran, "Autoencoder for words," *Neurocomputing,* vol. 139, pp. 84–96, 2 September 2014.

[165] J. Deng, Z. Zhang, and E. S. Marchi, B, "Sparse Autoencoder-Based Feature Transfer Learning for Speech Emotion Recognition," in *Affective Computing and Intelligent Interaction (ACII), 2013 Humaine Association Conference on*, 2013, pp. 511-516.

[166] I. T. Jolliffe, *Principal Component Analysis*, 2nd ed. (Spriner Series in Statistics). NY: Springer, 2002.

[167] A. V. Hall, "Methods for demonstrating Resemblance in Taxonomy and Ecology," (in en), *Nature,* vol. 214, no. 5090, pp. 830-831, 20 May 1967.

[168] M. N. Murty and A. K. Jain, "Knowledge-based clustering scheme for collection management and retrieval of library books," *Pattern Recognition,* vol. 28, no. 7, pp. 949-963, July 1995.

[169] M. S. Kankanhalli, B. M. Mehtre, and R. K. Wu, "Cluster-based color matching for image retrieval," *Pattern Recognition,* vol. 29, no. 4, pp. 701-708, April 1996.

[170] R. Krishnapuram, H. Fruigui, and O. Nasiraoui, "Fuzzy and Possibilistic Shell Clustering Algorithms and Their Application to Boundary Detection and Surface Approximation-Part I," *IEEE transactions on Fuzzy Systems,* vol. 3, no. 1, pp. 29-43, February 1995.

[171] R. Krishnapuram, H. Fruigui, and O. Nasiraoui, "Fuzzy and Possibilistic Shell Clustering Algorithms and Their Application to Boundary Detection and Surface Approximation-Part II," *IEEE transactions on Fuzzy Systems,* vol. 3, no. 1, pp. 44-60, February 1995.

[172] R. O. Duda and P. E. Hart, *Pattern Classification and Scene Analysis*. John Wiley & Sons, 1973.

[173] G. H. Ball and D. J. Hall, "A clustering technique for summarizing multivariate data," (in eng), *Behavioal Science,* vol. 12, no. 2, pp. 153-155, March 1967.

[174] S. P. Lloyd, "Least squares quantization in PCM," *IEEE Transactions on Information Theory,* vol. 28, no. 2, pp. 129-137, March 1982.

[175] S. N. Sivanandam and S. N. Deepa, *Introduction to Genetic Algorithms*. Springer, 2007.

[176] C. Darwin, *The origin of species*. United Kingdom: John Murray, 1859.

[177] D. Whitley, "A genetic algorithm tutorial," *Statistics and Computing,* vol. 4, no. 2, pp. 65-85, June 1994.

[178] A. Lipowski and D. Lipowska, "Roulette-wheel selection via stochastic acceptance," *Physica A: Statistical Mechanics and its Applications,* vol. 391, no. 6, pp. 2193–2196, 15 March 2012.

[179] G. H. Ball and D. J. Hall, "ISODATA, a novel method of data analysis and pattern classification," Stanford Research Institute, Menlo Park, California,April 1965.

[180] A. McNab and I. Stumpf, "Monolithic phased array for the transmission of ultrasound in NDT ultrasonics," *Ultrasonics,* vol. 24, no. 3, pp. 148-155, May 1986.